AFRL-RQ-WP-TR-2014-0158

SCIENTIFIC RESEARCH PROGRAM FOR POWER, ENERGY, AND THERMAL TECHNOLOGIES

Task Order 0001: Energy, Power, and Thermal Technologies and Processes Experimental Research

Subtask: Thermal Management of Electromechanical Actuation System for Aircraft Primary Flight Control Surfaces

Zachary A. Lammers

University of Dayton Research Institute

MAY 2014
Interim Report

AIR FORCE RESEARCH LABORATORY
AEROSPACE SYSTEMS DIRECTORATE
WRIGHT-PATTERSON AIR FORCE BASE, OH 45433-7542
AIR FORCE MATERIEL COMMAND
UNITED STATES AIR FORCE

NOTICE AND SIGNATURE PAGE

This report was cleared for public release by the USAF 88th Air Base Wing (88 ABW) Public Affairs Office (PAO) and is available to the general public, including foreign nationals.

Copies may be obtained from the Defense Technical Information Center (DTIC) (http://www.dtic.mil).

AFRL-RQ-WP-TR-2014-0158 HAS BEEN REVIEWED AND IS APPROVED FOR PUBLICATION IN ACCORDANCE WITH ASSIGNED DISTRIBUTION STATEMENT.

*//Signature//	//Signature//
GREGORY L. RHOADS	JACK U. VONDRELL, Chief
Program Manager	Mechanical and Thermal Systems Branch
Mechanical and Thermal Systems Branch	Power and Control Division
Power and Control Division	Aerospace Systems Directorate

*Disseminated copies will show "//Signature//" stamped or typed above the signature blocks.

REPORT DOCUMENTATION PAGE

Form Approved
OMB No. 0704-0188

1. REPORT DATE *(DD-MM-YY)*	2. REPORT TYPE	3. DATES COVERED *(From - To)*
May 2014	Interim	20 July 2012 – 01 May 2014

4. TITLE AND SUBTITLE
SCIENTIFIC RESEARCH PROGRAM FOR POWER, ENERGY, AND THERMAL TECHNOLOGIES
Task Order 0001: Energy, Power, and Thermal Technologies and Processes Experimental Research
Subtask: Thermal Management of Electromechanical Actuation System for Aircraft Primary Flight Control Surfaces

5a. CONTRACT NUMBER
FA8650-12-D-2224-0001

5b. GRANT NUMBER

5c. PROGRAM ELEMENT NUMBER
62203F

6. AUTHOR(S)
Zachary A. Lammers

5d. PROJECT NUMBER
3145

5e. TASK NUMBER
N/A

5f. WORK UNIT NUMBER
Q0Z7

7. PERFORMING ORGANIZATION NAME(S) AND ADDRESS(ES)
University of Dayton Research Institute
Energy Technology and Materials Division
300 College Park
Dayton, OH 45469-0170

8. PERFORMING ORGANIZATION REPORT NUMBER

9. SPONSORING/MONITORING AGENCY NAME(S) AND ADDRESS(ES)
Air Force Research Laboratory
Aerospace Systems Directorate
Wright-Patterson Air Force Base, OH 45433-7542
Air Force Materiel Command
United States Air Force

10. SPONSORING/MONITORING AGENCY ACRONYM(S)
AFRL/RQQM

11. SPONSORING/MONITORING AGENCY REPORT NUMBER(S)
AFRL-RQ-WP-TR-2014-0158

12. DISTRIBUTION/AVAILABILITY STATEMENT
Approved for public release; distribution unlimited.

13. SUPPLEMENTARY NOTES
PA Case Number: 88ABW-2013-4968; Clearance Date: 25 Nov 2013. This report is a Master of Science thesis.

14. ABSTRACT
Electromechanical actuation systems (EMAS) are a key component in the more electric aircraft (MEA). EMAS operate on a power-on-demand basis, reducing energy consumption typically required by hydraulic systems to maintain hydraulic pressure. Additionally, EMAS reduce system weight, lessening system maintenance and operating costs. EMAS convert electrical energy to mechanical energy via an electric rotary machine combined with a rotary to linear or rotary to rotary conversion mechanism. Electrical energy required to complete useful mechanical output depends on the efficiency of the system. Therefore, it is important to characterize electrical and thermal loads associated with an EMAS for primary flight control surfaces, such as an aileron. Electric power draw and thermal management are among the most important parameters of research in electromechanical actuation for a primary flight control (PFC) surface. The aim of this thesis was to build an experimental EMAS system and methodology to analyze EMAS performance against realistic duty cycles and mission environments. Thermal energy, in addition to the rate of change of temperature and temperature difference for temperature sensitive components, was used to determine the most thermally malignant profiles and potential thermal design points. It was found that transient missions of an EMAS presented the greatest electric demand of the aircraft electric power supply system, and holding presented the greatest thermal stress of the EMAS, where the EMAS operated at0 percent efficiency and all electric power was converted to heat.

15. SUBJECT TERMS
electromechanical, actuation, thermal management

16. SECURITY CLASSIFICATION OF:			17. LIMITATION OF ABSTRACT:	18. NUMBER OF PAGES	19a. NAME OF RESPONSIBLE PERSON (Monitor)
a. REPORT	b. ABSTRACT	c. THIS PAGE			Gregory L. Rhoads
Unclassified	Unclassified	Unclassified	SAR	242	19b. TELEPHONE NUMBER *(Include Area Code)* N/A

THERMAL MANAGEMENT OF ELECTROMECHANICAL ACTUATION SYSTEM FOR AIRCRAFT PRIMARY FLIGHT CONTROL SURFACES

Thesis

Submitted to

The School of Engineering of the

UNIVERSITY OF DAYTON

In Partial Fulfillment of the Requirements for

The Degree of

Master of Science in Renewable and Clean Energy

By

Zachary A. Lammers

UNIVERSITY OF DAYTON

Dayton, Ohio

May, 2014

TABLE OF CONTENTS

LIST OF FIGURES

LIST OF TABLES

LIST OF SYMBOLS & ABBREVIATIONS

AC	Alternating Current
ACM	Active Cooling Modules
AEA	All Electric Aircraft
CFD	Computational Fluid Dynamics
CG	Centre of Gravity
COE	Conservation of Energy
COP	Center of Pressure
DAQ	Data Acquisition
DC	Direct Current
EC	Environmental Chamber
EHA	Electro-Hydrostatic Actuator
EMA	Electromechanical Actuator
EMAS	Electromechanical Actuator System
EMATMS	Electromechanical Actuator Thermal Management System
EMI	Electromagnetic Interference
EOA	Energy Optimized Aircraft
EPAD	Electrically Powered Actuation Design Validation Program
FEA	Finite Element Analysis
FBW	Fly-By-Wire
FCC	Flight Control Computer
FHPCP	Flexible Heat Pipe Cold Plate
HPEAS	High Performance Electric Actuation System
HPU	Hydraulic Power Unit
HSM	Hydraulic Service Manifold
IAP	Integrated Actuator Package
IGBT	Insulated Gate Bipolar Transistor
INVENT	Integrated Vehicle Energy Technology program
LabVIEW	Laboratory Virtual Instrumentation Engineering Workbench
LHP	Loop Heat Pipe
LVDT	Linear Voltage Displacement Transducer
MACE	Micro-technologies for Air-cooled Exchangers
MATLAB	Matrix Laboratory
MEA	More Electric Aircraft
MIL-HDBK	Military Handbook
MIL-STD	Military Standard
MIT	Massachusetts Institute of Technology
NASA	National Aeronautics and Space Administration
NI	National Instruments
NJTT	Near Junction Thermal Transport
NTI	Nano-Thermal Interfaces
PBW	Power-By-Wire
PCE	Power Control Electronics
PCM	Phase Change Material
PCU	Power Control Unit
PCME	Power Control and Monitor Electronics

PFC	Primary Flight Control
PID	Proportional, Integral, Derivative
PWM	Pulse Width Modulation
PMDC	Permanent Magnet Direct Current
RT	Real Time
RTD	Resistive Temperature Detector
SNR	Signal to Noise Ratio
SRA	Systems Research Aircraft
TC	Thermocouple
TES	Thermal Energy Storage
TGP	Thermal Ground Plane
TM	Thermal Management
TMT	Thermal Management Technology
TMS	Thermal Management System
Vac	Volts Alternating Current
Vdc	Volts Direct Current
VI	Virtual Instrument
F	Force, N
v	Velocity, mm/s
$\frac{dW_e}{dt}$	Electrical Power, W
$\frac{dW_m}{dt}$	Mechanical Power, W
W_e	Electrical Work, J
W_m	Mechanical Work, J
Q	Heat, J
E	Energy, J
I	Electrical Current, A
V	Electrical Voltage, V
R	Electrical Resistance, Ω
Δt	Sampling Period, s
T_f	Final Time, s
T_i	Initial Time, s
x	Position, mm

ACKNOWLEDGEMENTS

First, I would like to thank my advisor, Dr. Quinn Leland, for providing me the opportunity to work on such a challenging and rewarding project. Secondly, I offer many thanks for the love and support offered by my family and fiancée, Kerry Allen. Additionally, I owe my committee members, Dr. Jamie Ervin and Dr. Bang Tsao a debt of gratitude for their guidance and participation. Lastly, I would like to thank the many individuals at AFRL who offered their valuable time and encouragement over the past 2 years.

CHAPTER 1

INTRODUCTION

In typical military jet, turbine engines provide the lifeline to the three major aircraft systems—power generation system, environmental control system, and fuel system. Accessory shafts power accessory drives which pressurize aircraft hydraulic systems and drive electrical power generators (Moir & Seabridge, 2008). In addition to providing the primary means of thrust, turbine engines supply bleed air to Environmental Control Systems (ECS). Additionally, bleed air provides pressure for hydraulic reservoirs and fuel tanks (Moir & Seabridge, 2008). This simple overview of aircraft systems interconnectedness and interaction highlights the complexity of conventional military aircraft systems. In short, four main forms of energy exist in the conventional architecture—pneumatic, hydraulic, mechanical, and electrical. Increasing complexity can reduce overall aircraft efficiency. For instance, a fault in bleed air valve or channel could cascade throughout each of the three major aircraft systems. An alternative to conventional aircraft architecture was found in a more electric aircraft (MEA), which alleviate the power generation system of its hydraulic components. Electrical power systems, which are believed to be far more efficient, would account for all on-board power management and drive systems (Rosero, Ortega, Albada, & Romeral, 2007). This would remove heavy hydraulic pumps, lines, and valves and reduce aircraft dependence on bleed air, a costly feature which requires conditioning to desired temperatures and pressures for use.

Flight control, one of the most important facets of powered flight, was transformed by the establishment of MEA architecture. Flight control systems have made considerable advances over the years, from the Wright's first glider which relied on manually warping wings to the F-35 Joint Strike Fighter (JSF) whose design is aerodynamically unstable and requires fly-by-wire technology. Modern aircraft employ fly-by-wire and auto stabilization processes executed by an on board flight computer in order to maintain flight control (Moir & Seabridge, 2008).

Flight control systems utilize primary and secondary control surfaces to maneuver in pitch, roll, and yaw situations and dampen oscillations associated with those tasks, such as a Dutch Roll under roll/yaw maneuvers. Primary flight control surfaces include the following components for a tactical jet: canard, flaperons (flaps and ailerons), and rudder. Canards are used in fixed wing airframes, like most modern fighter aircraft and render the aircraft unstable, necessitating an active computer driven control system (Moir & Seabridge, 2008). Secondary flight surface provide high lift control by increasing wing camber and improving wing aerodynamics (Moir & Seabridge, 2008). A cost associated with increased lift from secondary devices is increased drag. However, combat aircraft are equipped with high thrust capable engines which can overcome this penalty.

Flight control linkage systems connect the pilot with the control surfaces responsible for maneuvering. Combat aircraft typically employ a push-pull rod assembly while commercial aircraft utilize a cable and pulley scheme. In both setups, trim units, feel units, and power control units (PCUs) provide the pilot with the mechanical advantage necessary to execute maneuvering commands under enormous loads in high speed flight.

"The key element in the flight control system, increasingly so with the advent of fly-by-wire and active control units, is the power actuation" (Moir & Seabridge, 2008). Traditional

powered flight controls are made up of a hydraulically powered linear actuator, servovalve to direct hydraulic flow and mechanical feedback and summing linkages to achieve pilot command. Eventually, multiplex redundant actuation was made possible through fly-by-wire-solutions, comprising multiple electrical and hydraulic signals as opposed to one mechanical linkage. Introduction of alternating current electrical systems permitted the development of an Integrated Actuator Package (IAP) (Moir & Seabridge, 2008). IAP's utilized a three phase constant speed electrical motor to drive a variable displacement hydraulic pump and power the actuator ram. Continuous operation of the hydraulic pump, characteristic of IAP designs, presented significant power losses and heat generation over flight duration. Electro-Hydrostatic Actuators (EHA's) alleviated this problem via power on demand operation. Power on demand operation was made possible by using power electronics to drive a variable speed motor which pressurized a fixed hydraulic pump (Moir & Seabridge, 2008). EHA's offered improvements over traditional hydraulic flight controls, but still suffer from some disadvantages with the use of hydraulic fluid—leakage, weight, and maintenance (Pointon 2007). Finally, increasing pace in aviation towards a MEA through advancement in permanent magnet direct current (PMDC) motors operating at 270 Vdc, high power solid state switching devices, and lightweight microprocessors yielded the Electromechanical Actuation System (EMAS), which completely eliminated the need for hydraulic energy (Moir & Seabridge, 2008). Electromechanical Actuators (EMA's) utilize power/control electronics to operate an electric motor which drives a mechanical transmission typically made up of a reduction gear box and a ball/roller screw (linear actuator) or flanged housing (rotary hinge-line actuator) assembly (Pointon 2007). "The basic building blocks for control actuator are solid-state power electronics and variable speed motor drives." (Rosero, Ortega, Albada, & Romeral, 2007)

EMA's offer features such as power on demand, reduced weight and maintenance, and a reduction in lifecycle costs. EMAS provide an energy efficient means to flight surface control, thus reducing loads required by conventional hydraulic systems. However, several thermally related EMAS challenges remain unanswered. Therefore, an effort was undertaken in order to characterize the energy loads associated with this alternative actuation and its systems level effect. The work described in this thesis is primarily concerned with the thermal management of EMAS. The objectives of the research outlined herein include:

- Review of various thermal management methods and their effectiveness
- Research and analysis of dynamic environment conditions experienced in missions with respect to a modern tactical aircraft
- Construct a Test Apparatus capable of experimentally characterizing EMAS heat generation and subsequent cooling requirements which:
    - Implement dynamic environment conditions
    - Is capable of integrating thermal management proof of concepts

CHAPTER 2

BACKGROUND

EMAS architectures are distributed and can provide increased survivability and aircraft maintainability, and reduced ground service requirements when compared with traditional centralized hydraulic systems (Croke, 1994). EMA's substitute hydraulics with an electric motor and mechanical transmission to provide the motive force which moves the surface. EMA's have been used in the past for utility purposes, but the power and response times of such actuators were less than that required for flight control actuation (Moir & Seabridge, 2008). Three technology advancements supported EMA viability: rare earth magnets for 270 Vdc motors, high power solid state switches, and lightweight microprocessors for actuator control (Moir & Seabridge, 2008). EMA's became attractive candidates for hydraulic actuation replacement because of their power on demand characteristic which remedied inefficiency associated with continuous operation found in legacy aircraft. An image of a generalized EMA and its main components follows in Figure 2.1.

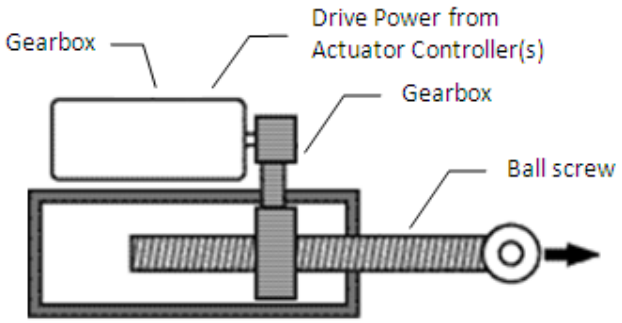

Figure 2.1 Electromechanical Actuator Cross Section (Jensen, 2000)

The foundation for EMAS characterization stems from experiences noted in "Flight Test Experience with an Electromechanical Actuator on the F-18 Systems Research Aircraft" (Jensen, 2000) completed by the NASA Dryden Flight Research Center in 2000. In their efforts to develop and test a power-by-wire (PBW) actuation technology for a primary control surface, the group replaced a conventional hydraulic actuator of an aileron with an EMA. The two primary pieces of hardware making up the system were the EMA and its Power Control and Monitor Electronics or PCME. Figure 2.2 is an image of both devices.

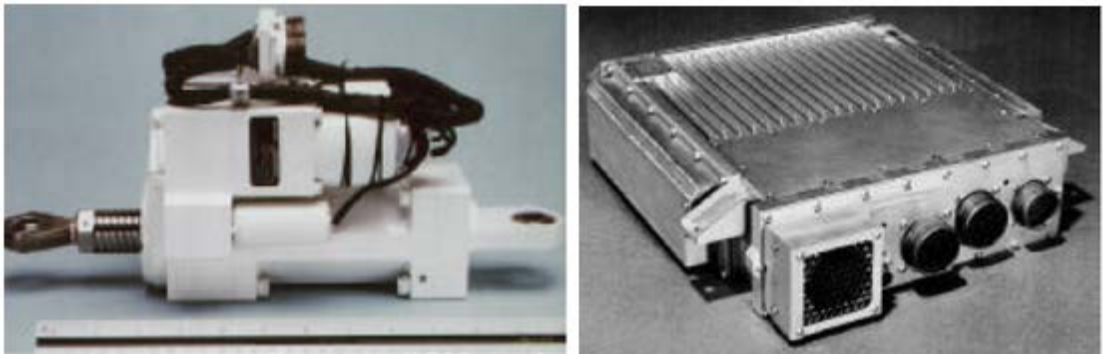

Figure 2.2 EMA and PCME from EPAD (Jensen, 2000)

Numerous parameters were recorded over the flight envelope in order to evaluate the performance of the EPAD EMA. Parameters measured during tests included but were not limited to flight conditions (altitude, Mach number, and atmospheric temperature), flight control parameters (acceleration and dynamic pressure), and EMA performance parameters (position and load). Several parameters were measured to capture EMA dynamics and compare its demands to conventional hydraulic means. In their work, it was thought highly transient actuation loads would account for the majority of heat generation over a mission. However, it was found majority of the heat was generated during steady level flight under constant mechanical load while the servomotor maintained constant torque, elevated current draw, and subsequent heat generation due to winding resistance. Identifying thermally malignant segments of flight envelopes and thermally stressful scenarios for an EMAS remain important issues in MEA development.

Modern EMA architectures drastically altered the dynamics of power flow on the electrical bus (Pigg, et. al 2012). In EMAS design and integration, actuation peak electrical loads led to the redesign of aircraft power generation systems. Representative transient power profiles demonstrated peak-to-average power ratios as high as 5-1 for 50 to 5000 milliseconds (Wells, et. al 2008). The nature of these electrical loads may pose a threat to the thermal stability of an EMAS. Therefore, EMAS associated electrical loads and heat generation is two key design constraints to the success of modern EMAS architectures.

"5^{th} generation aircraft have 3-5 times the heat load of legacy platforms while being limited in their ability to reject heat to the environment." (FedBizOps.Gov, 2009) Heat loads have grown exponentially in recent decades as a result of advanced avionics, advanced mission systems, and increased power density. Additionally, composite structures and aircraft skins exhibit greater thermal resistance than traditional aircraft materials such as aluminum, compounding thermal challenges.

Based on those challenges, an effort has been taken to experimentally characterize electrical and thermal parameters under a wide variety of simulated mission profiles. Simulated profiles aimed to provide insight to EMAS loads under varying mission tasks, such as roll, dive, high rate climb, steady level flight, and takeoff/landing.

CHAPTER 3

LITERATURE SURVEY

3.1 Thermal Management System Design Overview

Introducing thermal management will improve EMAS reliability and survivability. But weight constraints and actuator access in addition to increased power demands by the TMS all provide challenges for TMS designers. There are a few common approaches for TMS design. The first approach is to develop a solution which limits the maximum allowable temperature under the worst case heat load and environment conditions. This type of approach typically leads to heavy, costly, and overdesigned systems. Another approach to TMS design focuses on a nominal operating range while accepting short durations of operation beyond that range. For example, a TMS could be designed to limit EMAS operating temperature to 80 °C continuously and permit excursions up to 125 °C for 2 minutes.

Peak power levels in flight actuation can be significant but are typically short in duration and occur much less frequently than the average power demands. In the past actuator duty cycle was explained by the 80/20 rule: 20% of the load for 80% of the time and 100% of the load for 20% of the time (Bland 1992). This type of duty cycle lends itself to thermal energy storage, which when coupled with an effective heat transfer mechanism can significantly reduce size, weight, and volume of a thermal management system (TMS). Thus, TMS's can be designed for nominal heat rejection by incorporating thermal energy storage, TES. Thermal energy storage most generally takes on the form of a phase change material which is designed to melt at an elevated temperature.

Even with design efforts that account for maximum heat dissipation requirements, thermal margins are necessary to ensure the survivability of the system. Because aircraft environments have extreme variations and an EMAS duty cycle is transient in nature several uncertainties arise. Thermal uncertainty margin is a safety factor applied to the worst case temperature prediction through the vehicle's envelope (Thunnissen, 2004).

The flow diagram in Figure 3.1 highlights three primary areas of interest in thermal management system design. These components each can be independently analyzed; however under the application of flight are highly interrelated. In legacy aircraft hydraulic circuits provide waste heat removal produced by surface actuators; however EMA's have no such mechanism and are a distributed system. Fuel is a potential heat sink, but re-routing fuel circuit re-introduces reliability/maintainability/safety issues eliminated by the removal of hydraulic circuits (Bland 1992). Ultimately, aircraft structure and then ambient air surrounding the aircraft become the heat sink. In this work the sink was established as ambient air nearest the wing. The sink is a dynamic parameter as the aircraft moves throughout its envelope at varying speed and environmental conditions.

Lastly, transport which bridges the gap between source and sink is the principal component in managing the EMAS thermal state. The transport mechanism or medium which intends to improve heat transfer between source and sink can take several forms. A quick literature search will return technologies such as heat pipes, loop heat pipes, fan convective cooling, water cooling, heat spreaders, vapor-compression cycles, and phase change materials.

Each of these TM technologies contain unique benefits and pitfalls with respect to cost, weight, energy requirement, volume, and most importantly heat transfer performance under harsh conditions. Techniques and designs outlined in this section should aid in analyzing and comparing TM technologies for various source and sink configurations. Baseline EMAS configuration is characterized by free convection and whatever inherent means of cooling EMAS components possess.

Figure 3.1 TMS Flow Diagram

3.2 Heat Source

The groundwork for EMAS characterization and TMS efforts stems from experiences noted in NASA EPAD research (Jensen, 2000). Figure 3.2 is a simple overview of the hardware used in their test pertinent to analyzing EMAS thermal response.

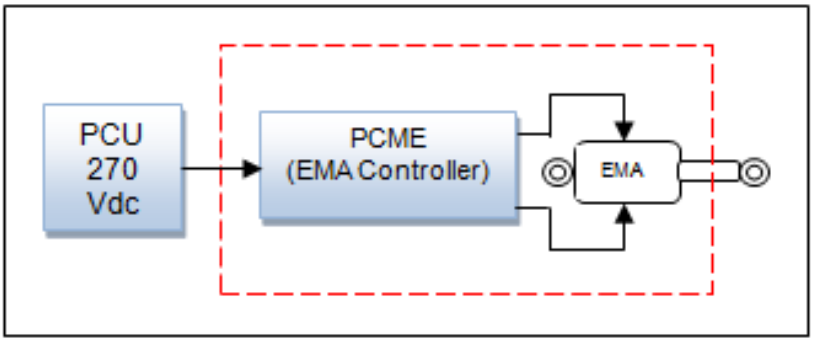

Figure 3.2 EMAS Architecture (Jensen, 2000)

Numerous parameters were recorded over the duration of a flight envelope. These parameters characterized the performance of the EMA as a function of typical mission tasks. In their research NASA found electrical power draw and subsequently thermal energy generation were key parameters while maintaining aircraft control loads (Jensen, 2000). Two major sources in EMAS heat generation include the PMDC motor and its drive. Additionally, it was thought highly transient actuation loads would account for majority of thermal generation over the duration of a mission (Jensen, 2000). However, it was determined majority of heat was generated during steady level flight under constant mechanical load, requiring the servomotor to maintain constant torque output, high current draw, and heat generation due to winding resistance (Jensen, 2000).

EMAS energy is a function of commanded position and aeroload exerted on the control surface. EMAS loads can vary enormously over the mission, changing with aircraft speed and commanded maneuvers such as roll, dive, high rate climb, steady level flight, and takeoff / landing approaches. Figure 3.3 shows a simplified load history for typical operation.

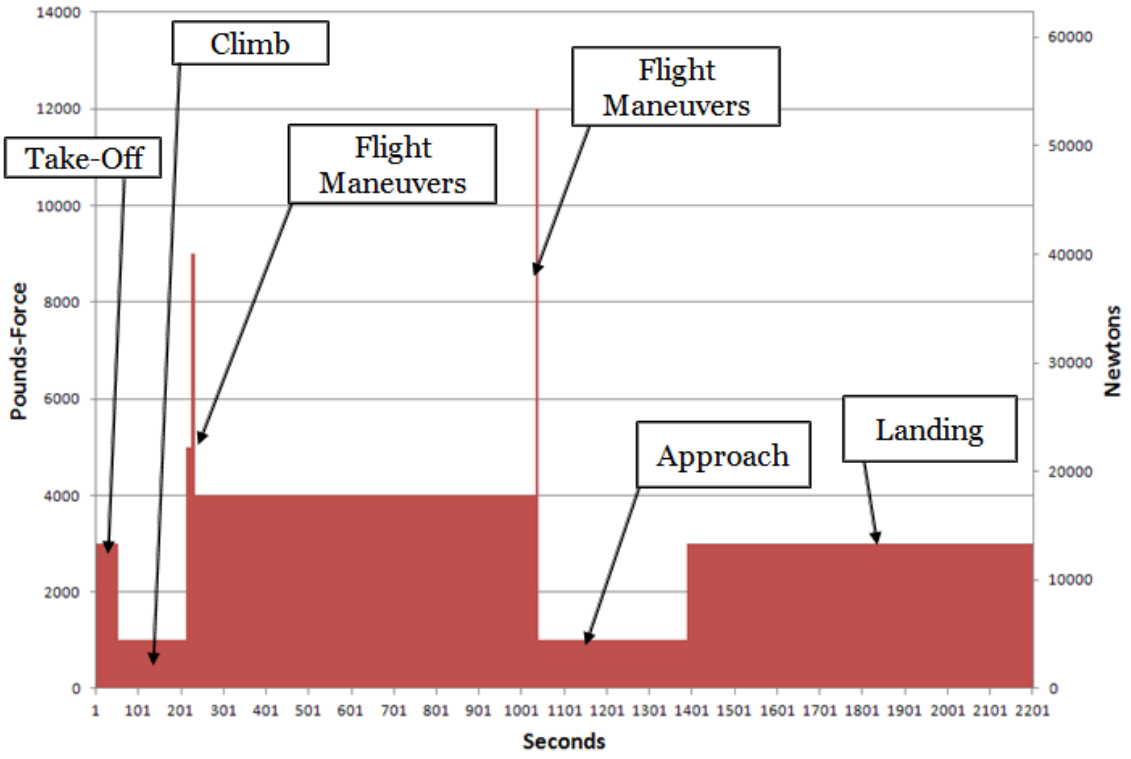

Figure 3.3 EMAS Typical Duty Cycle (Blanding, 2008)

Each of these maneuvers present varying degrees of heat generation. For instance, when aircraft stall speed becomes a concern and maximum lift is required by control surfaces, ailerons maintain large deflections for extended periods of time driving motor and controller temperatures up (Moir & Seabridge, 2008). With this, a TMS will require the ability to meet peak heat loads under intermittent actuation, but also shed heat for extended periods of time under continuous actuator operation.

Generally, peak heat load is determined in addition to the total heat dissipated during the flight. These values are used in determining the size and characteristics of each TM system. The potential for heat transfer being a function of temperature difference, suggests TM design must identify available sink temperatures and their variation.

3.3 Heat Sink

For majority of the TM technologies highlighted in this paper, the heat sink is either ambient air next to the wing's exterior or for the case of convective cooling, internal bay air. Typical thermal zones that exist in a tactical aircraft include conditioned and un-conditioned bays (Bar-shalom, 1989). Testing executed on NASA's SRA housed the EMAS in an un-conditioned bay within the wing (Navarro, 1997). An example location of actuators tested by NASA Dryden Flight Research Center is shown in Figure 3.4.

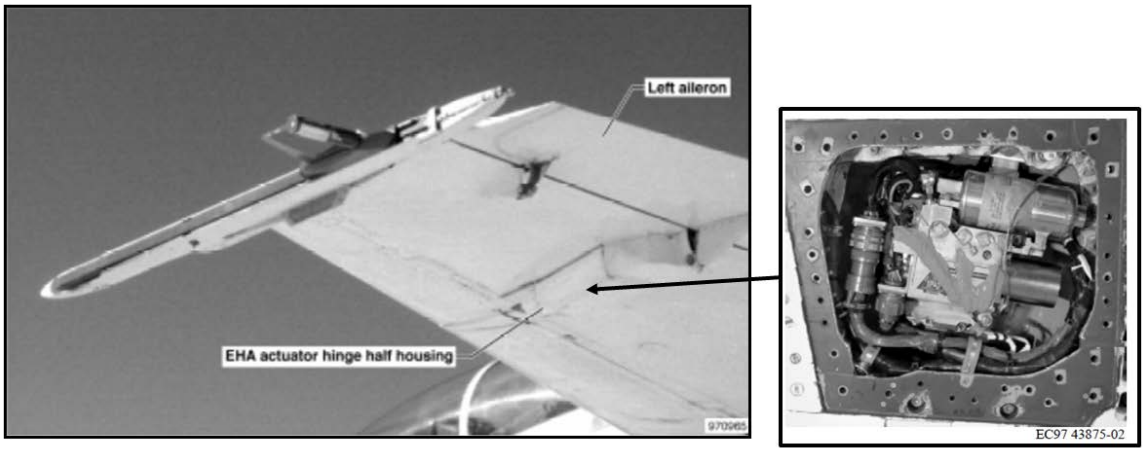

Figure 3.4 EHA/EMA Location (Navarro, 1997)

For the case of unconditioned bay, if bay temperature approaches that of the bay equipment less heat can be shed to the bay. Therefore, a different thermal path which links source and sink is required for additional heat removal. Additionally thermal energy storage could be used to store accumulated heat for dissipation at a later time. In these cases heat spreaders and heat pipes provide improved thermal paths and phase change materials offer energy storage. Loop heat pipes (LHP's) and Flexible Heat Pipe Cold Plates (FHPCP's) typically couple the condenser with aircraft skin (Gernert 1991). Boundary conditions at the condenser can be a controlling factor in cooling performance (Fleming, 2006). Establishing ambient, bay, and component temperatures throughout a flight envelope aids in defining the potential for heat transfer between regions.

In primary flight control (PFC) testing it is important to understand flight envelope and determine max altitude in addition to the number of excursions from this altitude. Military jets undergo rapid rates of change in altitude, which leads to rapid rates of temperature change. Aircraft are expected to operate in a wide range of temperatures, from arctic to desert conditions. The effect of the ambient temperature on equipment internal temperature, especially when powered on, is a major concern. Some additional design concerns include extreme temperature ranges, extended periods of hot/cold soak, direct sunlight exposure, and temporal variation of aircraft bay temperatures. In addition to the wide ambient operating temperatures, thermal management designs are expected to perform at altitudes up to 40,000 ft. under supersonic conditions and accommodate -3 to 9 g of body force.

Air properties vary considerably with altitude and also vary with day to day weather conditions. Understanding trends in temperature throughout the atmosphere in typical and hot or cold days is crucial for evaluating heat sinking potential and design of thermal management means. Ambient conditions in Figure 3.5 include two sources— "The International Standard Atmosphere" from (Cavcar, 2013) and MIL-HDBK-310. The atmospheric model serves as a baseline for typical conditions, whereas MIL-STD demonstrates atmospheric temperatures for extreme hot and cold, 1%, 5%, 10% and 20% frequency of occurrence hot and cold days. The range of the data is from 0-22km which covers the entire troposphere and tropopause boundary and a small portion of the stratosphere where the temperature is constant. Typical cruising altitude for subsonic transport jet is 11km and the ceiling for many fighter craft is a little more than 12km (Moir & Seabridge, 2008). The highest temperature occurs at sea level

(approximately 40 °C) and temperature decreases at a rate of about 6.5°C/km up to 12 km where temperature becomes relatively constant (Cavcar, 2013). These values characterize the envelope of the aircraft under consideration and provide information for conditions the aircraft will experience.

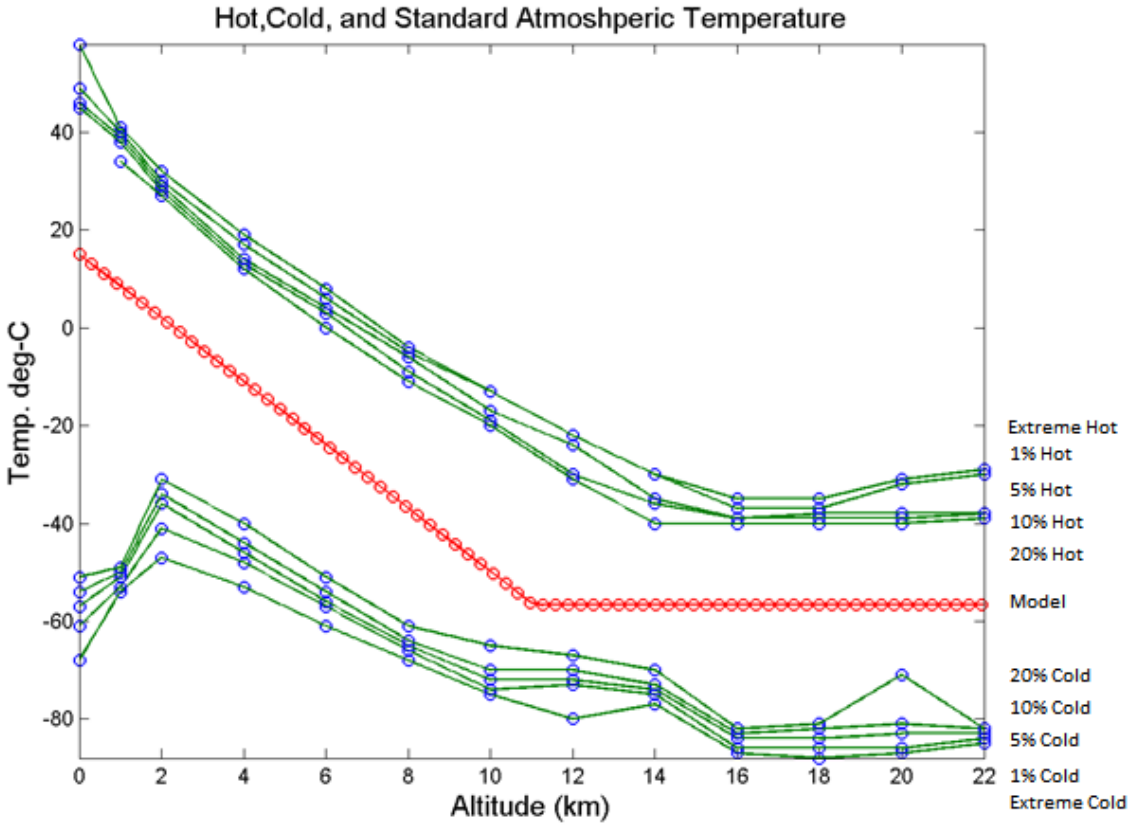

Figure 3.5 MIL-HDBK-310 and Model Atmospheric Temperature (Cavcar, 2013)

A typical Mach-altitude flight envelope of a modern tactical aircraft is shown Figure 3.6 (Bar-shalom, 1989). This information in conjunction with external atmospheric conditions highlighted above can be used in developing an adiabatic wall temperature envelope.

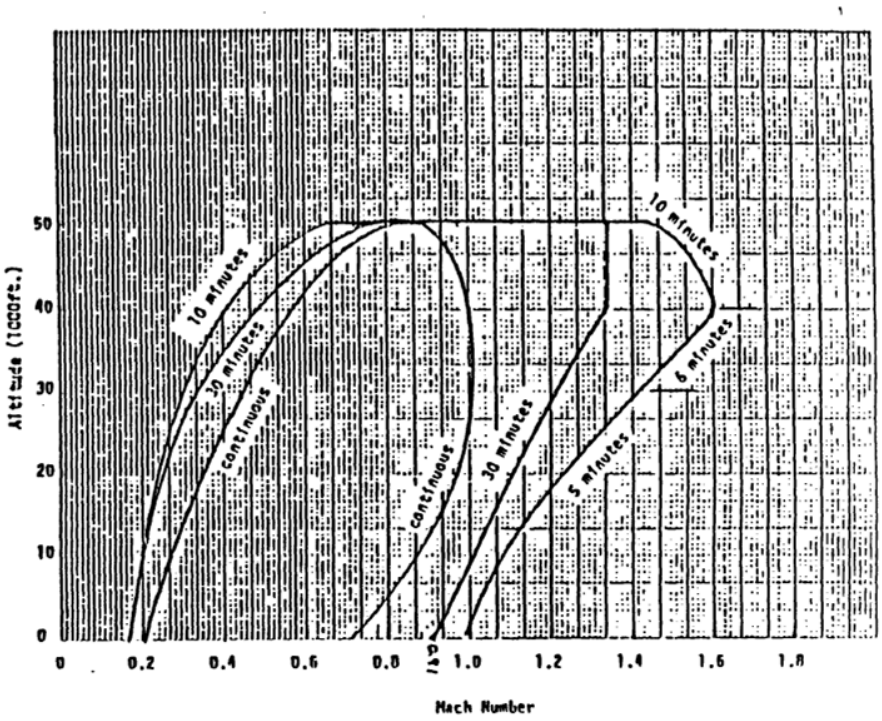

Figure 3.6 Typical Flight Envelope (Bar-shalom, 1989)

Occasionally flight speeds in the transonic and supersonic flight regimes are necessary. Under these scenarios temperatures in the aircraft boundary layer exceed that of ambient air due to frictional heating. Figure 3.7 demonstrates adiabatic wall temperature as a function of position and air speed in relation to free stream temperature.

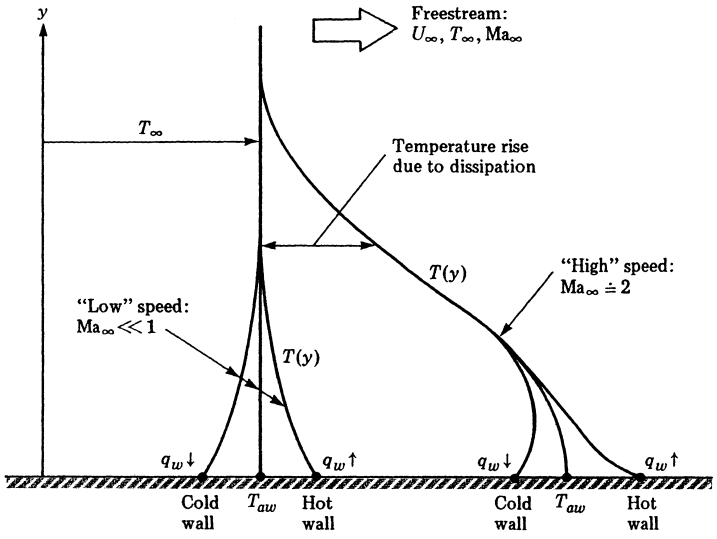

Figure 3.7 Temperature Profile over Flat Plate for Low & High Speed Flow (White, 1984)

Note, when Mach number M<<1, adiabatic wall temperature equals free stream temperature (White, 1984). For scenarios where M<1 it is common to utilize a standard atmospheric model to relate air temperature, pressure, and density to altitude or MIL-HDBK-310 for actual air temperature, pressure, and density conditions per altitude.

Adiabatic wall temperature as a function of altitude and flight speed can greatly affect the potential for heat transfer. Embedded in this relationship is the variation in air properties from varying altitude, climatic and local weather conditions. TM design can account for adiabatic wall temperature as a function of altitude and airspeed based on theory of high speed flow over a flat plate. This method was used by Flemming, et. al in "Aircraft Thermal Management Using Loop Heat Pipes: Experimental Simulation of High Acceleration Environments Using the Centrifuge Table test Bed." (Flemming 2006)

To demonstrate the importance of considering adiabatic wall temperature in heat sink characterization adiabatic wall temperature was calculated and compared with ambient air temperature for a simplified Mach-altitude envelope. The flight sequence included a climb from 0 to 10,000 ft., cruise at 10,000 ft. and Mach 0.9 for 800 seconds, followed by a return to sea level. Adiabatic wall temperature was a function of Reynolds number, ambient temperature, and Mach number:

$$T_{aw} = T_\infty \left(1 + r\frac{\gamma - 1}{2} M_\infty^2\right)$$

Ambient temperature is a function of altitude and was based on the atmospheric model derived in (Cavcar, 2013):

$$T_\infty = T_0 - 6.5 * \frac{h}{1000}$$

where, T_0 = 15 °C and $h = altitude, m$

Reynolds number was calculated based on the flow free stream properties and position along the plate (wing):

$$Re = \frac{U_\infty x}{\nu_\infty}$$

$$Re < 500000 \ \therefore Laminar \therefore r_{laminar} = 0.84$$

$$Re > 500000 \ \therefore Turbulent \therefore \ r_{turbulent} = 0.89$$

Free stream velocity was calculated from the product of Mach number and the speed of sound:

$$U_\infty = M_\infty a_\infty$$

$$a_\infty = \gamma R T_\infty$$

where, $T_{aw} = Adiabatic\ Wall\ Temperaure, °C$

$Re = Reynolds\ Number$

$U_\infty = free\ stream\ velocity, \ \frac{m}{s}$

$a_\infty = free\ stream\ speed\ of\ sound$

$M_\infty = free\ stream\ Mach\ number$

$x = position\ along\ plate, \ 0.5\ m$

$\nu_\infty = kinematic\ viscosity, \ 0.000015\ \frac{m^2}{s}$

$\gamma = specific\ heat\ ratio,\ 1.4$

$R = dyr\ air\ gas\ constant,\ 287\frac{J}{kg-K}$

$T_\infty = free\ stream\ temperature, ^\circ C$

$r_{laminar} = recovery\ factor\ for\ laminar\ flow$

$r_{turbulent} = recovery\ factor\ for\ laminar\ flow$

Figure 3.8 shows resulting adiabatic wall and free stream temperature trends from the example calculation carried out above, assuming Mach 0.9. During cruise, adiabatic wall temperature is considerably greater than free stream temperature, indicating the importance of accounting for adverse thermal gradients during TMS design.

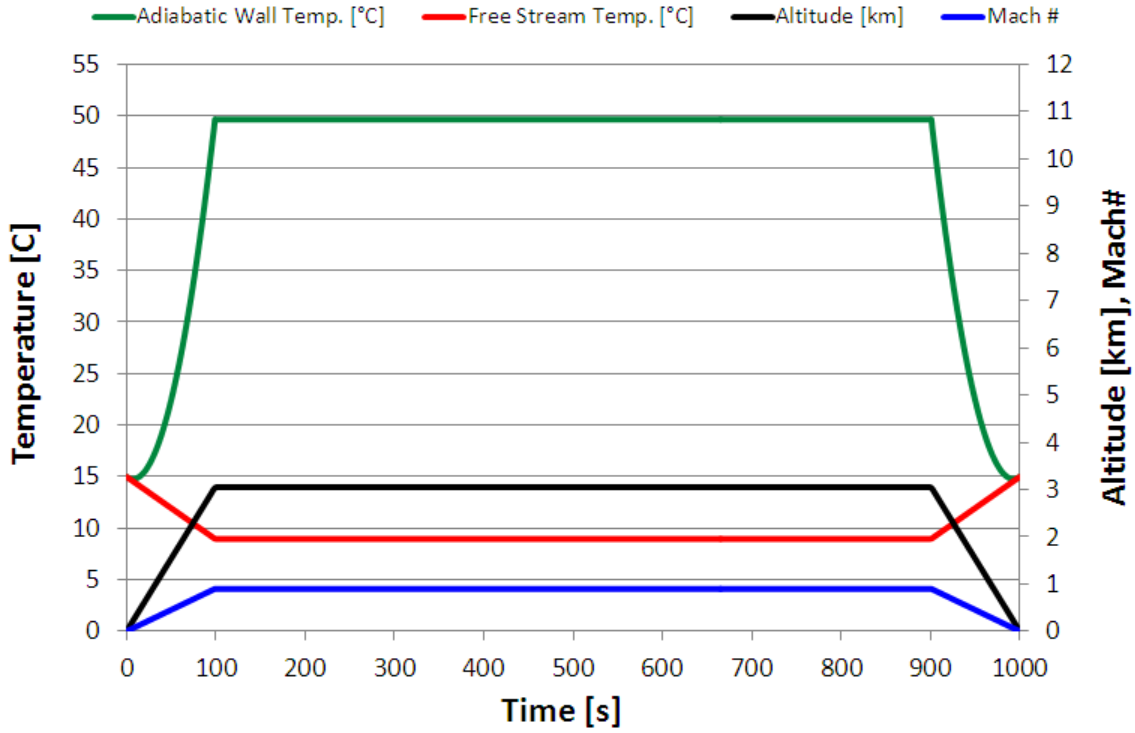

Figure 3.8 Calculated Adiabatic Wall Temperature

A typical mission flight profile for a medium sized military transport includes an initial ascent to 6 km (20,000 feet) followed by 100 minutes of cruise with intermittent periods of turbulence (Simsic, 1991). This sequence of events is completed by a descent to sea level, low-altitude terrain following, approach and landing. Figure 3.9 describes this variation in altitude as a function of flight phase. More importantly, it establishes the ambient temperature on a typical day over the course of a mission because ambient temperature is a well-known function of altitude (Cavcar, 2013).

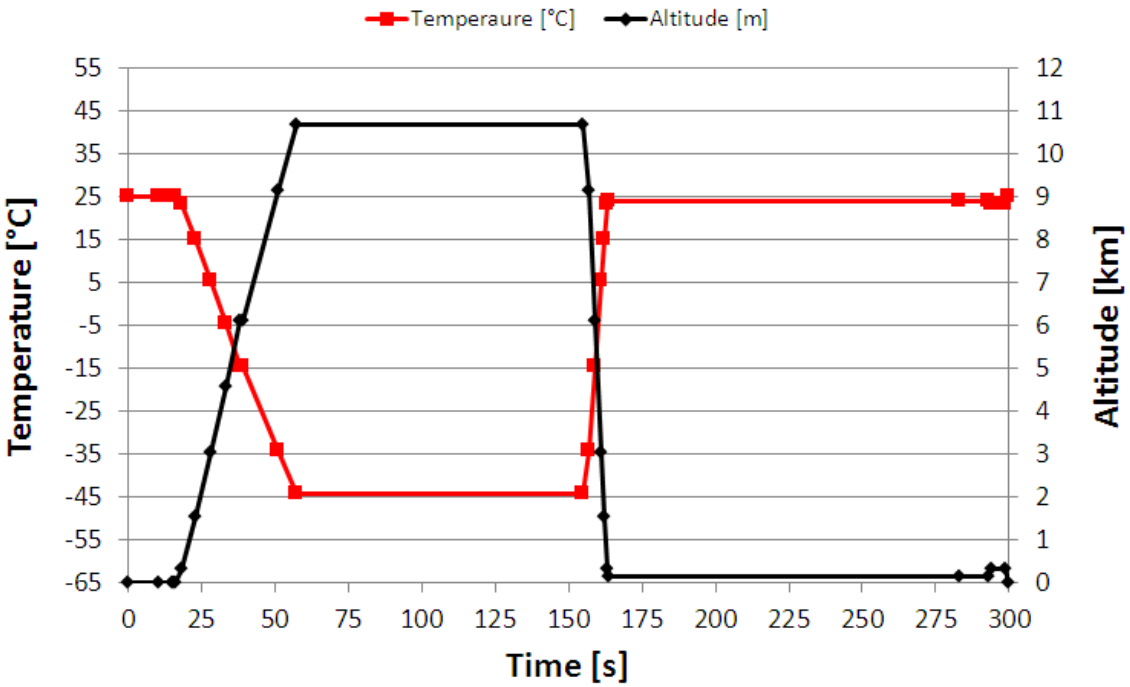

Figure 3.9 Flight Phase as Function of Altitude and Time (Simsic, 1991)

During ground hold conditions, bay cooling requirements are greater due to external heating of the aircraft surface and increased bay temperatures. But in flight, the temperature difference between the bay and ambient grows resulting in increased heat transfer through the aircraft skin (McCarthy, 2008). Heat sink conditions and worst case heat sink scenarios directly impact TMS design specifications. Therefore, knowledge of these parameters relative to flight envelope and variety of mission scenarios is required for effective TMS conceptualization, design, and commission. With these details cooling concepts for an EMAS can be developed and even verified for their respective application. The next several sections review some of the more promising means for thermoregulation of EMA systems that meet mass and space constraints.

3.4 Transport—EMA Thermal Management Systems

Because of the thermal challenges EMAS's have faced historically, several thermal management solutions have been proposed. These EMA thermal management systems have grown in complexity from simple heat spreaders to multi-technology miniature cooling packages. The next six sections provide specific examples of EMA thermal management systems and their relevant features.

3.4.1 Heat Spreader

During field testing of EMA technology by NASA Dryden the worst case thermal loading condition was determined to be when ailerons were used as flaps for extended periods of time (Jensen, 2000). Extended operation of the EMA against a steady load twice caused an alarming rise in actuator temperature, denoted in Figure 3.10 (Jensen, 2000). In order to combat actuator overheat the team responsible for EPAD testing had aluminum heat sinks fabricated and mounted the actuator, increasing the conductive path to the ambient. According to the report, this modification significantly improved the actuator's thermal performance. This is an example of

the simplicity and effectiveness associated with heat spreaders. However, heat spreaders can suffer from weight penalties when heat loads require greater surface areas to maintain component temperature.

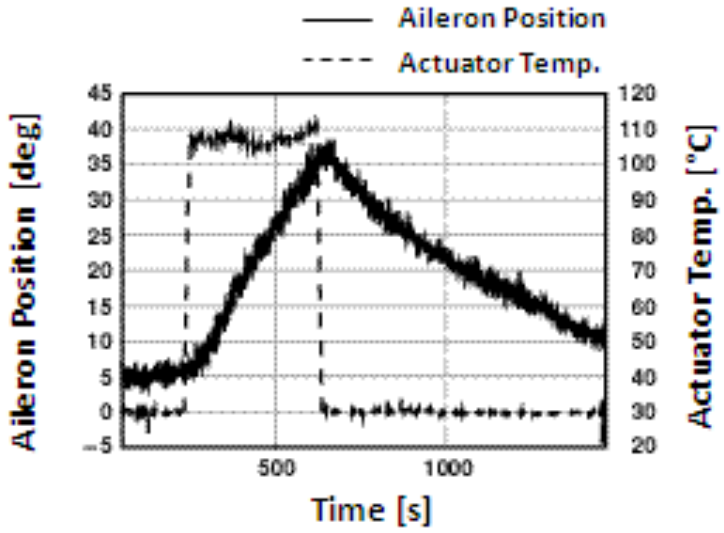

Figure 3.10 EPAD EMA Holding Temperature (Jensen, 2000)

3.4.2 Reflux Cooling coupled with PCM

According to (Bland, 1992) majority of waste heat in an EMAS platform is generated by the motor which may range in efficiency from 85 to 95%. Motor performance is much more sensitive to development of high temperatures than remaining EMAS components such as the gear box or ball screw mechanism. Therefore it becomes the point of interest for TMS adaption. Current EMAS technology employs permanent magnet brushless dc motors that have no rotor current losses and minimal rotor iron losses, relieving the need for direct rotor cooling which significantly simplifying motor cooling. Permanent magnet materials located on the rotor are sensitive to high temperature and lose strength at temperatures above 150 °C. Additionally, insulation life and durability of PMDC motors is shown to significantly decrease with extended high temperature operation. Passive cooling systems offer simplified means to maintaining system temperature without the use of pumps, valves, accumulators or additional power and control.

Thermal management methods must be capable of handling peak heat loads and heat fluxes while operating against adverse g loads and environments. The approach chosen in “Advanced Cooling for High Power Electric Actuators” (Bland 1992) was a passive reflux or thermosyphon coupled with Thermal Energy Storage, TES. A thermosyphon is made up of an evaporator and condenser which transfer heat from the source to sink by boiling a fluid, then utilizing buoyancy differences in vapor and liquid phases to pump the heat transfer fluid between the evaporator and condenser. In this particular design, the motor housing is wetted by the liquid phase of the two-phase fluid, and as heat is generated, the liquid boils generating vapor. This vapor flows upward due to density difference through centrally located vapor channels called risers and then condenses on the colder surface associated with the aircraft skin. Liquid condensate then flows back by gravity to reenter the liquid pool surrounding the motor housing. “The specific fluid that is selected as the coolant for this passive approach depends on peak operating temperature,

which is determined by heat sink characteristics, allowable operating pressures and minimum required operating temperatures." Extended surfaces are needed for efficient boiling and condensing, and this was accomplished in their design by a laminated structure. Ultimately, the thermosyhon developed reduced system thermal resistance from 52K/kW to 31K/kW. This design improved thermal conductance from EMA electric motors to ambient air, allowing EMA's to operate under more thermally malignant conditions. These features would improve EMAS operating life and reliability. Finally, TES was readily implemented into the cooling structure for further reducing operating temperature and leveling actuator heat loads throughout its duty cycle.

Electronics cooling is also a central thermal concern for EMAS thermal management because heat loads are approximately the same order as motor losses, but temperature limitations being more stringent. Mechanisms which are passive, lightweight and provide a rugged means of transferring heat from the EMAS to available heat sinks such as aircraft structure or skin are ideal. Peak power levels for electric actuators can reach 40 kW which for a motor drive efficiency of 96% imposes a 1.6 kW heat load on the heat sink (Schneider, Domberg 1998). Aircraft actuators operate at peak power for only brief durations when compared with mission length, and will operate at significantly reduced power levels during most of the flight duty cycle. This fundamental characteristic of flight control actuators permits heat storage during peak loss periods and dissipation of stored heat during lower loss periods. These energy storage techniques allow heat rejection to be designed for average heat loads rather than peak heat loads. "Test Results of Reflux and Phase Change Storage Electronics Cooler," (Schneider 1998) outlines how (Schneider, Domberg 1998) utilized these principles to develop an EMA drive cooler. This device also incorporated a passive reflux heat rejection and PCM similar to the one described above designed to cool an EMA electric motor. Similarly, it was found use of sensible in addition to latent thermal energy storage reduced cooling system size. Tests completed with this device applied to an IGBT module demonstrated 37% smaller case to sink resistance when compared with an air-only cooler at high air flow. Additionally, the device reduced case to sink resistance experienced under natural convection by 100%.

3.4.3 FHPCP coupled with PCM

A design which utilizes a cold plate to transfer electronics' heat to the most convenient heat sink by an integrally connected flexible heat pipe was developed in "Flexible Heat Pipe Cold Plates for Aircraft Thermal Control" (Gernert 1991). This design allows cooling to be provided to assemblies in awkward locations relative to the heat sink. Cold plate connections varied from convective air cooled fins to a solid plate bolted aircraft structure. Cold plates work in gravity assisted orientation but incorporating a wick structure supports operation in mild against gravity conditions. FHPCPs provide cooling in remote and constrained cavities like those experienced by primary flight control actuators. The advantages of FHPCPs are their passive nature and their geometric flexibility. In (Gernert 1991), the developed FHPCP met design thermal load (44.5 W) with a 4 °C temperature difference between the evaporator cold plate and the condenser mounting plate, emphasizing their ability to perform under reduce temperature differences.

3.4.4 Cold Plate with PCM

"A Thermal Management Concept for More Electric Aircraft Power System Applications" (Vrable 1998) explains how an innovative TMS was designed for effective heat transfer and high

passive thermal energy storage capacity. The design under this work integrated high latent heat advantages of PCM with an actively cooled cold plate. According to Vrable, the design has direct use on system applications where heat rejection varies with time. Advantages of the TMS proposed for electric actuator for MEA initiative include: significant weight savings, high thermal performance, high thermal energy storage capability, high reliability and reduced maintenance. Waste heat rejection for EMA's vary with time, with peak loads for short time periods substantially greater than nominal operating loads. Conventional designs would be specified to meet peak loads resulting in an oversized, costly, and heavy system. Overdesigning the system does however maintain component temperature at or below operating limits resulting in improved performance and life. Conversely, sizing TMS for average heat loads results in smaller and lighter systems but components experience higher temperature excursions during peak load operating points. A TMS design that synergistically combines thermal energy storage with effective heat transfer mechanisms can achieve a system that excels at maintaining component temperature during peak heat loads while being compact and lightweight (Vrable, 1998). Trade studies through CFD analysis confirmed high fin effectiveness coupled with large heat transfer surface to volume ratio are required to achieve effective thermal transport into the PCM. Aluminum foam was placed between adjacent fins with high surface area to volume in order to provide a fast thermal response of the PCM. For the EMA under test a thermal time constant of 30-50 seconds was necessary which allows the TMS time to respond under peak power conditions and effectively store excess heat. Without PCM and its latent heat capacity the cold plate mass would need to double in order to provide the same amount of energy storage in order to secure component temperature within its limits.

3.4.5 Loop Heat Pipe

Heat pipes obtain very high effective thermal conductivities by using a combination of thermally conductive metals filled with a phase change fluid. Heat pipes can obtain effective thermal conductivity 90 times greater than copper of the same dimensions (Faghiri, 1995). The principle components of a heat pipe include a metal tubing (commonly copper or aluminum) coupled with an interior wicking structure and filled with a working fluid. The choice of working fluid depends on the temperature range of the application. The wick utilizes capillary action to provide fluid transport between the evaporator and condenser. A concern for heat pipe performance under harsh g conditions in which the evaporator is above the condenser led to the development of the LHP. LHP's typically exhibit the following features: fine-pored wicks, effective heat exchange during evaporation and condensation stages, and minimized pressure loss in the transport (adiabatic) section (Yu, 2005). LHP's have high heat flux capability with no electrical or mechanical input and therefore are highly efficient passive heat transfer devices (Yu, 2005). Similar to the FHPCP discussed earlier the condenser section of LHP's can be easily adapted to mate with and meet heat exchange conditions of the external heat sink. Additionally, LHP technology permits the embodiment of distributed heat-transfer devices made up of parallel evaporators and or condensers.

In "Loop Heat Pipe for Avionic Thermal Control" (Baldassarre 1996) a successful LHP TMS was developed to transport a minimum of 160 W with the evaporator vertically above the condenser (adverse g-condition). The key design feature in this system was a dual compensation reservoir which ensured the evaporator remained fully wetted under any orientation. This enabled the LHP cold plate to outperform a fixed conductance heat pipe in the gravity-assisted-

orientation while experiencing an adverse g-condition (evaporator vertically above the condenser).

Another effort to verify LHP viability is covered in "Aircraft Thermal Management Using Loop Heat Pipes: Experimental Simulation of High Acceleration Environments Using the Centrifuge Table test Bed." (Flemming, et.al 2006) Under this work a full test bed was constructed to measure LHP effective heat transfer coefficient of evaporator and condenser and LHP thermal resistance with respect to radial acceleration. The LHP used in these test was designed for heat loads of 500 to 5,000 W and had direct application to EMAS cooling.

3.4.6 Forced Convection

EMAS's currently rely on natural convection as the primary mechanism to dissipate heat. In such an ineffective air cooling situation motor and power electronics temperatures can quickly approach thermal limits. Forced convection provides more effective heat transfer from the surface of EMAS components significantly reducing their operating temperature. Heat sink dimension and material would be optimized to most effectively remove heat from EMAS component surfaces and variable-speed fans which operate over a wide range of pressure and temperature to enhance convective heat transfer coefficients. Air-cooled modules made up of an effective heat sink and high efficiency fan capable of removing EMAS heat loads could be one form of forced convection cooling. One such example was developed by MIT under DARPA's Thermal Management Technologies (TMT) portfolio (Bloschok, Bar-Cohen 2012). DARPA's TMT portfolio was comprised of five technical areas aimed to enhance Department of Defense electronic systems performance. These areas included: Thermal Ground Plane (TGP), Microtechnologies for Air-Cooled Exchangers (MACE), NanoThermal Interfaces (NTI), Active Cooling Modules (ACM), and Near Junction Thermal Transport (NJTT) (Bloschok, Bar-Cohen 2012). Each of these five technical areas focused on a portion of the thermal resistance chain common in electronics. MIT developed a high-power air cooled heat exchanger capable of dissipating over 1000 W with 33 W of electrical input power with an overall thermal resistance less than 0.05 K/W for MACE (McMarthy, et. al 2010). Another significant feature of this device was its minute size in comparison with conventional TMT of similar heat dissipating performance. The device made up of an integrated blower and heat exchanger measured only 10.2 cm x 10.2 cm x 10.2 cm. TMT developed under DARPA's five technical thrust areas are directly applicable to EMAS power electronics and could be adapted for electric motors apart of EMAS's.

3.5 Summary

In summary, TMS systems with high heat transfer capacity, low thermal resistance, quick thermal responses, thermal energy storage, mechanical flexibility and situational adaptability have been developed. However, there remain several thermally related electric actuation challenges. Intermittent, pulsed heat loads significantly greater than mean levels poses a threat to components with insufficient thermal mass. In particular, the removal of hydraulic circuits which provided thermal reservoirs for surface actuators and EMA's lack of inherent thermal management necessitate an innovative means to thermoregulation and heat dissipation. Remote location of EMAS and locating power electronics near the EMA compounds heat related problems. Stagnant actuator bays which experience little air exchange with the environment and heating from other areas of the aircraft create an obstacle between the heat source and ultimate sink, ambient. Modern aircraft increasingly utilize composite structures and skins with low

thermal conductivities, which create thermal barriers to available heat sinks. Determining the capacity to reject heat at altitude where air density and convective heat transfer is reduced is another challenge in TMS design. Understanding the source of heat and available sink related to mission details is a solid first step in TM design. However, further information is required to link the two. Therefore, an experimental approach was developed to characterize heat generation as a function of typical mission duty cycle and EMAS thermophysical boundary conditions.

CHAPTER 4

EXPERIMENT

4.1 Overview and Purpose

Generally, actuators which provide mechanical thrust for a tail rudder require high load capabilities at low velocity responses. Whereas, flaperon actuators require high velocity capabilities and encounter moderate thrust loads. Therefore, the experiment design process focused on the ability to conduct tests for various EMAS platforms. In addition, the scale of an aircraft and its maneuverability shape EMAS specifications. Therefore, it was essential to create an experiment which was as flexible as possible and still acquire all necessary data for characterizing EMAS electrical, mechanical, and thermal behavior. Figure 4.1 highlights the primary hardware used in the experiment for EMAS characterization. Additionally, a control block which would execute commands (position, load, and temperature), maintain stability of the experiment, and trigger measurements at consistent time intervals had to be created. Finally, rated limits based on the specifications of each test component had to be evaluated in order to constrain the testing range to a safe test envelope.

In essence, the experiment consisted of the following tasks:

- Use an environmental chamber to simulate actuator bay temperature and servo-hydraulic system to simulate aero-loading

- Subject EMAS to representative flight load and stroke profile
- Accurately and synchronously record EMAS electrical, mechanical, and thermal parameters which provide a basis for energy analysis

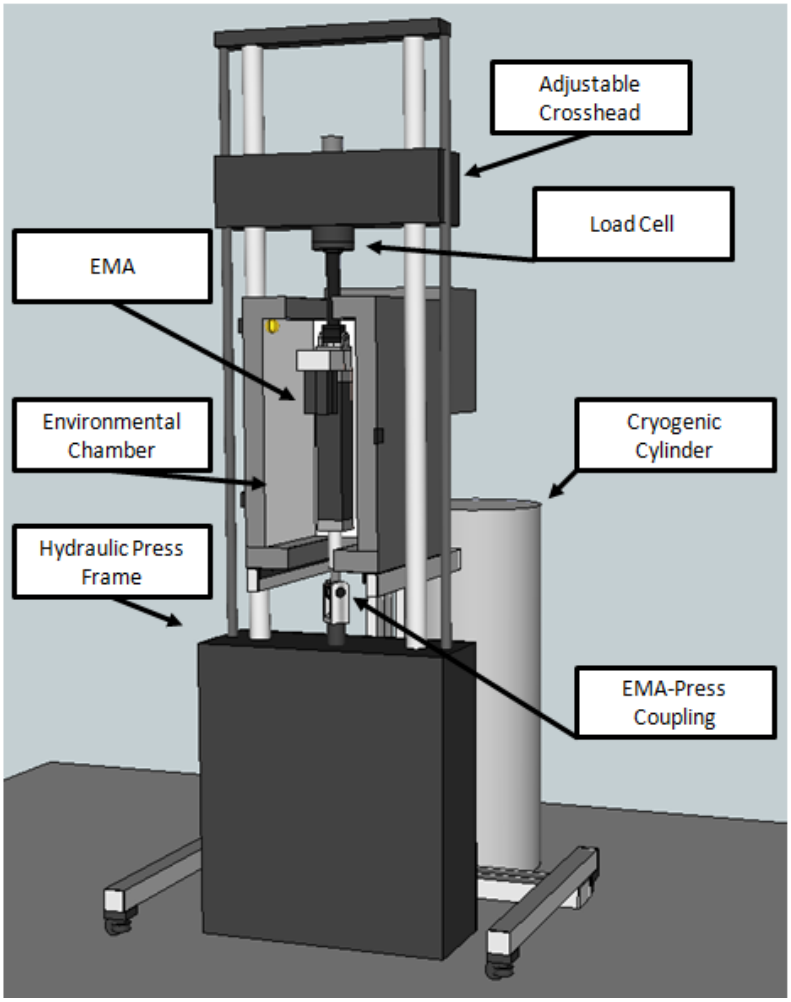

Figure 4.1 Overview of Experiment Setup

Under this experiment a linear EMA with a rotary motor was placed in line with a hydraulic press. The press was given load commands (emulating the loads that would be experienced by a real flight control surface actuator) while the EMA was provided position commands. Position and load commands were artificially created to replicate realistic velocity, load, and frequency found in modern PFC actuation for a tactical aircraft. However, these profiles needed to be scaled and restricted to the abilities of our test setup. Therefore, the EMA, hydraulic press, and environmental chamber each underwent characterization tests to establish a test envelope.

The EMA used was a Danaher Motion EC5 linear actuator driven by an S610 controller. The EMA performed under a load provided by an MTS servohydraulic system made up of a 100 kN hydraulic press driven by an 8-Channel FlexTest 60 controller. The hydraulic press and EMA were coupled together. Specifically, the EMA's stroke was seen as a disturbance to the hydraulic press as it attempted to realize a particular force and the press's force was seen as a disturbance to the EMA's stroke. The hydraulic press emulates the load that the EMA must overcome. As the motor in the EMA actuated, it heated up. Stroke, load or force, DC link voltage and current, and temperatures of selected points in and on the motor and controller were

recorded. These parameters were recorded using a National Instruments (NI) Real Time (RT) Data Acquisition (DAQ) system.

4.2 Test Apparatus

The test apparatus is made up of three main hardware components—EMAS under test, hydraulic press, and an environmental chamber. In addition to the main hardware, a RT DAQ system and a user interface provided control of test and measurement. The specific EMA under test was a Danaher EC5-AKM42G-100-32B-300-MP3-FS2 actuator. The servo drive rectified a 3 phase 240Vac supply and energized an internal DC bus. Additionally, the servo drive used a power module made up of 6 IGBT's (2 per phase) to execute a pulse width modulation (PWM) control scheme to power the motor. The PWM cycle was determined by a PID control loop inherent to the drive and aimed to produce the commanded speed setpoint.

A MTS hydraulic press assembly made up of a hydraulic power unit (HPU 505G2), hydraulic service manifold (HSM 292.22), three stage servovalve (257.04), 100 kN load frame (370.10), and real time closed loop controller (FlexTest 60) was used to load the actuator under test. The press controller supported 24 conditioned transducer inputs and function generation for 8 control channels. Only one control channel was configured which controlled press force. This channel was configured as an external command which was supplied by the NI RT DAQ.

A MTS 651.06E-04 environmental chamber provided the ability to simulate dynamic temperature profiles. Its removable U-plug sections on the top and bottom allowed the actuator's arm to move with the press while preventing significant heat loss from the chamber. Chamber temperature capability ranged from -129°C to 316°C—a range that met requirements with ample margin. A significant amount of fabrication and customization was required to integrate each piece of hardware and meet safety regulations (Appendix A).

The RT DAQ (NI PXIe-1071) was responsible for the execution of mechanical and thermal input commands in addition to synchronized sampling of electrical, mechanical, and thermal measurements. It connected each piece of hardware and their respective controllers through a LabVIEW VI. Appendix B details the VI's used throughout the experiment. Layers of control corresponded to each hardware used in EMA testing: hydraulic press, electromechanical actuator, and environmental chamber. Measurement loops were created to operate at frequencies which accurately captured the physics of our experiment, including electrical, mechanical, and thermal parameters. The control leveraged the NI RT DAQ system's ability to sync each control and measurement loop to a single clock; thus, ensuring accurate comparison of measured parameters at discrete points in time.

Stroke and load profiles generated before the test were interpreted by the program and converted to an analog output signal to the press and actuator controllers. The environmental chamber utilized digital communication and therefore required a separate scheme for setpoint and feedback transmission. The test control VI was structured such that a Master-Slave configuration synchronized each DAQ card and prevented temporal drift. The environmental chamber control scheme references the same clock but was not synchronized with the Master-Slave configuration. Synchronization of thermal control outside of matching start and stop times was not a priority since the system was much slower in response relative to the electrical and mechanical systems.

Three DAQ cards were employed, one for each aspect of the experiment. The card with the highest sampling rate (2 MS/s per channel, simultaneous) was responsible for recording higher frequency parameters—DC link voltage and current, and regenerative circuit current. A multiplexed card capable of up to 16 analog inputs and 1MS/s multichannel recorded mechanical parameters (stroke and load) and was responsible for analog output of stroke and force commands. Both DAQ devices provide 16-bit resolution for analog to digital conversion. Finally, a 32 channel, 24 bit, thermocouple input module and isothermal terminal block were used to record motor and drive related temperatures.

Figure 4.2 demonstrates the interactions between each layer of the experiment. Solid red arrows highlight communication active during a test and dashed red arrows indicate communication for initialization of the experiment. Prior to relinquishing control to the test control VI, the press, EMA, and chamber required initialization through their independent interfaces. Once each piece of equipment established successful communication, the test control VI provided a central interface where command profiles were automated and process monitoring was available. Appendix C provides details on steps executed as part of the test procedure.

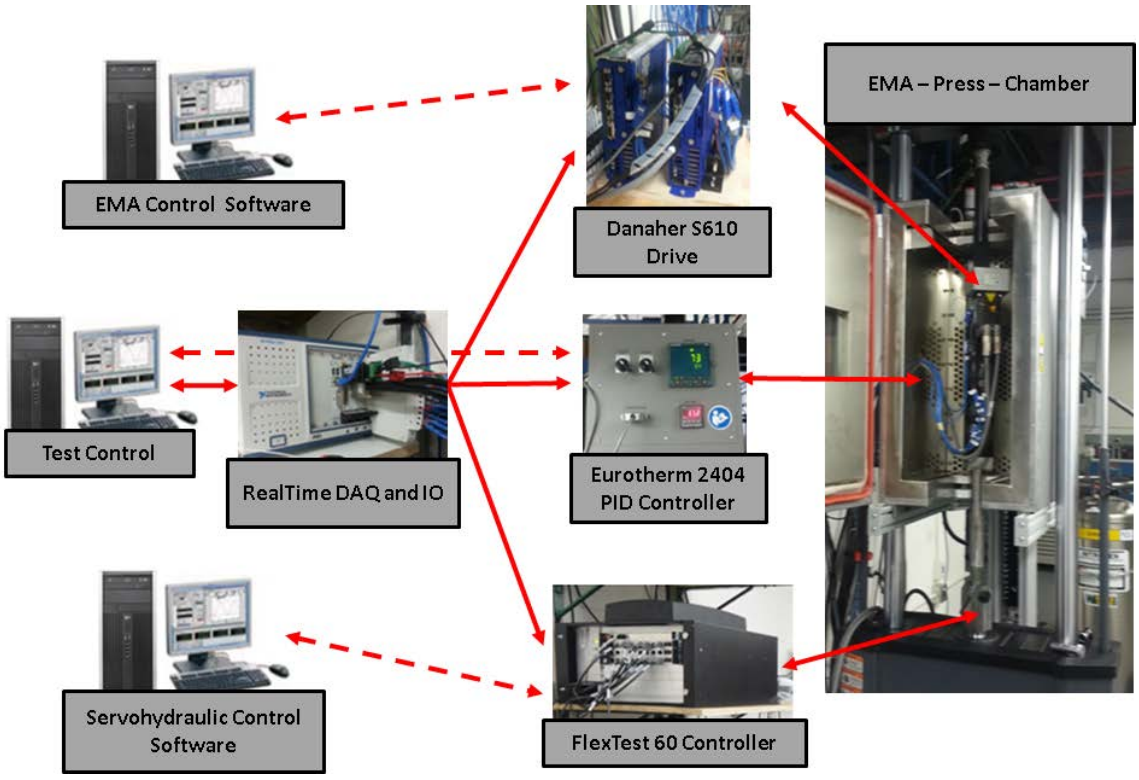

Figure 4.2 Test Apparatus Flow Diagram

Appendix D highlights detailed specifications of hardware used in the experiment and denotes their source. Appendix E summarizes those hardware and their pertinent specifications in a poster format.

4.2.1 Measurements

The sensors and their information used in the experiment are shown in Figure 4.3. Range denotes the sensor's applicable range, i.e. the range under which the sensor was calibrated. Force

transducer and LVDT calibrations were completed by the manufacturer, MTS. Thermocouples, current transducers, and voltage probes were calibrated in-house; therefore, their ranges were determined by in-house calibrations. Accuracy denotes the maximum error the sensor exhibited over the calibration range. Resolution is a function of the full scale range of the device and the DAQ card analog-to-digital (A/D) converter resolution. For example, both DAQ cards used in the experiment are 16 bit and support -10 to 10 V analog input signals. Therefore, the smallest voltage resolvable by both cards is 20 / (2^{16}) or 0.31 mV. The thermocouple card has 24 bit input channels and therefore can resolve voltage changes of 0.001 mV. An MTS Servohydraulic controller was reconfigured to use a range of ± 20 kN as opposed to ± 100 kN for several reasons. First, reducing the full scale range increased the resolution from 3 N to 0.3 N. Second, the maximum output of the press was effectively scaled from ± 100 kN to ± 20 kN, creating a safer environment for the EMA under test which was limited to 13.35 kN. Lastly, increasing the resolution of the force channel was thought to improve force control with respect to dynamic test profiles made up of higher resolution force data. See Appendix F contains detailed images of sensor locations.

Item	Manufacturer & Model	Purpose	Range/ Accuracy/ Resolution	Location
Force Transducer	MTS 661.20H-03	Actuator Load	± 20,000 N ± 12N 0.305 N	Load Frame Cross Head
LVDT	MTS	Actuator Position	± 140 mm ± 0.082 mm 0.002 mm	Hydraulic Cylinder Piston Rod
Thermocouple	Omega TMQSS-040U-12	Component Temperature	-20 to 150 °C ± 0.16 °C	Various Drive/Actuator Locations
Current Transducer	LEM LA55P	DC Link and Regen Circuit Current Draw	± 10 A ± 0.06 A 0.0002 A	Drive Back panel
Voltage Probe	Tektronix P5200	DC Link Voltage	± 900 V ± 1.35 V 0.08 V	Drive Back panel

Figure 4.3 Sensor Inventory

4.2.2 Sampling Rate

Sampling rates of measured parameters were determined based on Nyquist theorem and tenth harmonic of expected system frequencies in addition to the DAQ system capability. Commanded force and stroke profiles had frequencies limited to 10 Hz. Therefore, a sampling rate of 200 Hz was believed adequate. A sampling rate of 210 Hz was chosen to work with the DAQ system. DC bus voltage and current measurement sampling rates were loosely based on the motor's frequency. The motor's maximum speed was 2500 rpm. With 10 poles, its frequency is 10/2*2500/60 = 208 Hz. The tenth harmonic plus Nyquist frequency would be 4167 Hz. A sampling rate of 3012 Hz was chosen, which is not quite to the tenth harmonic. Temperature

measurements made by all thermocouples were completed at a sampling rate of 2 Hz. This sampling rate was sufficient due to the slow response time of the system.

Parameter	Bandwidth [Hz]	Nyquist [Hz]	Sampling Rate [Hz]
Mechanical (Stroke & Force)	6	12	210
Electrical (Voltage & Current)	210	420	3012
Thermal (Temperature)	<1	<=1	2

Figure 4.4 Experiment Sampling Frequencies

4.2.3 Analog Filters

In order to reduce noise on analog signals present in our experiment two analog low pass filters were constructed for mechanical measurements. They were built to filter EMA stroke and load measurements whose greatest frequency was roughly 10 Hz. Measurement were taken and an FFT analysis showed that noise appeared at frequencies of 500 Hz and higher. Two identical 2^{nd} order passive low pass filters were constructed to eliminate the higher frequency content but not attenuate actual mechanical frequencies experience by the EMA. Using existing resistors and capacitors in the lab: R1=4.6 kΩ, R2=4.6 kΩ, C1=0.1 µF and C2=0.1 µF, the theoretical cutoff frequency was calculated using the following formula.

$$F_c = \frac{1}{2\pi\sqrt{R_1 C_1 R_2 C_2}}$$

Fc = 346 Hz

For filters with order greater than 1, actual cutoff frequency or frequency corresponding to -3db attenuation was calculated as such:

$$F_{c(-3db)} = F_c\sqrt{2^{\frac{1}{n}} - 1}$$

where n is the filter order, in our case, 2.

Therefore, the actual cutoff frequency of the low pass filters was:

Fc(-3db) = 223 Hz

Figure 4.5 is a picture of the actual construction.

Figure 4.5 2nd Order Low Pass Filter for Mechanical Measurements

In order to confirm the frequency response of each analog filter (2nd order RC low pass), a sinusoidal signal at increasing frequencies was created utilizing a function generator while an oscilloscope measured input and output voltage. At discrete levels of frequency the filter gain was calculated as follows:

$$Gain = -20 * \ln\left[\frac{Output}{Input}\right]$$

As a result, Figure 4.6 was made from the calculated gain values. Based on the chart, the filter measured cutoff frequency (-3 dB) was approximately 150 Hz. The discrepancy between the calculated and measured cutoff frequencies is most likely due to the inaccuracy of the resistor and capacitor specifications used in the calculation. Nevertheless, measured cutoff frequency was well above attainable mechanical frequencies and therefore was not a threat of over-attenuation.

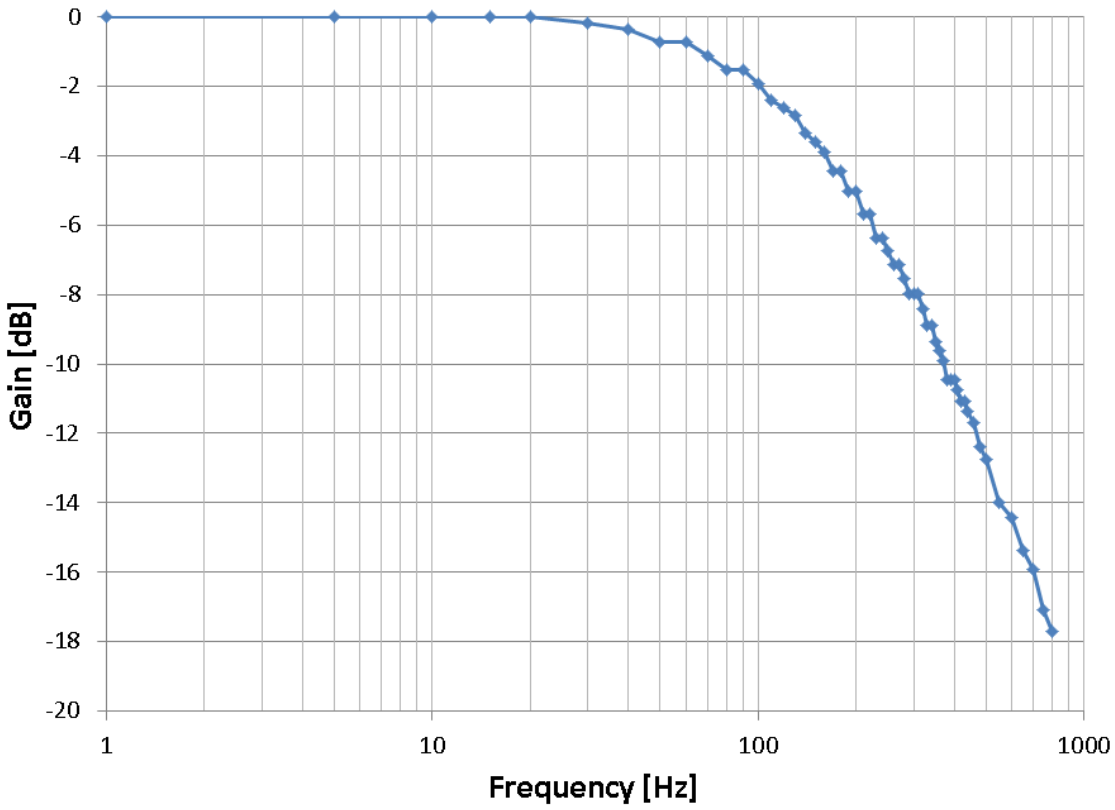

Figure 4.6 Frequency Response of Mechanical Filter

4.3 Hardware Characterization

In order to verify manufacture specifications of the primary hardware used in the experiment, preliminary hardware characterization tests were carried out. First, the EMA under test was subjected to a frequency sweep of 0-15 Hz at amplitude of 4 mm (1.33% of full range). At this amplitude the EMA was capable of 6 Hz with little overshoot, but failed at 7.5 Hz. This capability falls within the desired testing range. Next, the hydraulic press was subjected to a frequency sweep of 0-40 Hz at an amplitude of 1500 N (1.5% of full range) followed by a frequency sweep of 0-15 Hz at an amplitude of 13 kN (13% of full range). It was determined the press was capable of replicating forces and frequencies relevant to flight control surfaces. Lastly, the environmental chamber was provided various step inputs to determine its maximum heating and cooling rates above and below room temperature. It was found the environmental chamber was capable of affecting space temperature at rates comparable to ambient temperature fluctuations.

4.3.1 Electromechanical Actuator

A fixed amplitude linearly varying frequency sine wave was commanded to the actuator in order to determine its bandwidth and compare desired mechanical profile frequencies. Figure 4.7 demonstrates the input profile and actuator response. Position error grows significantly after 5 Hz and 7 Hz caused the EMA to fault. EMA response resulted in greater positive overshoot than negative overshoot. This was most likely caused by the orientation of the EMA such that positive stroke which corresponds to extension was aided by the force of gravity.

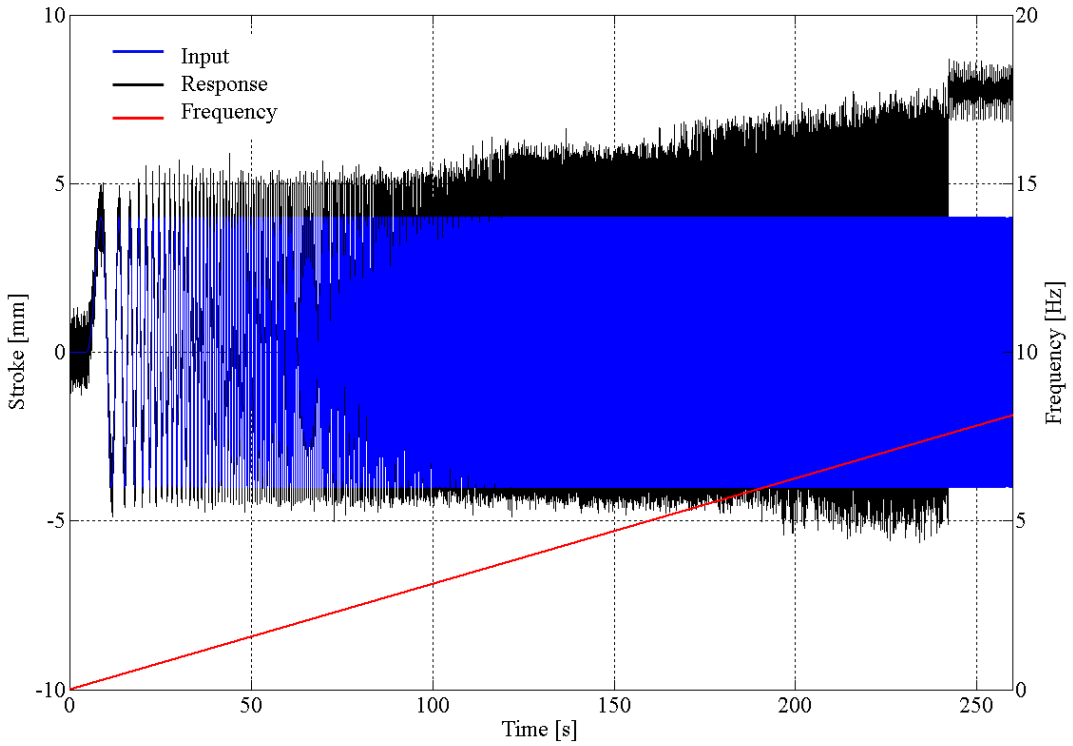

Figure 4.7 EMA Frequency Sweep Response

Figure 4.8 shows time slices of the EMA's performance from 0-2.5 Hz, near 6 Hz, and failure at 7.57 Hz.

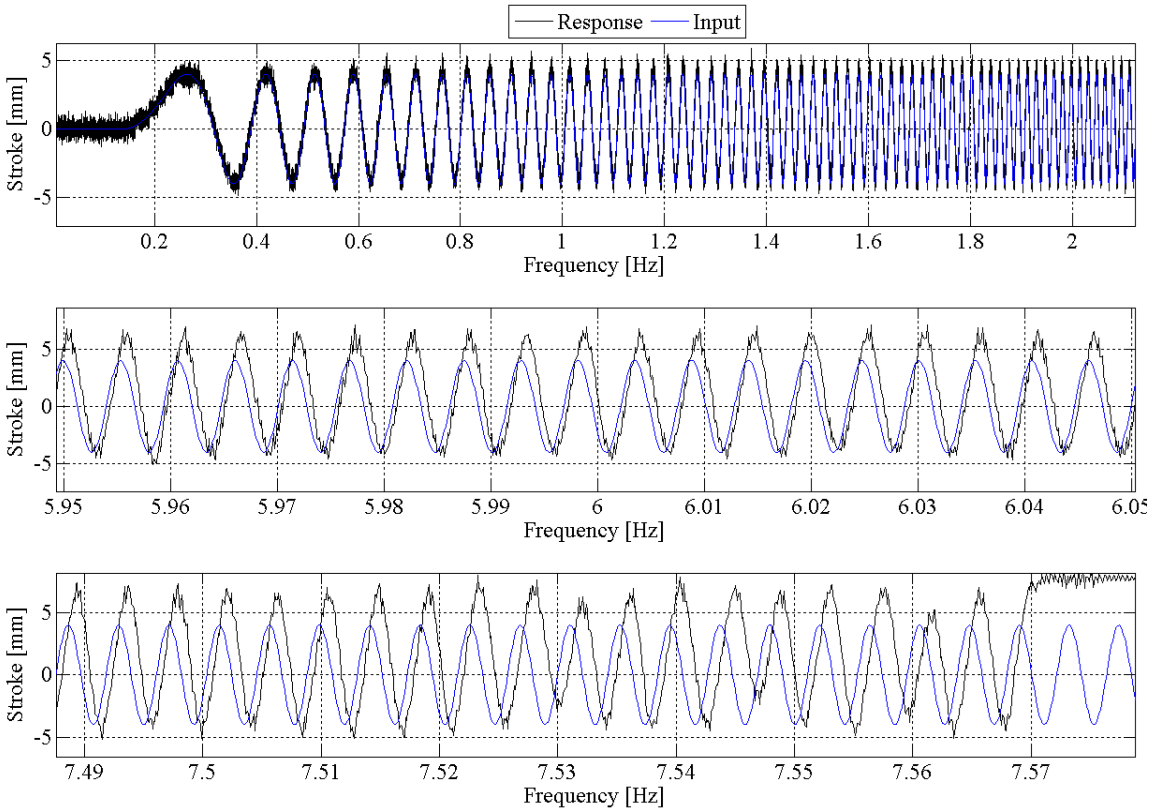

Figure 4.8 EMA Frequency Sweep Response Time Slices

Figure 4.9 is a Bode Plot of the EMA's response and shows at 6 Hz the actuator was 45° out of phase with the input.

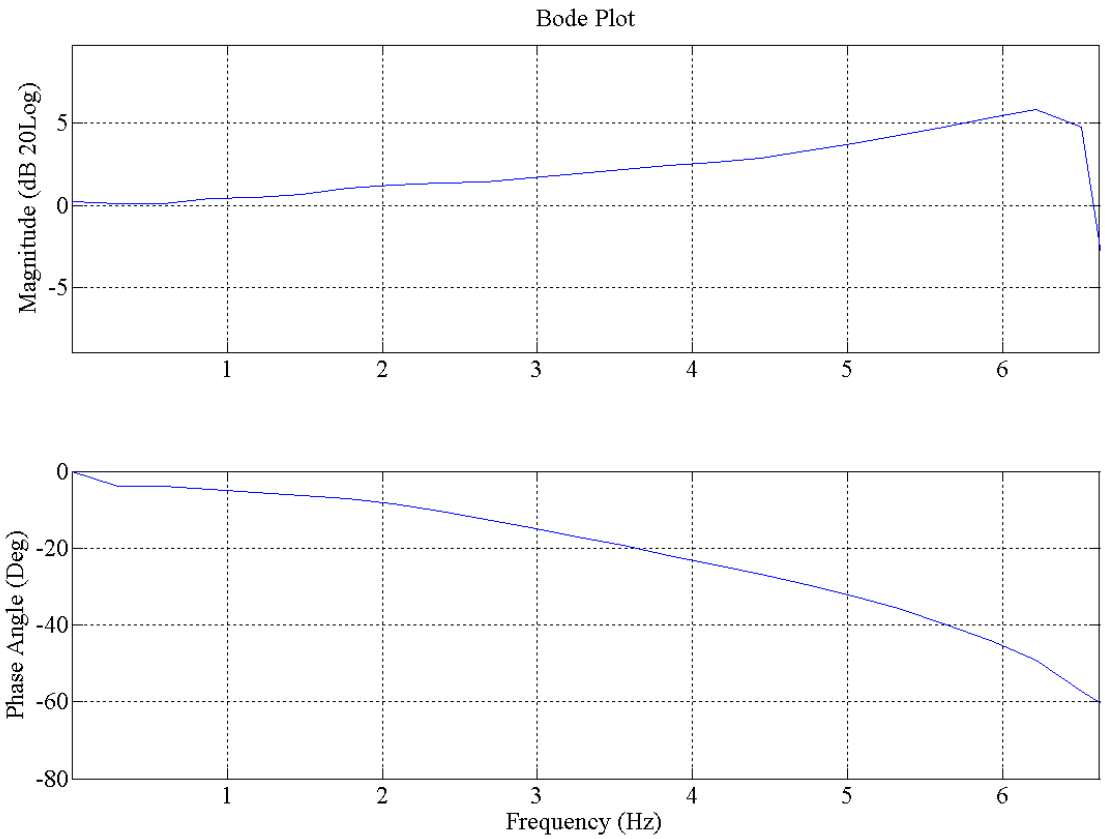

Figure 4.9 EMA Bode Plot

4.3.2 Hydraulic Press

Similarly, the hydraulic press was subjected to a frequency sweep first at 1500 N then at 13 kN. The purpose of these tests was to determine the bandwidth of the press at applicable force levels. Two aluminum plates, one connected to the press ram, the other to the load cell, were coupled using 4 structural bolts. This created a very stiff specimen and could be classified as a non-compliant specimen. Conversely, a spring or bushing would be categorized as a compliant specimen. Both types of specimens and their integration to the hydraulic press are shown in Figure 4.10. Ultimately, an EMA would be classified somewhere between the aluminum plates and a spring, but more closely to the aluminum plates.

Figure 4.10 Hydraulic Press Characterization Setup (Aluminum Plates)—Left and (Spring)—Right

A fixed amplitude, 1500 N, linearly varying frequency sine wave was commanded to the hydraulic press in order to determine its bandwidth and compare desired mechanical profile frequencies. Figure 4.11 demonstrates the input profile and hydraulic press response. Force error grows significantly after 20 Hz.

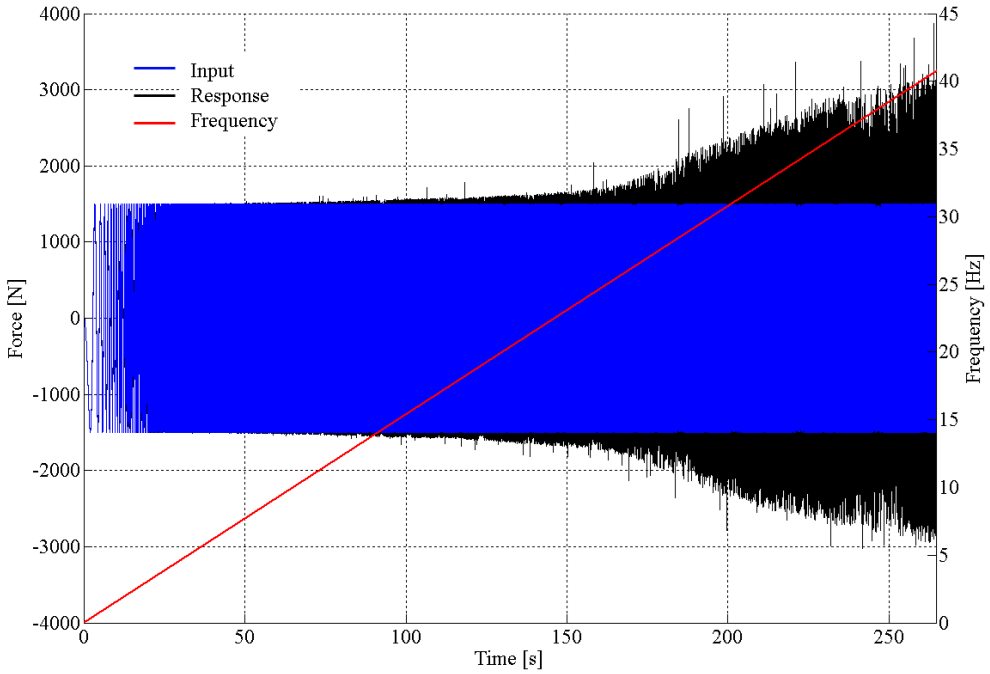

Figure 4.11 Hydraulic Press Frequency Sweep Response 1500 N

Figure 4.12 shows time slices of the hydraulic press performance from 0-2.5 Hz, near 15 Hz, and 38 Hz. Phase lag becomes evident at 15 Hz while the press response exhibits distortion at and

beyond 38 Hz.

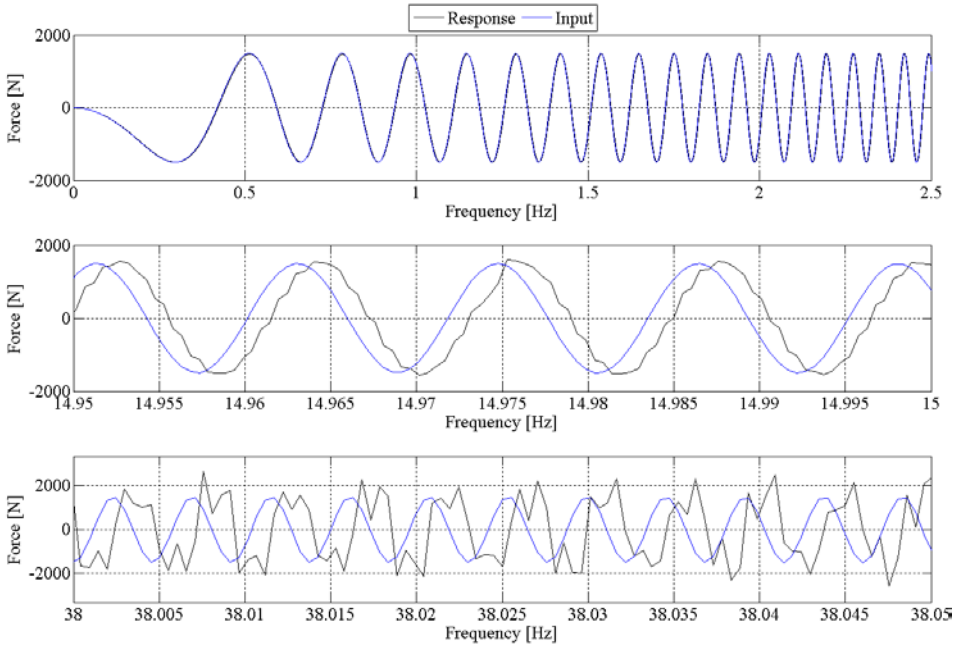

Figure 4.12 Hydraulic Press Frequency Sweep Time Slices 1500 N

Figure 4.13 is a Bode Plot of the hydraulic press response and shows the response was 45° out of phase at approximately 13 Hz and reached 3 dB in magnitude at approximately 30 Hz.

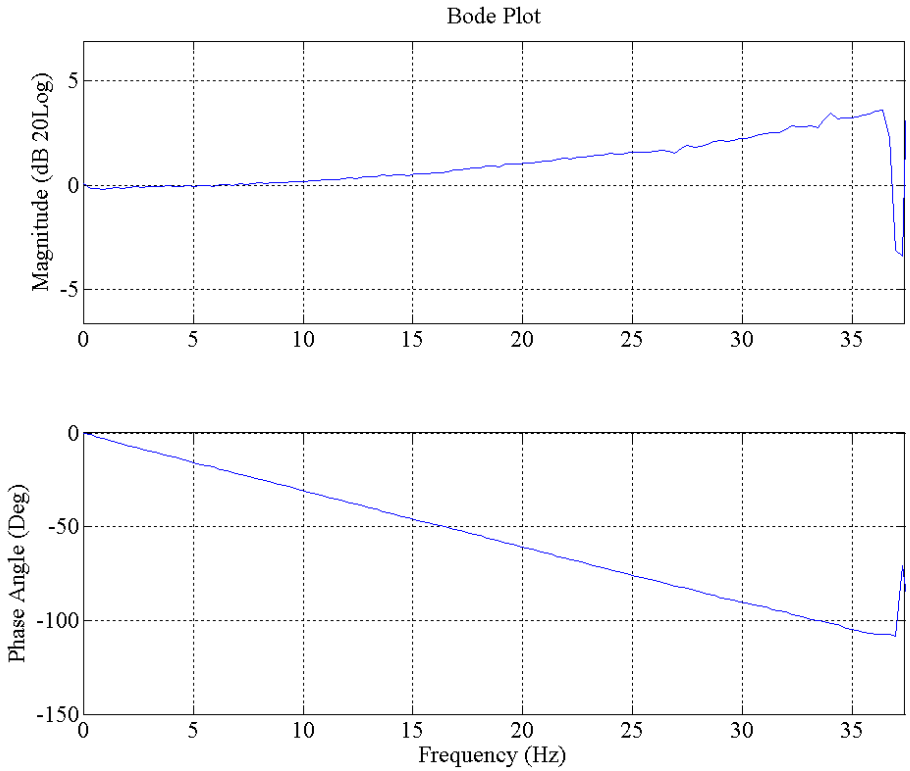

Figure 4.13 Hydraulic Press Bode Plot 1500 N

Next, a fixed amplitude, 13 kN, linearly varying frequency sine wave was commanded to the hydraulic press in order to further asses its bandwidth. Figure 4.14 demonstrates the input profile and hydraulic press response. Force begins to grow after 6 Hz.

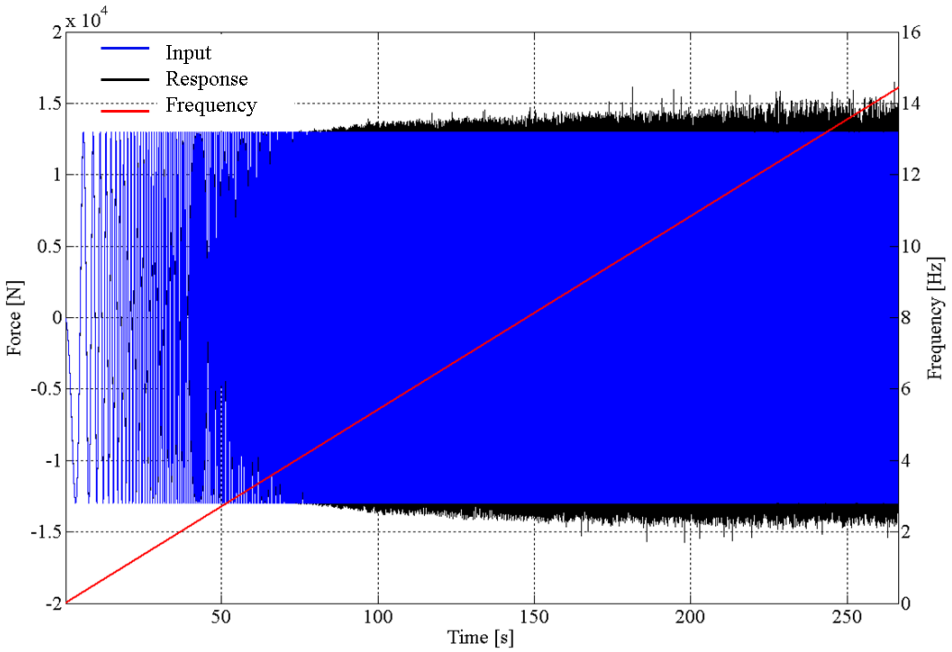

Figure 4.14 Hydraulic Press Frequency Sweep Response 13 kN

Figure 4.15 shows time slices of the hydraulic press performance from 0-2.5 Hz, near 6 Hz, and 14.4 Hz. Phase lag becomes evident at 14.4 Hz where the press response also exhibits a slight distortion when compared with the input signal.

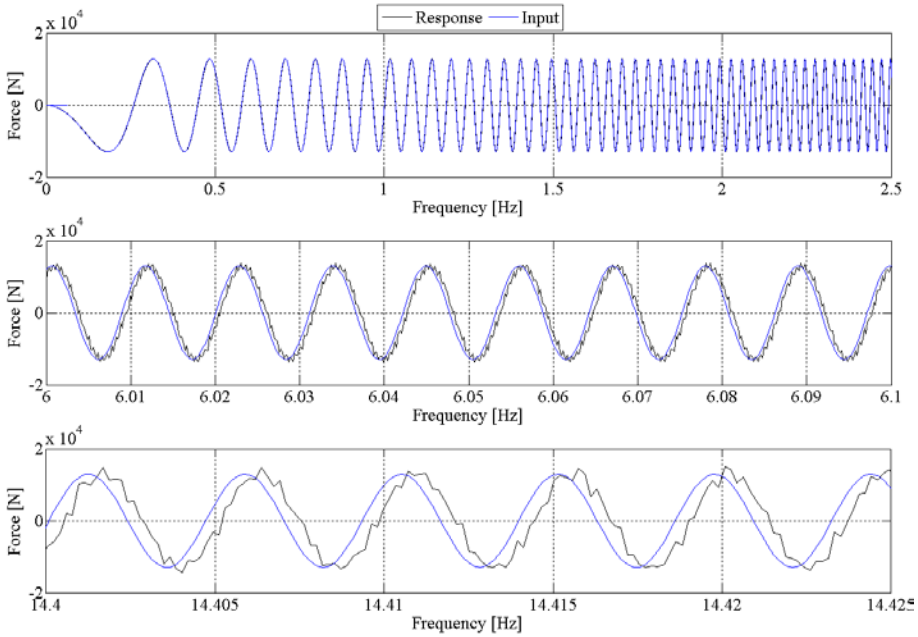

Figure 4.15 Hydraulic Press Frequency Response Time Slices 13 kN

Figure 4.16 is a Bode Plot of the hydraulic press response and shows phase lag grew linearly from 0 to 35° at approximately 12 Hz. The magnitude became erratic between 12 and 14 Hz.

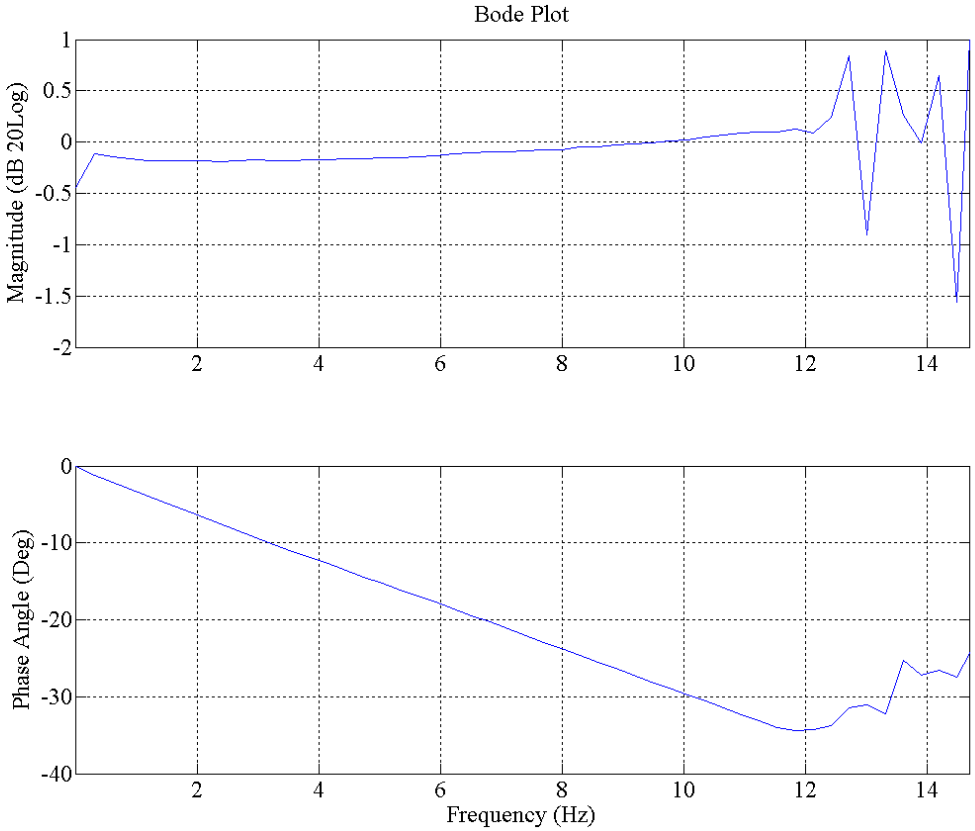

Figure 4.16 Hydraulic Press Bode Plot 13 kN

Based on the two hydraulic press trials completed, it was capable of replicating dynamic force profiles up to 30 Hz at 1500 N amplitude and 12 Hz at 13 kN. Both of those results are greater than typical mechanical frequencies experienced by an EMAS (10 Hz) and therefore substantiate the use of the hydraulic press to replicate aerodynamic loads of a flight control surface.

Finally, a dynamic force profile representative of primary flight control aero-loads was executed to qualitatively measure the Servohydraulic system control and response. Figure 4.17 demonstrates the system's ability to closely follow transient force trends for a non-compliant specimen.

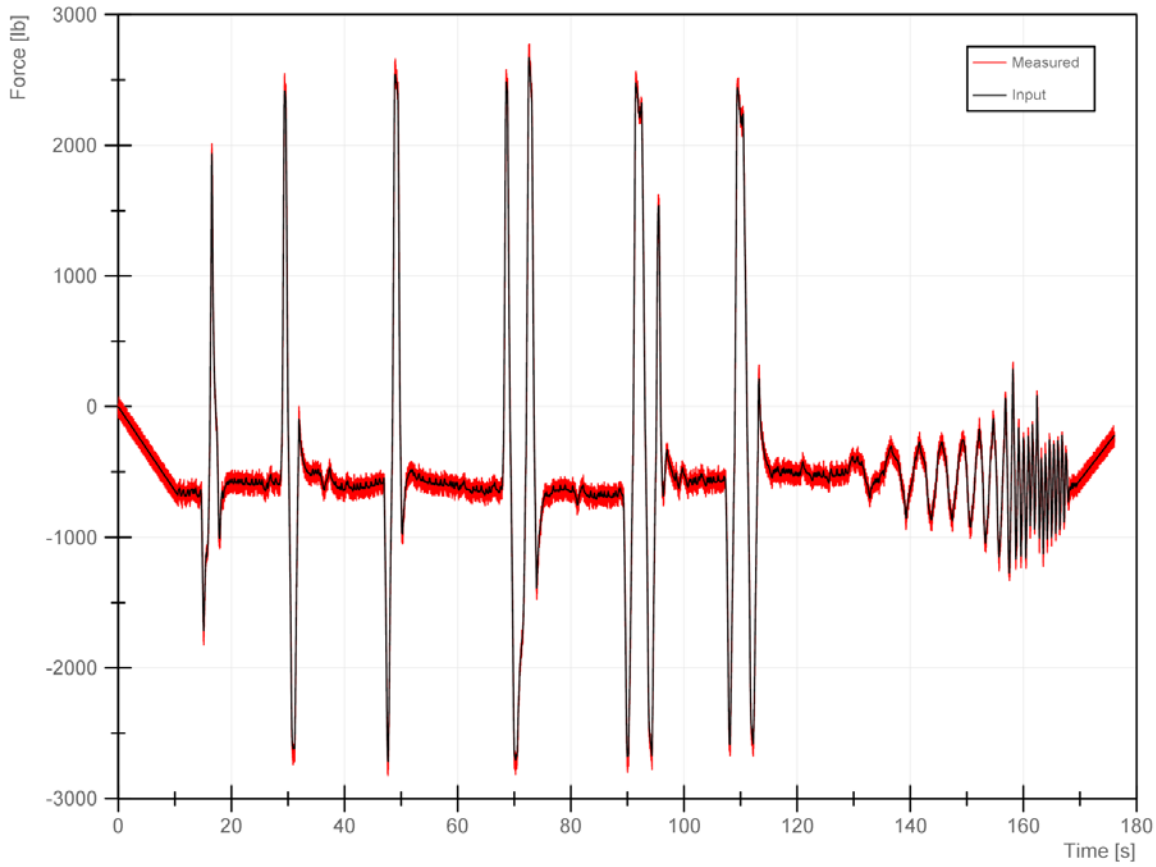

Figure 4.17 Hydraulic Press Dynamic Profile Performance

4.3.3 Environmental Chamber

The goal of each environmental chamber test was to evaluate system performance relative to an input that resembled portions of actual environmental flight conditions. Initial tests were done without any test specimens/articles within the chamber or modifications—"Original State". With that, there were no disturbances imposed on the system and baseline system performance was established. After that, modifications to the U-plugs were made to accept the hydraulic press-EMA couplings. Additionally, the EMA and its thermal mass were placed within the chamber to determine its effect on chamber performance. Modified U-plugs and the presence of the EMA within the chamber constituted a "Modified State." Figure 4.18 and Figure 4.19 show chamber performance in the original state and modified states, respectively.

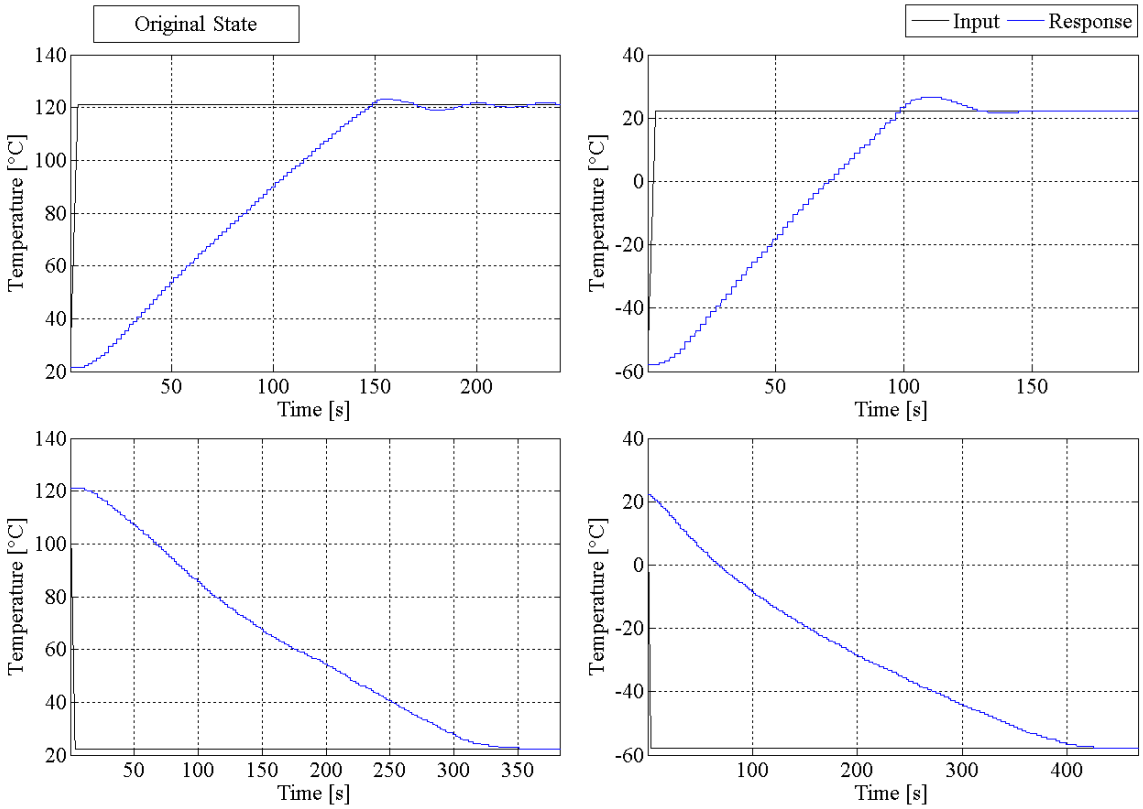

Figure 4.18 Environmental Chamber Step Responses in Original State

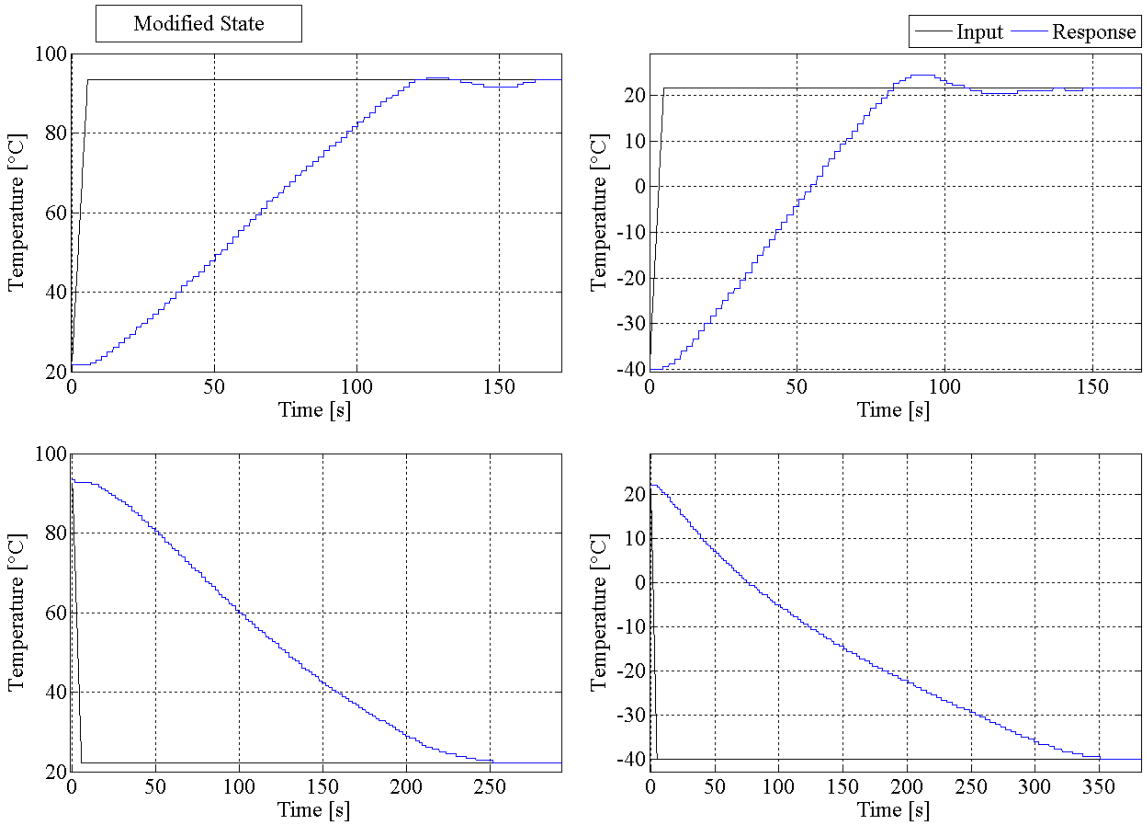

Figure 4.19 Environmental Chamber Step Responses in Modified State

Airborne electronic equipment must withstand transient thermal rating of 1°C/s between extremes of -54°C and 71°C (MIL-STD 2218). The chamber cooling rate was determined to be 0.5 °C/s when cooling below room temperature and 1.3 °C /s above room temperature. The chamber's heating rate 2.2 °C/s when heating above room temperature and 2.8 °C/s below room temperature. It was determined from the chamber's step response that it was tuned appropriately and was capable of generating desired heating and cooling rates commonly found in an aircraft envelope. More detail on the procedure and results for these values can be found in Appendix G.

4.4 Test Envelope

NASA's EPAD program served as a general guidance in constructing an EMAS test envelope (Jensen, 2000; Navarro, 1997). Several artificial mission profiles were generated to aid in the characterization of various EMA performance measures. These profiles were time-history waveforms made up of desired actuator position, hydraulic load, and chamber temperature. The following performance data of an EMA and EHA field tested by NASA EPAD on the SRA was used to create position and load commands: 5 HP (3.7 kW) EMA rated for 13 Kips (58 kN) at 6 in/s (150 mm/s) and limited to 4 inches (102 mm) of stroke (Jensen, 2000; Navarro, 1997).

In order to test an EMA under realistic flight conditions, mission representative stroke and load profiles were used as inputs to the experiment. However, stroke, force and the rate of change of both had to be scaled to the capabilities of our hardware. The EMA assembly under test was limited by its motor's duty cycle and environmental ratings. An EC5 EMA coupled with an AKM42G servomotor can withstand 3,000 lbf (13,350 N) intermittently at any speed before stall. The assembly can withstand a continuous force (compression or tension) of 1000 lbf (4500 N) at no speed. This continuous force limit decreases linearly to 850 lbf (3783 N) at a peak speed of 3.4 in/s (88.6mm/s). The performance curve for the EMAS under test is shown in Figure 4.20.

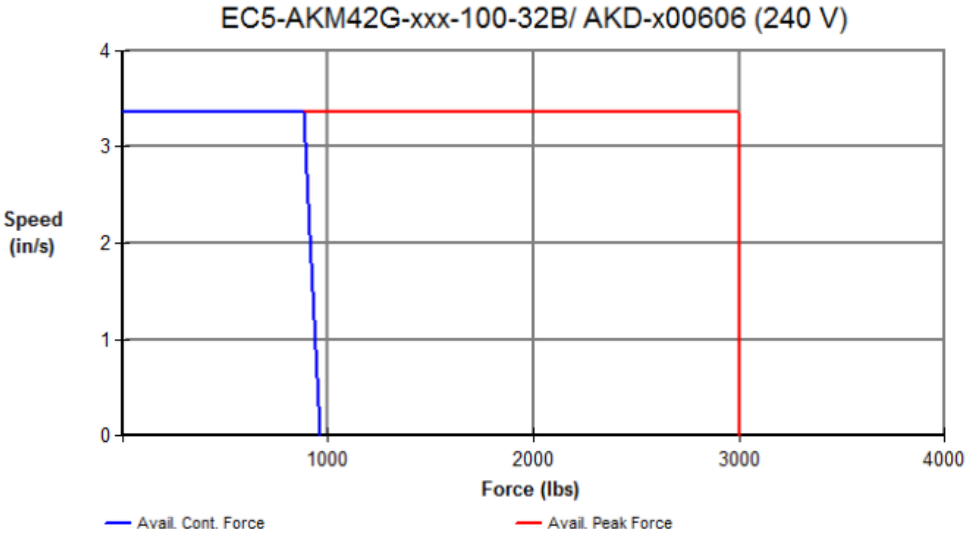

Figure 4.20 Danaher EMA Performance Curve (Kollmorgen.com)

Brushless servo systems are described by a torque/speed operating envelope, varying for intermittent and continuous duty zones. The continuous torque line is set by either the motor's maximum rate temperature or the controller's rated continuous current output, whichever is less. The system can operate continuously within the continuous duty zone if the ambient temperature is 40°C or less. The intermittent duty zone is bordered by the peak torque line and system

voltage line. Figure 4.21 is a performance curve for an AKM42G motor coupled with an S610 servo drive (320 Vdc bus). This servo system has the following performance factors under continuous duty: rated speed was 3500 rpm, motor power at rated speed was 1.06 kW, and continuous rated torque at rated speed was 2.14 lb-ft (2.9 N-m). The motor utilized Class F insulation and a 155°C over-temperature thermistor to prevent thermally related failures. Rated values were determined for 100°C winding temperature rise in a 40°C environment. Motor performance at increased environment temperatures will be reduced and therefore care was taken in developing testing conditions.

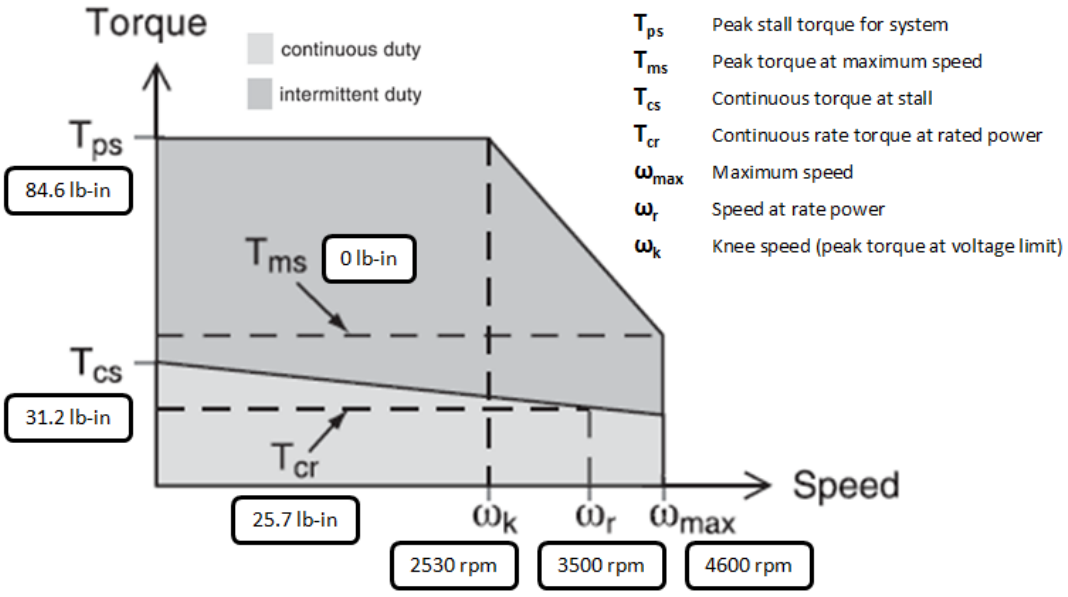

Figure 4.21 AKM42G Servomotor Torque-Speed Curve (Kollmorgen.com)

INVENT, a program aimed at addressing thermal management challenges in modern military aircraft, solicited that actuator bay temperature can vary from -58 to 71 °C continuous, -65 to 87 °C for 30 minutes, and -78 to 107 °C for one minute (FedBizOps.Gov, 2009). Additionally, flight demonstration testing executed under EPAD utilized similar continuous, intermittent, and shock temperature values (Navarro, 1997). These values are shown in Figure 4.22 and were used to create environment temperature inputs.

Parameter	Units	Requirement
Altitude	ft	70,000
Rate of change	ft/min	40,000
Temperature		
Continuous	°F	–40 to 160
Intermittent	°F	180 10 min
Shock	°F	–40 to 160

Figure 4.22 EHA Design Requirements (Navarro, 1997)

The thermal environment was created via the MTS environmental chamber equipped with an 8 kW resistive heating system, LN_2 cooling system, and fan for reduced temperature gradients. An electric motor driven fan provided forced convection for consistent and rapid heat transfer while the use of liquid nitrogen provided rapid cooling in order to accurately develop a

quickly changing atmosphere. From specification the chamber can heat up from room temperature to 316 °C in less than 30 minutes and cool from room temperature to -129 °C in less than 20 minutes, while providing a temperature gradient less than 2 °C and temperature stability of ± 2 °C (www.mts.com). Preliminary tests revealed the chamber heating and cooling rates were sufficient for replicating aircraft free stream and bay time dependent temperatures. Also Appendix G demonstrates the chamber's ability to follow dynamic temperature trends.

Figure 4.23 summarizes temperature range and heating/cooling rates versus MTS chamber values. Furthermore, Appendix H reports environmental chamber liquid nitrogen consumption. It was determined a 50-100 liter cryogenic cylinder would suffice for one hour of temperature ramps and dwells during testing.

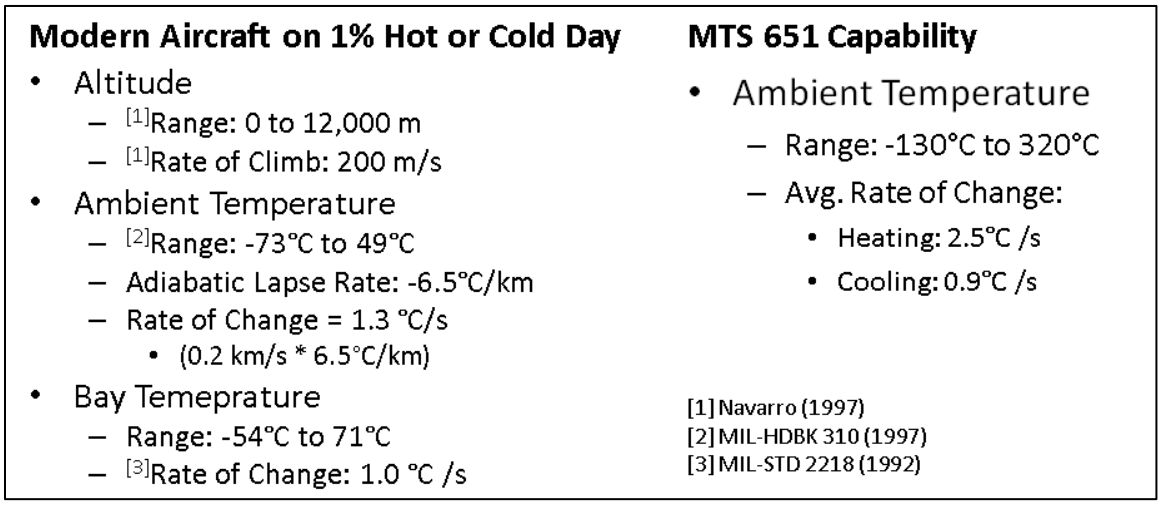

Figure 4.23 Temperature Range and Rates of Change

NASA's SRA EHA system exhibited the following performance parameters: 13,000 lbf (58 kN) in tension or compression, 4" (102 mm) of stroke, and 6 in/sec (150 mm/s) rate (Navarro, 1997). A summary of these performance characteristics compared with in-house hardware capabilities is given in Table 1.

Table 1 In-House Hardware Performance Summary

	Danaher EMA	MTS Press	MTS Chamber	Mission
Stroke [mm]	± 150	± 140	--	± 50
Force [kN]	± 3.8	± 20	--	± 58
Rate [mm/s]	± 86	± 1500	--	± 150
Temp. [°C]	-30 to 70	--	-129 to 316	-30 to 70

Limiting factors in the test envelope include: EMA force, rate, and operating temperature. Experimental profile stroke and load commands were scaled to meet these limiting factors. Environment temperature profiles were created to replicate bay conditions on standard and hot days in addition to design requirements specified in aerospace related EMAS designs. These conditions, similar to stroke and force, were constrained by the in-house EMA capability.

4.5 Test Matrix and Development of Profile Inputs

Various combinations of stroke, load, and temperature profiles were constructed in order to sufficiently establish a baseline performance for the EMAS and compare increasingly demanding scenarios. Mechanical profiles made up of stroke and force grow in complexity from static holds which simulate extended cruise periods at constant load and environment to transient stroke, force, and temperature experienced in actual flight. The test matrix in Table 2 was constructed in order to characterize power draw and thermal energy under duty cycles typically experienced by a flight actuator under different environment temperatures. For instance, the first profile type (Holding in Tension) was executed with three different environment inputs. The first environment lacked active temperature control of the chamber in order to compare with the impact of actively controlling the chamber air to a specified setpoint. Next, a test at elevated environment temperature determined this impact on EMAS performance and efficiency. Finally, dynamic mechanical profiles at varying environment temperatures were completed to analyze EMAS energy flow. All tests were completed with the EMA inside the environmental chamber.

Table 2 Test Matrix

Test Matrix				
Profile	**Stroke Input**	**Force Input**	**Environment Input**	**Profile Description**
Holding in Tension	Constant	Constant	No Control	0 velocity against 25% of stall force *without active temperature control*
			Constant	0 velocity against 25% of stall force at environment temperature 22°C
			Constant	0 velocity against 25% of stall force at environment temperature 70°C
Holding in Compression	Constant	Constant	Constant	0 velocity against 25% of stall force at environment temperature 22°C
Short Mission	Simulated Segment	Simulated Segment	Simulated Segment	Mission segment representative stroke, force at environment temperature ~15°C
			Constant	Mission segment representative stroke and force at environment temperature 70°C
Full Mission	Simulated Mission	Simulated Mission	Constant	Full mission segment representative stroke and force at environment temperature 22°C
Extended Mission	Simulated Mission	Simulated Mission	Simulated Mission 1% Hot Day	Full mission representative stroke, force at 1% Hot Day environment temperature

4.5.1 Holding in Tension

Figure 4.24 shows stroke, force, and environment temperature inputs for holding tests in tension. All holding in tension profiles were 1200 seconds in length and had constant stroke (0 mm) and force (1500 N) inputs. Holding tests in tension were executed under three different environments: without active temperature control, with active temperature at 22°C, and with active temperature control at 70°C.

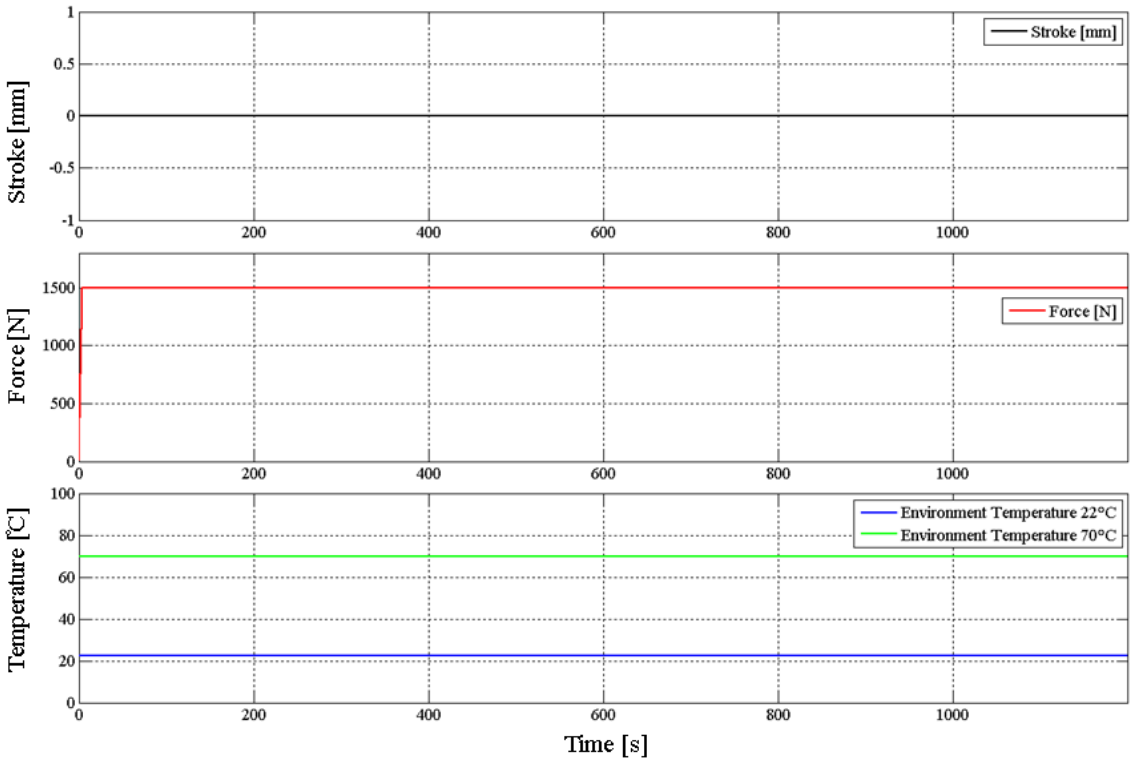

Figure 4.24 Holding in Tension Input Profiles

4.5.2 Holding in Compression

Figure 4.25 shows stroke, force, and environment temperature for holding tests in compression. A holding test in compression was completed at only one environment temperature (22°C) and was used to compare the EMAS performance of holding in tension versus holding in compression. The holding test in compression was a carbon copy of the holding test in tension except the force input was -1500 N instead of +1500 N.

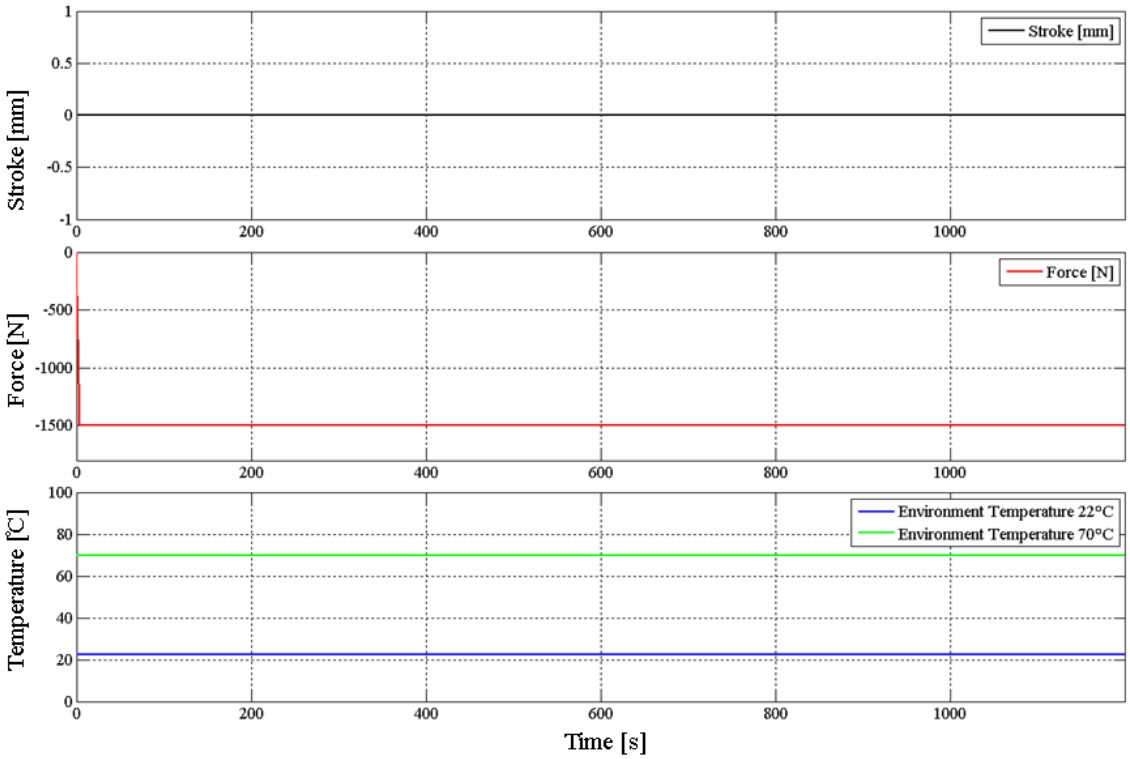

Figure 4.25 Holding in Compression Input Profiles

4.5.3 Short Mission

A short mission, 230 seconds in length, made up of several stroke and force peaks and valleys was created to gauge the performance of the EMAS under a dynamic profile at varying environment temperatures. Figure 4.26 shows the resulting inputs and how they're made up of several reversal sequences followed by a lateral frequency sweep near the end of the profile.

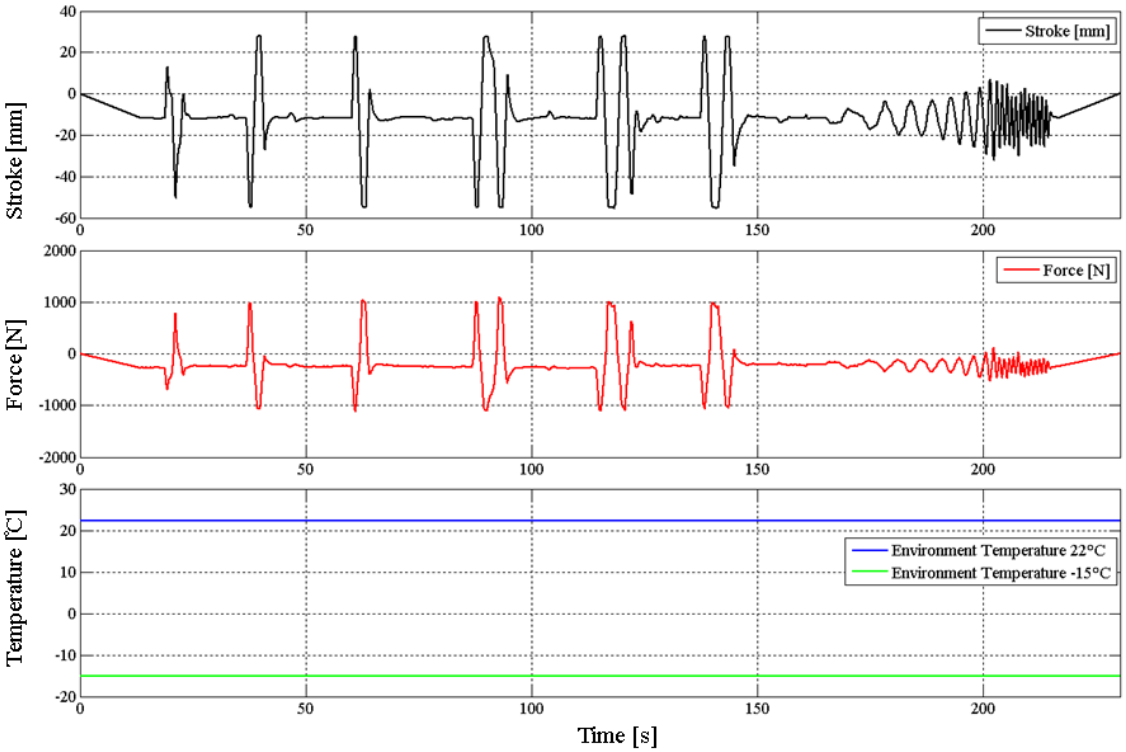

Figure 4.26 Short Mission Segment Profile Inputs

4.5.4 Full Mission

A full mission, just over 900 seconds in length, was artificially created to stress the EMAS. The first third of the profile is made up of artificially replicated dynamic stroke and force commands. The last two-thirds of the full mission profile were a hold in tension at an elevated force (5000 N). The hold portion of the full mission profile was similar to an approach and landing where the control surface would be deployed to maintain lift resulting in a constant load for an extended period of time.

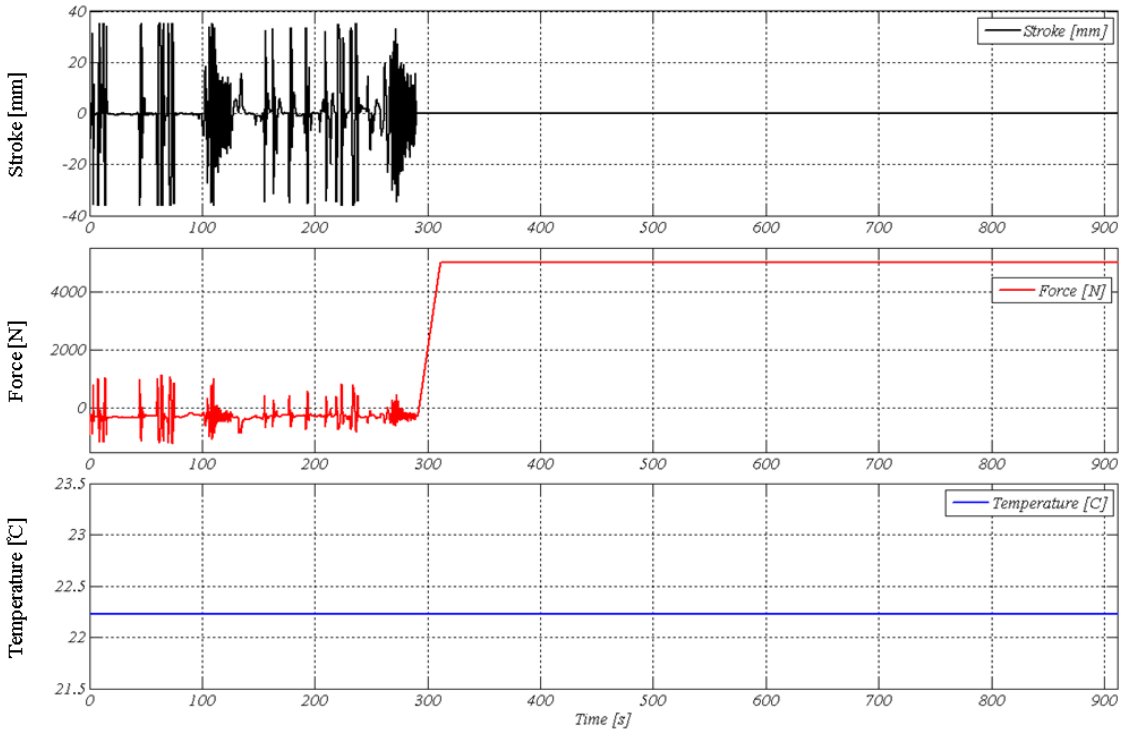

Figure 4.27 Full Mission Profile Inputs

4.5.5 Extended Mission

Average difference in typical and 1% hot day temperature for increasing values of altitude was calculated as 31°C. This average offset is shown in Figure 4.29 which is a plot of typical and 1% hot day temperatures as a function of altitude. Therefore, the typical day ambient temperature profile was offset 31°C to simulate 1% hot day conditions. Mechanical and thermal inputs as a function of time for a 2 hour representative mission are described in Figure 4.29

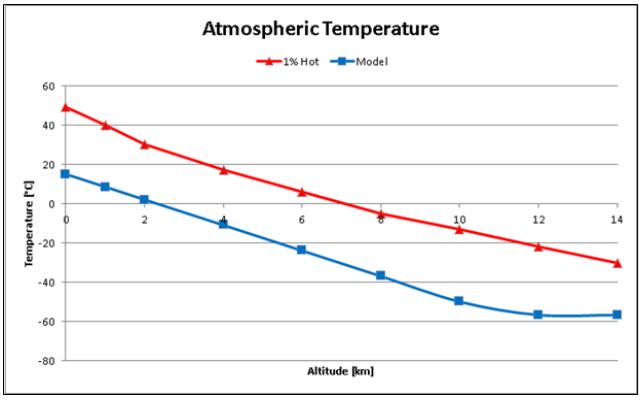

	Temperature		
	Model	MIL-HDBK-310	
Alt	Typical Day	1% Hot Day	Temperature Difference [°C]
0	15	49	34
1	9	40	31
2	2	30	28
4	-11	17	28
6	-24	6	30
8	-37	-5	32
10	-50	-13	37
12	-57	-22	35
14	-57	-30	27
		Average	31
		Standard Deviatoin	3.5

Figure 4.28 Bay Temperature for 1% Hot Day Methodology

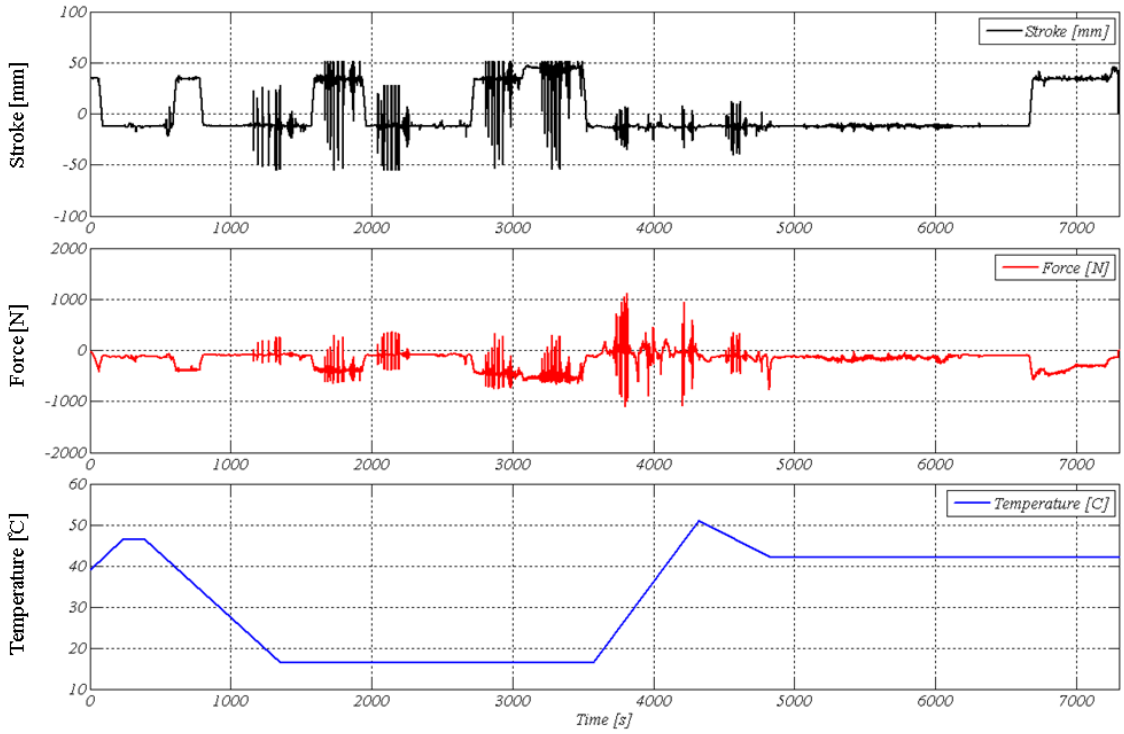

Figure 4.29 Extended Mission Profile Inputs

4.6 Measurement Uncertainty

Measurement uncertainties can come from the measuring instrument, from the item being measured, from the environment, from the operator, and from other sources (Bell 1999). In relation to the test setup of an EMAS, measuring instruments and the environment were the primary sources for uncertainty. Therefore, work was done to quantify uncertainty associated with both sources. From this, uncertainties in power and energy calculations used to assess the performance of the EMA were determined. Additionally, efforts were taken to reduce any errors in measurement by calibrating each measurement device, including the load cell, current transducers, voltage probes, and thermocouples.

4.6.1 Instrument Uncertainty via Calibration

Each device was calibrated against a known input. The load cell was calibrated by MTS personnel in 2011. For added assurance we loaded the force transducer in tension with a known weight and recorded the output as a function of those known inputs. DC bus voltage was measured using Tektronix P5200 Voltage probes, which were rated to 1300 V and provided 500X attenuation. Our experiment included nominal driver voltages of 320 Vdc and possible spikes upwards of 900 V. Therefore, in order to check the attenuation of the probes a Voltage Source which could provide upwards of 400Vdc was necessary. It was found over a wide range of DC Voltage inputs that the average attenuation of both probes was indeed 499-505. Thus, this value was used in transducer transfer function. Similar efforts were completed for the current transducers in which a power source generated a range of current values absorbed by a resistor bank.

Thermocouples were calibrated with the use of a thermal bath and high precision RTD. All of the thermocouples were fixed to the temperature sensing region of the RTD, to minimize

spatial errors, and submerged in a temperature-controlled silicon oil bath. The bath was commanded by a LabVIEW program to reach temperatures of -20°C to 150°C at 5°C degree intervals. The bath was considered at equilibrium when the standard deviation of the last 100 RTD samples was less than .005 °C. Once the bath reached equilibrium an RTD and thermocouple value was sampled every second for 15 seconds. This process was completed for the increasing temperature curve, from -20°C to 150°C, and for the decreasing temperature curve, 150°C to -20°C, to identify any hysteresis errors. Thermocouple temperatures recorded were then associated with RTD temperature readings and fit to an equation for each thermocouple, which was used by the RT DAQ to calculate true temperature based on measured temperature.

Figure 4.30 provides a summary of calibration uncertainty results and manufacturer reported uncertainties. For more detail on calibration procedures see Appendix I.

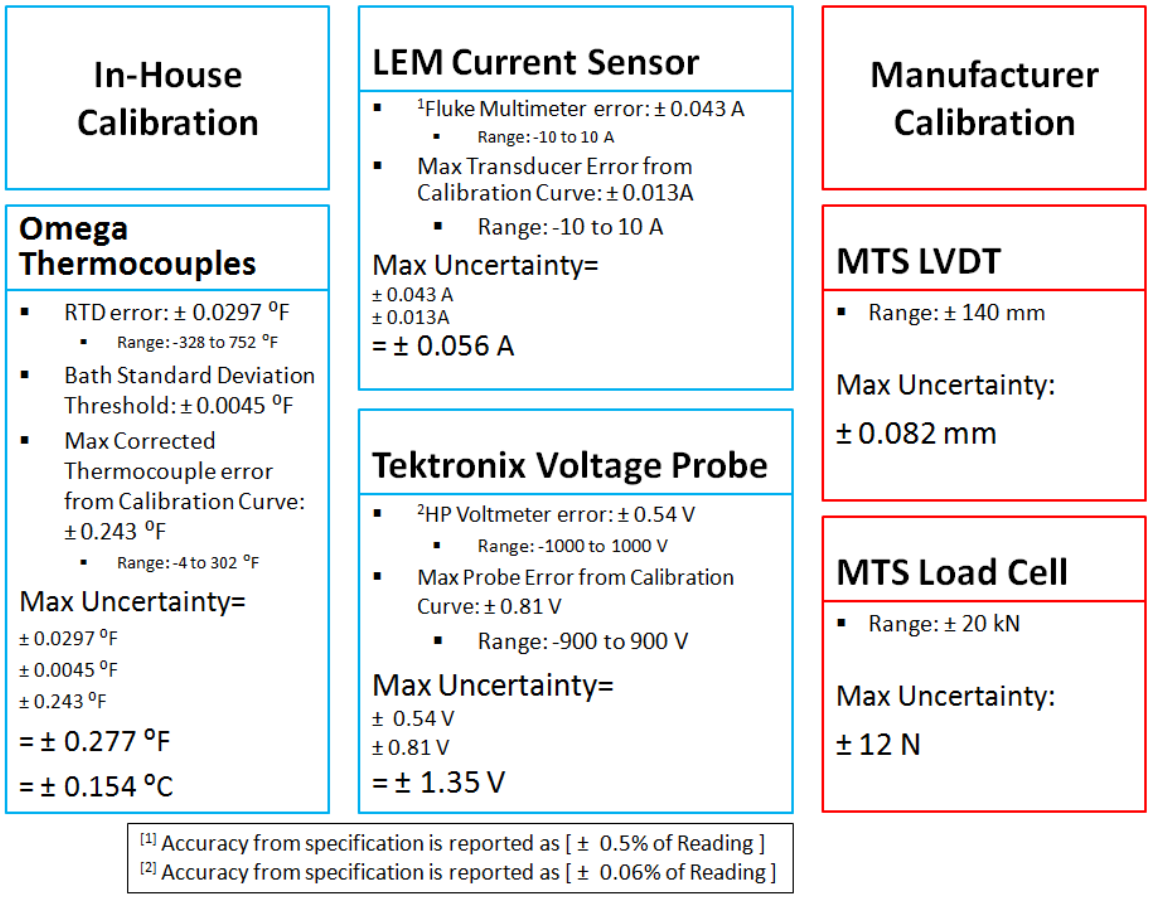

Figure 4.30 Transducer Uncertainties

4.6.2 Environment Induced Uncertainty

It was found laboratory air temperature was relativity constant over the course of several months of testing. The laboratory temperature varied approximately 2 degrees C, resulting in negligible effect on our measurement system (instruments, transducers, DAQs). However, special attention was afforded to the variation in DAQ readings as a function of board temperature and duration of operation. Both electrical and thermal DAQ boards required at least 15 minutes of warm-up (engaging Analog to Digital Converter) in order to reach a steady state. This was identified when electrical measurements showed a tendency to drift from zero to some

offset over the first 15 minutes of measurement when EMAS was off (no electrical power draw). Additionally, a substantial source of electromagnetic interference (EMI) was present in the laboratory. In order to characterize the DAQ error due to EMI, the EMAS was powered on but in an unloaded state with no power draw or movement (0 velocity), while stroke, force, voltage, and current were sampled for 30 seconds. Measured responses in Figure 4.31 were smoothed using the Savitzky-Golay method and then their range determined as the difference in the maximum and minimum value over 30 second period.

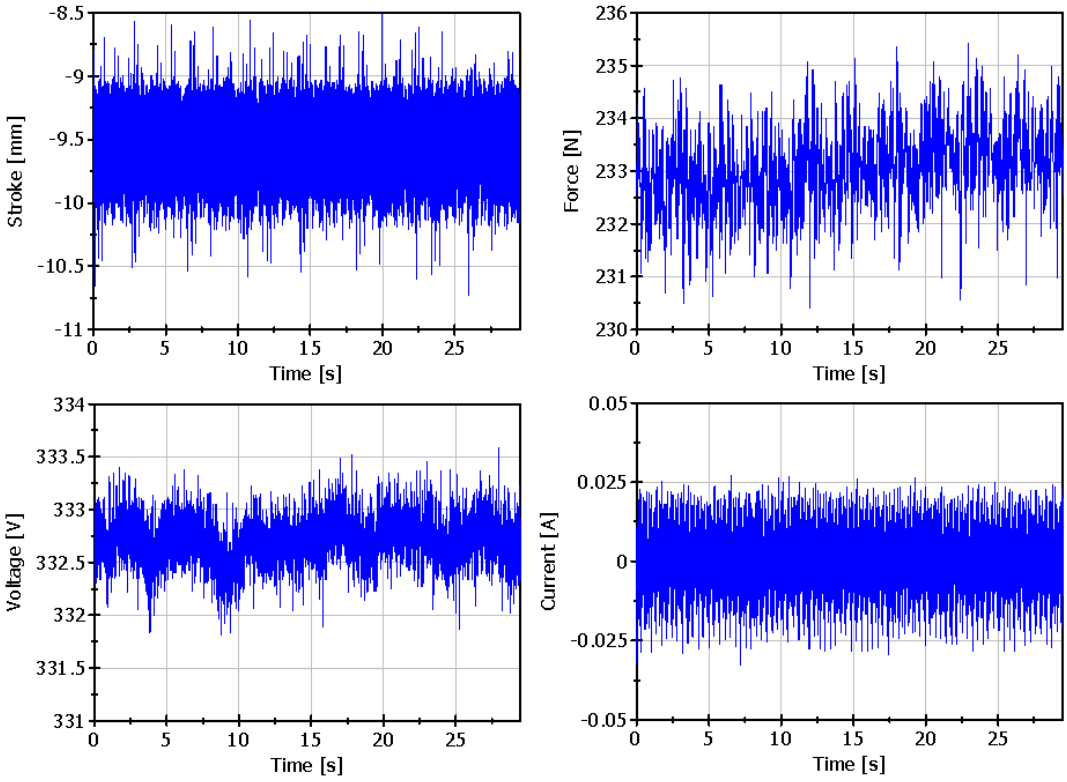

Figure 4.31 Laboratory Environmental Noise Characterization

Based on that analysis, environmental uncertainty for each of the measurements was assumed to equal the range of each measurement and can be found in Table 3. Appendix J further develops analysis of environment noise and some methods to eliminate aliasing.

Table 3 Environment Noise per Sensor

Measurement	Noise Band	Sensor Range	% of Range
Stroke [mm]	± 1.0	± 140	± 0.70%
Force [N]	± 2.5	± 20,000	± 0.01%
Voltage [V_{dc}]	± 1.0	± 900	± 0.11%
Current [A_{dc}]	± 0.025	± 10	± 0.25%

4.6.3 Final Uncertainty

In summary, the magnitude of each measurement uncertainty as a result of environment and instrument influences were assessed. The maximum uncertainty whether environment or instrument related was used to determine uncertainty propagated to mechanical and electrical

power calculations. Current, voltage, and load measurement uncertainty was fixed by transducer calibrations while stroke measurement was fixed by environment uncertainty analysis. These uncertainty bounds were utilized against calculated parameters in post-test energy analysis. Based on McClintock's method, the uncertainties present in each measurement have been accounted for and their impact on power calculations determined (Kline & McClintock, 1953). These values with their derivation can be found in Figure 4.32.

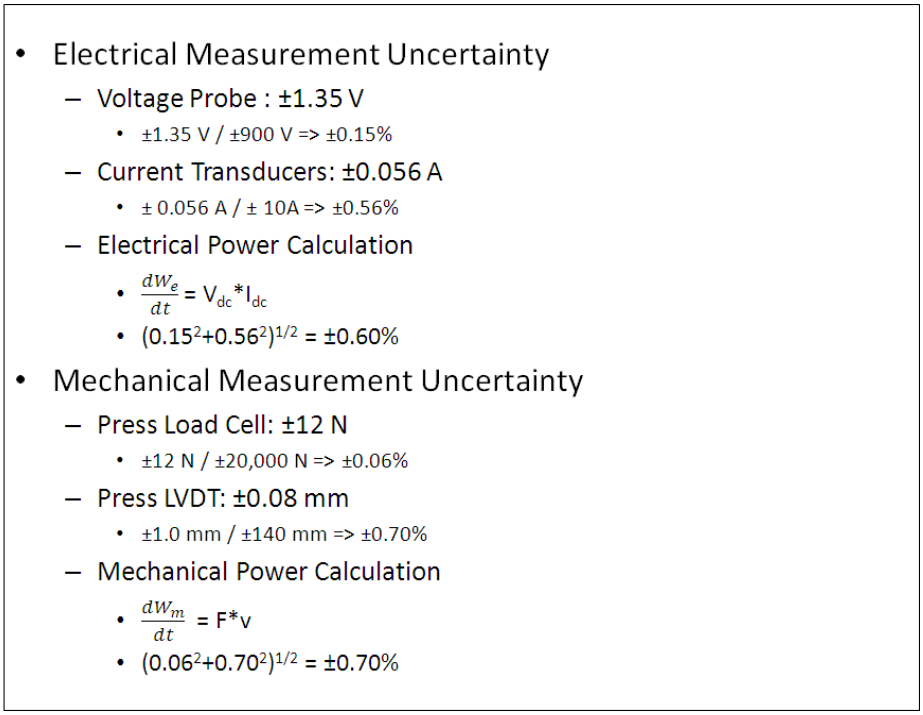

Figure 4.32 Final Measurement Uncertainty and Propagation

4.7 Post Test Analysis

A methodology was created for organizing test data, screening the results for accuracy, and applying an energy analysis to the results. This methodology was improved for efficiency and honed to reduce down time between tests. Some of the pertinent details are covered in the following subsections.

4.7.1 Post-Processing and Smoothing

DIAdem was used for post-processing due to its ability to store and generate calculations on large data sets, more so than MATLAB and EXCEL. Additionally DIAdem offered a few built in functions for signal filtering which was required as result of power electronics induced noise. Various approaches were tested when smoothing actuator measured parameters. Some of the approaches included a moving average function, Savitzky-Golay function, and a built in low pass digital filter function. The first technique calculated an arithmetic mean for each value from the channel value and a specified number of neighboring values. The second technique smoothed a signal by fitting a polynomial function section-wise to the signal via the least squares method. The third method filtered all frequencies above a specified limit frequency. This method retained characteristics of the signal better than the first and second technique. Figure 4.33 demonstrates the effect of all three methods when applied to a noisy temperature signal. In Figure 4.33, the smoothing function result is covered by the Savitzky-Golay function result. Both the smoothing

and Savitzky-Golay functions removed measurement noise but attenuated realistic variations of temperature when using a 12 point window. Qualitatively, digital filter function removed noise from the signal without distorting the characteristic trend and was therefore the best approach. Savitzky-Golay function with a 12 point window was utilized for measured and calculated parameters such as: stroke, force, velocity, temperature, and rate of change temperature.

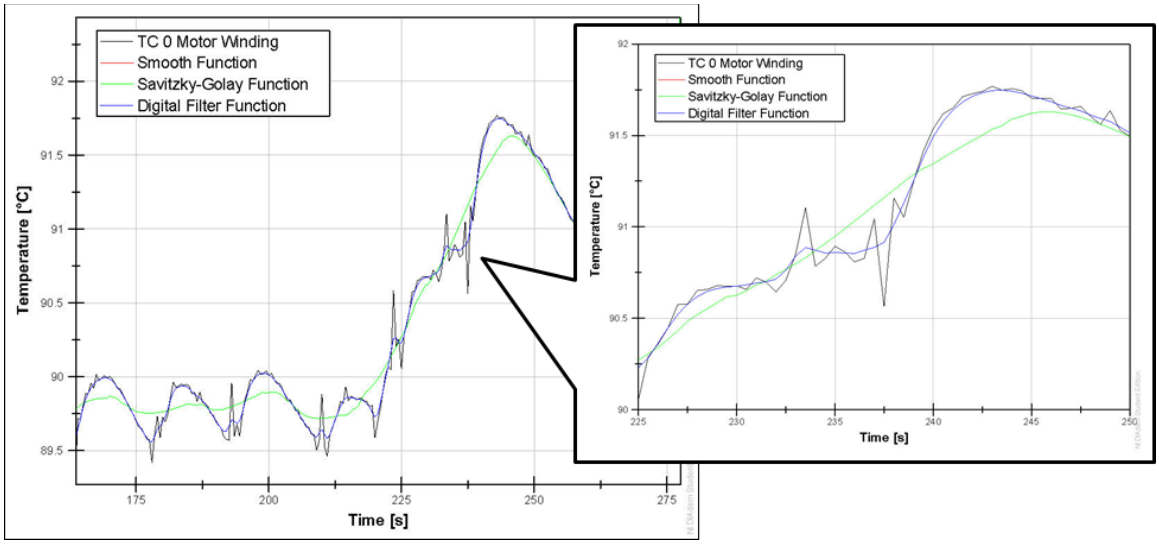

Figure 4.33 Post-test Smoothing (Smooth Function in red covered by Savitzky-Golay Function in green)

4.7.2 Sign Convention

Sign convention was important in determining energy flow direction. Figure 4.34 shows force and stroke sign convention established by the independent measurement and control systems. Work was done by the EMA if the load was opposing the direction of EMA velocity. Work was done on the EMA if the load and velocity shared the same direction. Due to the sign convention already established in the laboratory, extending against a load in compression or retracting against a load in tension resulted in a negative value of mechanical power. Therefore, the sign of mechanical power was adjusted in post processing to positive when work was being done by the system in order to coincide with the convention of Figure 4.35.

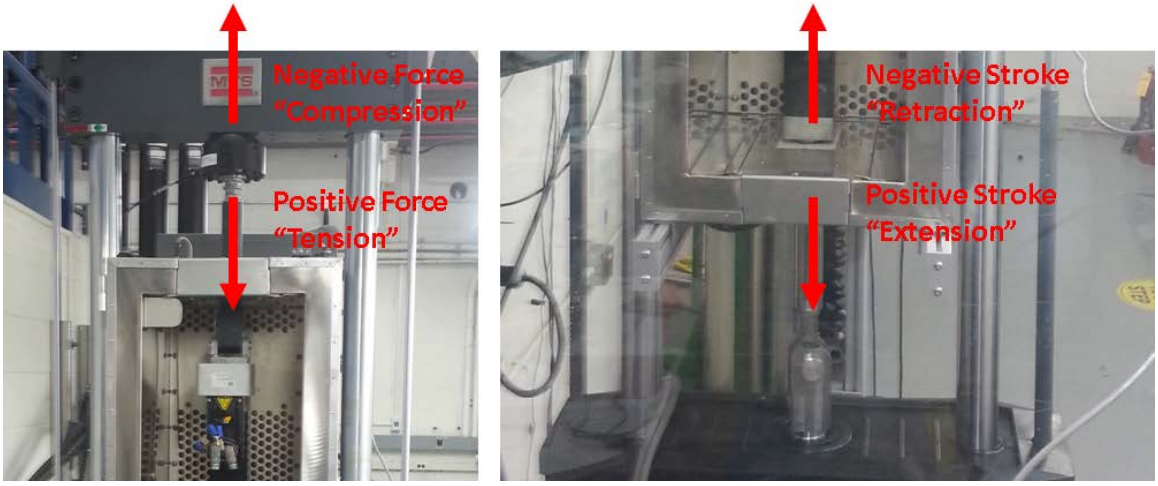

Figure 4.34 Mechanical Parameters Sign Convention

4.7.3 Energy Analysis

The block diagram in Figure 4.35 depicts an EMAS and its primary components. The red outline in Figure 4.35 represents the control system utilized to analyze EMAS energy flows. The control system included the following primary energy users: servo drive, electric motor, and actuator. The control system was defined to include these components because traditionally they are the hottest components in an EMAS (Zhou, 2010). The block diagram accounts for work and heat transfer in and out of the system.

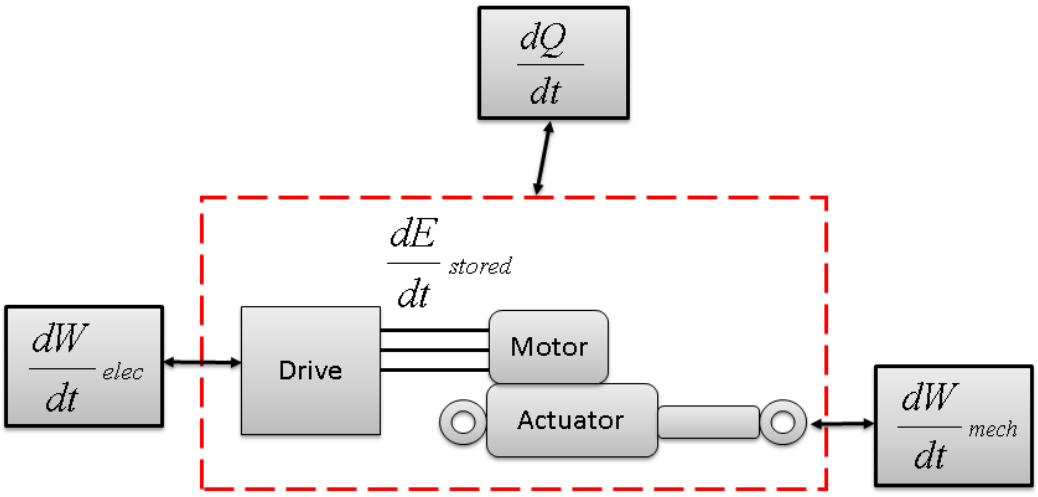

Figure 4.35 Experiment EMAS Block Diagram

The first law of thermodynamics when applied to this control system:

$$\frac{dE}{dt} = \frac{dW}{dt} + \frac{dQ}{dt}$$

where energy increase of the system equals the heat received plus the work received (White, 1984). Electrical power drawn by the system was calculated as the product of measured DC bus voltage and current at discrete intervals:

$$\frac{dW_e}{dt} = VI$$

Electrical power was numerically integrated from the profile's initial to final time, resulting in electrical work:

$$W_{e_{T_i \to T_f}} = \int_{T_i}^{T_f} \frac{dW_e}{dt}\, dt$$

Mechanical power exerted by the system was calculated as the product of measured force and calculated ram velocity at discrete intervals:

$$\frac{dW_m}{dt} = Fv$$

Ram velocity was calculated by a central difference method where Δt equals the sampling period:

$$v_i = \frac{x_{i+1} - x_{i-1}}{2\Delta t}$$

Mechanical power was numerically integrated from the profile's initial to final time, resulting in mechanical work:

$$W_{m_{T_i \to T_f}} = \int_{T_i}^{T_f} \frac{dW_m}{dt} dt$$

By re-arranging the first law of thermodynamics, net work was defined as thermal energy:

$$E_{T_i \to T_f} - Q_{T_i \to T_f} = W_{e_{T_i \to T_f}} - W_{m_{T_i \to T_f}}$$

where,

$$E_{T_i \to T_f} - Q_{T_i \to T_f} = Thermal\ Energy$$

$$W_{e_{T_i \to T_f}} = Electrical\ Work$$

$$W_{m_{T_i \to T_f}} = Mechanical\ Work$$

Under regeneration mechanical energy can overcome the motor causing it to behave as a generator and produce electrical energy. Under this scenario, the difference in mechanical work and electrical work is also defined as thermal energy. Bidirectional arrows in the block diagram indicate the system's ability to operate in both modes.

Thermal control was developed to simulate realistic EMAS environmental conditions. However, lack of pressure control limited the ability to realistically simulate air pressure and density as a function of altitude over the mission test. As a result, heat transfer modes and their magnitude throughout the test are not wholly representative of an actual flight. For instance, on a 1% Hot Day at altitude (7.8 km) the air density is 46% of its value at sea level (MIL-HDBK-310). "Thermal conductivity, specific heat, viscosity, are all nearly independent of pressure for gasses and liquids from "soft" vacuum to several atmospheres. But the density of gases varies widely with pressure (MIL-HDBK-251)." Therefore, air at high altitudes is a poor medium for convection. This can have significant implications for platforms that rely heavily on convection as their primary means of cooling.

4.7.4 Reduced Energy Analysis

Upon post-test analysis, it was noticed that there was little to no work done on the system and therefore negligible regenerative energy. There was negligible regenerative energy because the EMA system was nearly always expending mechanical work with little to no mechanical work being done on the system. The EMA system was nearly always expending mechanical work because the hydraulic press response was delayed which caused the load to always impede the direction of EMA acceleration. Additionally lack of regenerative resistor (TC 8) and transistor temperature (TC 9) change over all profiles suggested negligible amounts of regenerative energy were realized. Figure 4.36 demonstrates this claim for a dynamic mission where regenerative cycles are most likely to occur. Measured force overshoot as a result of the hydraulic press delayed response was significant throughout the entire profile and is shown on the left. Throughout the entire profile the load impeded the direction of EMA acceleration. On the right regenerative resistor (TC 8) and transistor temperature (TC 9) show little to no change, supporting the claim that negligible amounts of regenerative energy were experienced.

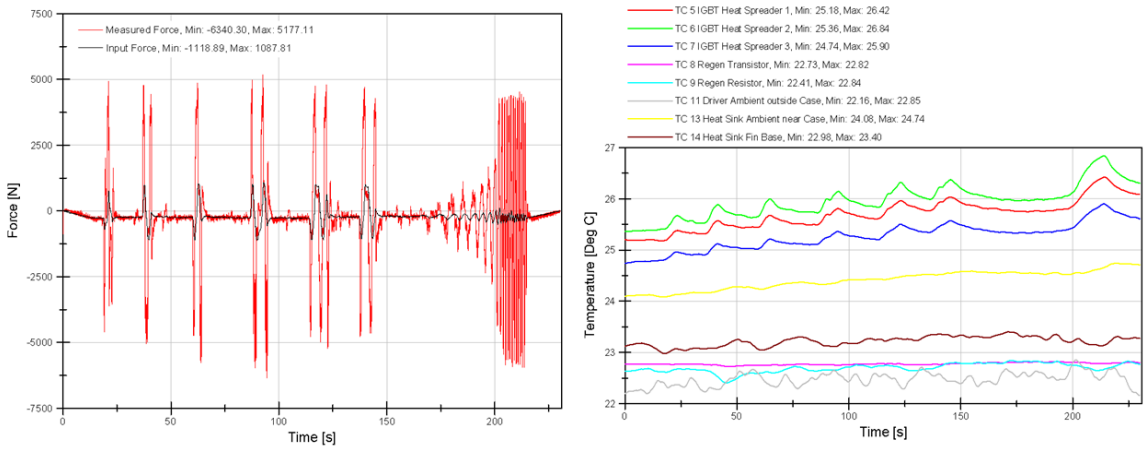

Figure 4.36 Force Control (Left) and Regenerative Component Temperature (Right)

Therefore, the EMA control system defined in Figure 4.35 could be simplified to include only electrical energy input, mechanical energy output, and thermal energy stored and or transferred to the environment. Figure 4.37 is a simplified diagram of these energy flows and their typical magnitude.

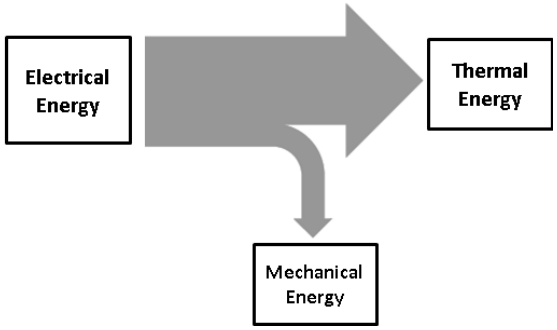

Figure 4.37 Typical Energy Flow throughout Tests

As a result of the simplification, thermal energy which accounted for heat stored within the control system and transferred to its sink was determined as the difference in electrical input energy and mechanical output energy for each test. Moving forward, thermal energy in addition to the rate of change of temperature and temperature difference for temperature sensitive components was used to determine thermally malignant portions of profiles and their thermal design points. Additionally, conservation of energy figures are used to highlight the proportion of electrical, mechanical, and thermal energy for each test.

CHAPTER 5

TEST RESULTS

5.1 Full Mission Test Overview

A full mission profile was artificially created based on EMA performance data and realistic EMAS duty cycle and ambient conditions. The test was just over 900 seconds in length and aimed to stress the EMAS. Measured mechanical data stroke and force and electrical data voltage and current are shown in section 5.2 and 5.4 to demonstrate how the following parameters were calculated: velocity, power, and energy. Environmental chamber performance is highlighted in section 5.3. Thermal results are discussed in section 5.5. Lastly, these parameters were used to generate insights for EMAS performance in section 5.7. *Note, only test results for full mission test are presented in this section, additional results for remaining test matrix profiles are presented in Appendix K.*

5.2 Full Mission Mechanical Results

Figure 5.1 is a plot of measured and input stroke as a function of time. This plot demonstrates the EMAS's capability to replicate a dynamic stroke profile. The full mission profile consisted of a dynamic actuation phase followed by an extended holding phase.

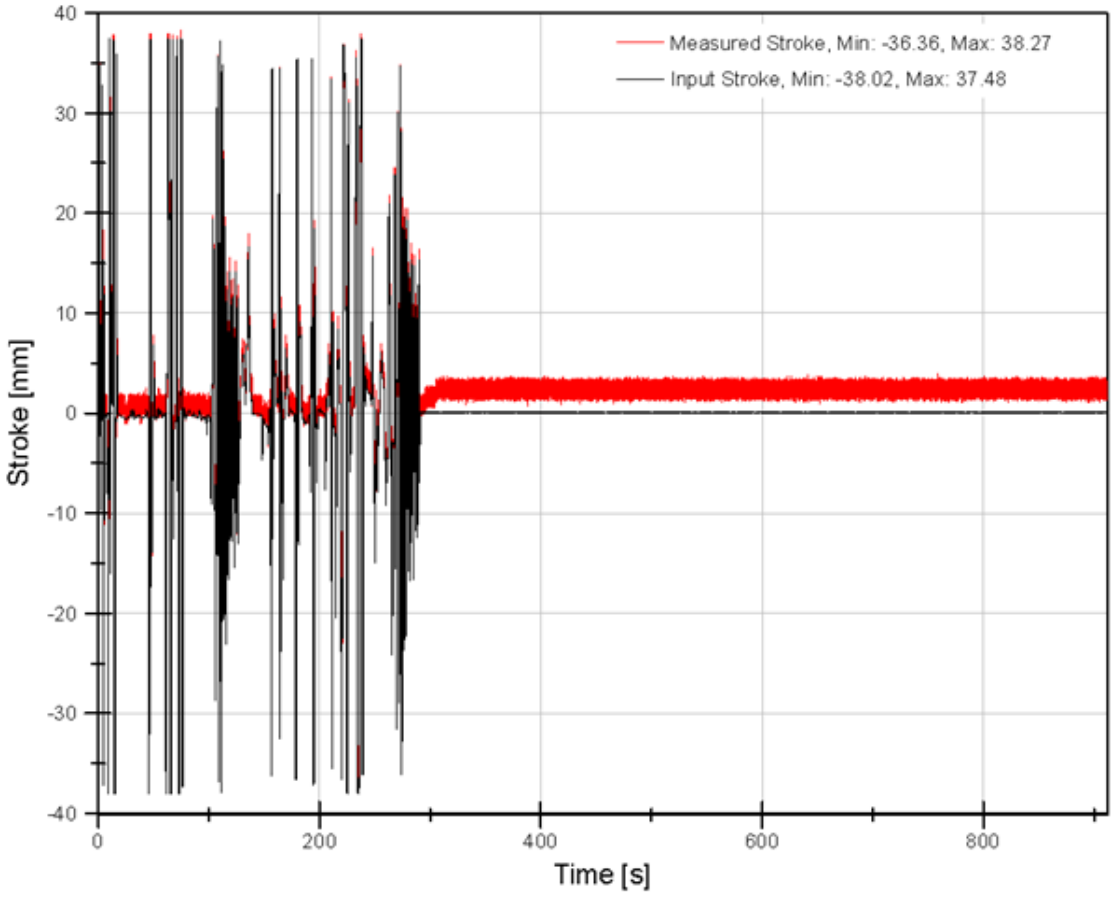

Figure 5.1 Full Mission—Input and Measured Stroke

Figure 5.2 is a plot of measured and input force as a function of time. There was a large discrepancy between measured and input force during the dynamic portion of the profile. This was due to the lack of dynamic controllability of the MTS hydraulic load frame at the time of the test. It was believed feed forward PID control and signal conditioning would greatly improve force following and reduce the discrepancy experienced under these tests. This area was established as future work. The magnitude of force under dynamic portions of the profile led to higher levels of electrical power than if there were no discrepancy and as a result greater component temperatures were realized. During the holding portion of the profile the force discrepancy was virtually eliminated.

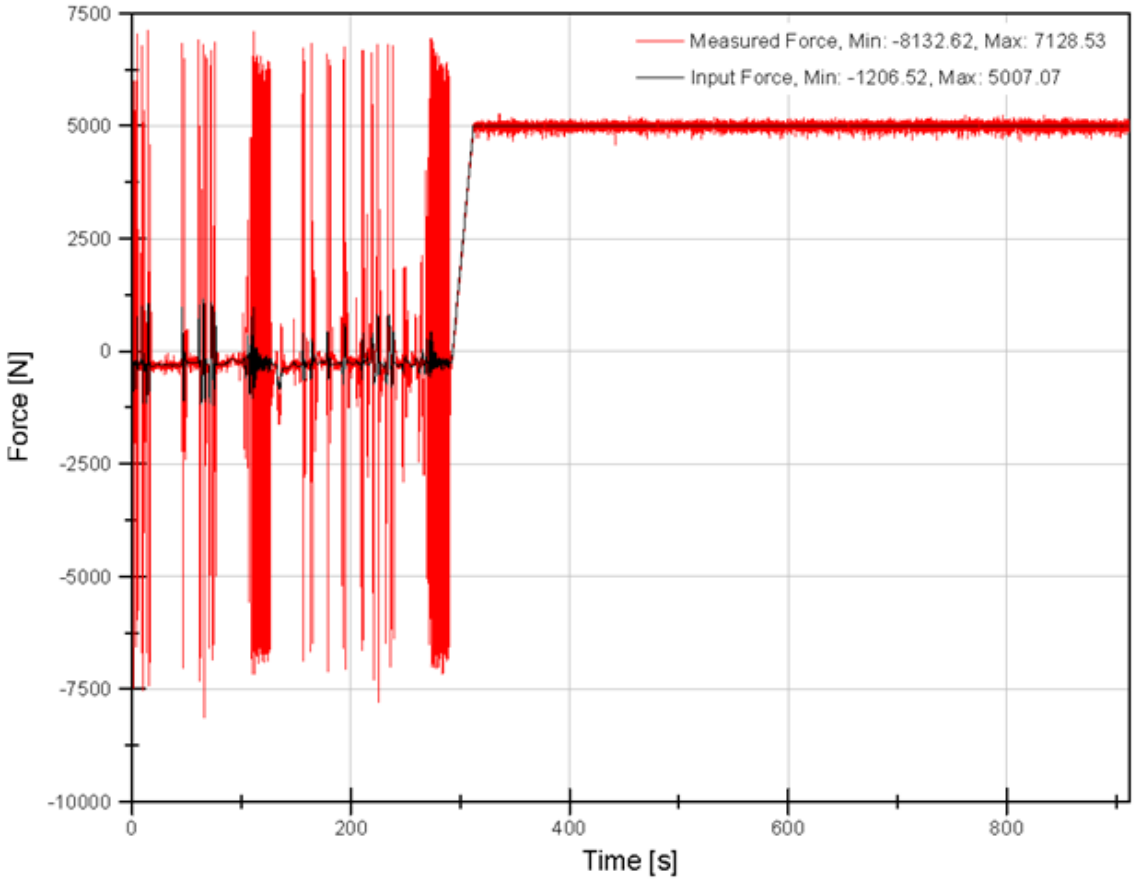

Figure 5.2 Full Mission—Input and Measured Force

Figure 5.3 is a plot of calculated velocity based on the procedure developed in section 4.7.3. Under the dynamic portion of the profile, the EMA reached over 100 mm/s several times. Velocity was approximately 0 mm/s from 300 seconds to 900 seconds of the profile.

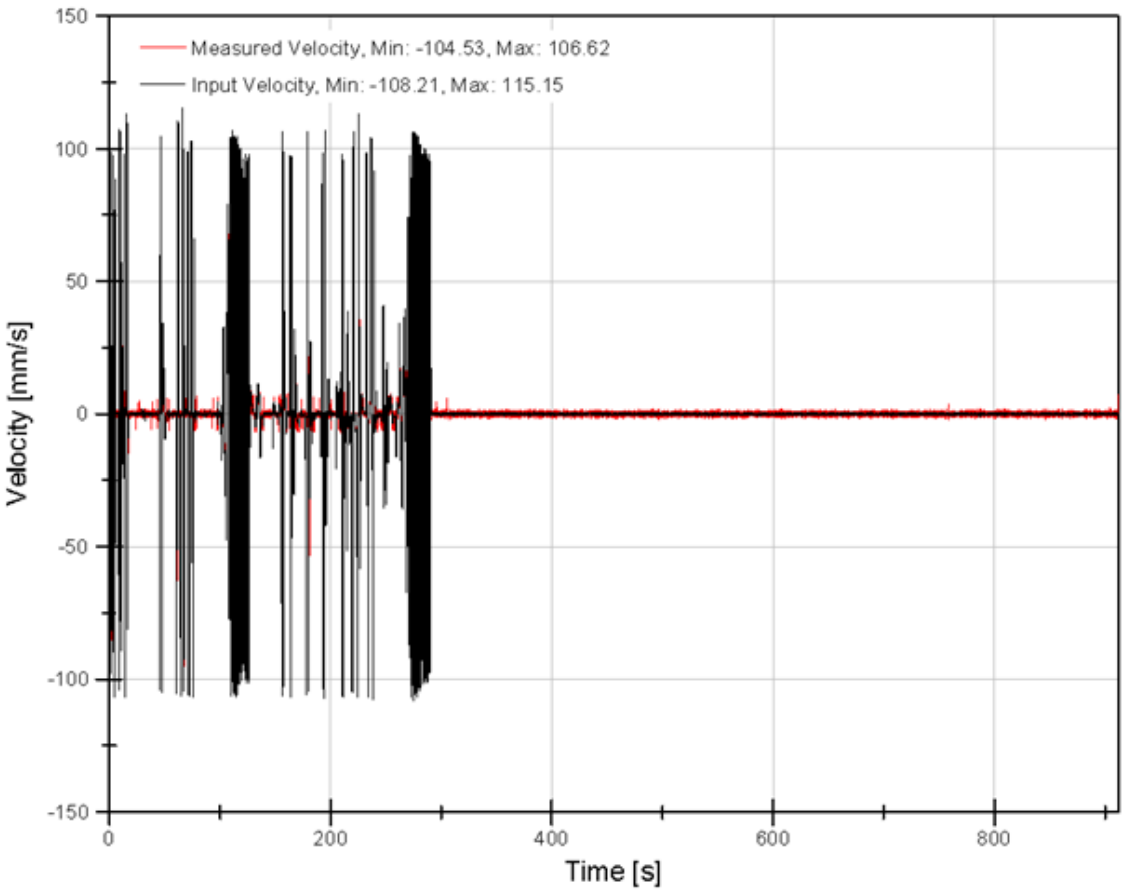

Figure 5.3 Full Mission—Calculated Velocity

Figure 5.4 shows the result of the mechanical power calculation. Mechanical power was integrated with respect to time in order to determine mechanical energy. Peak mechanical power values correspond with times of peak velocity and force. Peak mechanical power values reached approximately 800 W. Mechanical power was 0 W during the holding portion because velocity was effectively 0 mm/s.

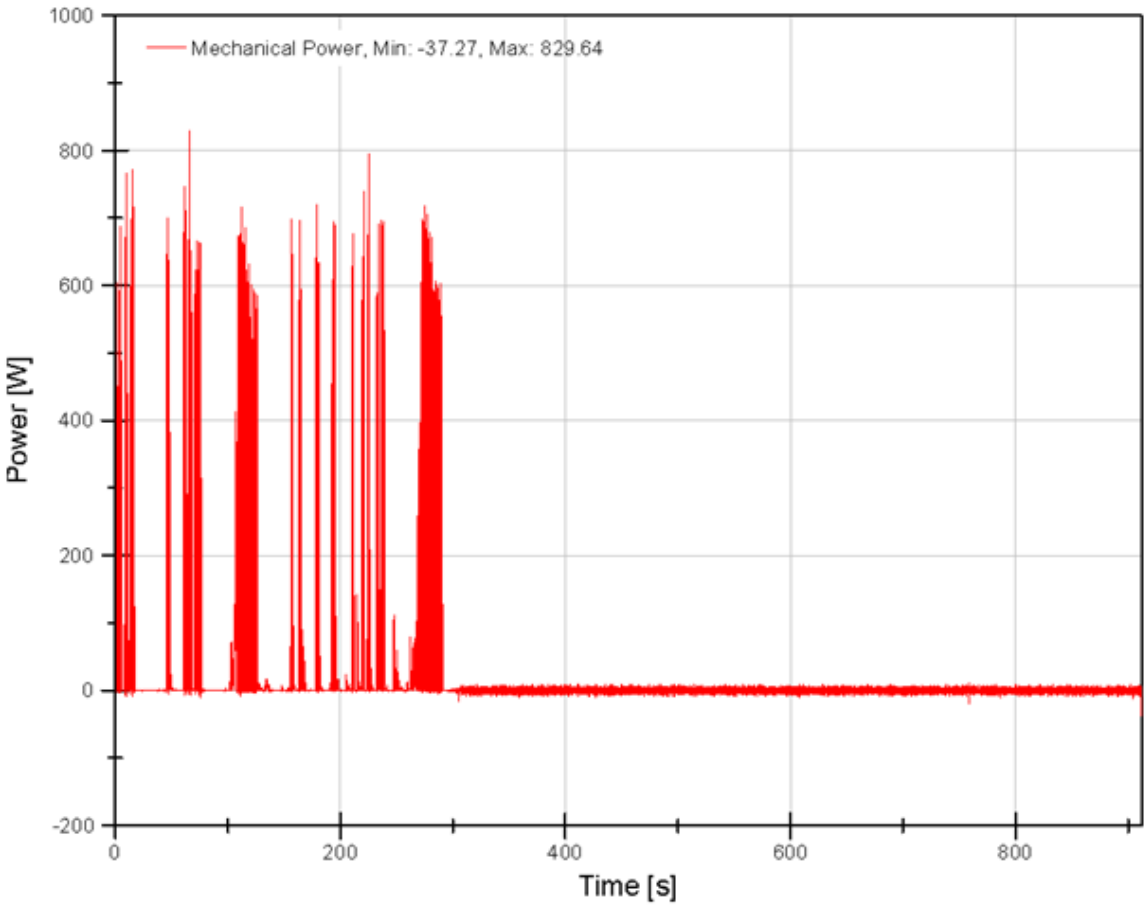

Figure 5.4 Full Mission—Calculated Mechanical Power

5.3 Full Mission Electrical Results

Figure 5.5 shows DC bus voltage as a function of time. During periods of peak velocity and force, where DC current draw was also at its peak, the DC bus voltage was reduced from 328 Vdc to approximately 315 Vdc. During the holding portion of the full mission profile, DC bus voltage was virtually constant at 326 Vdc.

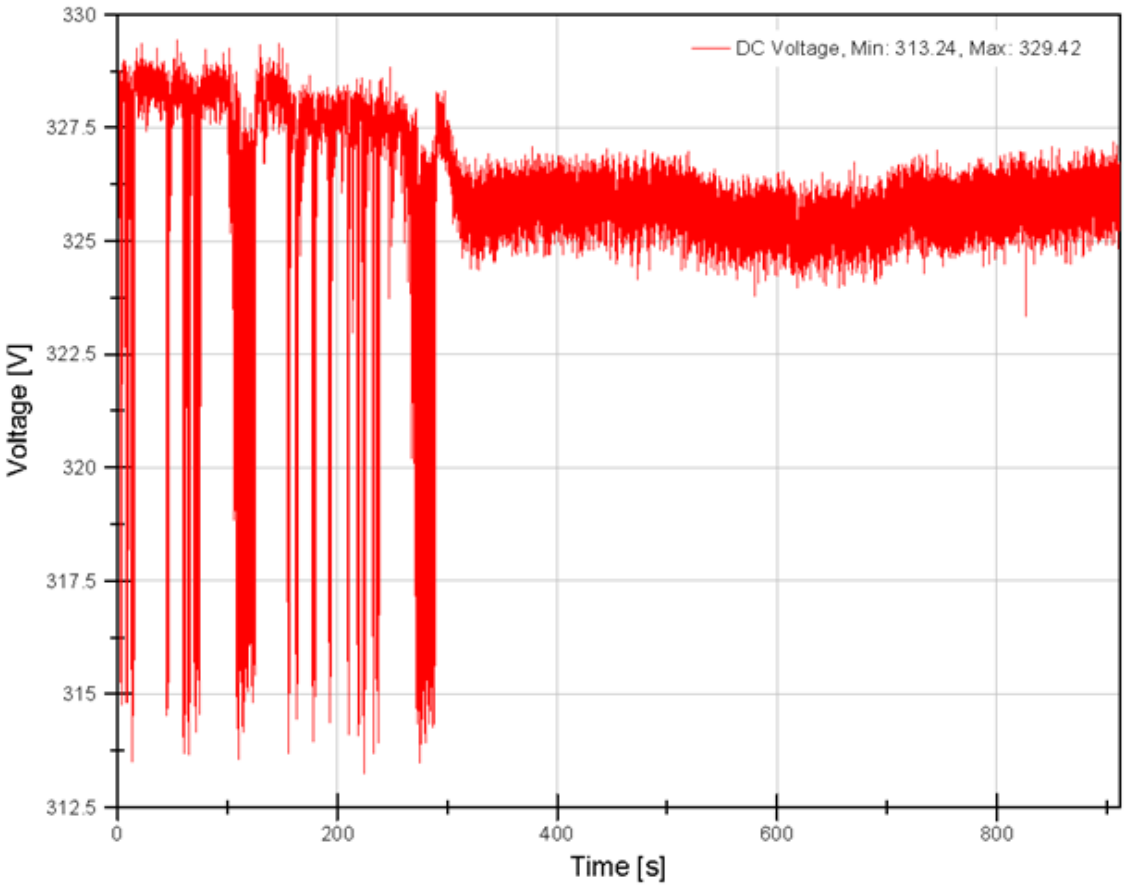

Figure 5.5 Full Mission—Measured DC Bus Voltage

Figure 5.6 shows DC bus current as a function of time. During periods of acceleration DC bus current reached 5.5 A. Average DC bus current to hold a constant position against 5000 N was approximately 3.4 A.

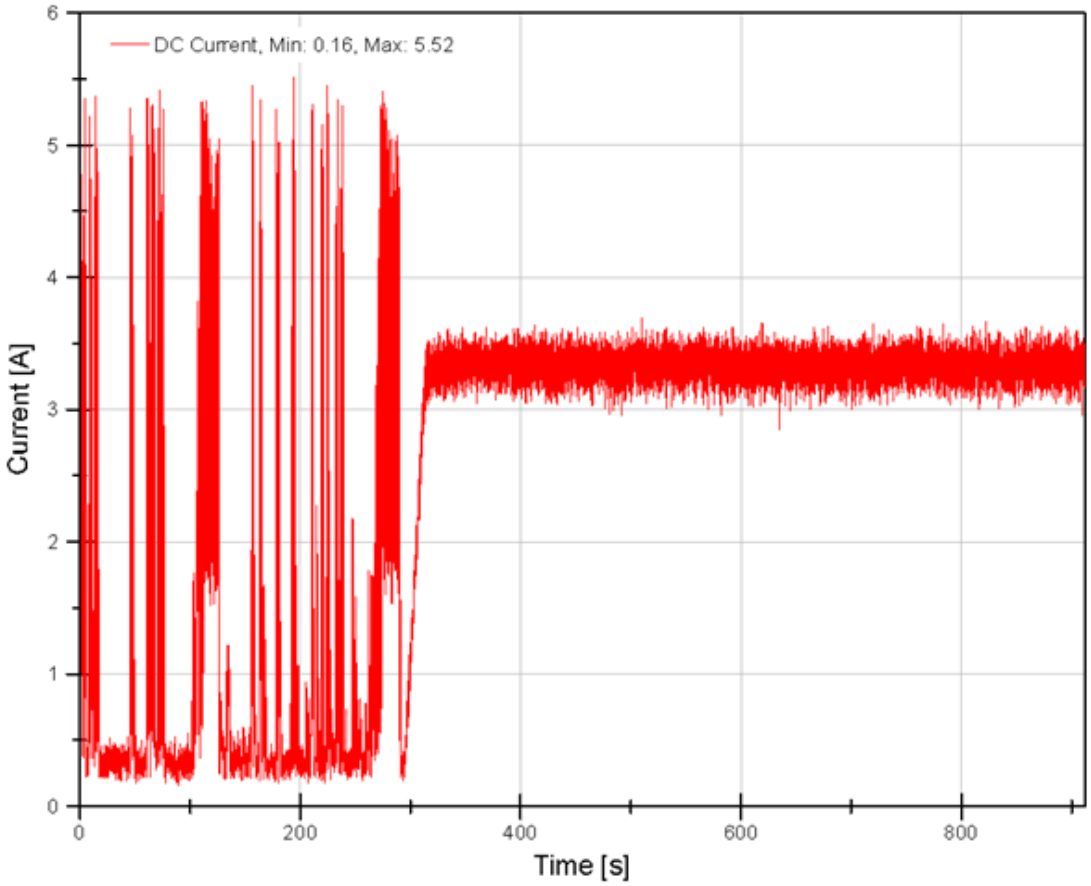

Figure 5.6 Full Mission—Measured DC Bus Current

Figure 5.7 shows measured regenerative circuit current. This plot highlights the fact that very little (maximum 50 mA) regenerative circuit current was generated. It indicated that the DC bus capacitor was large enough to absorb all the regenerative energy without engaging the breaking resistor.

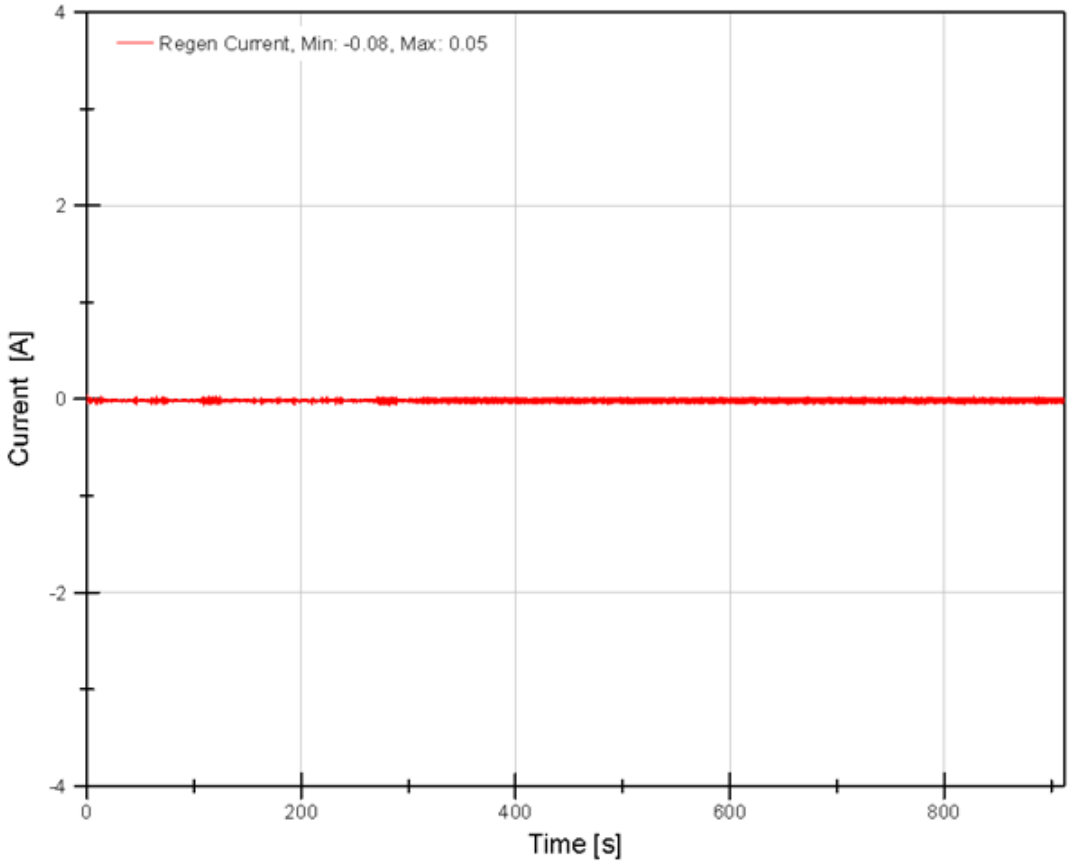

Figure 5.7 Full Mission—Measured Regenerative Circuit Current

Figure 5.8 shows the result of the electrical power calculation. Electrical power was integrated with respect to time in order to determine electrical energy. Peak electrical power values correspond with times of peak current draw, peak velocities and force. Electrical power was approximately 1,100 W while holding a constant force and reached over 1700 W during the dynamic portion of the profile.

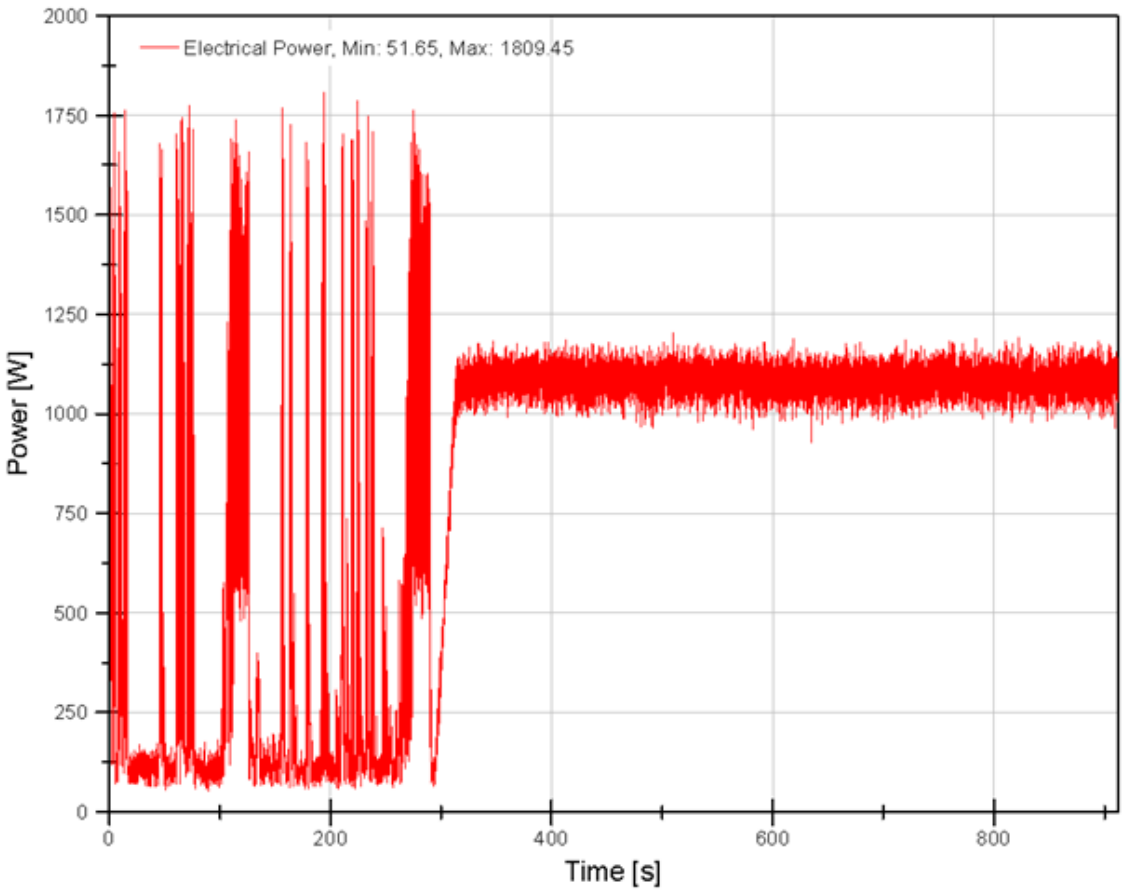

Figure 5.8 Full Mission—Calculated Electrical Power

5.4 Full Mission Thermal Results

Figure 5.9 shows resulting EMA temperature trends. Environment temperature was held constant at 22°C. Motor ambient increased over the course of the test and was slightly higher than the environment temperature, thus reducing the temperature difference between the motor case and motor ambient. Motor windings (TC 1 and TC 2) temperature experienced significantly greater temperature rise than TC 0 during the holding phase. Thermocouple TC 0, TC 1, and TC 2 were embedded near each of the three motor phases at the end turn. Therefore, it was believed the two phases associated with TC 1 and TC 2 were actively engaged during the holding, and therefore exhibited greater current than the third phase indicated by TC 0. Consequently, the two phases associated with TC 1 and TC 2 incurred higher copper loss and therefore higher temperature. However, this could not be verified because motor phase current was not measured. Overall, motor case and winding temperature approached but did not reach steady state during the holding portion of full mission.

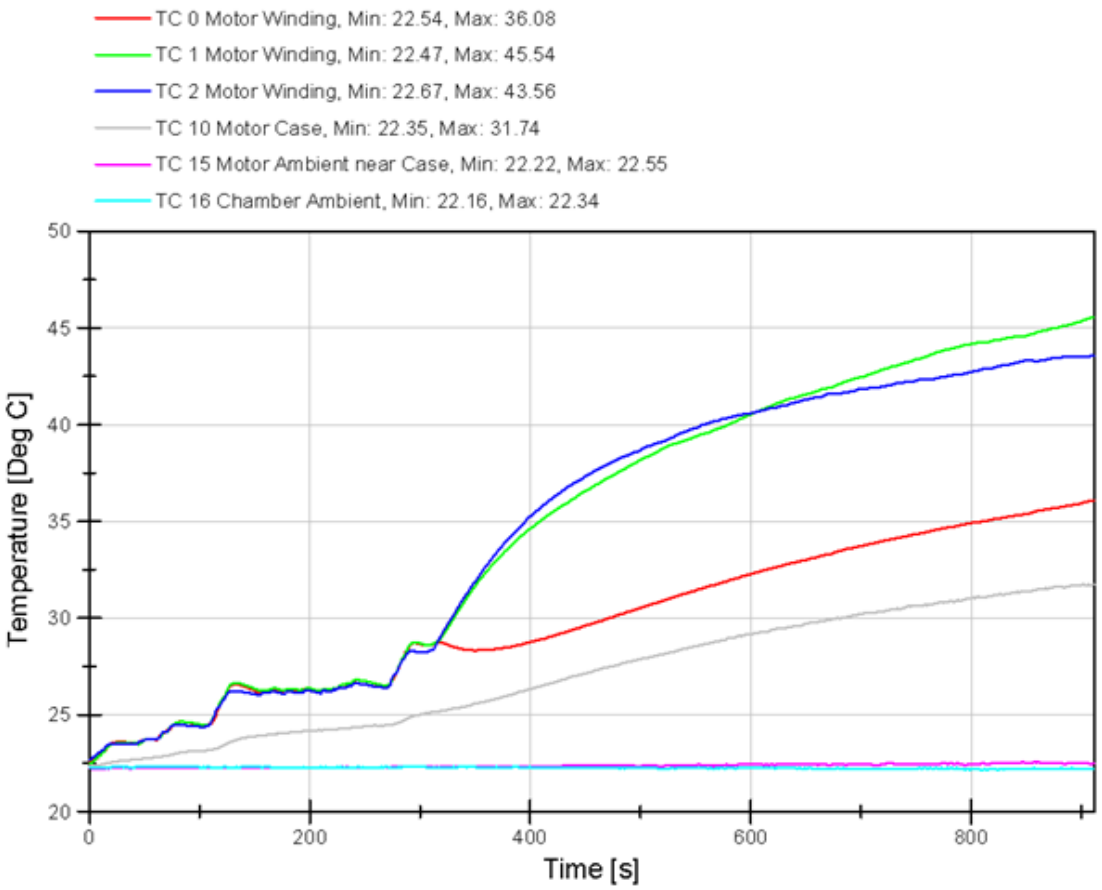

Figure 5.9 Full Mission—EMA Temperature

Figure 5.10 shows resulting motor controller temperature trends as a result of the full mission profile. TC 5, TC 6, and TC 7 which were coupled to the heat spreader of the motor controller's IGBT power module experienced the greatest operating temperatures. TC 8 and TC 9 were placed atop the regen transistor and resistor and experienced the lowest operating temperatures. TC 8 and TC 9 did not experience a temperature rise during the holding portion of full mission while all the remaining component temperatures did (TC 5, TC 6, TC 7, TC 13, and TC 14). This observation was consistent with the low measured regenerative circuit current shown in fig. 5.7. Note: the motor controller was outside the environmental chamber.

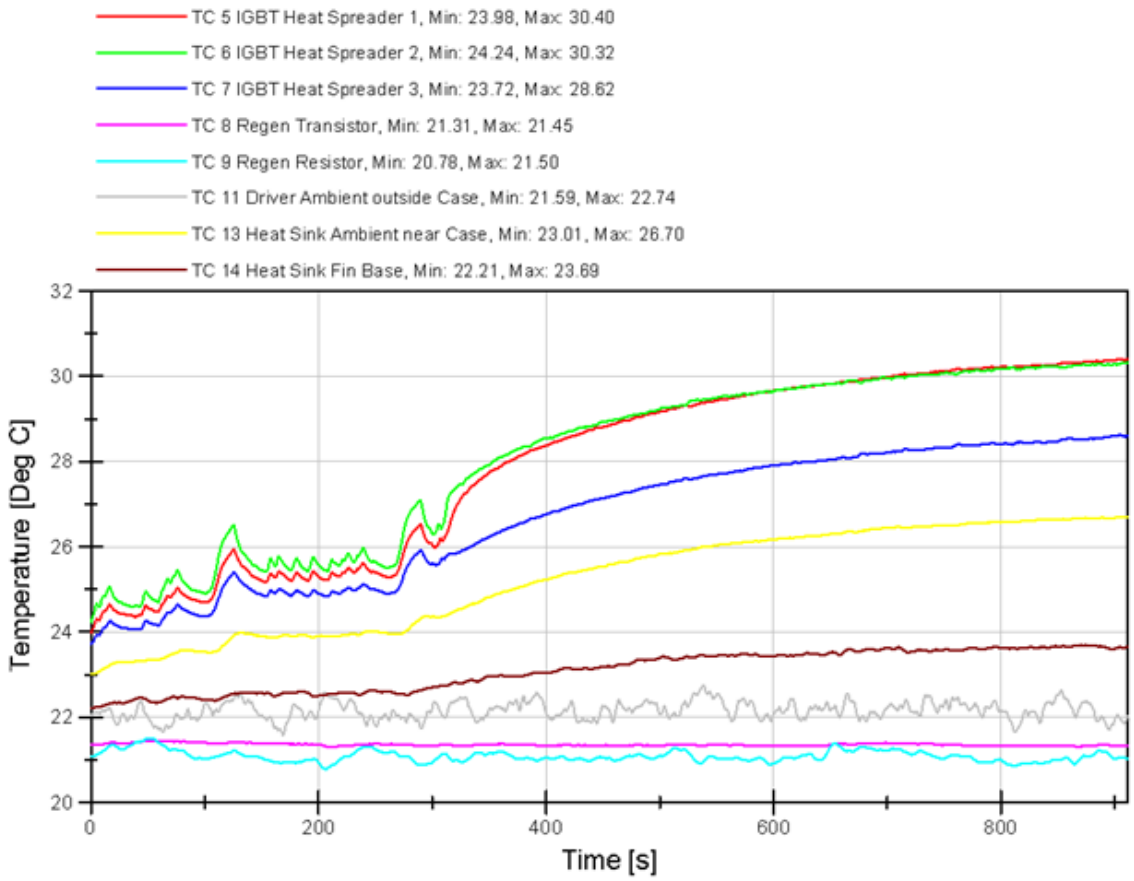

Figure 5.10 Full Mission—Motor Controller Temperature

Figure 5.11 offers more details of each motor winding temperature TC 0, TC 1, and TC 2. All three motor winding thermocouples experienced the greatest temperature rate of change just after 100 seconds and before 300 seconds in the full mission profile. Those two time periods corresponded with portions of peak velocity and force. Motor winding temperature rate of change neared zero as the length of the holding period increased, indicating an approach to steady state. The temperature differences between motor winding TC 1 and TC 2 and the motor case grew to more than 10°C during the holding scenario. But, the temperature difference between motor winding TC 0 and the motor case increased only a couple degrees. Near the end of the profile the temperature difference between the motor case and ambient (~10°C) approached the temperature differences between TC 1 and TC 2 and the motor case (~13°C).

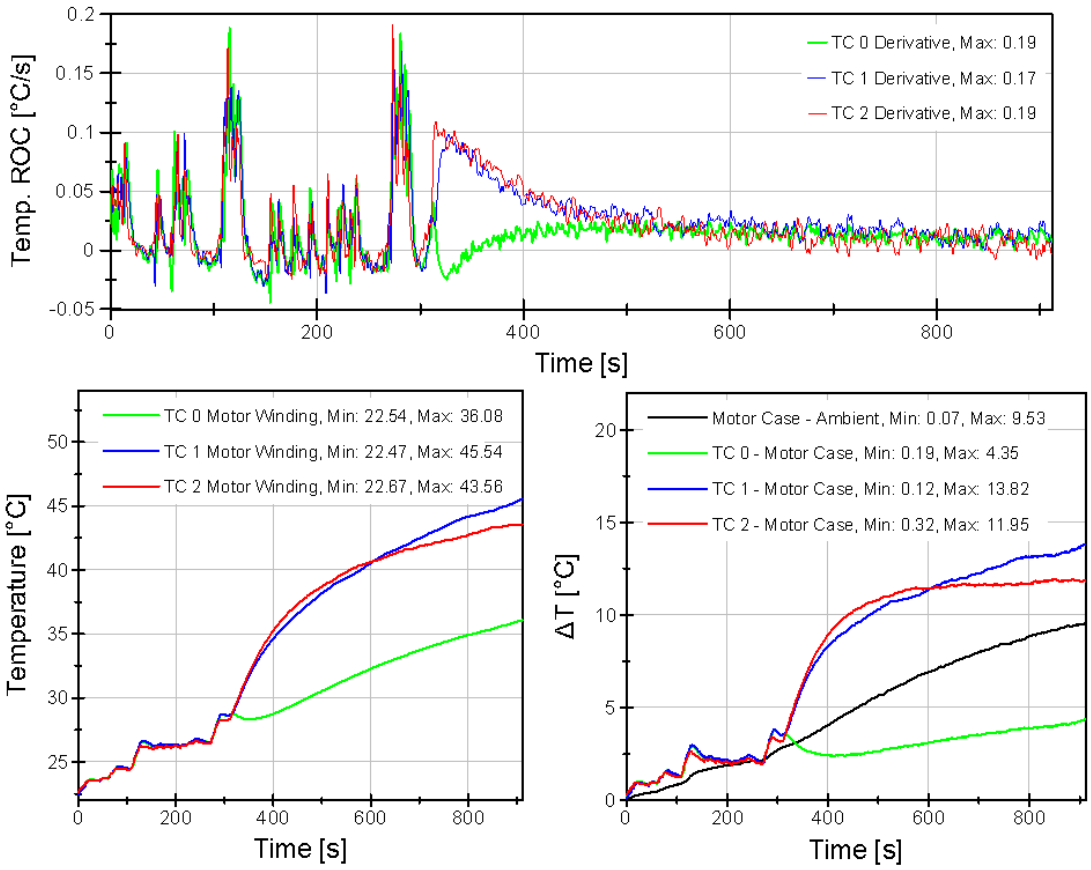

Figure 5.11 Full Mission—Thermal Results

5.5 Full Mission Conservation of Energy

Figure 5.12 provides a time history trend of calculated electrical, mechanical, and thermal energies. Mechanical energy remained constant after the holding phase was engaged near 300 seconds. Electrical energy was greater than mechanical energy and the difference was calculated as a gauge of thermal energy. Based on the energy analysis proposed thermal energy was most severe during holding in the full mission profile.

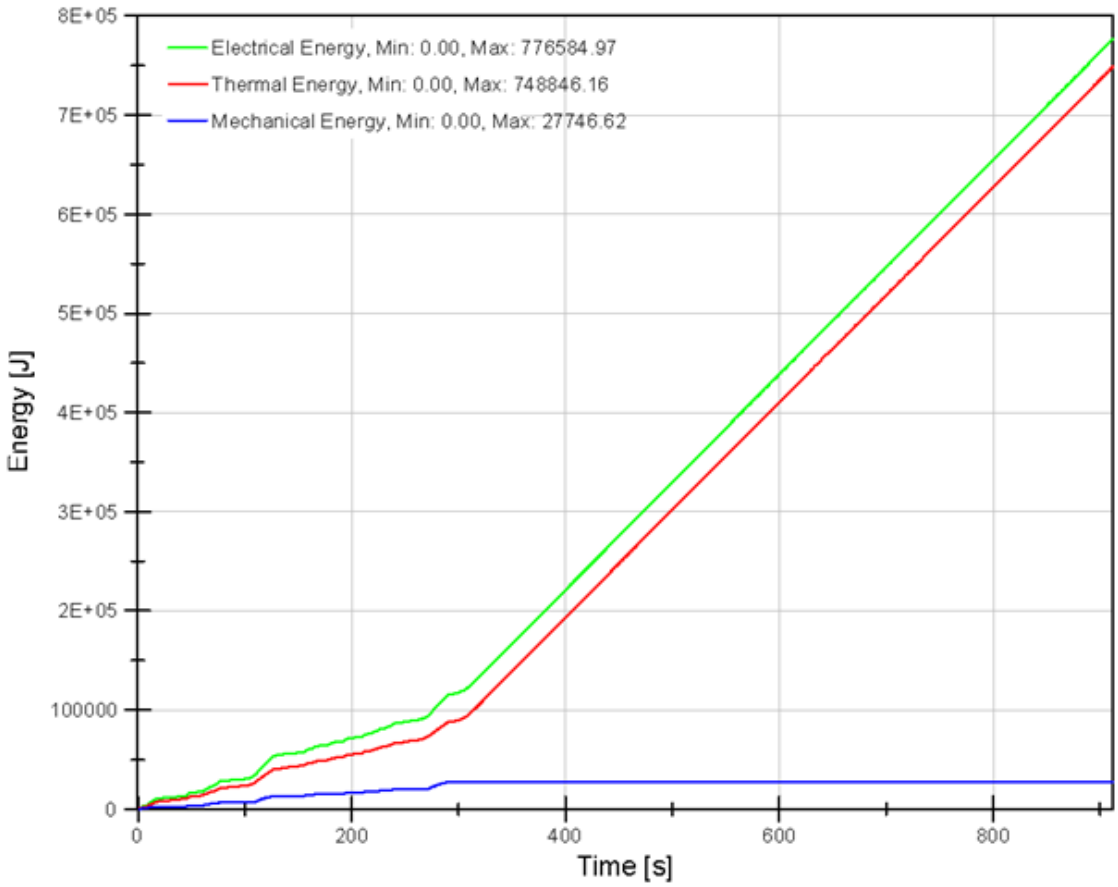

Figure 5.12 Full Mission—Calculated COE

5.6 Full Mission Test Summary

Overall efficiency of the EMAS for the entire mission was 4%, because the EMAS was operating at low to near zero velocity for a large portion of the time. In this case, efficiency was an average efficiency for the total profile and therefore was not a reflection of the EMA's capability, but rather an insight to the nature of control surface duty cycle. Potentially, improved control schemes or mechanical breaking which would eliminate the need for an EMA to operate under conditions in which all electrical energy is converted to heat would increase their average efficiency. Total electrical, mechanical, and thermal (difference between electrical and mechanical) energy as a result of the full mission profile is presented in table 4.

Table 4 Full Mission Test COE Summary

Test		Post Test Analysis			
Profile	Profile Description	Electrical Energy [J]	Mechanical Energy [J]	Thermal Energy [J]	Efficiency
Full Mission	Full mission segment representative stroke and force at environment temperature 22°C	776,585 ± 4660	27,746 ± 277	748,846 ± 4493	4%

Table 5 highlights peak rate of change of temperature, maximum motor case and ambient temperature difference, and average and peak current.

Table 5 Full Mission Test Thermal Summary

Test		Post Test Analysis			
Profile	Profile Description	Peak TC ROC [°C/s]	Max Motor Case-Ambient ΔT [°C]	Avg. Current [A]	Peak Current [A]
Full Mission	Full mission segment representative stroke and force at environment temperature 22°C	0.19	9.53	2.62	5.50

CHAPTER 6

CONCLUSIONS AND FUTURE WORK

6.1 Conclusions

A test matrix made up of varying mechanical demands and environment temperatures was constructed in order to highlight thermally stressful situations and potential thermal design points. Mechanical profiles made up of stroke and force grew in complexity from static holds which simulated extended cruise periods at constant load and environment to dynamic stroke, force, and temperature experienced in actual flight. Table 6 summarizes thermal parameters used to analyze each test.

Table 6 Test Matrix Thermal Summary

Test		Post Test Analysis			
Profile	Profile Description	Peak TC ROC [°C/s]	Max Motor Case-Ambient ΔT [°C]	Avg. Current [A]	Peak Current [A]
Hard Hold Tension	0 velocity against 25% of stall force *without active temperature control*	0.03	4.18	1.15	1.32
	0 velocity against 25% of stall force at environment temperature 22°C	0.03	2.95	1.19	1.35
	0 velocity against 25% of stall force at environment temperature 70°C	0.02	1.39	0.99	1.31
Hard Hold Compression	0 velocity against 25% of stall force at environment temperature 22°C	0.04	3.15	1.63	1.95
Short Mission	Mission segment representative stroke, force at environment temperature ~15°C	0.22	15.11	1.86	8.23
	Mission segment representative stroke and force at environment temperature 70°C	0.06	1.04	0.77	5.13
Full Mission	Full mission segment representative stroke and force at environment temperature 22°C	0.19	9.53	2.62	5.50
Extended Mission	Full mission representative stroke, force at 1% Hot Day environment temperature	0.09	22.00	0.46	6.43

Supporting mechanical, electrical, and thermal data for holding, short mission, and extended mission tests can be found in Appendix K.

The first environment lacked active temperature control of the chamber in order to compare with the impact of actively controlling the chamber air temperature to a specified setpoint. Without active control, the ambient temperature rose steadily due to the heat generated by the motor. Next, a test at elevated environment temperature aimed to measure the impact on EMAS performance and efficiency. At 70°C, electrical power draw was less than runs at room temperature, and therefore the winding temperature rise was approximately 50% less. Lastly, a test (Holding in Compression) with active temperature control and environment temperature of 22°C caused the greatest average and peak current draw. Because of this, temperature rise of the EMA motor under this test was greater than the three holding in tension tests.

A dynamic short mechanical profile was executed at minimum bay temperature (~ -15°C) and maximum bay temperature (70°C). The minimum bay temperature tests exhibited the greatest average and peak current draw in addition to the greatest motor TC temperature rate of

change and temperature difference between motor case and ambient. Lastly, short mission at minimum bay temperature exhibited the greatest thermal energy of the two short mission tests.

Another full complex mechanical profile which included several periods of variable stroke and force followed by an extended portion of holding was executed at 22°C environment temperature. Additionally, an extended mission (2 hours in length) made up of representative stroke, load, and environment temperature was completed.

Each of the aforementioned profiles shed light on thermally significant portions of flight. Overall, it was found that transient missions of an EMAS presented the most electric demand of an aircraft electric system, and holding presented the most severe thermal stress of an EMAS. Holding scenarios presented themselves as the most thermally stressful scenario, where the EMAS operated at 0% efficiency and the most heat was produced.

6.2 Future Work

With the knowledge gained through EMAS experimentation suitable thermal management methods can be designed and included in the experiment for thermal performance testing and verification of cooling concepts. More detailed testing at the component level could be used to capture spatial, temporal, and temperature dependent properties and their effect on EMAS efficiency. Currently, the test apparatus and laboratory capability permit extraction of parameters which could lead to improved EMAS design for PFC actuation. In addition to the application of various cooling technologies an additional control parameter could be introduced—pressure. This additional control parameter could be realized through the use of an altitude chamber. Air pressure can be reduced to 0.2 atmospheres within the flight envelope, and therefore, reduced air density, which has a significant impact on convective heat transfer (MIL-HDBK-310C). Controlling pressure as a function of altitude would increase the fidelity of EMAS thermal management testing. Pressure control would also permit a more accurate assessment of thermal limitations for the EMAS under test, resulting in clearer design specifications for thermal management techniques.

As the force test data showed, there was a significant discrepancy between input and measured load supplied by the hydraulic press. Improvement of the MTS hydraulic press dynamic force control is critical to accurate simulation of the aerodynamic load of a flight control surface.

Lastly, the test apparatus, data acquisition system, and control scheme developed under this project permit continued investigation of electromechanical actuation and its place in modern aviation.

BIBLIOGRAPHY

Baldassarre, G., Gernert, N., and Gottschlich, J., "Loop Heat Pipe for Avionics Thermal Control," SAE Technical Paper 961318, 1996

Barnett, S., Lammers, Z., Razidlo, B., Leland, Q. et al., "Test Set-up for Electromechanical Actuation Systems for Aircraft Flight Control," SAE Technical Paper 2012-01-2203, 2012

Bar-shalom, D. (1989). ALTITUDE EFFECTS ON HEAT TRANSFER PROCESSES ALTITUDE EFFECTS ON HEAT TRANSFER PROCESSES. <http://hdl.handle.net/1721.1/39011>.

Bataille, N. (2006), “Electrically Powered Control Surface Actuation” (MS thesis), Cranfield University, Bedfordshire, UK.

Baudendistel, T., Boyd, M., and Zumberge, J., "Data Acquisition Uncertainty," SAE Technical Paper 2012-01-2206, 2012

Bell, S. (1999). A Beginner's Guide to Uncertainty of Measurement. Tedington, Middlesex, UK: National Physical Laboratory.

Benedict, R. P. (1984). Fundamentals of Temperature, Pressure and Flow Measurements. Wiley. <http://books.google.com/books?id=ecSn5SDXDTkC>.

Borel, L., & Favrat, D. (2010). *Thermodynamics and Energy Systems Analysis: From Energy to Exergy*. Efpl Press.

Bland, T. J. and Funke, K. D. (1992), "Advanced Cooling for High Power Electric Actuators", SAE, Aerospace Atlantic Conference, Dayton, OH; USA; 7-10 Apr. 1992, SAE 921022, Society of Automotive Engineers (SAE), Warrendale, PA, USA.

Blanding, D., & Krulshreshtha, A. (2008). “Power and Thermal Challenges for Electric Aircraft”, SAE, Power Systems Conference, Seattle, WA; USA

Bloschock, K., Bar-Cohen, A. "Advanced thermal management technologies for defense electronics", Proc. SPIE 8405, Defense Transformation and Net-Centric Systems 2012, 84050I (May 3, 2012)

Cavcar, M. (n.d.). The International Standard Atmosphere (ISA). Anadolu University, Eskieshir, Turkey.

Charrier, J.-J., & Kulshreshtha, A. (2007). Electric Actuation for Flight and Engine Control; Evolution and Current Trend. *45th AIAA Aerospace Sciences Meeting and Exhibit*. American Institute of Aeronautics and Astronautics.

Croke, S.; Herrenschmidt, J., "More electric initiative-power-by-wire actuation alternatives," *Aerospace and Electronics Conference, 1994. NAECON 1994., Proceedings of the IEEE 1994 National* , vol., no., pp.1338,1346 vol.2, 23-27

Cronin, M. J. (1988), "The All Electric Airplane Revisited", Proceedings of the Aerospace Technology Conference and Exposition, Anaheim, CA, 3-6 Oct. 1988, SAE 881407, Society of Automotive Engineers (SAE), Warrendale, PA, USA.

Gernert, N. J., Sarraf, D. B. and Steinberg, M. (1991), “Flexible Heat Pipe Cold Plates for Aircraft Thermal Control”, SAE 912105, Society of Automotive Engineers (SAE), Warrendale, PA, USA

Gernert, N. J., Sarraf, D. B. (1992), “A Thermal Analysis of an F/A-18 Wing Section for Actuator Thermal Management”, SAE 921023, Society of Automotive Engineers (SAE), Warrendale, PA, USA

Faghri, A. (1995). Heat Pipe Science and Technology. Taylor & Francis Group. <http://books.google.com/books>

FedBizOps.Gov. Integrated Vehicle Energy Technology (INVENT) Development Program for the 6th Generation Energy Optimized Aircraft (EOA). Jun. 2009. <https://www.fbo.gov>.

Fleming, A. J., Leland, Q. H, Yerkes, K. L., Elston, L. J., S. K. Thomas, “Aircraft thermal management using loop heat pipes: experimental simulation of high acceleration environments using the centrifugal table test bed,” 2006 SAE Power System Conference, Paper No. 2006-01-3066, New Orleans, LA, Nov. 2006.

Jensen, S. C., Jenney, G. D., Raymond, B. and Dawson, D. (2000), "Flight Test Experience with an Electromechanical Actuator on the F-18 Systems Research Aircraft", Proceedings of the 19th AIAA Digital Avionics Systems Conference, 7-13 Oct. 2000, Philadelphia, PA, USA.

Kline, S. J., and F. A. McClintock: "Describing Uncertainties in Single-Sample Experiments", Mech. Eng., p. 3, January 1953

Koran, L.R.; Tesar, D., "Duty Cycle Analysis to Drive Intelligent Actuator Development," Systems Journal, IEEE , vol.2, no.4, pp.453,463, Dec. 2008

McCarthy, K., Walters, E., & Hetzel, A. (2008). Dynamic Thermal Management System Modeling of a More Electric Aircraft. SAE, Power Systems Conference, Seattle, WA; USA

McCarthy, M.; Peters, T.; Allison, J.; Espinosa, A.; Jenicek, D.; Kariya, A.; Koveal, C.; Brisson, J.G.; Lang, Jeffrey H.; Wang, E.N., "Design and analysis of high-performance air-cooled heat exchanger with an integrated capillary-pumped loop heat pipe," Thermal and Thermomechanical Phenomena in Electronic Systems (ITherm), 2010 12th IEEE Intersociety Conference on, pp.1-8, 2-5 June 2010

Moir, I. (1998), “The All-Electric Aircraft - Major Challenges”, Proceedings of the IEE Colloquium on All-Electric Aircraft,17 June 1998, Ref. no. 1998/260, The Institution of Electrical Engineers (IEE), Savoy Place, London, UK.

Moir, I., & Seabridge, A. (2008). Aicraft Systems; Mechanical, Electrical and Avionics subsytems integration. West Sussex, England: Wiley.

NAVAIR 00-110AA6-3. “Standard Aircraft Characteristics EA-6B Grumman” (1971)

<http://www.history.navy.mil/planes/ea-6b.pdf>.

Navarro, R. (1997). *Performance of an electro-hydrostatic actuator on the F-18 systems research aircraft*. < http://www.nasa.gov/centers/dryden/pdf/88524main_H-2210.pdf>.

Pigg, Paul, Roach, Jeff, Morinishi, Ron. “Energy Optimized Aircraft Modeling, Simulation, and Analysis”. AIAA Sciences Conference. Nashville TN. Jan 2012

Pointon, J.M. (2007), “Thermal Management of Electromechanic Actuation on an All-Electric Aircraft” (MS thesis), Cranfield University, Bedfordshire, UK.

Rosero, J., Ortega, J., Albada, E., & Romeral, L. (2007). “Moving Towards a More Electric Aircraft”. IEEE A&E Systems Magazine , 3-9.

Schneider, M. G., Thomson, S. M., Bland, T. J. and Yerkes, K. L. (1994), “Test Results of Reflux-Cooled Electromechanical Actuator”, SAE 942176, Society of Automotive Engineers (SAE), Warrendale, PA, USA.

Schneider, M. G. and Domberg, D. P. (1998), “Test Results of Reflux and Phase Change Energy Storage Electronics Cooler”, SAE 981290, Society of Automotive Engineers (SAE), Warrendale, PA, USA.

Simsic, C.J., "Electric actuation system duty cycles," Aerospace and Electronics Conference, 1991. NAECON 1991., Proceedings of the IEEE 1991 National , vol., no., pp.540,545 vol.2, 20-24 May 1991

Sitz, Joel R. “F-18 systems Research Aircraft Facility” (1992). NASA TM-4433.pdf.

Theodore, L., Ricci, F., & Vanvliet, T. (2009). *Thermodynamics for the Practicing Engineer*. Wiley.

Thunnissen, D. P., & Tsuyuki, G. T. (2004). Margin Determination in the Design and Development of a Thermal Control System. Proceedings of the 34th International Conference on Environmental Systems, Colorado Springs, CO, USA, July 2004, SAE-04ICES-239

U.S. Department of Defense (1997). Global Climatic Data for Developing Military Products (MIL-HDBK-310).

U.S. Department of Defense (2000). Environmental Engineering Considerations and Laboratory Tests (MIL-STD-810F).

U.S. Department of Defense (1992). Thermal Design, Analysis and Test Criteria for Airborne Electronic Equipment (MIL-STD-2218).

U.S. Department of Defense (1979). MIL-E-5400T Military Specification: Electronic Equipment, Airborne, General Specification For

Vrable, D. L. and Yerkes, K. L. (1998), “A Thermal Management Concept for More Electric Aircraft Power System Applications”, SAE 981289, Society of Automotive Engineers (SAE), Warrendale, PA, USA.

Wells, J., Amrhein, M., Walters, E., Iden, S., Page, A., Lamm, P., Matasso, A., “Electrical Accumulator Unit for the Energy Optimized Aircraft,” SAE International Journal of Aerospace, 1(1): pp. 1071-1077, 2008.

White, F. M. (1984). Heat Transfer. Addison-Wesley Publishing Company.

Yu.F. Maydanik, Loop heat pipes, Applied Thermal Engineering, Volume 25, Issues 5–6, April 2005, Pages 635-657, <10.1016/j.applthermaleng.2004.07.010.>.

Zhou, L., Leland, Q., Gregory, E., Brokaw, W. et al., "Lumped Node Thermal Modeling of EMA with FEA Validation," SAE Technical Paper 2010-01-1749, 2010

APPENDICES

APPENDIX A

TEST SETUP FABRICATION

Safety Shields

Safety shields were constructed from 6mm lexan in order to protect lab personnel from high pressure fluid and or flying objects in case of a fluid line rupture. The shields in addition to hydraulic plumbing clamps were critical in achieving safety plan approval. Figure A-1 shows shields constructed for the hydraulic service manifold on the left and hydraulic press on the right.

Figure A-1 Laboratory Safety Shields

U-plug modification

U-plug accessories accompanied the environmental chamber and afforded the user the ability to affix test specimens to fixtures outside of the chamber. U-plug material (white in Figure A-2) was very brittle and took significant care not to crack or break. A hole-saw was determined to be the most efficient method of cutting a circle in the U-plug material. Two halves were sandwiched together (exactly as they are when placed within the chamber) and held tight with two clamps. Next a cordless drill was used to slowly drill through each side of the U-plug, creating an opening just larger than the fixture the U-plugs surround. ½ inch plywood was placed under the white insulation material to reduce blow out when the drill bit broke the surface on the backside. Sandpaper and fine toothed files were used to clean any remaining rough edges. Ultimately, this method resulted in a clean fit around both ends of the actuator. Figure A-2 and A-3 demonstrate the upper and lower U-plug fit within the test apparatus, respectively.

Figure A-2 Environmental Chamber outfitted with Modified U-Plugs—Upper Section

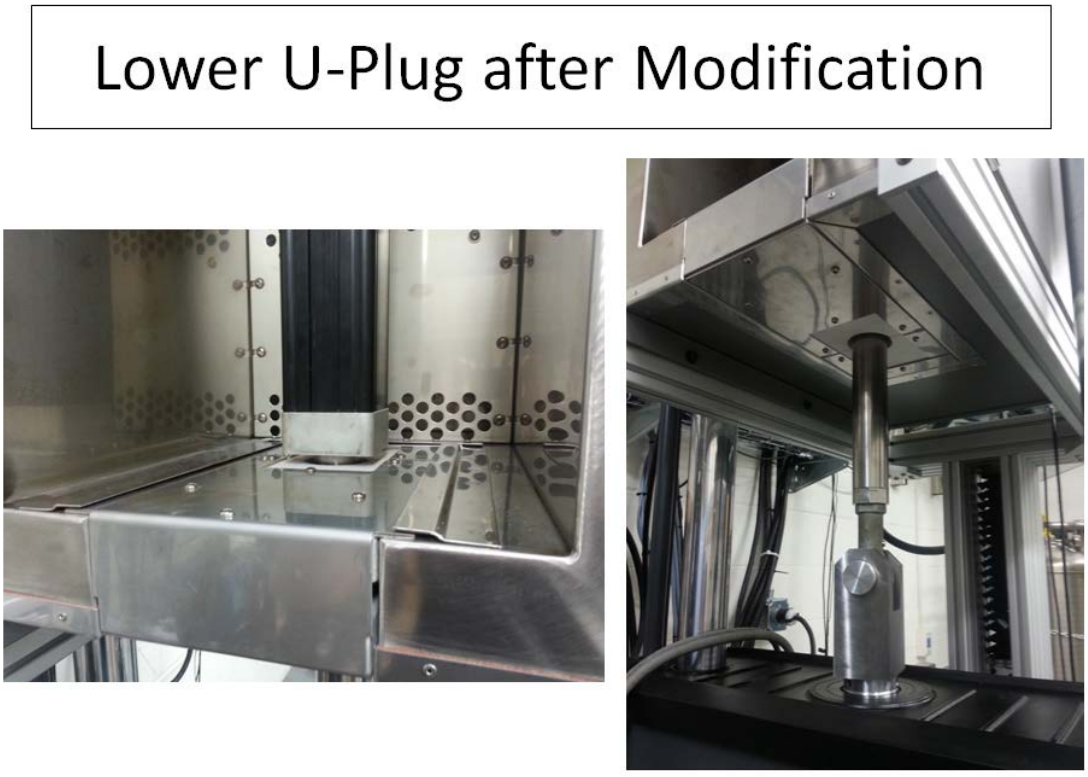

Figure A-3 Environmental Chamber outfitted with Modified U-Plugs—Lower Section

Press-Chamber Fitting/Installation

Three primary concerns were observed when determining how to most efficiently install a test article within the load frame. First, the bulk of the actuator needed to be surrounded by the environmental chamber. Secondly, sufficient space and material was required between the heated/cooled interior of the chamber and load cell to prevent temperature related error. Lastly, sufficient space for the press-EMA coupling to cycle up and down without bottoming out the hydraulic cylinder or striking the bottom of the chamber was required. These requirements were used in addition to the dimensions of the actuators under test in order to find the most appropriate position of the press frame crosshead, environmental chamber height, and home position for the press-EMA coupling. Figure A-4 highlights the resulting hydraulic press - EMA - environmental chamber configuration. The cross head height measured from top of press table to top of cross head was 76.5 in. The height of the environmental chamber was set to its maximum in order to provide ample space outside the chamber for actuation throughout the desired range of ± 2 in. The press-EMA coupling is capable of utilizing the entire 10" range between the press table top and chamber's bottom. However, software end limits were set to prevent the coupling from striking the bottom of the chamber or bottoming out the hydraulic piston.

Figure A-4 Environmental Chamber-Hydraulic Press Configuration

EMA-Press Fixtures

In order to meet the three requirements outlined in press-chamber fitting/ installation section a few mechanical connections were designed and machined. Each of these connections and their mating components within the test apparatus are shown in Figure A-5.

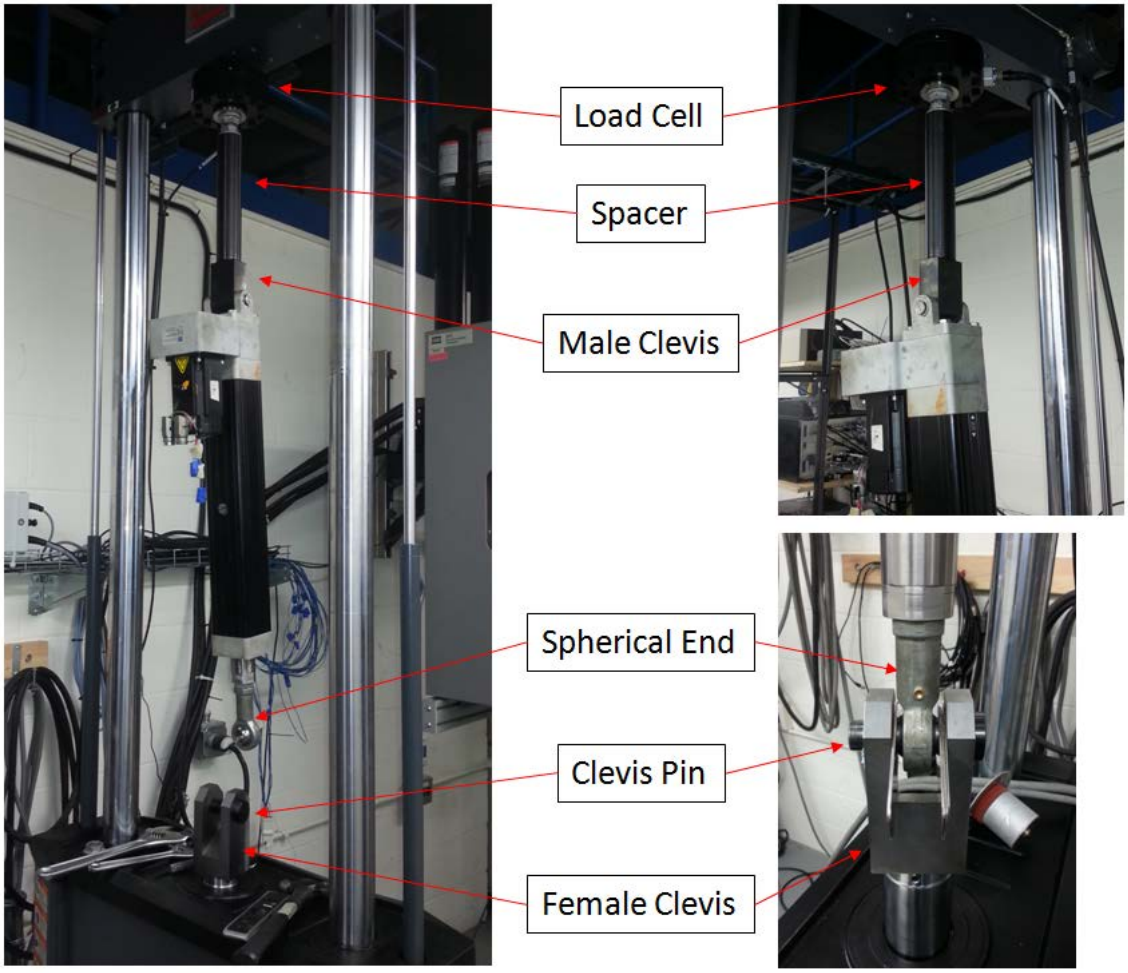

Figure A-5 Fixture Hardware in place

Both the MTS hydraulic ram and load cell threading were M27 x 2.0 mm, a very uncommon thread and therefore required some additional work for proper mating. Two 12” M27 x 2.0 mm threaded rods were purchased to use in connecting the female clevis to the press hydraulic ram. A male clevis was developed to connect the rear side of the EMA to the load cell and ultimately the load frame. The male clevis and spacer block were both bored with female threading to permit male threaded rod to connect the two. Lastly, the spacer block connects to the load cell via M27 x 2.0 mm threaded rod. All threaded connections were designed to engage the threads a distance of at least two diameters of the threaded rod used in the connection. Finally, a clevis pin or in this case a shear pin was designed to mate the female clevis on the hydraulic ram to the spherical joint on the EMA. Figure A-6 highlights the three components designed and machined—Male Clevis, Spacer Block, and Shear Pin.

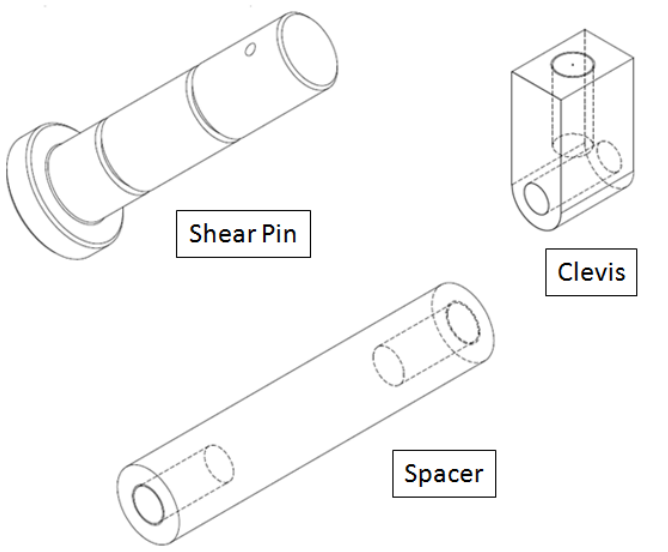

* These drawings are not to scale; rather representative images of the actual hardware

Figure A-6 Drawings of Fixture Designs

Exlar EMA Anti-Rotation Concept

A larger and more powerful EMA was purchased for future testing that would extend the testing envelope beyond the capability of the current EMA under test. This EMA was capable of stroke rates, stall force, and output power that correlated with specifications PFC actuators used in EPAD testing. However, the EMA purchased for this application utilized a roller screw assembly which requires an anti-rotation device to prevent the EMA ram from rotating throughout its stroke. The manufacture suggested an anti-rotation accessory. However, the accessory would interfere with the use of an environmental chamber. Therefore, an in-house anti-rotation concept was developed which would prevent the EMA arm from rotating while extending/retracting and did not interfere with other testing equipment (hydraulic press and environmental chamber). Figure A-7 demonstrates the mechanism and its attachment points. The device consists of a uni-strut frame, an aluminum arm with a machined section to act as a clamp, and roller bearings. The aluminum arm joins the EMA-Press coupling to the uni-strut riser and prevents any rotation based on its geometry. Roller bearings permit translation along the uni-strut riser section while the Press-EMA coupling moves up and down. The assembly was designed such that all components have sufficient clearance of the environmental chamber and hydraulic press. Design, material, and machining costs were estimated to be much lower than purchasing an accessory anti-rotation device.

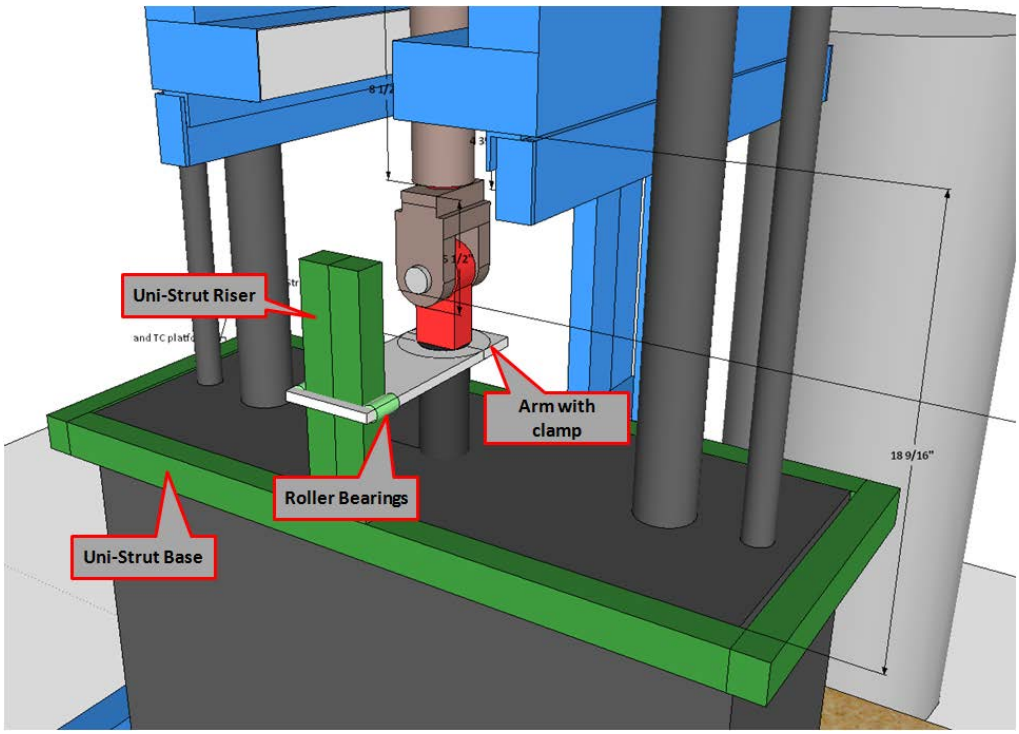

Figure A-7 SketchUp Drawing of Anti-Rotation Concept

APPENDIX B

LABVIEW VI'S AND ITOOLS

Throughout the course of the project several VI's and sub-VI's were constructed to help with experiment control, data acquisition, troubleshooting, and several other tasks. The most pertinent routines are highlighted below with a screen shot of the block diagram and short explanation of their purpose/function.

ChannelSetup.vi

Shown in Figure B-1 is the block diagram of a subVI responsible for analog input channel setup. Parameters defined in this routine are measurement type (differential), channel range (maximum and minimum voltage), channel units, channel sampling rate (10003 Samples/sec), and sampling method (continuous). This particular template was used repeatedly for analog input channels including but not limited to measurements of stroke, force, voltage, and current.

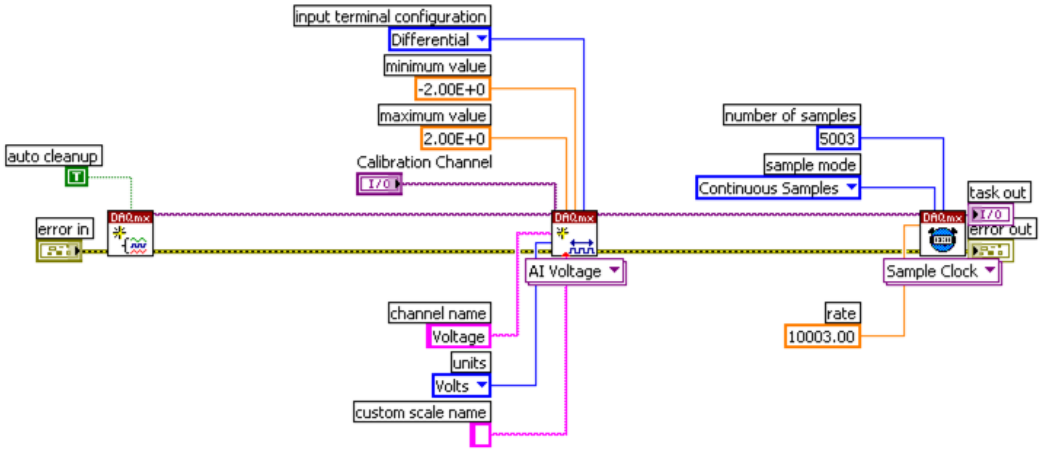

Figure B-1 Channel Setup VI

CurrentTransducerCalibration.vi

Figure B-2 is the block diagram of a VI used to calibrate current transducers. Two sub-VI's placed before two cascaded for-loops were responsible for channel setup/configuration. The cascaded for-loops were responsible for continuously acquiring data and when commanded recording, writing, and calculating the average of 5003 samples 5 times. This program permitted quick and accurate calibration of current transducers against a digital multimeter at varied levels of input current. This same program was duplicated then modified as necessary for voltage probe calibrations.

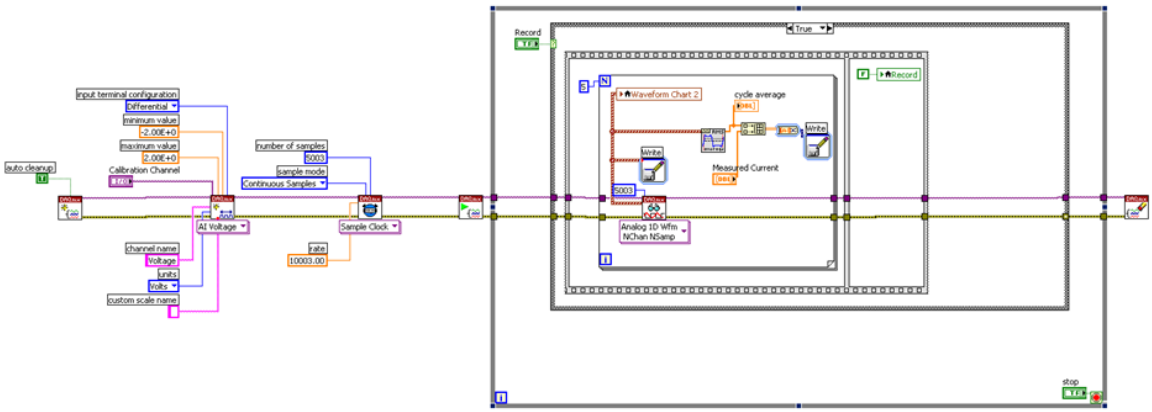

Figure B-2 Current Transducer Calibration VI

SerialCommunication.vi

Serial Communication VI was written to help troubleshoot and configure serial communication between the RealTime machine (Control DAQ) and environmental chamber's temperature controller (Eurotherm controller). This program permitted the user to input alphanumeric values and verify serial port settings by comparing read and write buffers. If the read buffer mirrored the write buffer successful communication was established. Figure B-3 identifies the block diagram and front panel.

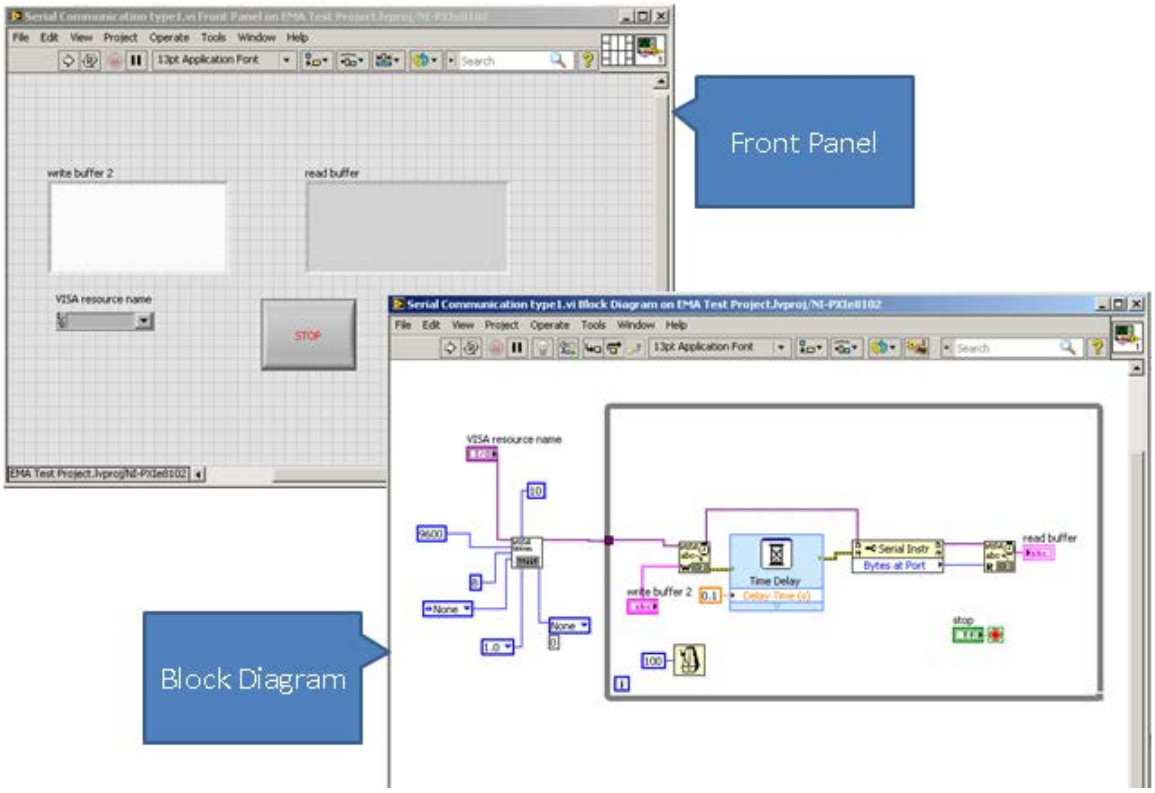

Figure B-3 Serial Communication VI

TCcorrelationequations.vi

Correlation equations created from thermocouple calibration procedures were constructed within a subVI to be used within the experiment control program. This subroutine applied a linear formula specific to each thermocouple (TC 0, TC 1, TC 2, etc.) every recording before it was written to a file. The block diagram depicts its structure and how the array of thermal data is disaggregated by index, corrected by a calibration curve, and concatenated to an output array for writing. Figure B-4 shows the block diagram of this subVI.

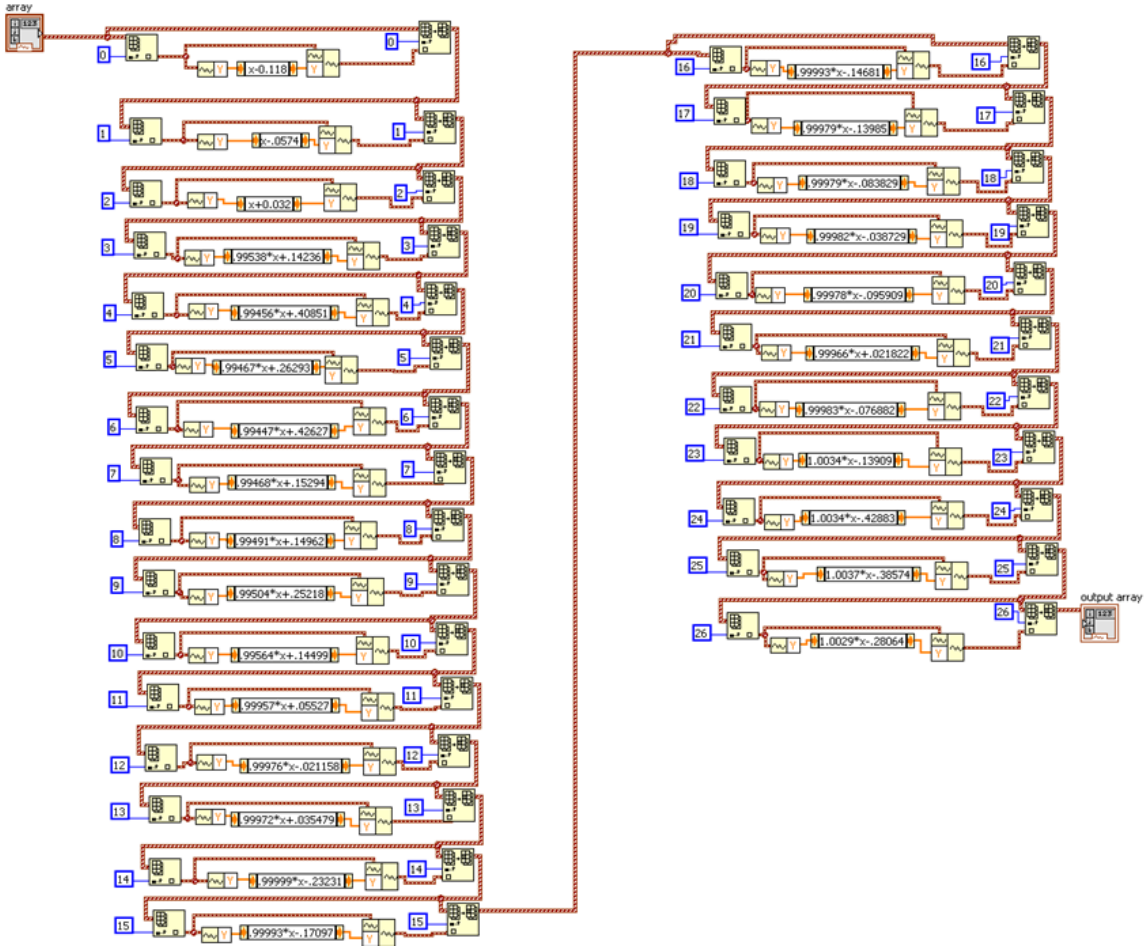

Figure B-4 TC Correlations VI

TrialChamberControl.vi

Trial Chamber Control VI was developed in order to gain remote control of the environmental chamber within the LabVIEW environment. This program was based on a VI provided by Inventsys Eurotherm, the maker of Eurotherm 2404 temperature controller. First, communication settings were set to specific values shown in the block diagram for both the VI and within the temperature controller settings menu. Next, since the temperature controller was outfitted with an RS-485 comm-module and National Instruments RealTime DAQ machine only supported RS-232 a bidirectional RS-232 to RS-485 converter was purchased and placed in line with the RealTime DAQ and EC temperature controller. Finally, the temperature controller utilized Modbus communication protocol. This required a Modbus subVI supplied by Inventsys

Eurotherm to ensure correct data transmission. With that, a loop with a 10 millisecond wait was constructed around the necessary set sub-VI's for stable and continuous data transmission. These features are shown in Figure B-5, the block diagram of TrialChamberControl.vi.

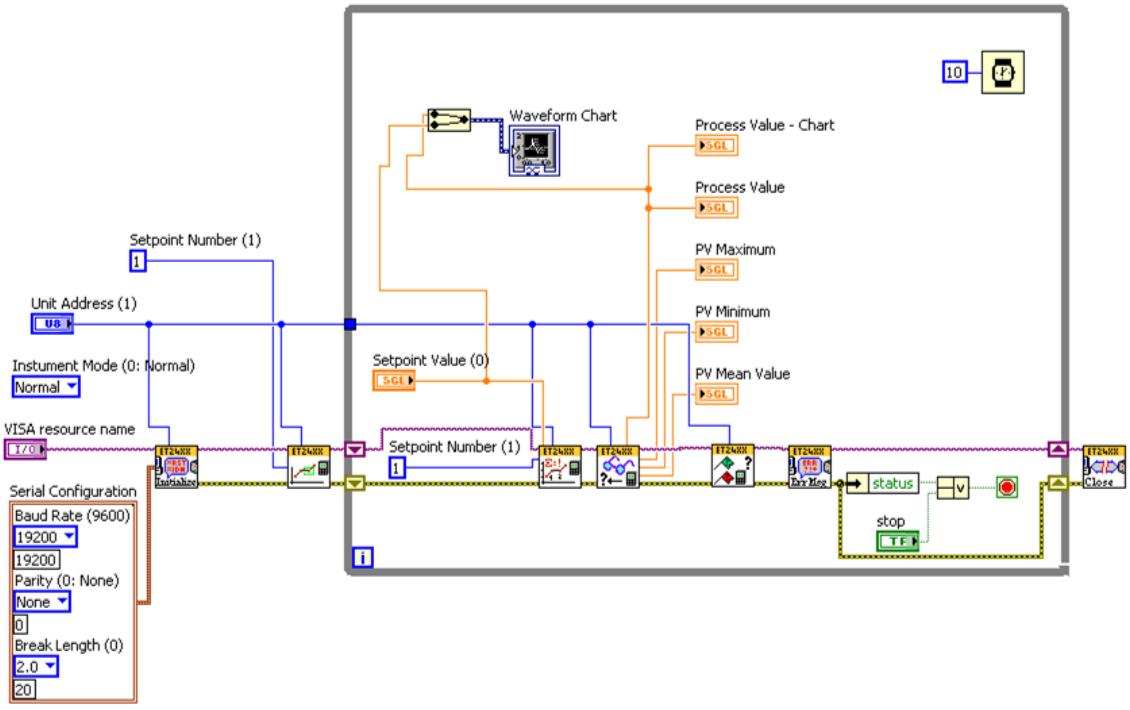

Figure B-5 Trial Chamber Control VI

Trial Chamber Control front panel supports interactive input of chamber setpoint, monitoring of process value feedback, some statistics, and viewing of two waveform charts that display setpoint and process value trends. The front panel is shown in Figure B-6.

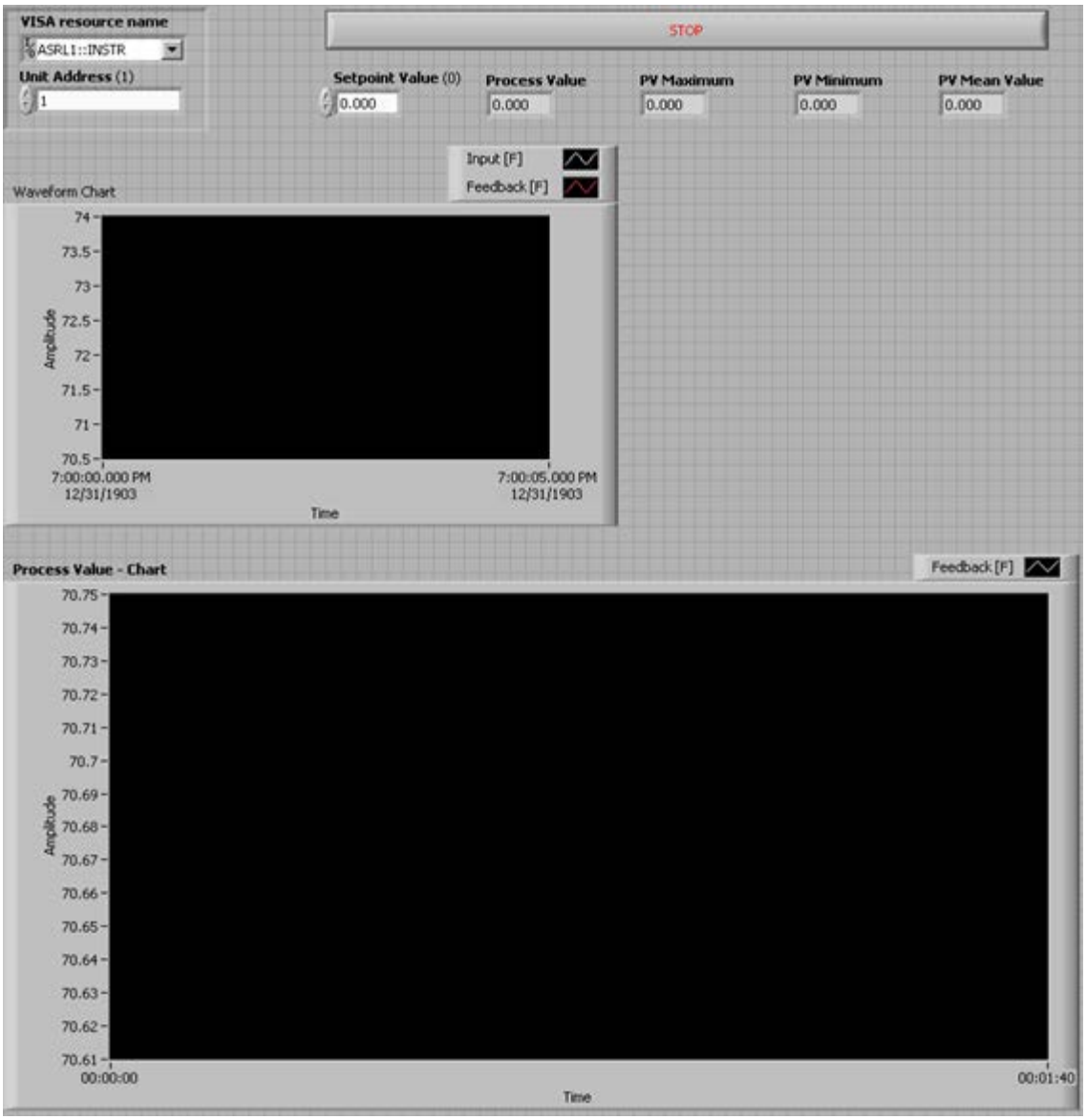

Figure B-6 Trial Chamber Control Front Panel

TrialChamberControl_withProfile.vi

Trial Chamber Control VI was utilized as a template for a VI (Trial Chamber Control with Profile) integrated into the experiment's overall control. A few modifications were made which permitted input of desired temperature profiles which are interpreted by the program and relayed to the temperature controller at specified intervals. Temperature profiles were created based on a rate of one command per second. That rate was chosen to ensure adequate representation of simulated bay conditions and maintain stable data transmission by operating within the temperature controller's update rate. Figure B-7 is a block diagram of the program used to autonomously control chamber air temperature as a function of time. The development of this program was crucial to the success of simulated environment conditions because Eurotherm 2404 temperature controller's profile creation capability was limited by its memory. The controller was only capable of 8 individual segments of either ramp or dwell commands. Without

remote control this limitation prevents the temperature controller from replicating environment dynamics experienced by typical EMAs in the field.

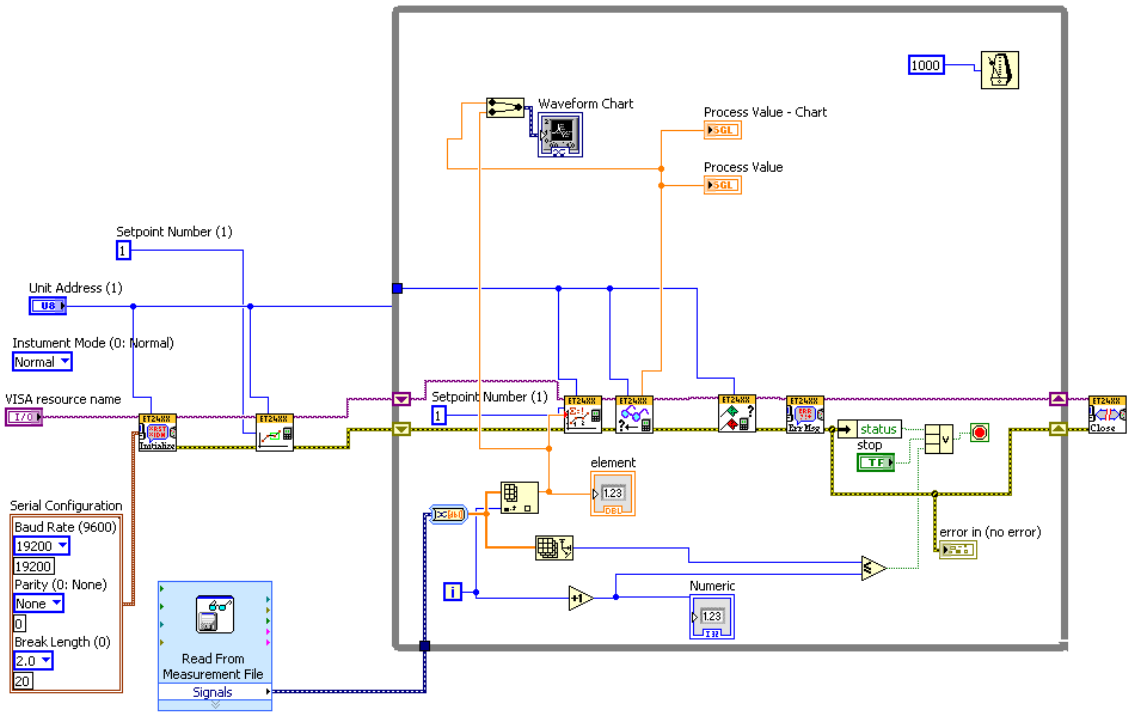

Figure B-7 Trial Chamber Control with Profile Input VI

The front panel of TrialChamberControl_withProfile.vi is a carbon copy of TrialChamberControl.vi front panel shown in Figure B-6. The front panel was sufficient so no further modifications were made.

iTools

Lastly, another important piece of software related to the operation of the Eurotherm temperature controller was iTools. iTools is independent of LabVIEW and resides as an application on the development PC in the laboratory. This software package provides backup and interactive configuration of the temperature controller settings. This program was used to generate a backup of the correct device settings which included but not limited to high/low alarm values, PID constants, comm settings, heating and cooling configuration, and access levels. A file was generated called “20130315 Eurotherm2404TempControllerConfiguratoin.UIC” and can be used to reset the temperature controller to the appropriate settings in the event of misapplied changes. Figure B-8 is a screenshot of the software interface and location of temperature controller configuration backup file.

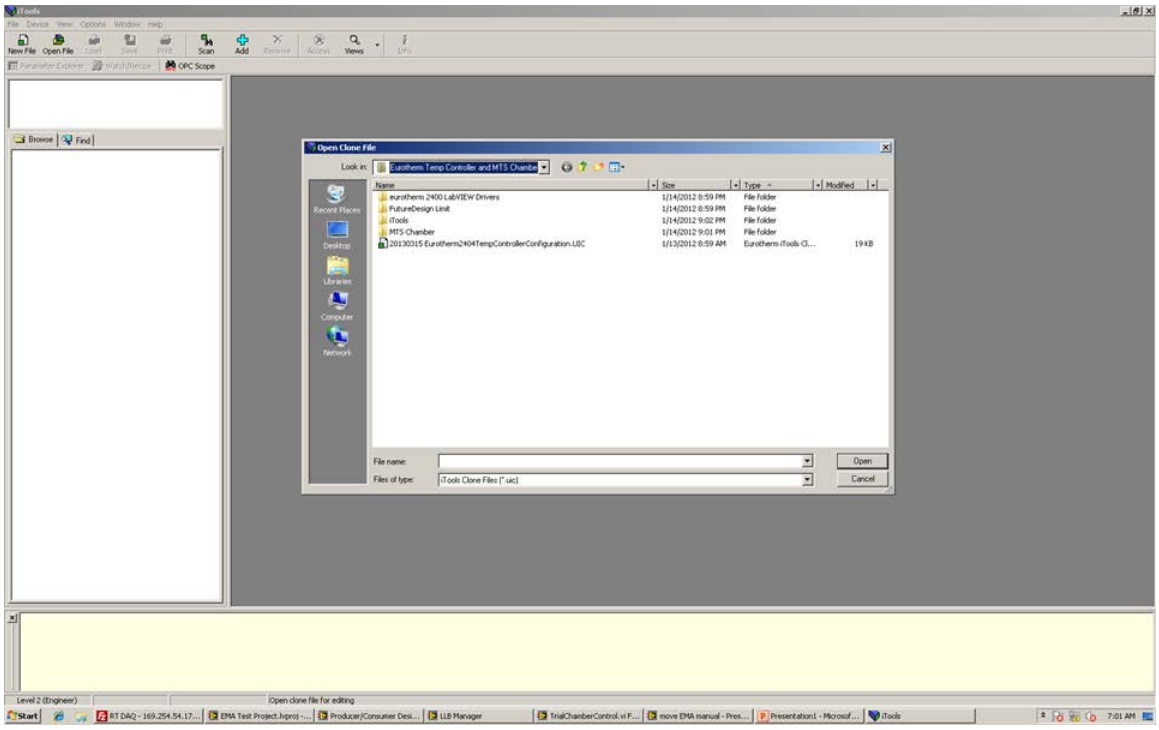

Figure B-8 iTools Software Config File

Shown in Figure B-9 is another example of the interface and how it mirrors navigation properties of the temperature controller when manually modifying values.

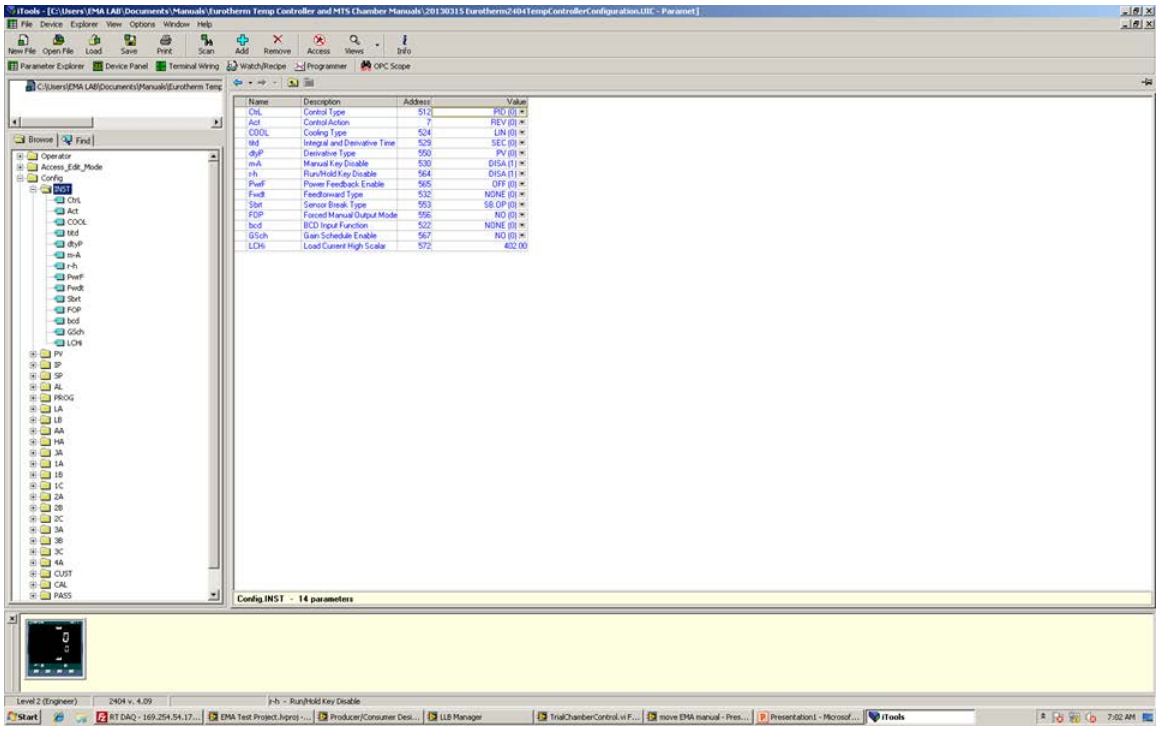

Figure B-9 iTools Software User Interface

APPENDIX C

TEST PROCEDURE

Main hardware involved: EMA, hydraulic press, DAQ system, Thermo chamber.

Sequence summary:

- Prep the Servohydraulic System
- Power on and Enable the HPU
- Power on and Enable the EMA
- Power on and Enable the Environmental Chamber
- Open most recent LabVIEW Test Control Program
- Power off the Experiment
- Collect and Analyze Test Data

Ensure all 3 components shown in Figure C-1 are powered on. From left to right these components include: 3 PCs (EMA PC, MTS PC, LabVIEW PC), NI RealTime machine, and a 24 V Power Supply.

Figure C-1 PCs for Test setup

Prep the Servohydraulic System

Move the throw switch to the on position. Power the water pump via the switch at the bottom of the panel (digital readout typically reads between 5 and 7 Amperes; ensure current is not greater than 10 A)

Figure C-2 Water Pump Breaker

Open hydraulic supply and return circuit valves at both the hydraulic service manifold (HSM) and hydraulic power unit (HPU). Figure C-3 and C-4 demonstrate the appropriate valve position for the HSM and HPU, respectively. The valve handle should be in line with the direction of fluid flow.

Figure C-3 HSM Supply and Return Valves

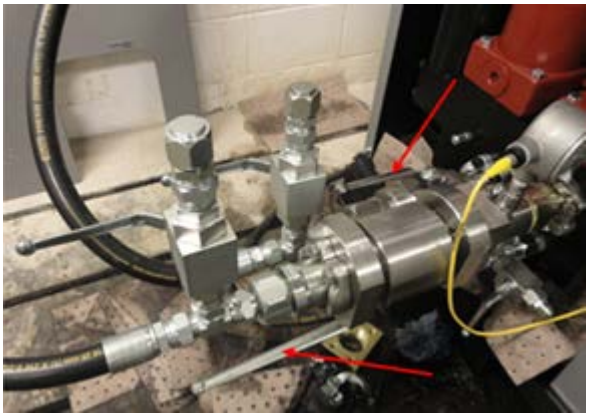

Figure C-4 HPU Supply and Return Valves

Additionally, ensure supply and return water valves are opened in a similar fashion.

Figure C-5 Water Valves at Pump System

Power on and Enable the Hydraulic Pump Unit

Power the HPU by turning the power disconnect switch or latch.

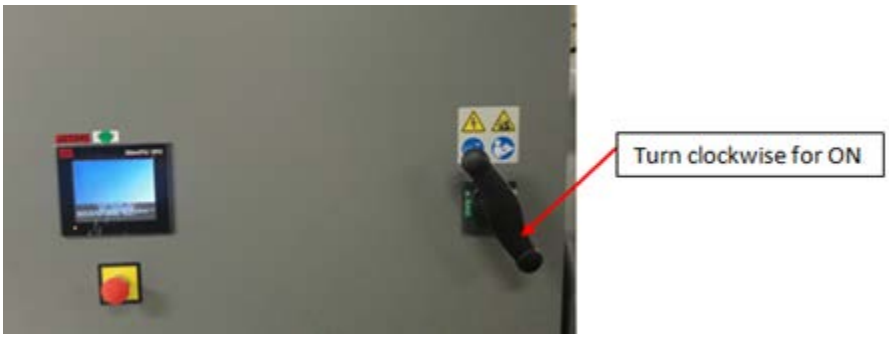

Figure C-6 Control Panel on Hydraulic Pump System

Once the HPU touch screen has completed loading choose a language then touch MAIN DISPLAY.

Figure C-7 Control Screen on Hydraulic Pump System

The pump will show faulted at start. In order to enable the pump you must choose a module (module #3) and touch REMOTE OPERATION. Ensure REMOTE OPERATION remains highlighted as shown in Figure C-8.

Figure C-8 Control Screen on Hydraulic Pump System

Next, touch status followed by reset to remove the fault. Touch the MAIN option to return to the main screen, shown in Figure C-9.

Figure C-9 Control Screen on Hydraulic Pump System

Pump is now ready to be operated remotely. Figure C-10 shows the correct configuration as a result of the previous steps.

Figure C-10 Control Screen on Hydraulic Pump System

Open Hydraulic Press Control Software

Open Station manager which is located in the bottom left corner of the taskbar on the MTS PC. Choose the config file named '22kip Ext force Command.cfg." Next provide operator control by checking the 'Exclusive Control' box as shown in Figure C-11. Finally, choose External Command from the control scheme options on the left.

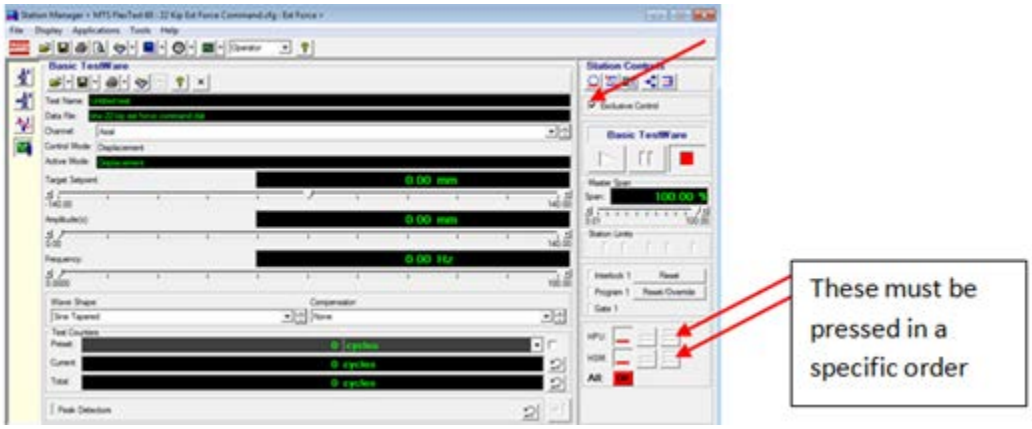

Figure C-11 System Manager Program for MTS Press

Power the HPU & HSM by clicking the buttons in the sequence outlined by Figure C-12. Wait 15-30 seconds between each selection to provide the Servohydraulic system ample time for startup.

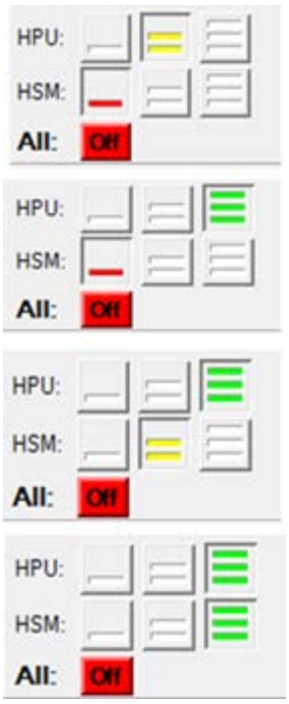

Figure C-12 Control button sequence for MTS Press

****Toggle the flow control switch on the hydraulic press from turtle (low flow) to rabbit (high flow) before testing. This will ensure the press is capable of utilizing its full capacity.

Power on and Enable the EMA

Turn on EMA controller via the toggle switch highlighted in Figure C-13.

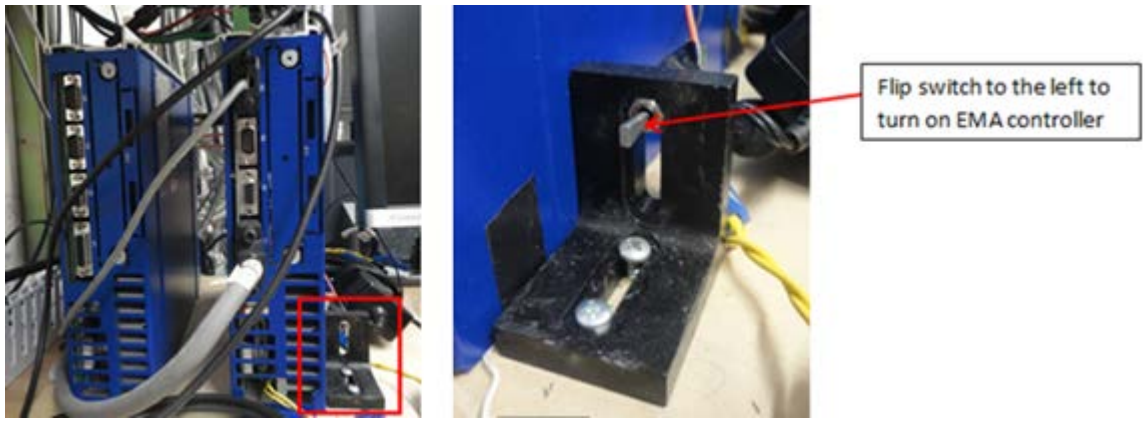

Figure C-13 EMA ServoDrive and Toggle Switch

Insert the EMA power cable into the marked $240V_{AC}$ outlet.

Figure C-14 240 V_{AC} Outlet for EMA

Navigate to the start menu of EMA PC and open DRIVE (ServoDrive Program). Once the coupled drives have fully initiated (approximately 15-20 seconds after toggling the power switch) click 'COM1' as shown in Figure C-15.

Figure C-15 Drive Software for EMA

Choose from the OPMODE dropdown 0 Digital Speed. This will permit the operator the ability to command constant speed commands and ensure the EMA and its control is fully functional before running a test. Next click the Enable button.

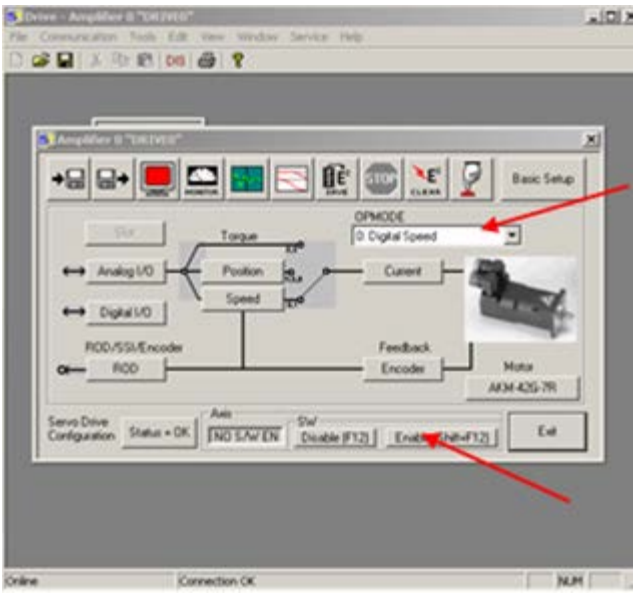

Figure C-16 DRIVE interface (Enable Button)

Click on the terminal button shown in Figure C-17.

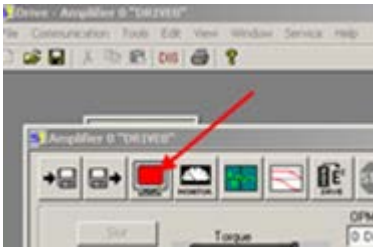

Figure C-17 DRIVE interface (Terminal Button)

Now jog the EMA by typing in "J (then the speed and direction '+' or '-') in units of RPM to ensure the EMA has no faults. Once the operator is satisfied with the EMA's response jog the EMA to a predefined home position and enter MH to home the EMA within the software control.

Figure C-18 Drive Software for EMA (Terminal)

One can check the location of the EMA by observing the analog output value. 4.678 Volts corresponds to the home position.

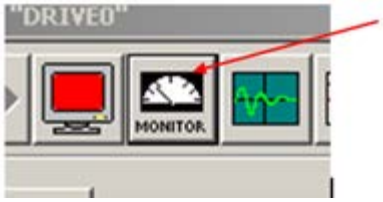

Figure C-19 DRIVE Interface (Monitor Button)

In order to manually move the EMA rod or when using the hydraulic press displacement control ensure to utilize 2: Digital Toque from the OPMODE dropdown and input T 0. This corresponds to zero torque and permits free movement of the EMA rod. Once the EMA has reached a desired starting position retype 'MH' in the Terminal. Next, choose 5: ext. Position Nodes which is the external command operational mode.

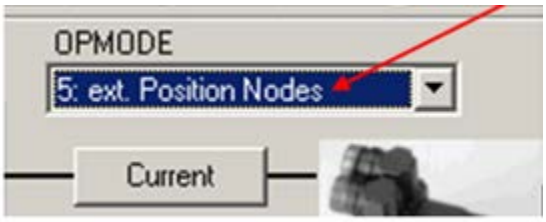

Figure C-20 Drive Software for EMA (Switching to OPMODE 5)

Power on and Enable the Environmental Chamber

First, insert the environmental chamber power cord into the marked $220V_{AC}$ outlet.

Figure C-21 Plug for Thermo Chamber

Ensure the cryogenic cylinder is properly connected with environmental chamber. The steel braided hose is outfitted with two different end fittings; thus, care must be taken to match the appropriate end with its mate. Fittings do not require excessive tightening, simply a snug fit. When ready for liquid nitrogen (LN_2) completely open the valve marked 'LIQUID' to permit the flow of LN_2 to the chamber. Always wear required personal protective equipment (PPE) throughout this process. Figure C-22 shows the correct configuration.

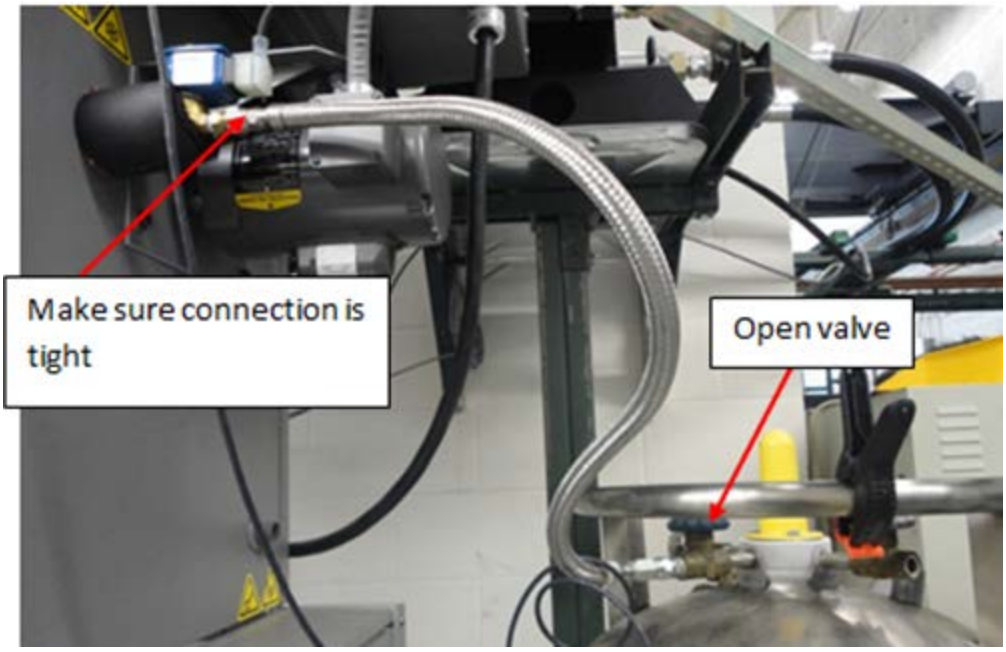

Figure C-22 Cryo-cylinder connection with Environmental Chamber

Next ensure the high limit switch on the environmental chamber is not tripped and turn the power switch on. Figure C-23 shows where this process should take place. This will power the fan and enable heating or cooling depending on the process value and the current setpoint. Run the chamber in heating and cooling mode by changing the setpoint to a value several degrees greater and less than room temperature. This can be done by utilizing a LabVIEW VI (TrialChamberControl.vi) contained in 'eurotherm2404.lib' on the LabVIEW PC desktop. Note the chamber door must be closed for heating or cooling to occur.

Figure C-23 Environmental Chamber Panel

Open most recent LabVIEW Test Control Program

If LabVIEW 2012 is not already open, open that program from the LabVIEW PC.

Under projects, choose the most recent experiment project, for example: ‘example1.lvproj’. Then expand the RealTime Target and open the lasted test control VI. In Figure C-24, the latest test control program is ‘testingv3.vi’.

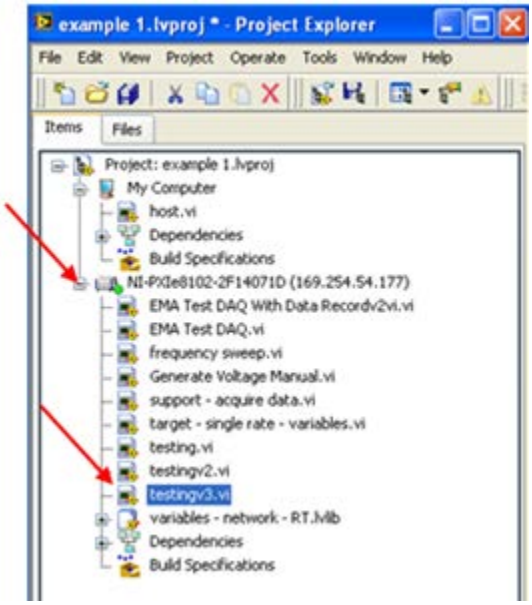

Figure C-24 LabVIEW Project window for 'example 1.vi'

Prior to running the control program, ensure the safety shield is placed between the operator and the test setup. If for any reason the experiment is unsuccessful or immediate disabling is necessary an emergency stop button is available on the operator’s work station. This emergency button is shown the bottom right of Figure C-25.

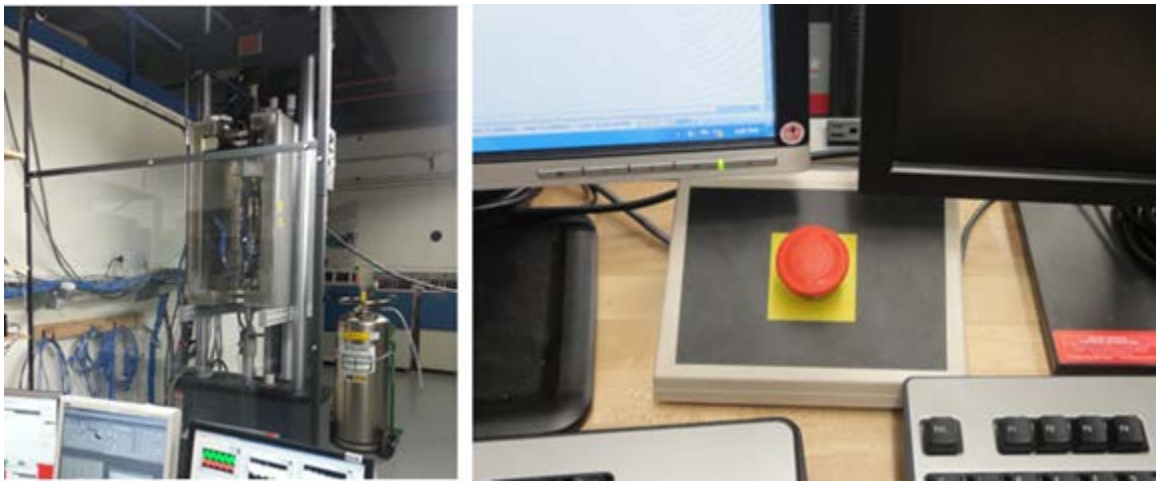

Figure C-25 Safety Shield and Emergency Stop Button for Press-EMA

If the emergency stop button is pressed, it will disable the hydraulic press and the EMA.

If the EMA is not disabled via DRIVE software as shown in Figure C-12, the EMA will return to the enable state once the emergency stop button is released. Therefore, it is imperative to disable the EMA through the DRIVE software immediately after the emergency stop button is activated.

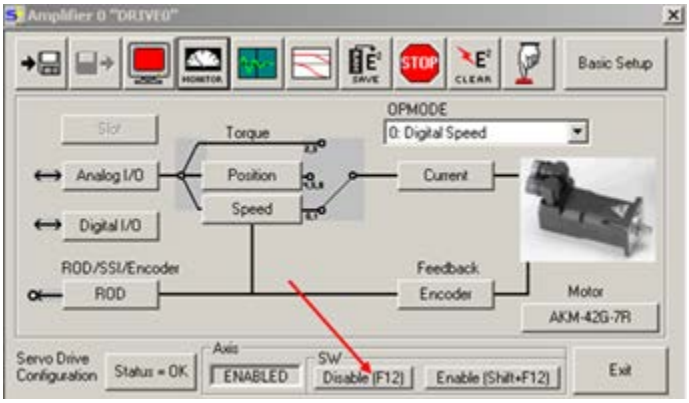

Figure C-26 Disable Button in Drive Software for EMA

Once the operator is comfortable, run the VI clicking the Run button on the front panel as shown in Figure C-27.

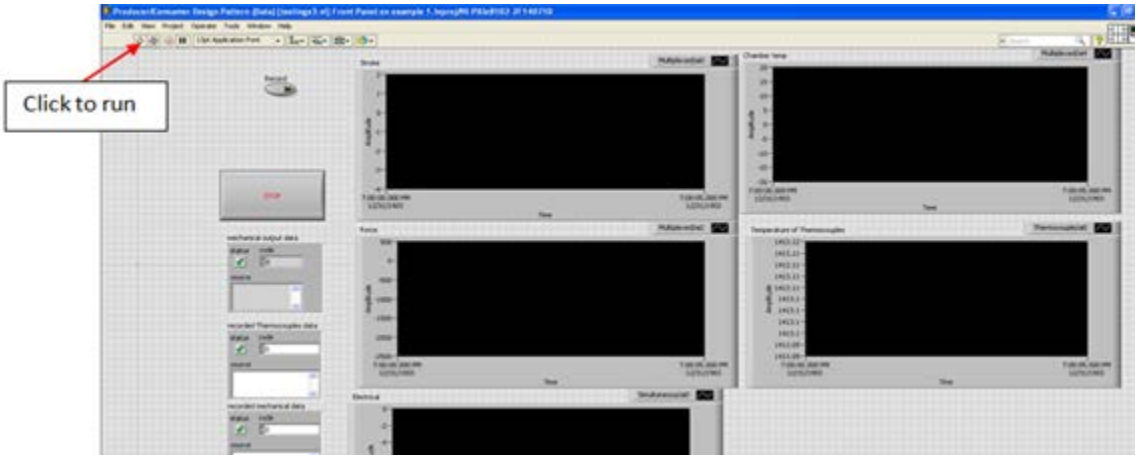

Figure C-27 LabVIEW 'testingv3' VI Front Panel

Power off the Experiment

Once the experiment is complete, the LabVIEW VI will stop automatically.

Disable the EMA by clicking the disable button on the EMA Drive window.

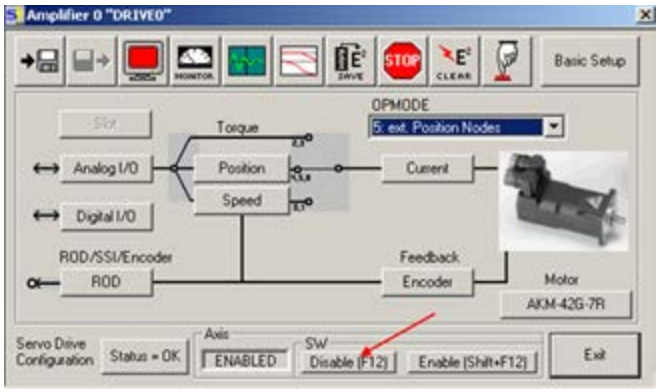

Figure C-28 Drive Software for EMA (Disabling EMA)

Next, disable the Servohydraulic system by following the button sequence in Figure C-29. The sequence is the reverse of the sequence used to enable the sevohydraulic system in

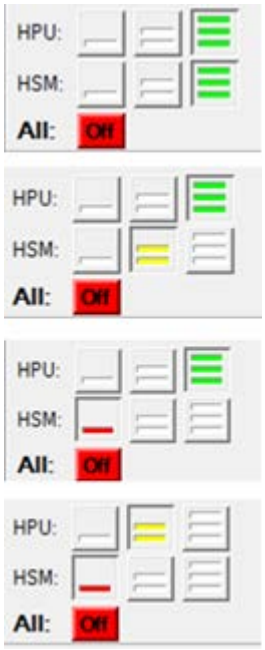

Figure C-29 Station Manager control button sequence to power down MTS Press

Completely close the valve marked 'LIQUID' on the cryogenic cylinder. Utilize TrialChamberControl.vi once more to command a setpoint below room temperature to enable cooling mode and exhaust any leftover over LN_2 in the braided hose. Once this is complete the operator may stop power off the chamber and remove the braided hose connection from it. Completely power off the environmental chamber by removing the chamber's power cord from the 220 V_{AC} outlet. Next, toggle the flow control button on the hydraulic press from Rabbit (high flow) to Turtle (low flow). Remove the EMA power cord from the 240 V_{AC} outlet. Power off the water pump by toggling the switch on the bottom right of the panel to the off position. Power off the HPU by turning the power disconnect latch all the way to the left. Close all hydraulic and water valves previously opened. All valve handles should reside perpendicular to the flow of fluid. Finally, flip the lever on the panel to off.

Collecting and Analyze Test Data

Run FileZila located on the LabVIEW PC.

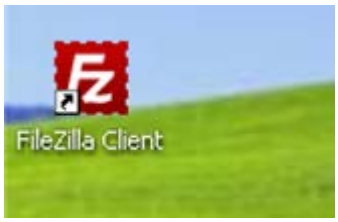

Figure C-30 FileZila Desktop Icon

Click on the down arrow of the ‘Open the Site Manager’ icon in the top left corner and choose ‘DAQ RT’

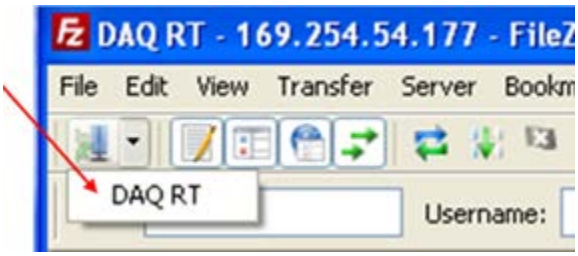

Figure C-31 FileZila Software Window

Next, open ‘Test Data’ folder which houses all data collected during the test (mechanical, thermal, and electrical).

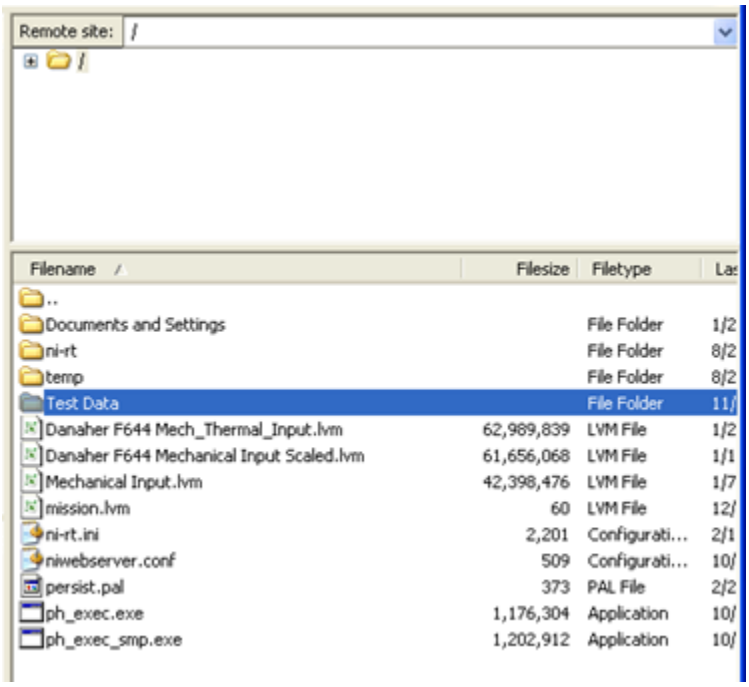

Figure C-32 FileZila Software Application (Location of Recorded Data)

Finally, Figure C-33 is an image of the test setup after a successful test procedure.

Figure C-33 Test Setup after Experiment

APPENDIX D

HARDWARE SPECIFICATIONS

Kollmorgen EC5 Electromechanical Actuator

Source: Linear Positioners Catalog_en-US_revA

http://www.kollmorgen.com/en-us/products/linear-actuators/electric-cylinders/ec5-series

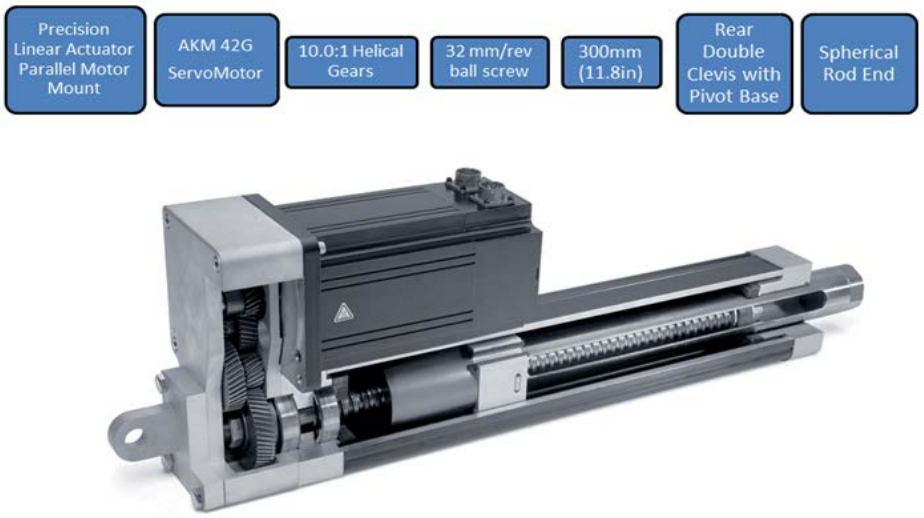

Figure D-1 Industrial EMA under test

Kollmorgen AKM42G Servomotor

Source: AKM_Selection_Guide_en-US_revA.pdf

http://www.kollmorgen.com/en-us/products/motors/servo/akm-series/akm-series-ac-synchronous-motors/ac-synchronous-servo-motors

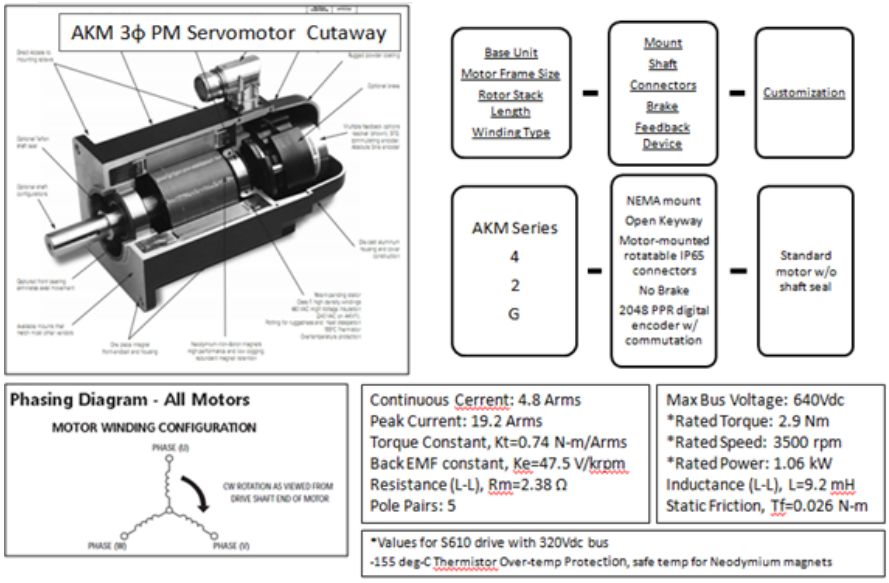

Figure D-2 EMA motor specifications

Kollmorgen S610 Servodrive

Source: S300_S600_Catalog_en-US_RevA

http://www.kollmorgen.com/en-us/products/drives/servo/serviced-drives/s600/

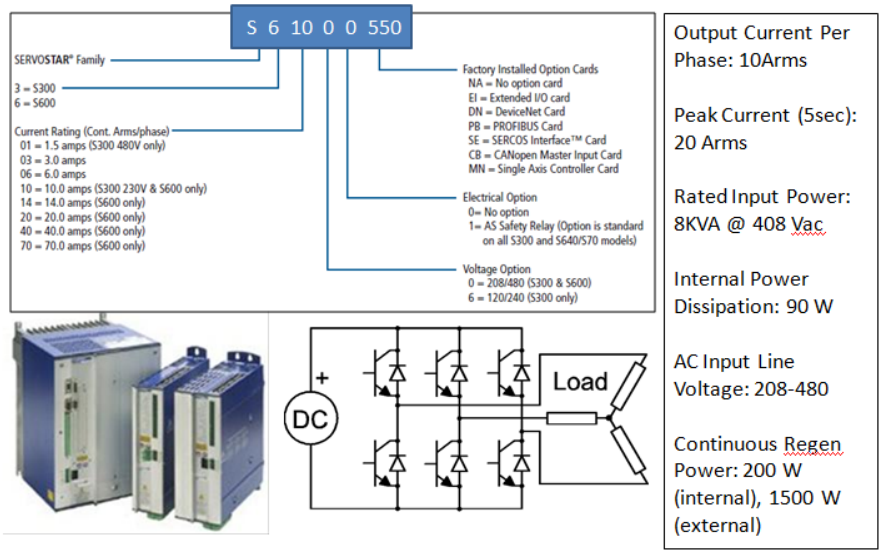

Figure D-3 EMA drive specifications

MTS Servohydraulic Load Frame

Source: http://www.mts.com/en/products/producttype/test-systems/load-frames-uniaxial/servohydraulic/standard/index.htm

MTS 370.10 22 KIP Load Frame

Shown with optional hydraulic grips

Actuator Type	Axial
Vert. Test Space (min/max)	Ext 363/1753 mm (14.3/69.0 in)
Load Frame Column Spacing	533 mm (21.0 in)
Load Frame Column Diameter	76.2 mm (3.0 in)
Actuator Location	Integral to Base
Actuator Force Rating	100 kN (22 kip)
Load Cell Force Rating	100 kN (22 kip)
Actuator Dynamic Stroke	250 mm (10 in)
Crosshead Positioning	Hydraulic Powered Adjustment
Crosshead Locks	Hydraulic Powered Adjustment
HSM Maximum Flow Rating	228 lpm (60 gpm) 4 servovalve
Floor Standing HSM	Included
Controller Platform	494 Platform
Calibration - Site	Standard Factory Calibration
Calibration - Electronics	494.16/494.25/494.26
Calibration - Cable Length	7.5 m (25 ft)
Calibration - Output Polarity	Tension (+), Compression (-)
Calibration - Full Scale	250 mm, +/- 150 mm
Installation	On-site

Figure D-4 Hydraulic Press specifications

MTS Servohydraulic Controller

Source: http://www.mts.com/en/products/producttype/test-components/controllers/flextest-controllers/index.htm

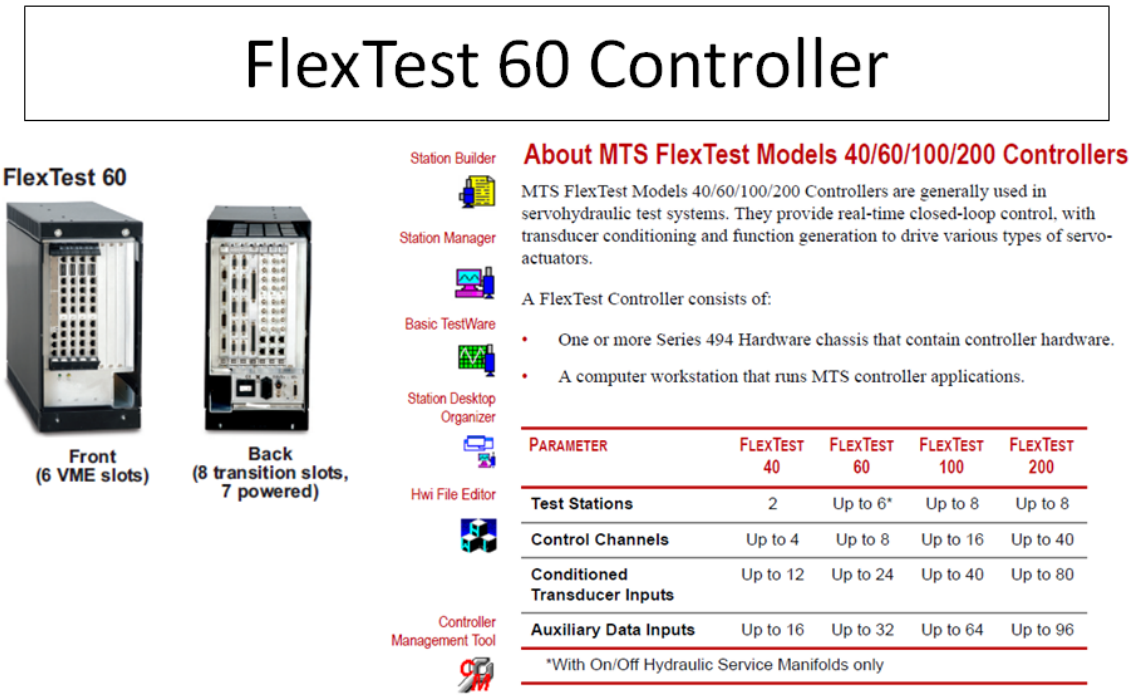

Figure D-5 Hydraulic Press Controller specifications

MTS Force Transducer

Source: http://www.mts.com/en/products/producttype/test-components/grips-fixtures-accessories/load-cells-force-transducers/index.htm

MTS 661.20H-03 Load Cell

Controller Platform		494 Platform
TEDS		Included
Load Cell Model Number		661.20H-03
Thread Type		Metric
Load Cell Force Rating		100 kN (22 kip)
Load Cell Thread Form		M27 X 2MM-6H
Load Cell Cable Connector Type		JT
Electronics		494.16/494.25/494.26
Calibration - Site		Standard Factory Calibration
Cable Length		7.5 m (25 ft)
Calibration - Output Polarity		Tension (+), Compression (-)
Calibration - Full Scale		100 kN (22 kip)

MTS 661 Series Load Cells are designed for a wide array of static and dynamic testing applications. The cells are designed for cyclic operation in through zero tension/compression modes.

- Low deflection and high degree of stiffness gives better dynamic performance.
- High output shear web design resists off-axis loading and moments, increasing accuracy and resolution.
- Proprietary wiring techniques reduce electrical noise.
- Temperature compensation helps ensure stability.
- Designed for easy integration with other accessories, platens, and fixtures.
- Manufactured with aircraft-quality steels, specially heat-treated to minimize distortion.

Figure D-6 Hydraulic Press Load Cell

MTS Environmental Chamber

Source: http://www.mts.com/en/products/producttype/test-components/environmental-simulation/chambers/index.htm

651.06E-04 Environmental Chamber

Specs

- Temperature Range: -129°C to 316°C
- Power: 8kW
- Fan Power: 0.2 kW
- Air Temp. Performance:
  - Heating: Ambient to 300°C in <30 min
  - Cooling: Ambient to -129°C in <20 min
  - Temperature Gradient: ± 2% or 2°C, whichever is greater
  - Temperature Stability: ± 2°C
- Recovery Time to set point temperature
  - Door open 1 min : 4 min
  - Door open 2 min : 5 min
- Weight: 141 kg
- Eurotherm 2404 PID Temperature Controller
  - RS 485 COM
  - K-type TC feedback

Dimensions

- Test Space Dimensions: 36x43x81cm
- External Dimensions: 51x79x97cm

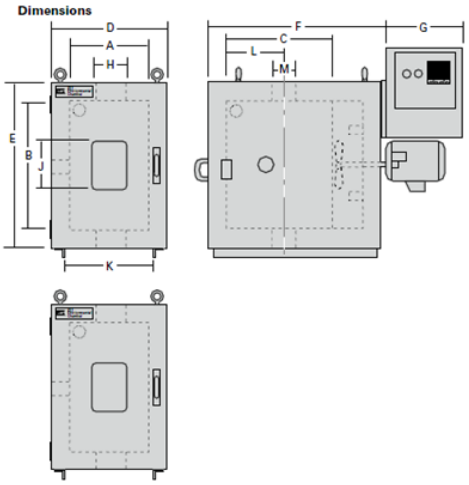

Figure D-7 MTS Environmental Chamber

National Instruments Data Acquisition Machine

Source: NI PXIe-1071 User Manual and Specifications

http://sine.ni.com/nips/cds/view/p/lang/en/nid/208933

The DAQ machine is made up of an NI PXI chassis outfitted with a Real-Time controller, and three modules or cards—one for electrical, mechanical, and thermal measurements.

NI PXIe-1071, 4-Slot 3U PXI Express Chassis

781368-01

- 3 hybrid slots
- 230 W total power available from 0 to 50 °C
- High performance - up to 1 GB/s per-slot dedicated bandwidth and 3 GB/s system bandwidth
- Compact and lightweight PXI chassis, 13.1 lb (5.94 kg)
- Compatibility with PXI, PXI Express, Compact PCI, and Compact PCI Express modules

Figure D-8 PXI Chassis

NI PXIe-8102 1.9 GHz Dual Core Real-Time Embedded SW
781184-33

- Deployment platform for LabVIEW Real-Time and LabWindows™/CVI Real-Time applications
- Execution target for NI LabVIEW Real-Time Version 8.6.1 or later applications
- 1 GB (1 x 1 GB DIMM) 800 MHz DDR2 RAM standard, 2 GB maximum
- 1 GB/s maximum system and 250 MB/s maximum slot bandwidth
- Integrated hard-drive, USB, serial, Gigabit Ethernet, and other peripheral I/O

Figure D-9 PXI Controller

NI PXIe-6361, X Series DAQ (16 AI, 24 DIO, 2 AO)
781055-01

- 16 analog inputs, 2 MS/s 1-channel, 1 MS/s multichannel; 16-bit resolution, ±10 V
- Two analog outputs, 2.86 MS/s, 16-bit resolution, ±10 V
- 24 digital I/O lines (8 hardware-timed up to 10 MHz)
- Four 32-bit counter/timers for PWM, encoder, frequency, event counting, and more
- Analog and digital triggering and advanced timing with NI-STC3 technology
- Support for Windows 7/Vista/XP/2000

Figure D-10 Module 3—Electrical Card

NI PXIe-6366, X Series DAQ (8 Simultaneous AI, 24 DIO, 2 AO)
781057-01

- 8 simultaneous analog inputs at 2 MS/s/ch with 16-bit resolution; 16 MS/s total AI throughput
- Two analog outputs, 3.33 MS/s, 16-bit resolution, ±10 V
- 24 digital I/O lines (8 hardware-timed up to 10 MHz)
- Four 32-bit counter/timers for PWM, encoder, frequency, event counting, and more
- Analog and digital triggering and advanced timing with NI-STC3 technology
- Support for Windows 7/Vista/XP/2000

Figure D-11 Module 2—Mechanical Card

NI PXIe-4353 32-Ch Thermocouple Input
781348-01

NI TB-4353 Isothermal Terminal Block for PXIe-4353
781349-01

- Front mounting terminal block for the NI PXIe-4353
- Built-in cold-junction compensation
- Screw terminal connectivity
- Autodetected; hot swappable

- 32 thermocouple input channels; 8 built-in cold-junction compensation channels; 0.3 °C accuracy
- 90 S/s/ch sample rate in high-speed mode; 1 S/s/ch sample rate in high-resolution mode
- 300 Vrms CAT II channel-to-earth ground safety isolation
- Autozero channels for offset error compensation; open-thermocouple detection
- Multidevice triggering and synchronization via PXI Express
- NI-DAQmx driver software and NI LabVIEW SignalExpress LE interactive data-logging software

Figure D-12 Module 3—Thermal Card

LEM Current Transducer and Tectronix Voltage Probe

Source: High-voltage Differential Probes, Current Transducer LA 55-P

http://www.tek.com/differential-probe-high-voltage

http://www.alldatasheet.com/datasheet-pdf/pdf/114818/LEM/LA55-P.html

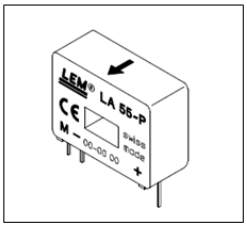

Current Transducer LA 55-P
DC, AC, and pulsed current measurements
Galvanic isolation between primary circuit (high power) and secondary circuit (electronic circuit).
Primary nominal r.m.s. current: 50 A
Primary current, measuring range :0 .. ± 70 A
Accuracy @ 50 A , TA = 25°C @ ± 15 V (± 5 %): ± 0.65 %

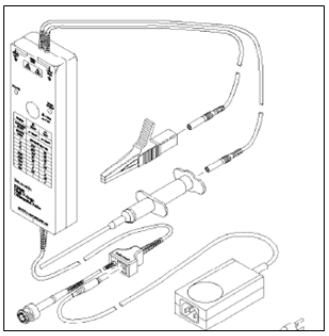

High Voltage Differential Probes P5200
Bandwidth: 25Mhz
Diff Mode Voltage: 1000 RMS or DC, 1300 peak
Attenuation: 50X/500X
Power Source: AC Wall Adapter
Accuracy: ± 3.0 %

Figure D-13 Electrical Sensors

Omega Thermocouples Probes

Source: http://www.omega.com/pptst/JMQSS.html

Quick Disconnect Thermocouples with Miniature Connectors

(*)MQSS Series -JMQSS, KMQSS, EMQSS, TMQSS,NMQIN

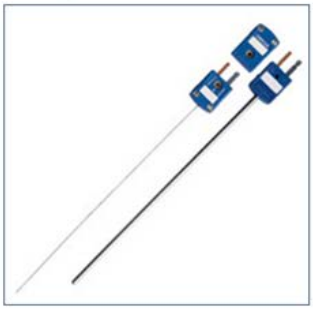

- 6" and 12" Lengths in StocK
- Sheath Diameters from 0.010" to 0.125"
- 304SS or 321SS Sheath
- Grounded, Ungrounded or Exposed Junction
- Color-Coded SMP Miniature Connector Termination
- Mating Connector and Cable Clamp Included FREE!
- Custom Lengths Available
- Made from Special Limits of Error Material
- Glass Filled Nylon Connector Body Rated to 220°C (425° F)

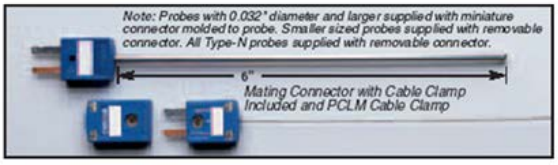

OMEGA's Quick Disconnect Thermocouples with Miniature Connectors are high quality, economical thermocouple probes. They feature a glass filled nylon connector which is rated for temperatures up to 220°C (425°F). The probes are available in with diameters as small as 0.25mm(0.010 inches) and as large as to 3.0mm(0.125 inches).

Figure D-14 Thermocouples

APPENDIX E

LABORATORY CAPABILITY SUMMARY

A poster-summary of hardware and software utilized to create a test setup for EMA integration and thermal management testing was created as a high level overview. This poster is shown in Figure E-1.

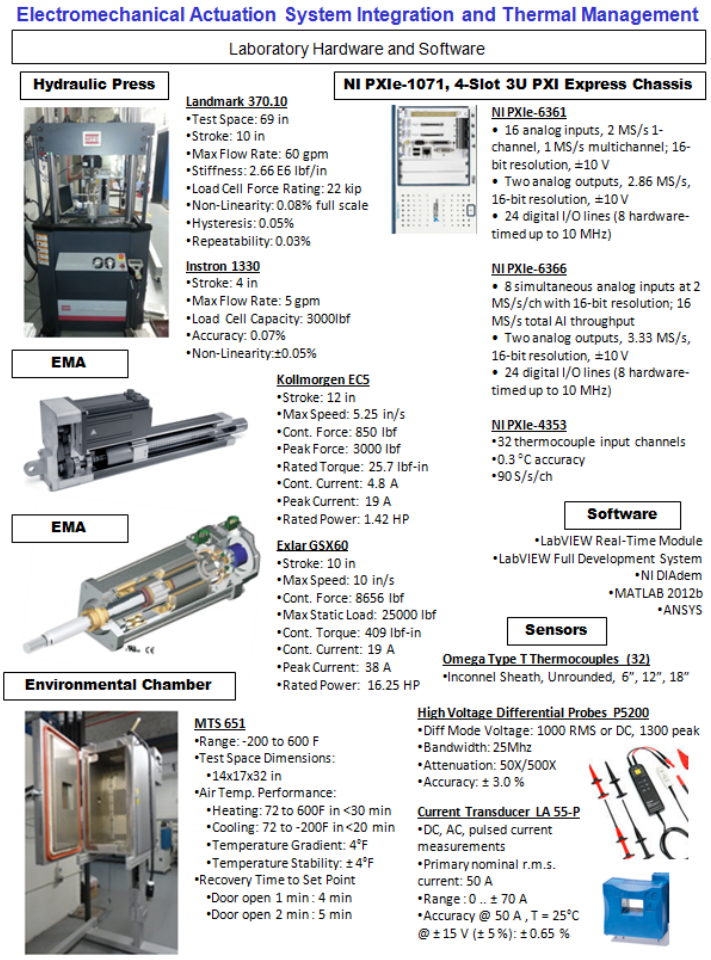

Figure E-1 Lab Capability Poster

APPENDIX F

SENSOR LOCATIONS

Thermocouples

Both servodrives were instrumented with thermocouples (TCs) on traditionally heat intensive components. Drive 1 in the dual drive setup functioned primarily as the EMA control generating PWM power to drive the EMA motor while Drive 2 provided 240 V_{AC} mains supply rectification to 330 V_{DC}. Figure F-1 is a high level overview of thermocouple locations and their placement relative to the dual drive setup and the actuator.

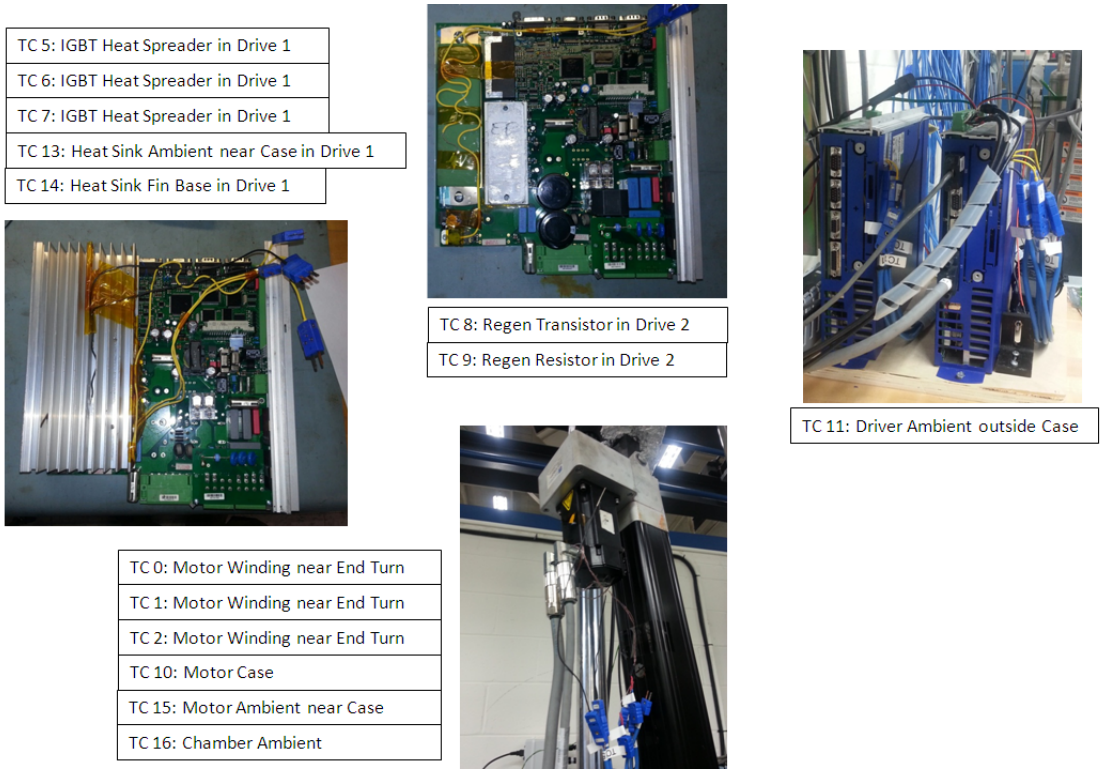

Figure F-1 Thermocouple Identification

Drive 1 (Control and Inverter)

Drive 1's board was removed from its case and the heat sink shown in Figure F-2 was detached. The red rectangle highlights the heat spreader, housing six primary IGBT switches. Points 5, 6, and 7 denote the location of TC 5: IGBT heat spreader, TC 6: IGBT heat spreader and TC 7: IGBT heat spreader. TC 13 was placed in the center of the heat sink half the distance from the fin base and end. TC 13 has no contact with the heat sink and therefore was named TC 13: Heat sink ambient near case. TC 14: Heat sink fin base was placed in the same trough as TC 13 but in contact with the fin base.

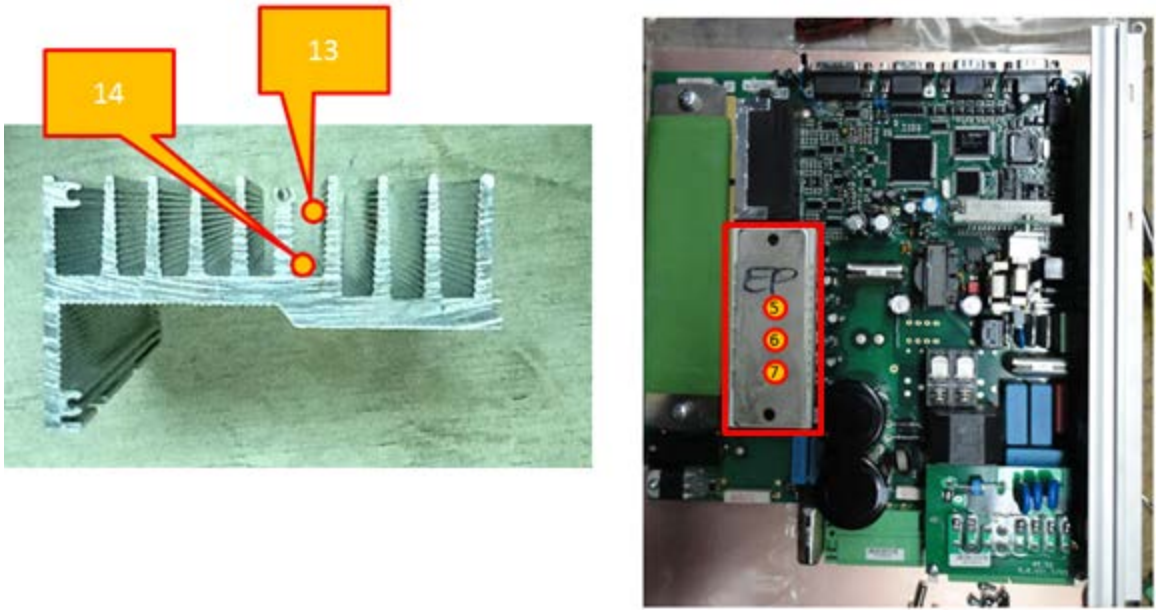

Figure F-2 Heat sink (left) and Servodrive board (Right)

In order to reassemble the heat sink atop the heat spreader with thermocouples 3 equally spaced trenches were machined into the heat sink. Figure F-3 is 3-D design of the heat sink and the corresponding thermocouple trenches. Thermal compound was used near these locations to reduce thermal resistance between the heat spreader and heat sink.

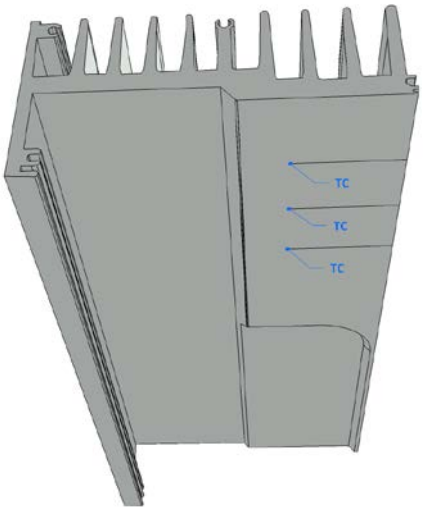

Figure F-3 Underside of heat sink with placement of thermocouples shown

Figure F-4 demonstrates the use of electrically insulated Kapton tape to help route TC leads from the point of measurement to outside the driver case.

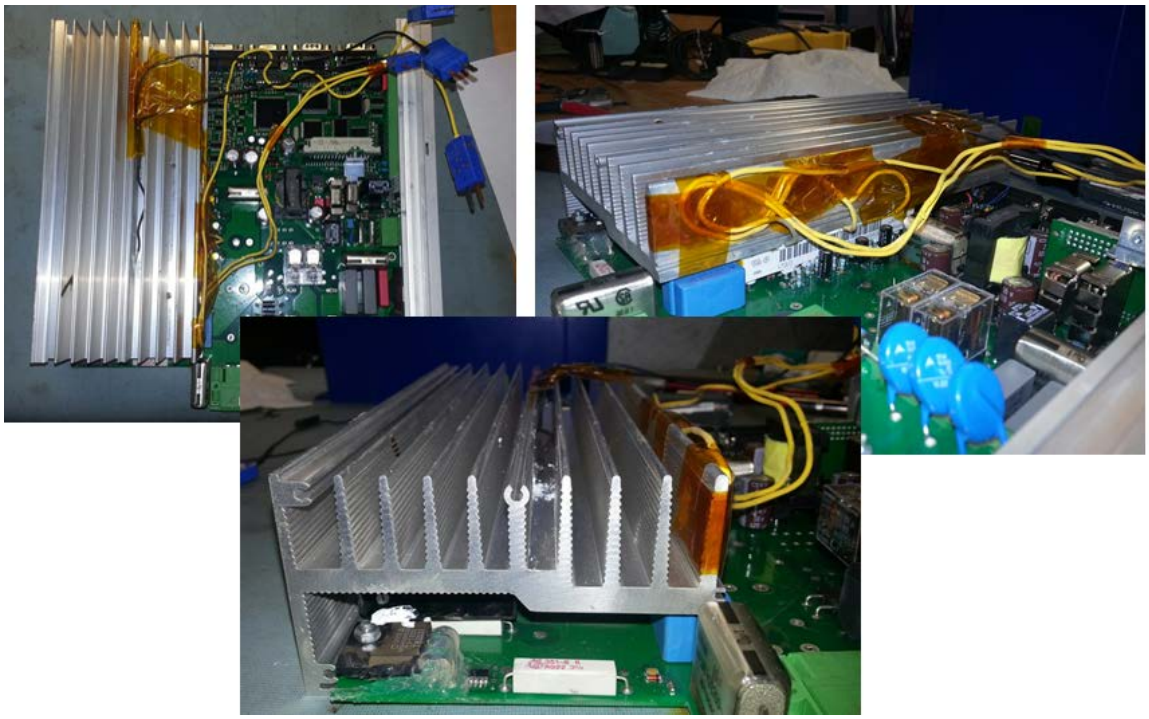

Figure F-4 Thermocouples embedded in Drive 1

Drive 2 (Rectifier)

Drive 2's board was removed from its case and the heat sink shown in Figure F-5 was detached. The red rectangle highlights the regenerative resistor (33 Ω), responsible for dissipating energy during regeneration. TC 9: Regen resistor was place atop the regenerative resistor near the center of its longitudinal axis. TC 8: Regen Transistor was placed on the case of the transistor or switch responsible for opening and closing of the regenerative circuit. Figure F-6 shows how TC 8 and 9 leads were molded for best fit and secured with Kapton tape.

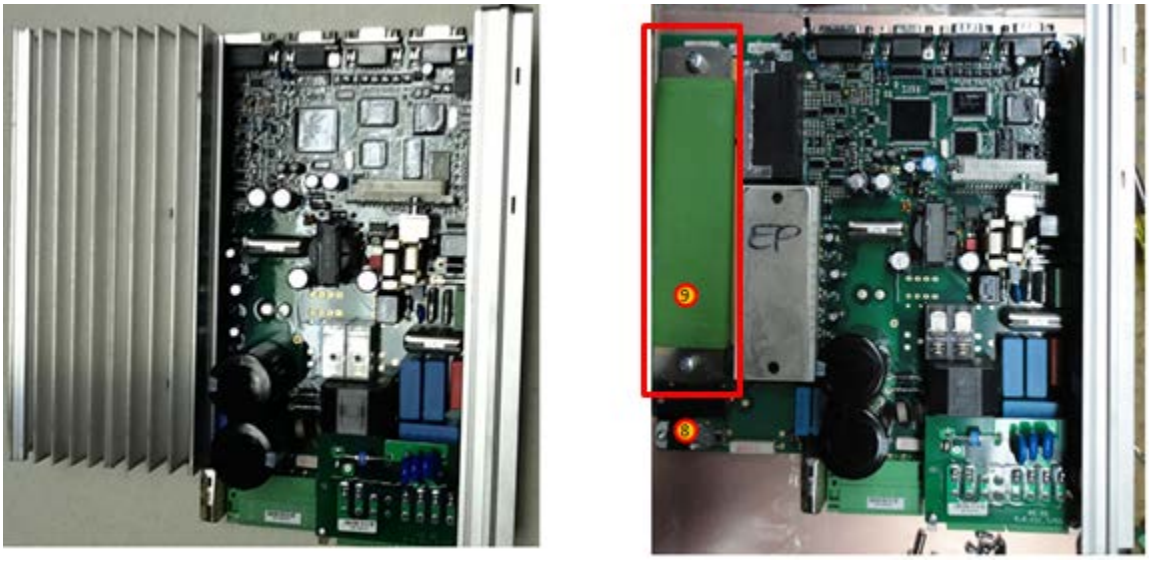

Figure F-5 Servodrive board with Heat Sink (left) and without Heat Sink (Right)

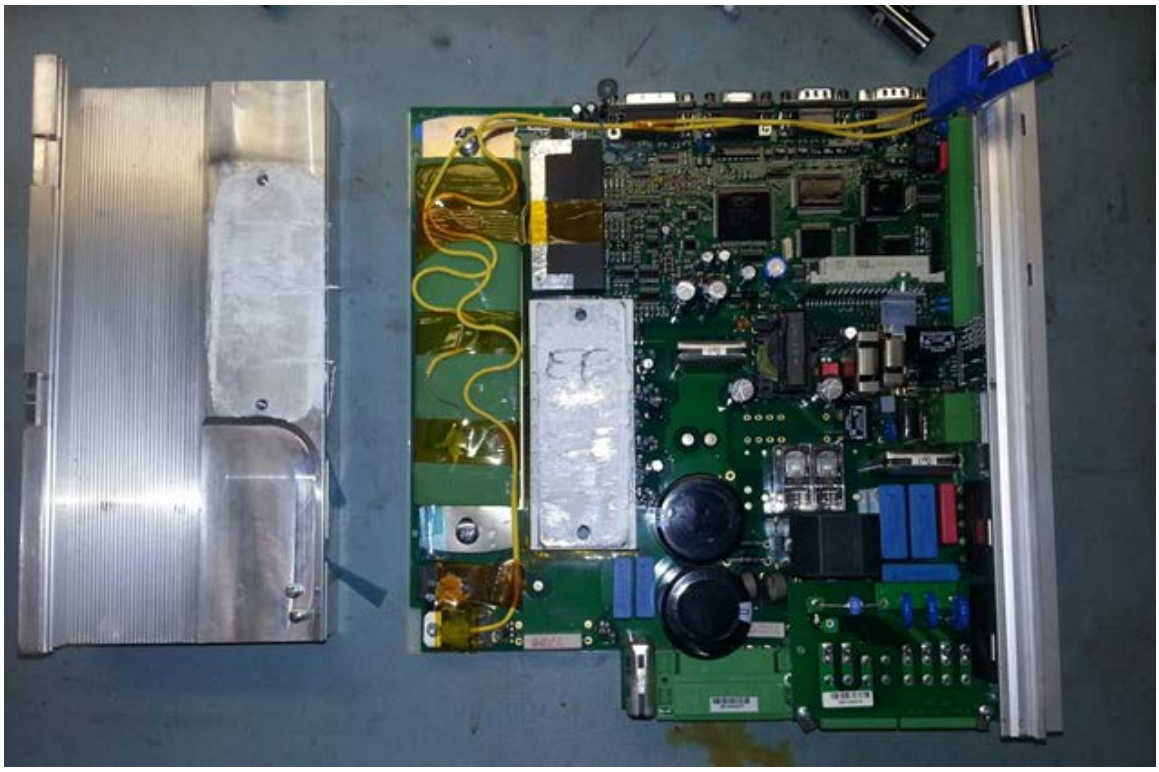

Figure F-6 Thermocouples embedded in Drive 2

Drives outfitted with Thermocouple Probes

Figure F-7 shows the final result of drive fabrication for thermal instrumentation.

Figure F-7 Servodrive System Completed with Thermocouples

Actuator

Figure F-8 highlights the routing of shielded TC wires into the environmental chamber, their fixture to the actuator for rigidity, and TC lead location.

Figure F-8 Thermocouples embedded in motor and within environmental chamber

Servodrive Overview

Figure F-9 shows the EMA power electronics setup and pertinent measurement points. A small opening was fabricated within each driver case as a thermocouple entry point. Current transducers were affixed to PCB for greater reliability and resistance to motion. Thermocouple leads were organized with coiled cable tubing.

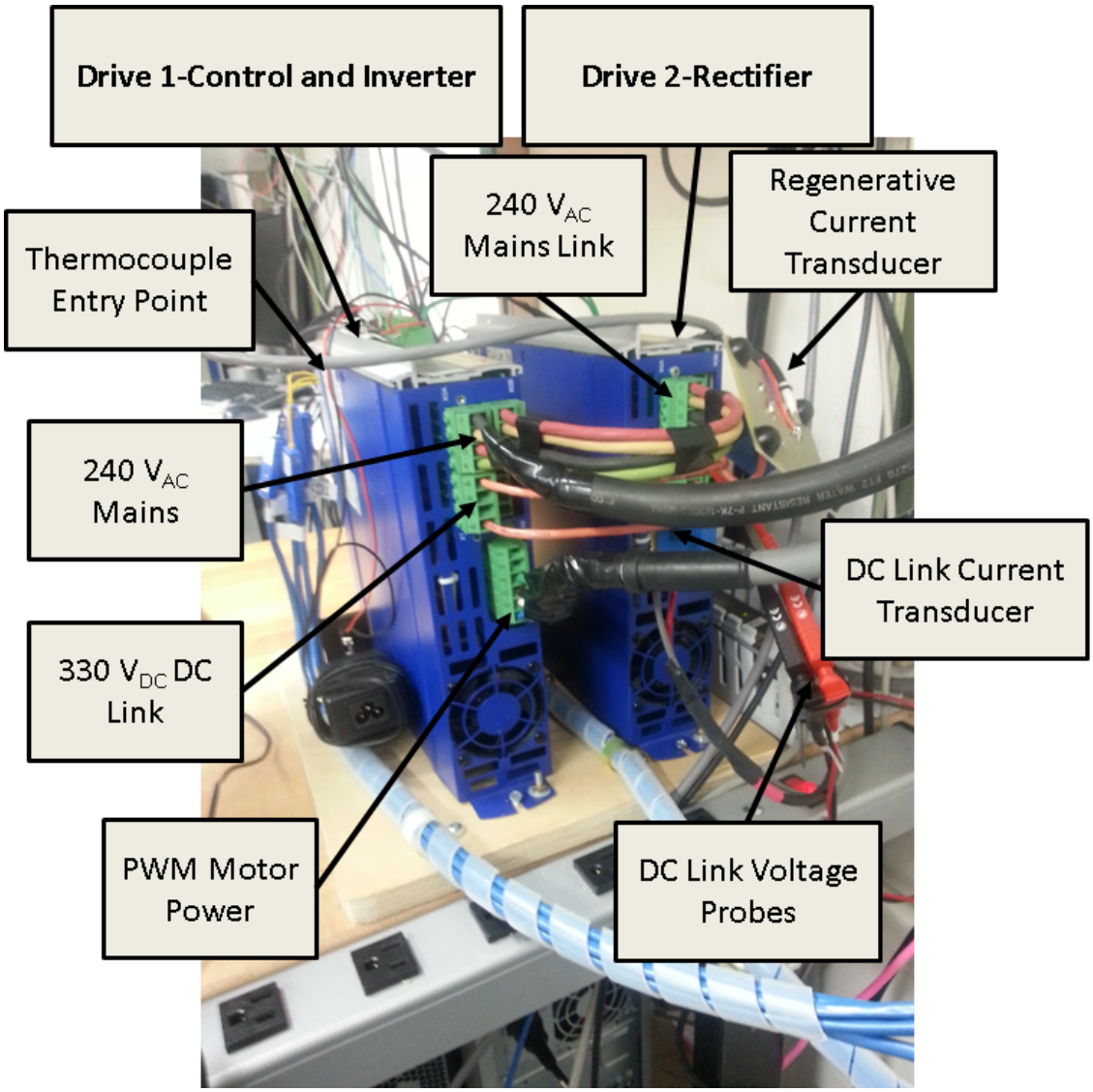

Figure F-9 EMA Drive Setup with Thermocouples, Current Transducers, and Voltage Probe

APPENDIX G

EXPERIENCE WITH ENVIRONMENTAL CHAMBER

MTS 651.06E environmental chamber coupled with an MTS hydraulic press replicated real-world thermal and mechanical conditions to test a representative EMA. The chamber's internal dimensions (36 x 43 x 81 cm) supplied an adequate testing area for the EMA and its instrumentation. Modified upper and lower U-plug sections permitted the actuator's arm to extend outside of the chamber while preventing significant heat loss. Environmental chamber temperature range was -200°F - 600°F—a range that can easily test the EMA's ability to comply with military standards. In addition, an electric motor driven fan provided forced convection for consistent and rapid heat transfer while the use of liquid nitrogen provided rapid cooling in order to accurately portray a dynamic environment.

Overview

Several pieces of equipment were used in analyzing EMAS thermal management. Figure G-1 shows the primary equipment used and their interaction: MTS 651 environmental chamber, Eurotherm 2404 PID temperature controller, FutureDesign L91 limit controller (temperature limit switch), and a FlexTest60 digital controller.

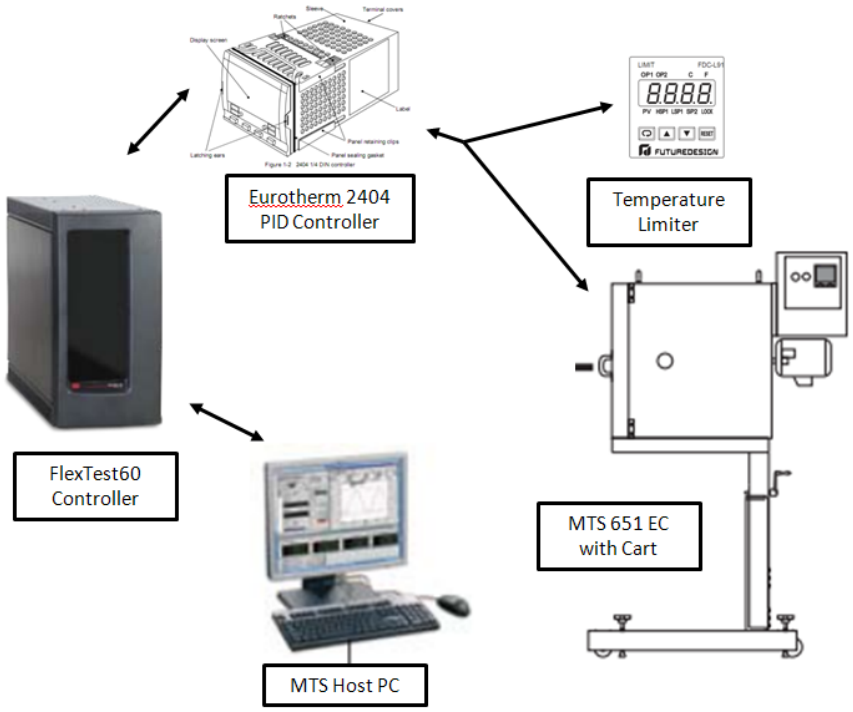

Figure G-1 Thermal Management Test Hardware

The environmental chamber was an insulated oven outfitted with two electrical heating elements, electric fan, and solenoid valve. Cooling was accomplished with the use of extremely cold vapor (LN_2) introduced to the chamber via solenoid valve. The fan and interior baffle were developed to ensure uniform internal temperatures. Eurotherm temperature controller was mounted within the chamber electrical box. The electrical box also housed an electrical panel

made up of relays, transformers, fuses, and more which conditioned the mains supply and distributed it to the fan motor and heating elements. Figure G-2 is an overview of the individual chamber components.

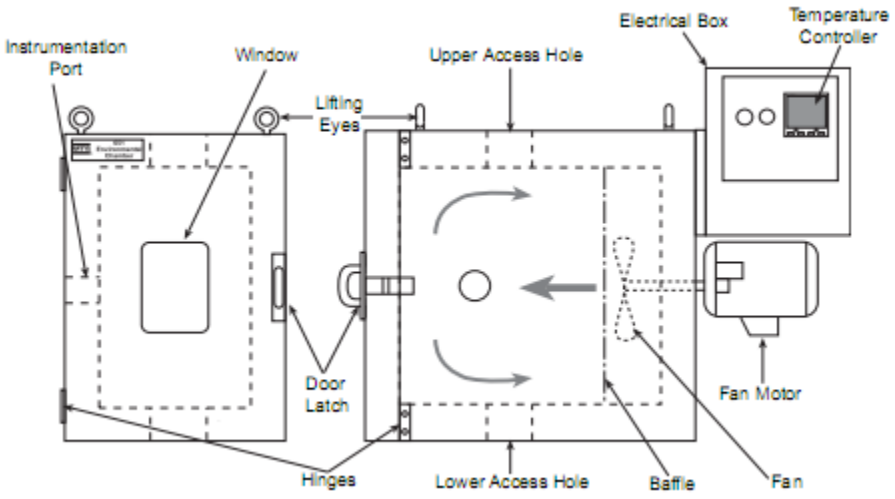

Figure G-2 MTS 651 Oven

Eurotherm PID temperature controller utilized thermocouple feedback in closed loop control to modulate heating or cooling until the predefined set point was met. Temperature set point could be set manually, programmed into a procedure of up to 8 ramp or dwell cycles, or remotely controlled via serial communication. Ultimately, remotely controlling temperature setpoint permitted the greatest replication of EMA bay conditions and atmospheric temperature as a function of varying altitude. Two methods of remote temperature control were sought. First, the FlexTest60 digital controller and its software (MultiPurpose TestWare) were used to complete remote communication with the temperature controller. This method proved reliable and convenient while independently controlling the environmental chamber for configuration, troubleshooting and characterization. However, MultiPurpose TestWare permitted one control channel to be active at a time. In order to apply a load to the EMA that single control channel was dedicated to hydraulic press control. Therefore, a second method was required. The second method utilized a real-time NI DAQ to remotely control temperature. This method required a communication adapter but permitted the simultaneous control of the hydraulic press, EMA, and environmental chamber.

Environmental Chamber Preparation

Majority of initial experiences with the environmental chamber were saturated with installation and configuration tasks. These trials and tribulations are outlined in this section. Eurotherm temperature controller arrived configured with a heating, cooling, and communication plug in module. Additional space exists for a third plug in module and a second communications module. In Figure G-3 MODULE 1 corresponds to the heating module (red), MODULE 2 is the cooling module (blue), and COMMS 1 is used to remotely control the chamber (green). Rear terminal layout shown in Figure G-3 can be accessed by removing the rear panel on the electrical box of the environmental chamber or by pulling the controller out of its assembly.

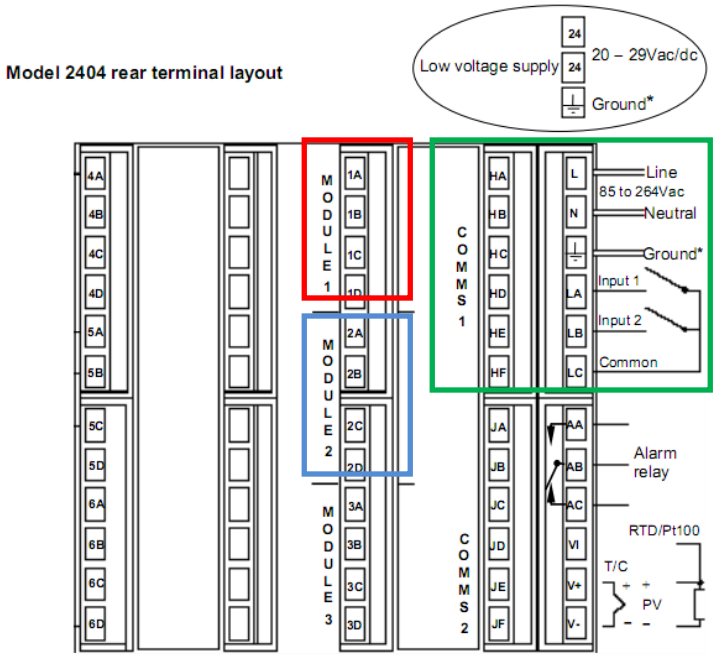

Figure G-3 Eurotherm Temperature Controller rear terminal layout

Each of these connections were checked and confirmed. Configuring the controller required the user to parse the menu to the access submenu and enter a password to obtain *configuration level* access. The controller has four access levels: operator level, full, level, edit level, and configuration level. For test purposes operator level was sufficient, but to configure the device configuration level was required. Configuration parameter tables in the controller handbook demonstrated how to alter parameters such as remote setpoint configuration, communications protocol, address, and baud rate. These parameters were crucial to successfully establishing communication and had to be the same on both ends of communication.

In order to limit the testing range high and low limits were set to 170 °F and -76 °F, respectively. Low temperature limit corresponded to ambient temperatures at upper reaches of aircraft flight envelope. High temperature limit corresponded to the smallest maximum operating temperature of all devices housed within the environmental chamber. EMA maximum operating temperature was 160°F. Therefore, the high limit was set just above that value to prevent an interlock due to overshoot of 160°F setpoint. This range could be altered appropriately depending on the test objective, whether it's to verify EMAS operation at high altitude or analyze EMA power de-rating at elevated ambient temperatures. The range mentioned above will remain because no serious safety threat exists if extended contact with the interior of the chamber is prevented.

Remote Control Method 1

Unfortunately, communication between FlexTest60 and Eurotherm controllers was not plug-and-play. Achieving communication between FlexTest60 and Eurotherm controllers required several steps. First, Eurotherm COMM module was established as 2-wire RS485 serial communication link. Next, we connected a serial cable supplied with the chamber to the 25 pin connection on the chamber and to port J3A of the FlexTest controller. Port J3A was designated

for serial communication in FlexTest60 manual. Figure G-4 shows the 25 pin connection on the right and port J3A on the left.

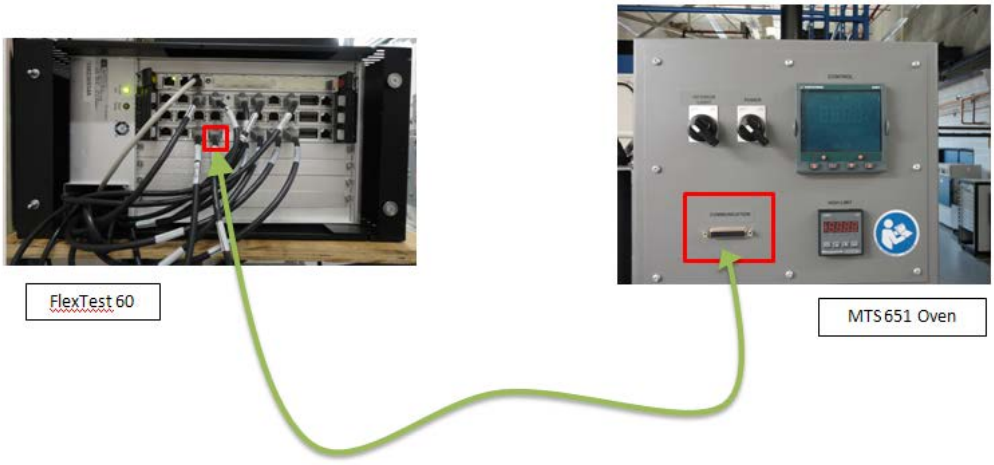

Figure G-4 Installing Environmental Chamber RS485 Communication line

FlexTest60 controller did not recognize the Eurotherm controller even with the comm-link connected. It was determined an additional channel had to be created specifically for J3A serial communication within MultiPurpose TestWare's station configuration file. This was completed using Station Builder, an application of MTS 793 software. The following was required to configure a new channel, *TemperatureControl* channel:

- *TemperatureControl channel* created used the resource *Temp Control 1-1-input*.
- HWI editor application configured *Temperature Control* to use port J3A on carrier 4 of the FlexTest.
- Serial Comm 1 under Carrier 4 and 494.47 Dual UART/Encoder/External Clock was modified
    - Baud rate was set to 9600 to match Eurotherm controller Baud Rate
    - Connection type was defined as 2 wire

After these steps, Station Manager was launched and a serial communication link was established between the FlexTest60 controller and Eurotherm controller.

This section reviews the acclimation period after communication between the MTS controller and Eurotherm controller was achieved. During this time period, chamber setpoint temperature was remotely controlled through MTS Station Manager application. Within Station Manager there existed 4 operational modes. The operator modes were manual command, Basic TestWare, multipurpose TestWare (MPT), and MPT elite, from simplest to most complex. Manual command provided the user with ability to execute single setpoint commands. Basic TestWare expanded user ability to run various wave shapes and define target setpoint, amplitude, frequency, number of cycles, and duration. Basic TestWare also had the ability to record measurements. Multipurpose TestWare required the user to create a procedure made up of individual processes chosen from a process palette. MPT had parallel process capability, meaning several processes could be executed simultaneously. But, as long as a control channel is

in use by one process, it could not be called by another. Data acquisition in MPT was capable of sampling numerous signals. In addition to procedure creation, the user was required to create or define a specimen to run the procedure against. The following figures demonstrate various operational modes within Station Manager.

Manual command operation only offered channel selection and command value. Figure G-5 is a screenshot of Manual Command interface.

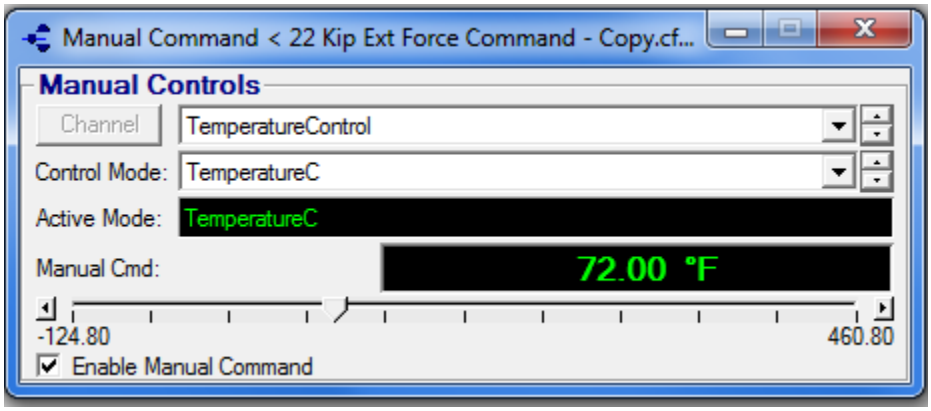

Figure G-5 Manual Command Operation Mode screenshot

Basic operation mode provided a target setpoint, similar to manual operation, but also permitted definition of input wave shape and its characteristics. Also, one could define the number cycles to be executed. Figure G-6 is a screenshot of Basic TestWare.

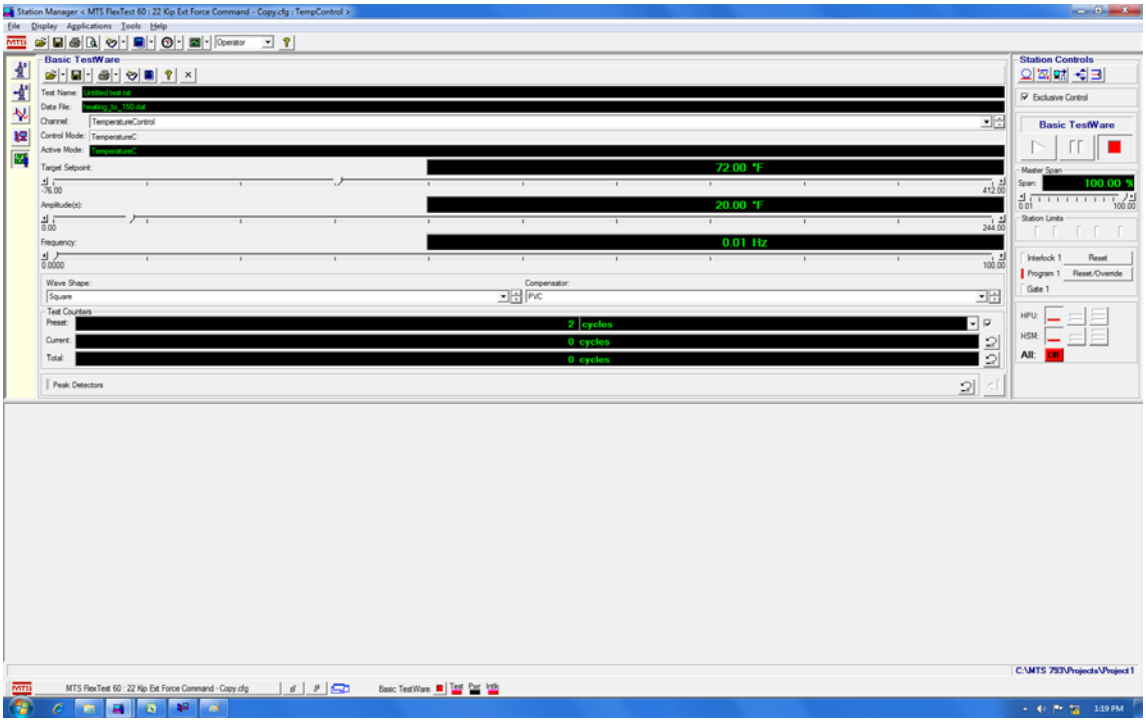

Figure G-6 Basic TestWare Operation Mode screenshot

MPT mode requires the use of the procedure editor. Test specimen and operator events created by the user within the procedure editor are available via MPT interface shown in Figure G-7.

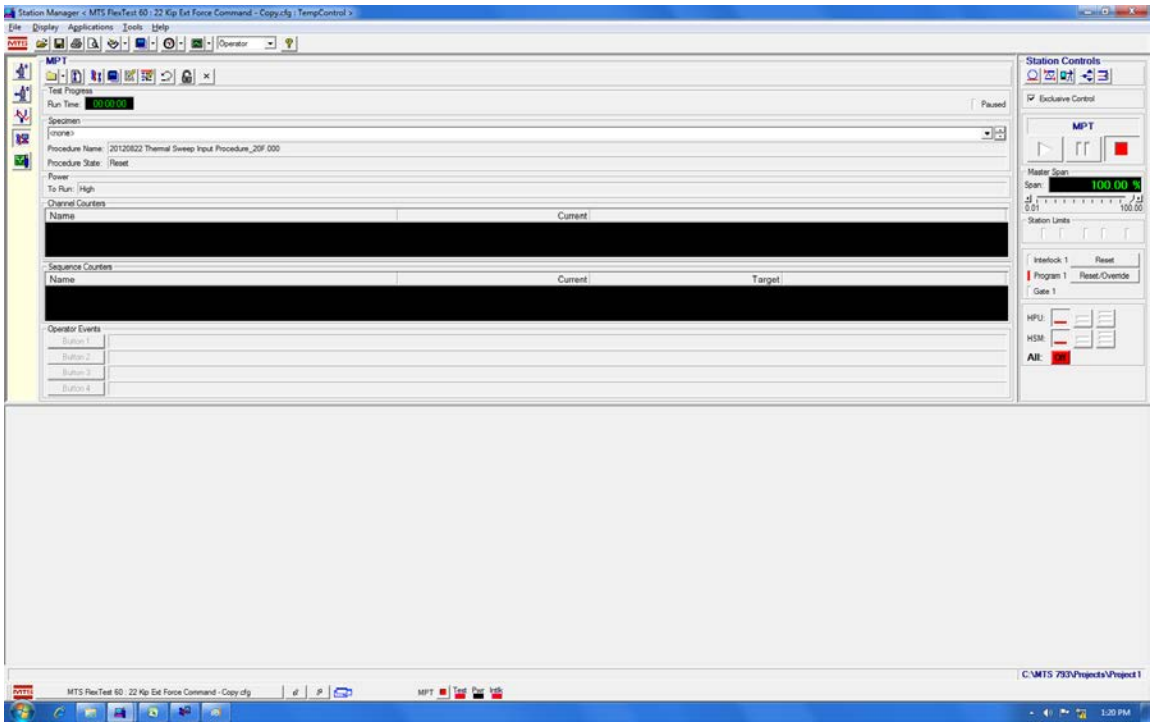

Figure G-7 MPT Operation Mode screenshot

Figure G-8 shows a typical procedure within the procedure editor. Process palette resides on the left while processes on the right make up the procedure. Each process can be modified by selecting the process and changing parameters under setting, options, and general tabs.

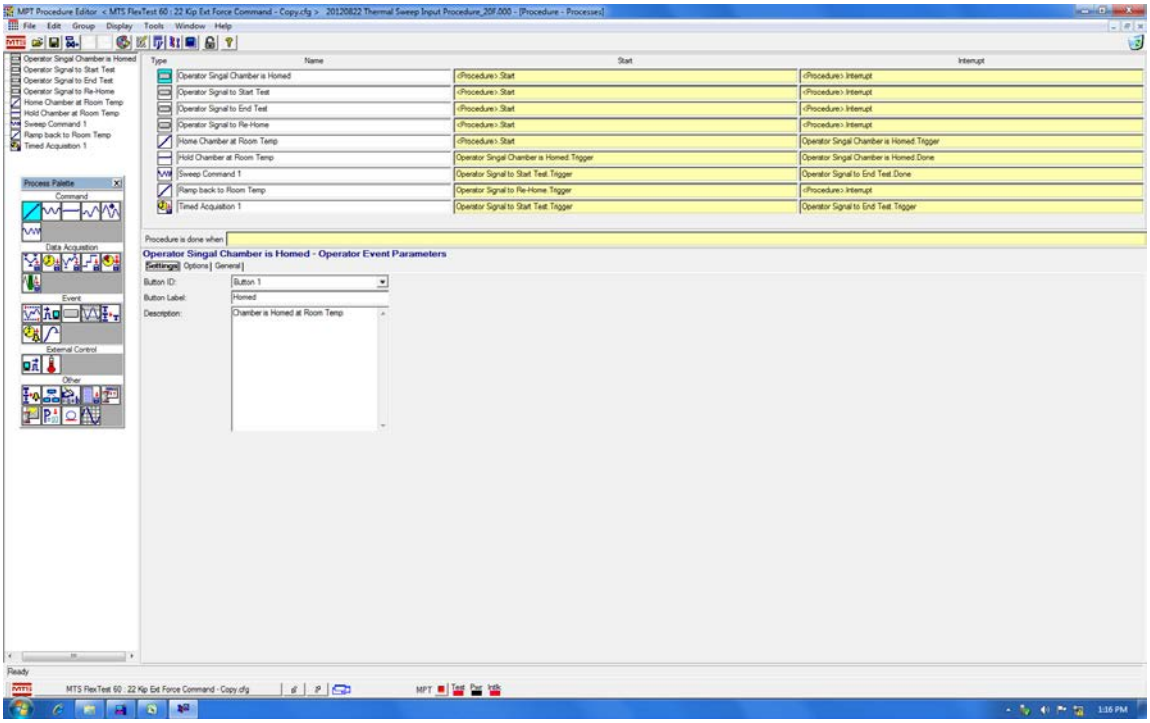

Figure G-8 MPT Procedure Editor Screenshot

MPT also provides the ability to create a temperature profile and automate temperature control. With that in mind, MPT profiles utilize specific parameter syntax. Contact with MTS technical support shed light on this syntax and helped prevent future profile syntax errors. Figure G-9 shows a comparison of an erred format that prevented profile execution with the corrected format. In summary, an additional parameter had to be defined in the file for Station Manager to recognize the channel in the file. That parameter was dimension. This is not mentioned in the latest application manual.

Original Format	Corrected Format
Filetype = Block-Arbitrary	Filetype = Block-Arbitrary
Date=24-Jul-12	Date=24-Jul-12
Channels=1	Channels=1
Channel(1)= TemperatureControl	Channel(1)= TemperatureControl
	Dimension= Temperature
Time=0.2	Time=0.2
Level1	Level1
deg_F	deg_F
75	75
75…	75…

Figure G-9 Profile file format

Figure G-10 shows results of an MPT Procedure that used a profile process to generate temperature commands defined in a thermal profile file over the course of 900 seconds. Not only did the program execute flawlessly but the environmental chamber was actually capable of following a highly dynamic temperature profile.

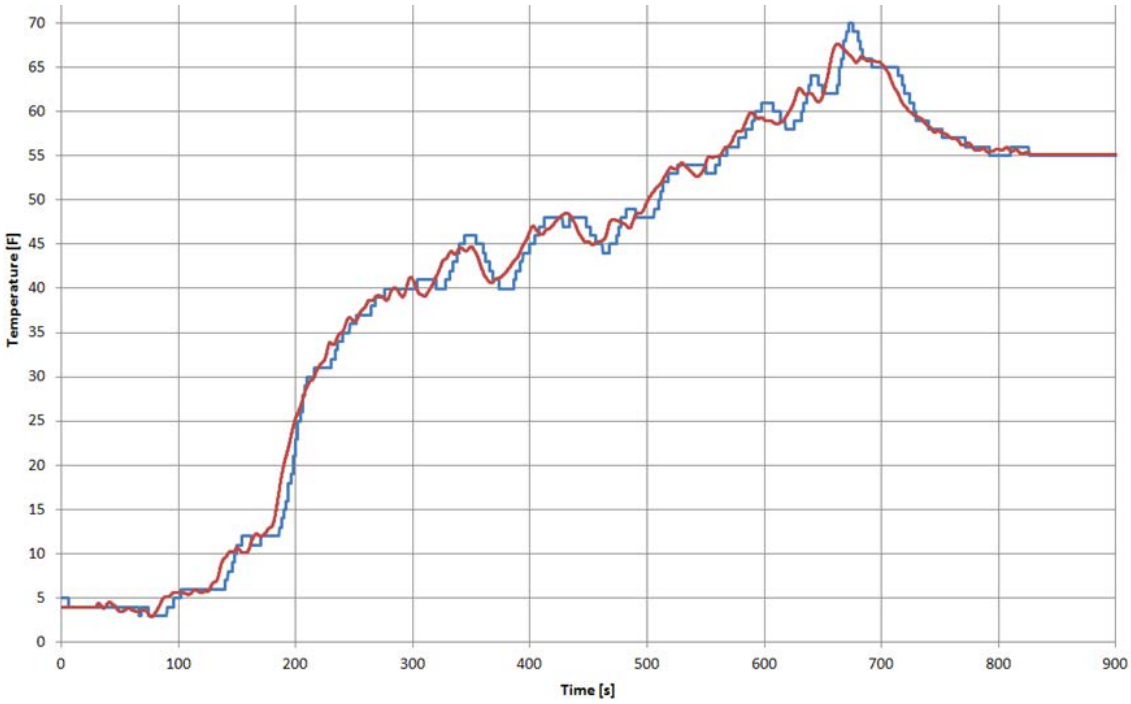

Figure G-10 MPT Procedure execution

Exercising the various control modes improved turnaround time between tests and developed an ability to test EMAS's for a wide variety of purposes and applications. For instance, using Eurotherm Controller's programming feature to replicate temperature profiles was limited to eight ramp or dwell intervals. However, through FlexTest60 and MultiPurpose TestWare we were able to remotely control temperature as a function of time. This resulted in more dynamic flight profiles where temperature setpoint was updated every second rather eight segments of time. Figure G-11 demonstrates the lack of resolution an eight segment procedure has when compared with a dynamic temperature profile.

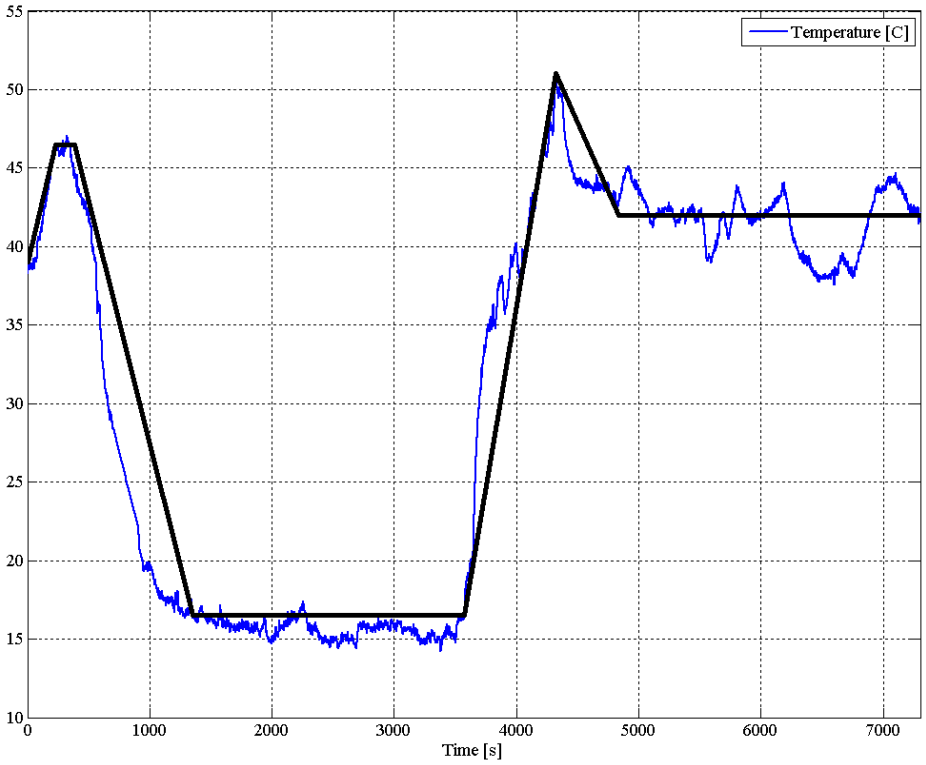

Figure G-11 Potential 8 segment representation of temperature profile

Remote Control Method 2

In order to achieve remote control of the environmental chamber via real-time DAQ machine, a comm-link between the DAQ and the temperature controller had to be established. NI DAQ machine was outfitted with an RS232 port; which was not compatible with the environmental chamber temperature controller outfitted with RS485. Therefore, an RS 232-485 bi-directional serial converter was required. The product of choice was L-com's SC-232-G which only required 5V external power. L-com's serial converter pin-out is shown in Figure G-12 and demonstrates proper connection between an RS232 and RS485 device. Screw terminal A on the converter corresponded to Tx of the Eurotherm comm-module. Screw terminal G corresponded to Rx of the Eurotherm comm-module. Tx was pin 2, Rx was pin 3, and GND was pin 5 on the 25-pin connector used with the Eurotherm controller.

Communication

Standard	Accord EIA RS232, RS485 standard
RS232 signal	TX, RX, GND
RS485 signal	A+, B-, GND
Operating format	A synchronism, point to point or multi-point, 2 line half duplex
Direction	Automatic Send Data Control-no software drivers needs
Band rate	300-115,200 bps, auto sense serial signal rate
Loading	can order 128 point
Transmission	RS485 side 1500M(9600bps)

PIN Setting

RS 485				RS232	
Terminal	Pin 1,2	Pin 3,4	Pin 5	DB9 female	RS232
Define	A+	B-	GND	Pin 2	RXD
RS485	485+	485-	GND	Pin 3	TXD
				Pin 5	GND

1. RS485 point to point/2 wire half-duplex

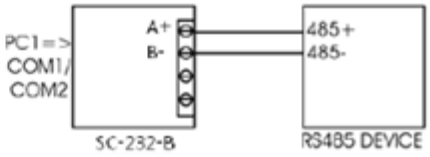

Figure G-12 L-com SC-232-G Pin out

Figure G-13 shows the converter in use and how red (screw terminal A) and black (screw terminal G) push clips connect converter output with the input of the environmental chamber temperature controller. Important to note is that LabVIEW VI's used for controlling the environmental chamber are currently deployed to the RealTime Machine shown in the picture, but can utilized on a regular PC and therefore the RS232-485 converter would need to be placed on the PC serial port instead of the RealTime machine. Also shown in Figure G-13 are two green wires which are 5V and GND supplied by a DC Power Supply.

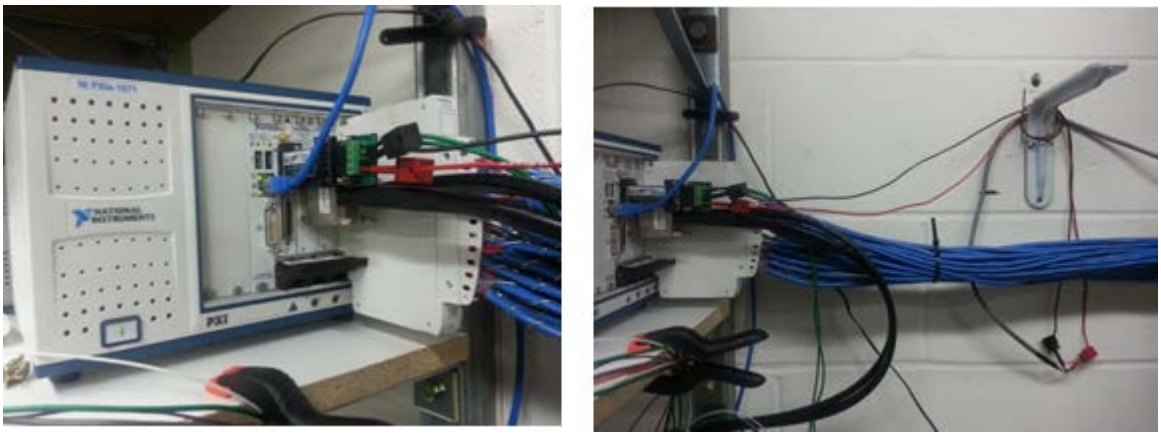

Figure G-13 Serial Converter connection to NI DAQ

Figure G-14 shows how fixed 5V was provided by two terminals on the right of the Laboratory DC Power Supply.

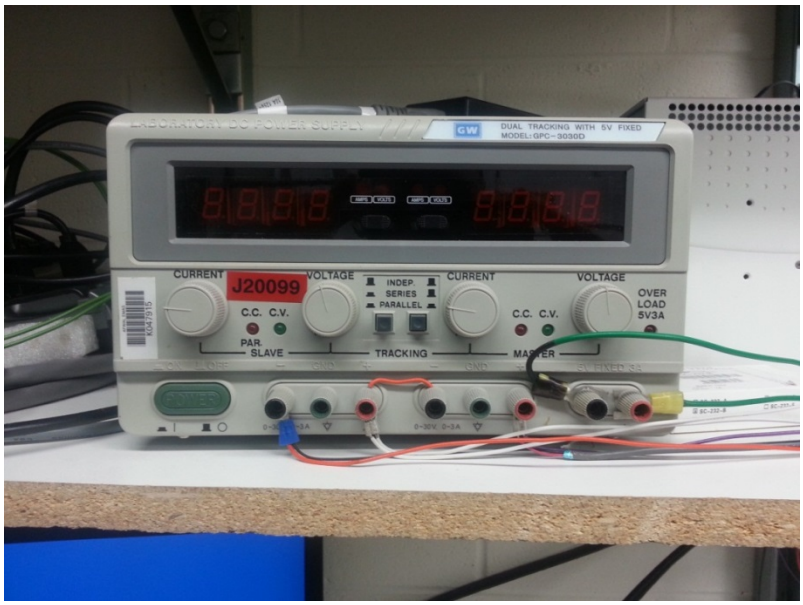

Figure G-14 Serial Converter connection to NI DAQ

Finally, G-15 demonstrates where the 25-pin end of communication cable connected to the environmental chamber.

Figure G-15 Environmental Chamber Electrical Box with Communication Port

Also important to note was comm port settings for the transmitting and receiving devices must match, in addition to the configuration settings any LabVIEW VI's used to remote control the chamber. In other words, NI DAQ comm port settings were configured to match those on the Eurotherm temperature controller.

Similar to remote control method 1, once comm-link was established, a program to read profiles files and administer transmission of those values was required. Therefore, a LabVIEW VI which supported profile input was created and responsible for timing, data interpretation,

transmission, and recording. Desired temperature profiles were interpreted by the program and relayed to the temperature controller at specified intervals. Figure G-16 highlights the front panel of this program and its features.

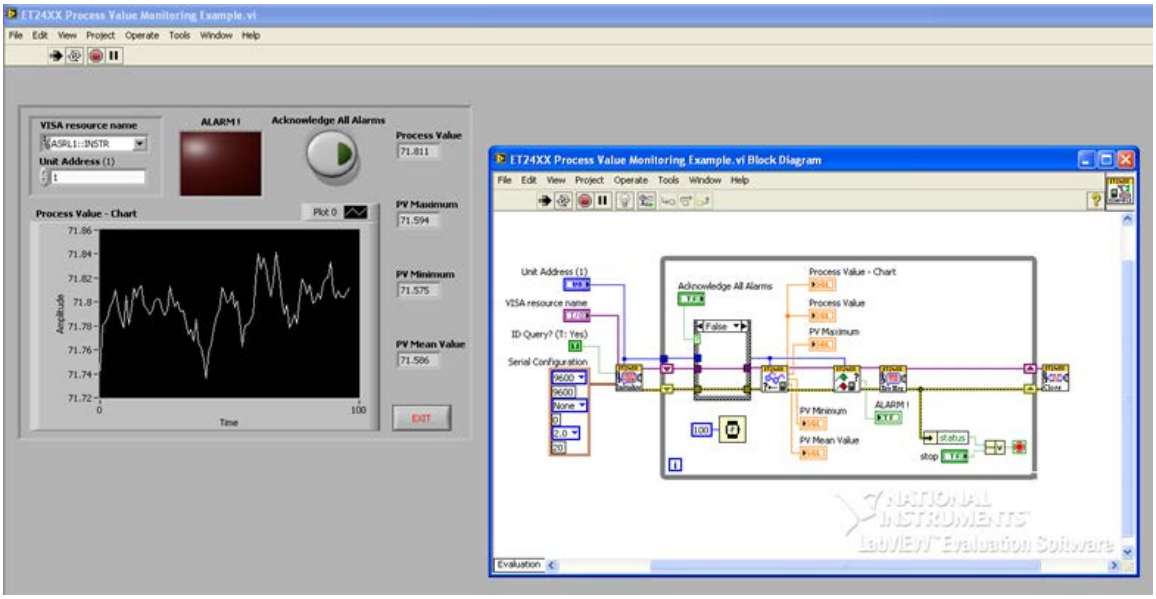

Figure G-16 LabVIEW VI for Temperature Control

Addition of Cooling Capability

The environmental chamber utilized extremely cold nitrogen vapor in order to cool the interior space. These gasses originated from a cryogenic cylinder which was capable of storing LN_2 for several weeks. Hardware used for this application is shown in Figure G-17. A pressure regulator on the vapor stem regulated cryogenic cylinder pressure below 22 psi. The chamber was also outfitted with an Alcon flow control valve to control the flow of nitrogen vapor into the chamber. A screenshot of the valve is shown in Figure G-18. This valve was designed for low pressure cryogenic applications.

Figure G-17 Environmental Chamber /Cart and Cryogenic Cylinder/Cart

Figure G-18 Alcon Flow Control Valve

Once a cryogenic cylinder was procured some additional plumbing was required to connect the cylinder and environmental chamber. A cryogenic hose and appropriate fittings were required. Figure G-19 shows plumbing fittings on the chamber and cylinder. The cryogenic cylinder required a male 3/8 inch NPT fitting to couple with the female fitting already on the cylinder liquid stem. The chamber fitting required a female ½ inch 45° flare SAE fitting to couple with the male fitting already on the chamber. It was decided ordering a LN_2 hose (metal braided and specified for low temp and high pressure) with these fitting already attached would be the most cost effective and convenient.

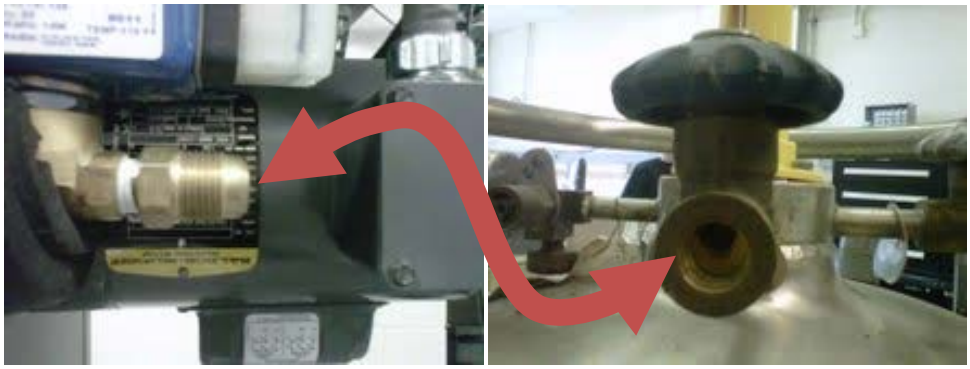

Figure G-19 Environmental Chamber and Cryogenic Liquid Cylinder Fittings

Figure G-20 shows the hose that was purchased from Parker Hannifin and its installation. The hose is 3 foot in length, perfectly sized for the distance between the chamber and cylinder. Not oversizing the hose was advantageous for cooling performance because the pressure drop from the cylinder to the chamber was minimized, providing the greatest flow into the chamber within the limit of the flow control valve.

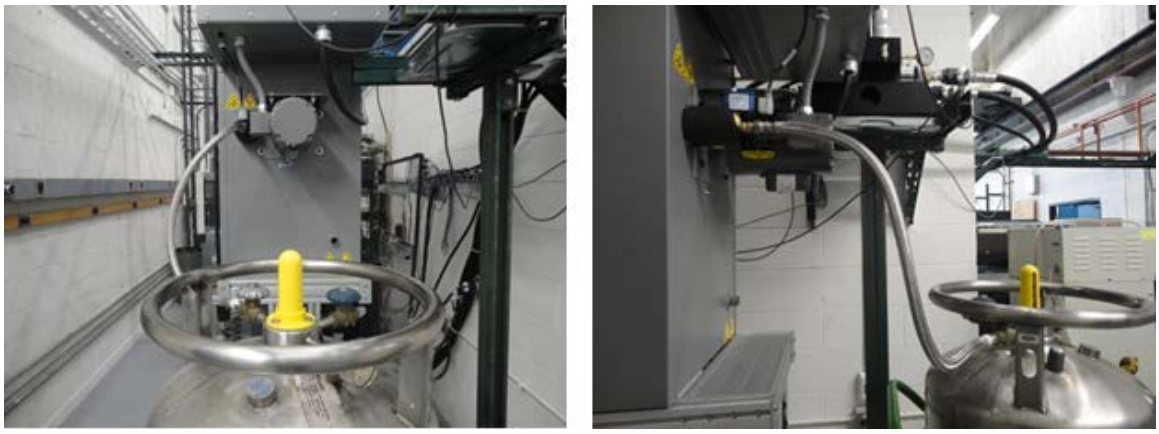

Figure G-20 Environmental Chamber and Cryogenic Liquid Cylinder Connected via LN_2 hose

Environmental Chamber Characterization and Measured Performance

Two plots were created to resemble environmental chamber specifications for air temperature performance. Figure G-21 was created using a linear regression, ambient temperature, min/max temperature, and time required to achieve min/max temperature.

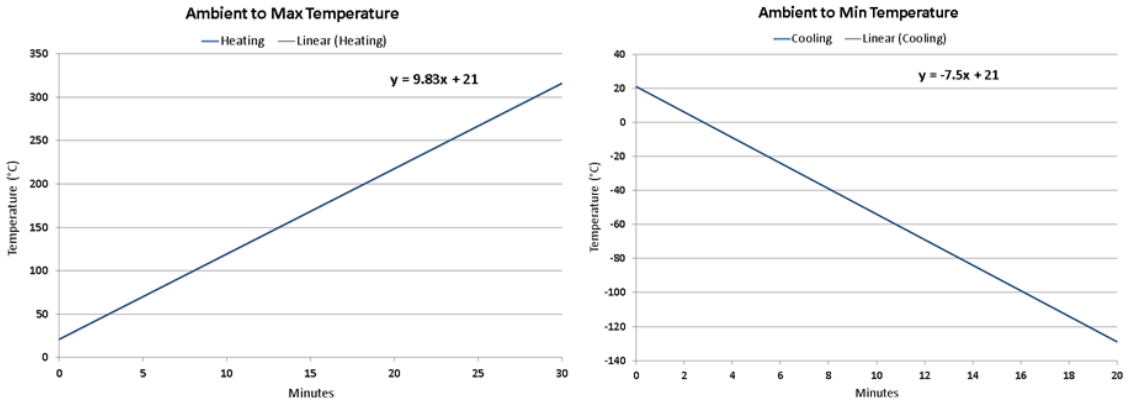

Figure G-21 Environmental Chamber Nominal Heating and Cooling Performance

A matrix of thermal profiles was created in order to evaluate the environmental chamber's response to varying types of inputs. Each input was constructed with a specific purpose and yielded valuable information about chamber capability. The environmental chamber outfitted with a PID temperature controller was considered a dynamical system and evaluated as such. Therefore, important parameters such as stability, rate, and overshoot were considered when evaluating chamber performance. Thermal profiles within the test matrix were designed to highlight each of these parameters. The goal of each test was to evaluate system performance relative to an input that resembled portions of actual environmental flight conditions. Initial tests were done without any test specimens/articles within the chamber or modifications—"Original State". With that, there were no disturbances imposed on the system and system performance was established. After that, modifications to the U-plugs were made to accept the hydraulic press-EMA couplings. Additionally the EMA and its thermal mass were placed within the chamber to determine its effect on chamber performance. Modified U-plugs and the presence the EMA within the chamber constitute a "Modified State."

Step Input Original State

The response from a step input was used to determine the system's maximum rate of heating and cooling. This style of input also highlighted overshoot and settling time associated with the factory control and tuning.

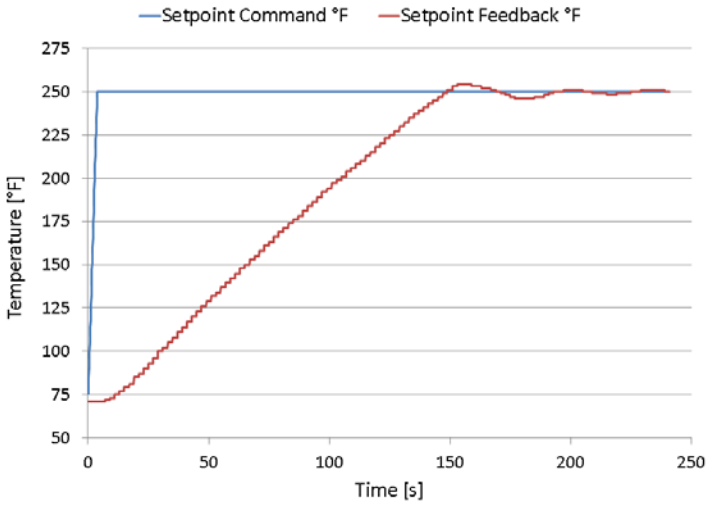

Figure G-22 Environmental Chamber Heating Performance above Room Temperature

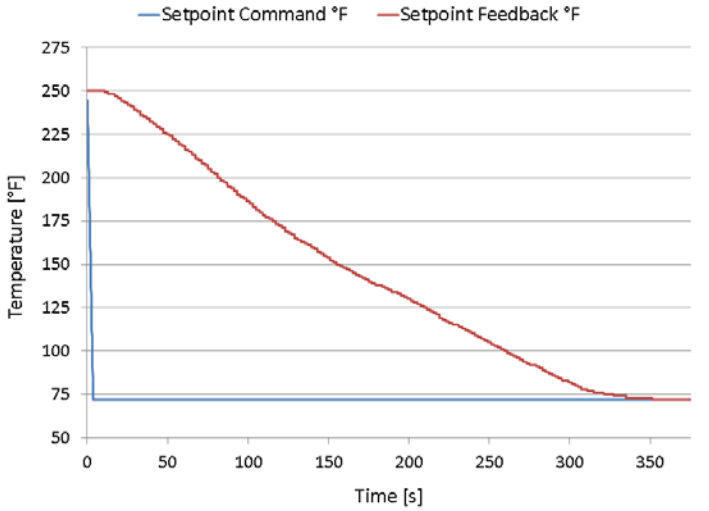

Figure G-23 Environmental Chamber Cooling Performance above Room Temperature

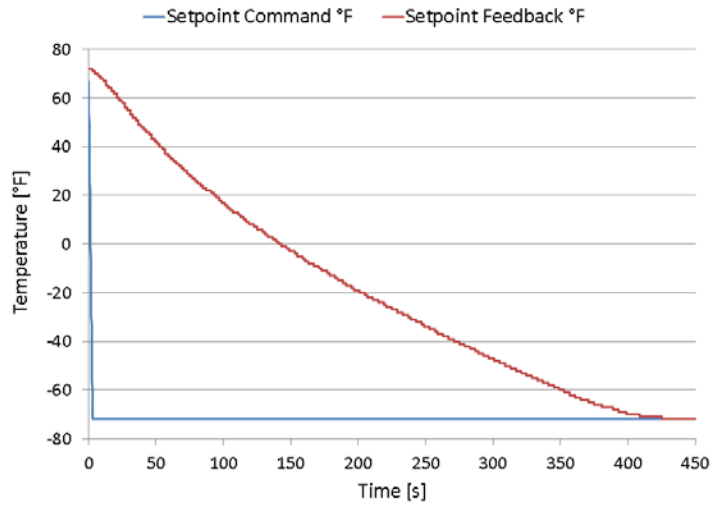

Figure G-24 Environmental Chamber Cooling Performance below Room Temperature

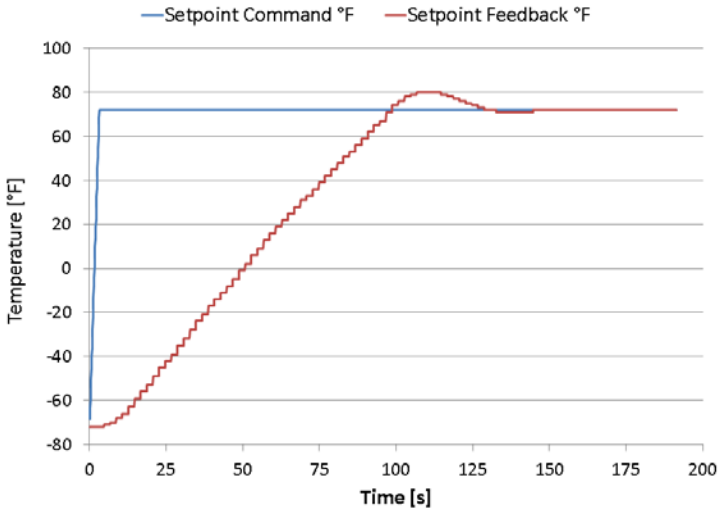

Figure G-25 Environmental Chamber Heating Performance below Room Temperature

Step Input Modified State

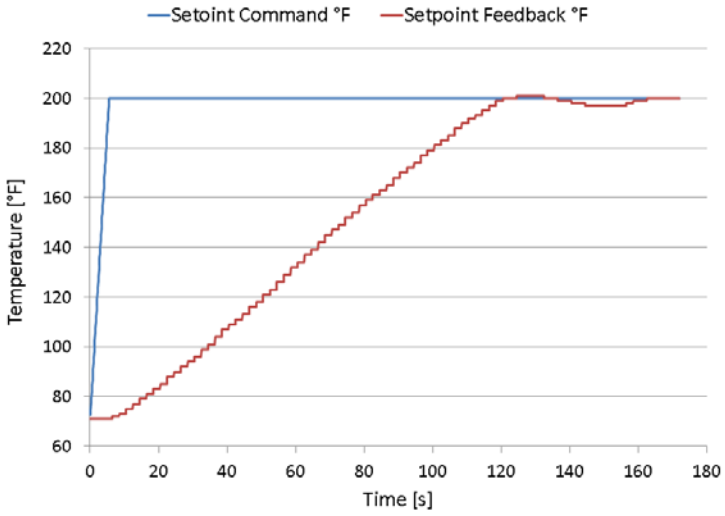

Figure G-26 Environmental Chamber Heating Performance above Room Temperature

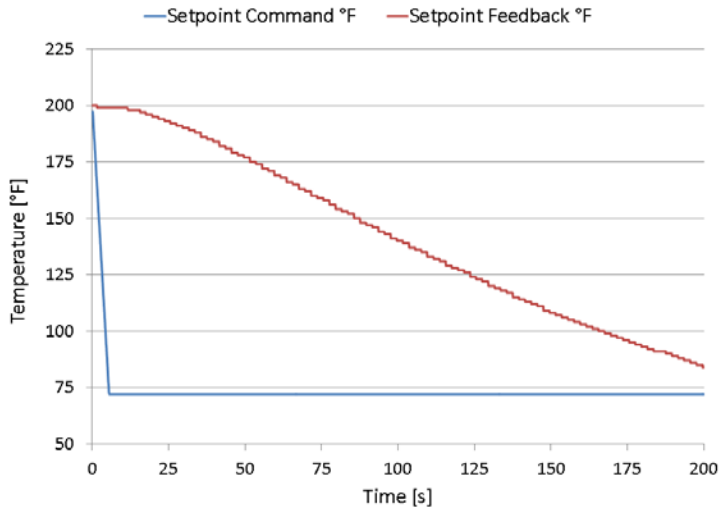

Figure G-27 Environmental Chamber Cooling Performance above Room Temperature

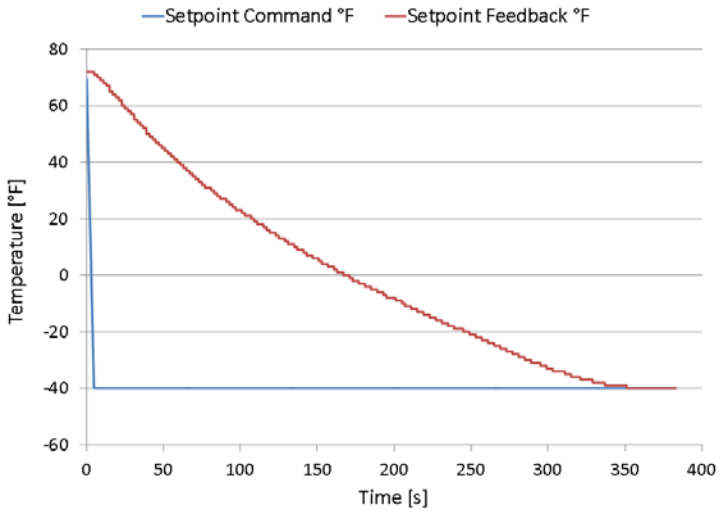

Figure G-28 Environmental Chamber Cooling Performance below Room Temperature

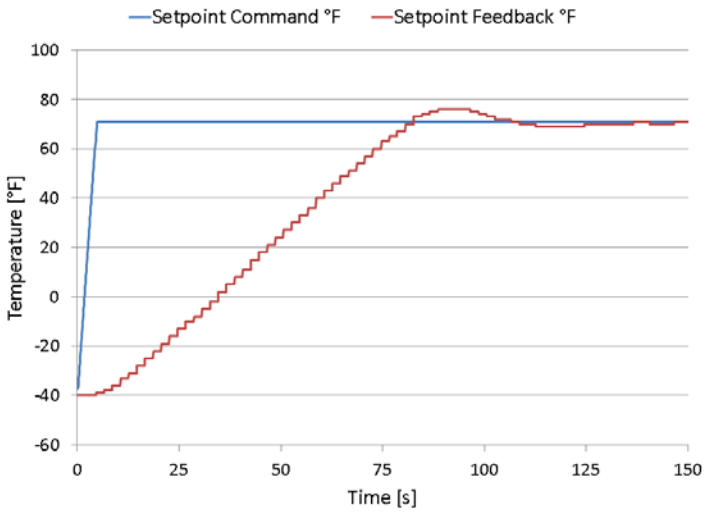

Figure G-29 Environmental Chamber Heating Performance above Room Temperature

The heating and cooling rates regressed from step input responses shown above are tabulated in Table G-1. Original column title means the chamber was tested in factory condition without an EMA inside. Modified column indicates u-plugs had been fabricated with holes to accommodate EMA-Press coupling and the EMA was inside the chamber during test. Based on the performance of the chamber little modification to the control and zero tuning were required. Differences in heating/cooling rates experienced from Original to Modified state were deemed negligible.

Table G-1 Environmental Chamber Heating/Cooling Performance

	Heating & Cooling Rates [°F/s]		
	Original	Modified	% Difference
Heating Above Room Temperature	1.319	1.207	8%
Cooling Down to Room Temperature	0.727	0.685	6%
Cooling Below Room Temperaure	0.332	0.288	13%
Heating Up to Room Temperature	1.678	1.544	8%

Dwell Input

A constant input of 71 °F (21.7 °C) was commanded to the environmental chamber for nearly 3.5 minutes. Over the duration of the dwell period there was no detectable change in chamber temperature indicating a superior ability to maintain constant temperature without disturbance.

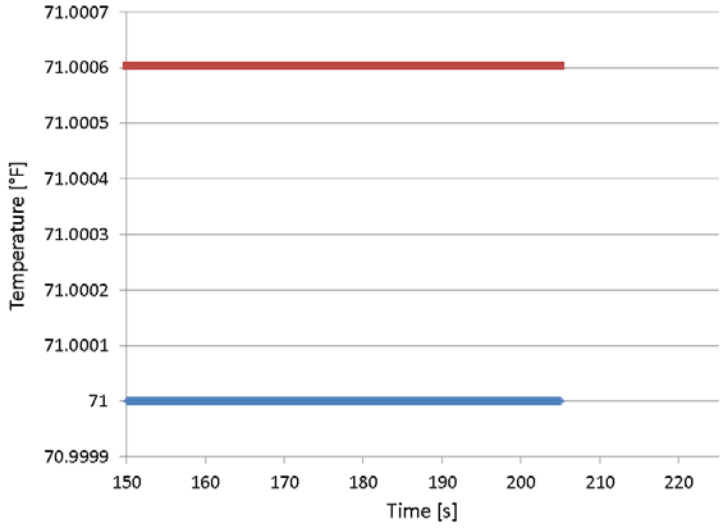

Figure G-30 Environmental Chamber Thermal Stability Performance at Room Temperature

Mission Profile Input

Modern aircraft altitude, ambient temperature, and bay temperature values provided a benchmark to compare the environmental chamber's average heating and cooling rates derived above. An overview of these values is shown in Figure G-31. Based on these values the environmental chamber heating capability was more than adequate for desired thermal profiles. The chamber's cooling capability was much less than its heating capability but just great enough to replicate aircraft ambient cooling rates.

Modern Aircraft on 1% Hot or Cold Day

- Altitude
  - [1]Range: 0 to 12,000 m
  - [1]Rate of Climb: 200 m/s
- Ambient Temperature
  - [2]Range: -73°C to 49°C
  - Adiabatic Lapse Rate: -6.5°C/km
  - Rate of Change = 1.3 °C/s
    - (0.2 km/s * 6.5°C/km)
- Bay Temeprature
  - Range: -54°C to 71°C
  - [3]Rate of Change: 1.0 °C /s

MTS 651 Capability

- Ambient Temperature
  - Range: -130°C to 320°C
  - Avg. Rate of Change:
    - Heating: 2.5°C /s
    - Cooling: 0.9°C /s

[1] Navarro (1997)
[2] MIL-HDBK 310 (1997)
[3] MIL-STD 2218 (1992)

Figure G-31 Flight Envelope compared with MTS 651 Capability

In order to test the environmental chamber's controllability a dynamic thermal profile was artificially created and used as a baseline. Figure G-31 demonstrates the trend used to determine heating and cooling rate. The most severe heating and cooling portions were extracted and used to generate dynamic thermal profiles. These portions are denoted by the red dotted lines in Figure G-32.

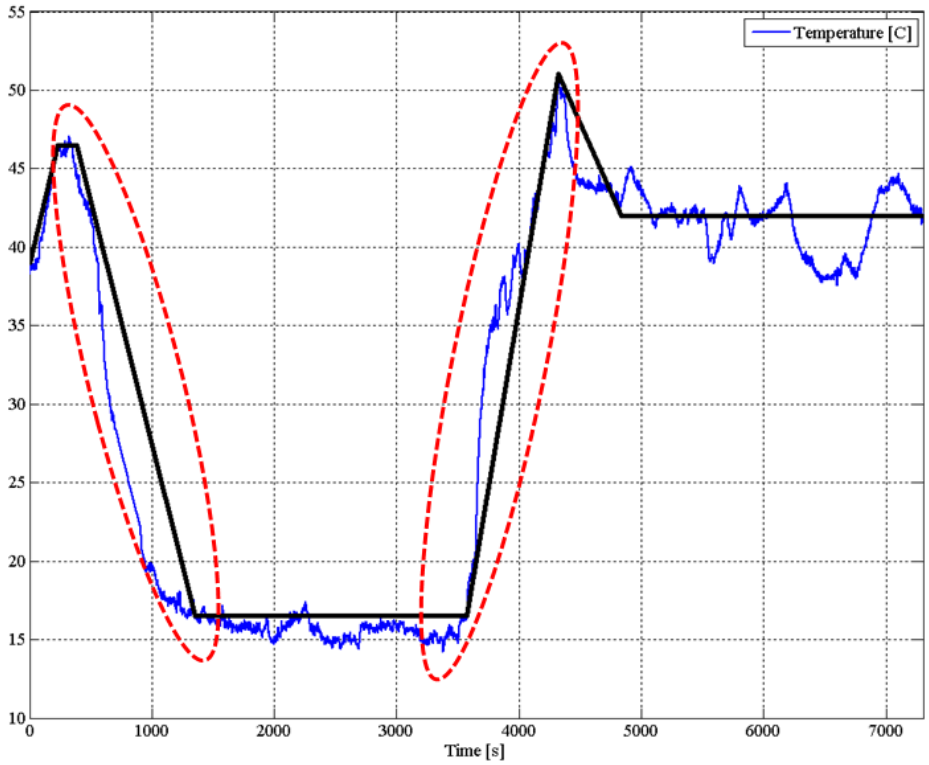

Figure G-32 Environmental Chamber Thermal Stability Performance at Room Temperature

The cooling portion which most likely corresponds to a climb in altitude was tested followed by the heating portion. Figures G-33 and G-34 demonstrate how well the chamber was able to

follow temperature setpoint as a function of time. In both scenarios the error was less than 4 °F for majority of the profile.

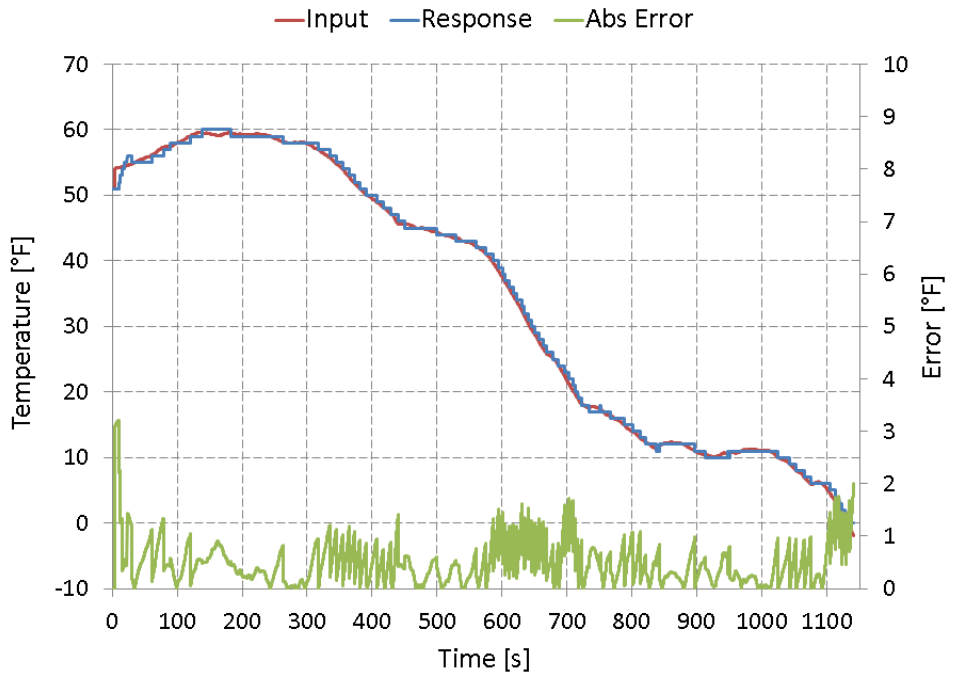

Figure G-33 Environmental Chamber Dynamic Cooling Performance

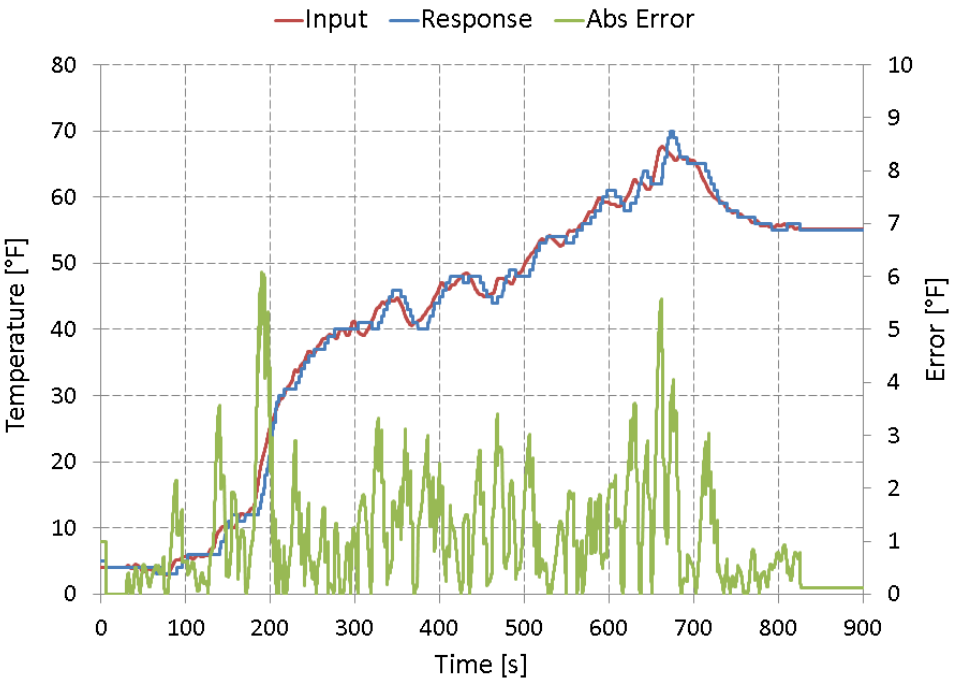

Figure G-34 Environmental Chamber Dynamic Heating Performance

Liquid Nitrogen Safety

Liquid Nitrogen is an inert, colorless, odorless, non-corrosive, non-flammable and extremely cold. Nitrogen makes up a major portion of the atmosphere and does not support combustion or life. Containers rated for the pressure and temperature associated with LN_2 storage must be used. Liquid nitrogen is a cryogenic liquid, meaning it is a liquefied gas and has a normal boiling point less than -238 °F (-150°C). In order to maintain this state special containers are needed. These containers typically include the following components: cryogenic storage tank, one or more vaporizers, and a pressure and temperature control system. A typical container is shown in Figure G-35. The cryogenic storage tank acts in principle like a vacuum bottle while the vaporizer converts liquid nitrogen to its gaseous state. Cryogenic cylinders are outfitted with a blast cap and a pressure relief valve. The pressure relief valve expels any additional vapor until the pressure within the container equals the valve setting. This setting can vary from 22 psi for low pressure applications to 230 psi for high pressure applications. The blast cap is fail safe mechanism such that if a pressure relief valve malfunctioned it would burst at a rated pressure before the cylinder would explode.

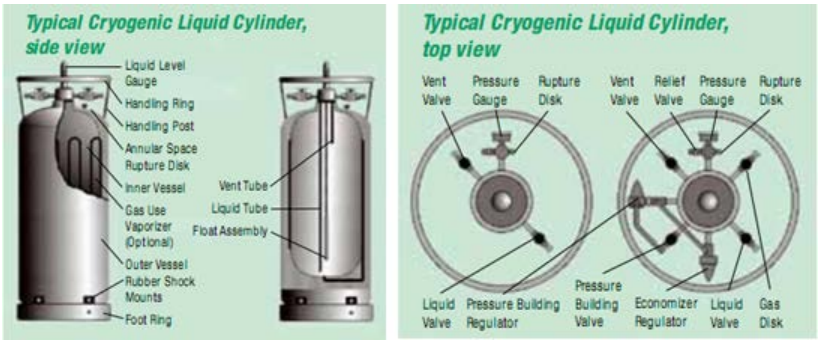

Figure G-35 Cryogenic Liquid Cylinder (Source: Air Products Safetygram #7 Liquid Nitrogen.pdf)

Nitrogen can be an asphyxiant by displacing oxygen in the air to levels below which support life. Personnel should not enter areas where oxygen levels are below 19.5% of total air volume. For high bay areas like rooms 15 and 13 in Building 18 this should not be a concern. These rooms have makeup air which pulls in new air every so often, ensuring adequate healthy breathing conditions. Additionally, the amount of nitrogen vapor expelled during thermal chamber cooling processes is insignificant when compared with the total volume of oxygen in the high bay areas.

Cryogenic cylinders are heavy and require a cart or forklift for transportation. Always push containers in an athletic position rather than pull to avoid being crushed by the cylinder. Avoid contact between unprotected parts of the body and the cylinder. Liquid nitrogen can also cause extensive tissue damage or burns from direct contact. Personal protective equipment must be worn when handling LN_2 or extremely cold nitrogen vapor. Recommended PPE includes the following: face shield over safety glasses, thermal insulated or leather gloves, long sleeve shirt and pants, and closed toed shoes. A thermally insulated vest or apron is also recommended. Fire precautions in the presence of LN_2 are not necessary because nitrogen is non-flammable. However, special attention is required to prevent streams of water from freezing on the pressure relief valve, which could cause container failure.

Note: at least two trained personnel should be present when transferring liquid nitrogen from a storage tank to a cryogenic cylinder. Appropriate PPE must be worn. Finally, adequate ventilation is required when using cryo-cylinders or dewars indoors.

APPENDIX H

LN_2

MTS 651 environmental chamber nominal usage rates of liquid nitrogen are as follows: 0.0234 L/s for ramp cooling and 0.00234 L/s for holding a setpoint. Therefore, dynamic thermal profiles will use much more LN_2 throughout the duration of a test, with ramps using ten times more LN_2. For example, in order to cool from 22°H to -29 °H, which the chamber could complete in approximately 300 s, would consume 7 liters of LN_2. A simplified representation of aircraft ambient air over the duration of a mission was developed below and is made up of a 100 s of climb to 3 km, 800 seconds of steady and level flight at 3 km, and a descent for 100 s from 3 km to 0 km.

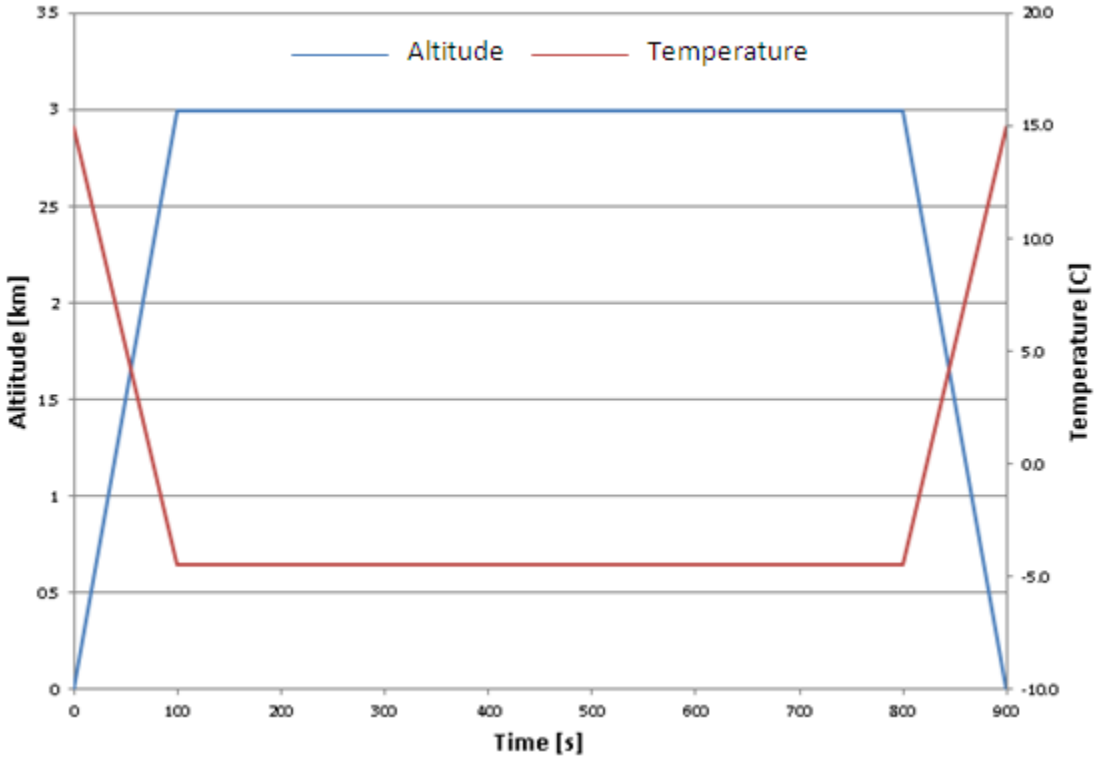

Figure H-1 Simple Altitude and Temperature Profile for LN_2 Consumption Estimation

This type of profile requires ramp cooling for the first 100 seconds and hold cooling for 800 seconds. So, this style of test would consume approximately 100 (0.0234) + 800 (0.00234) or a little more than 4 liters. Based on these calculations a 50-100 liter cryogenic cylinder would be sufficient for an hour long test made up of several ramp and dwell periods.

APPENDIX I

CALIBRATIONS

Omega Type T Thermocouple Calibration

24 Thermocouples were calibrated using a Hart Scientific 7320 Calibration Bath and Hart Scientific 1502A resistive temperature detector (RTD). The bath offered a calibration range of -20°C to 150°C. More specific data on the capability and characteristics of the bath can be found in "7320 Calibration Bath User's Guide" found at http://us.flukecal.com.

The calibration bath utilized Dow Corning 200.10 silicon oil for greater calibration range and stability than water. Specs for Dow Corning 200.10 can be found in the Bath User Guide. Lower and upper temperature limits for the oil were -35°C and 165°C, respectively. The calibration process was limited by the Bath operating range (-20°C to 150°C). Appropriate oil level was maintained to mitigate overflow due to thermal expansion throughout the calibration process. The following relationship was used to determine desired fill depth for the bath:

$$D_S = \frac{D_E}{[K(T_E - T_s) + 1]}$$

Where:

K=expansion coefficient

T_E=ending temperature

T_S=starting temperature

D_E=ending depth

D_S=starting depth

A LabVIEW control program was constructed to interface with the data acquisition system, calibration bath, and RTD. The program incremented temperature by 5°C from -20°C to 150°C (determined by 200.10 oil operating range) while providing RTD and thermocouple readings. All 24 type T thermocouple probes were placed in the bath simultaneously. Figure I-1 shows the setup and the quantity of thermocouples.

Figure I-1 Calibration Setup (Left) Close Up of Thermocouples in Bath (Right)

At each temperature setting, the RTD was allowed to reach steady state. Steady State was determined by monitoring the standard deviation of the previous 100 RTD values, sampled every 5 seconds, and comparing to a 0.005 ºC threshold. Once this condition was met, one RTD and thermocouple value was sampled every second for 15 seconds. An average RTD and thermocouple value was calculated from the 15 samples and recorded to a file. This process was done simultaneously for every thermocouple which resulted in an excel data sheet made up of 33 columns of data. The first column contains RTD values while columns 2-33 contain the 32 thermocouple values. Figure I-2 is a screenshot of the resulting data in an excel file.

	A	B	C	D	E	F	G	H	I	J	K	L	M	N	O	P	Q	R	S
1	Time	RTD	TC0	TC1	TC2	TC3	TC4	TC5	TC6	TC7	TC8	TC9	TC10	TC11	TC12	TC13	TC14	TC15	TC16
2	[s]	[°C]	[°F]	[°F]	[°F]	[°F]	[°F]	[°F]	[°F]	[°F]	[°F]	[°F]	[°F]	[°F]	[°F]	[°F]	[°F]	[°F]	[°F]
3	0	-19.772	-119446	-119447	-119446	-3.56567	-119501	-3.84867	-3.6916	-3.87843	-3.58844	-3.58333	-3.68648	-3.53345	-119445	-3.46702	-3.40058	-3.47072	-3.17507
4	1.588091	-19.771	-119446	-119452	-119446	-3.55336	-119501	-3.83589	-3.70049	-3.86176	-3.58976	-3.56281	-3.6785	-3.50507	-119445	-3.45676	-3.39703	-3.43373	-3.18057
5	3.177182	-19.771	-119449	-119451	-119449	-3.557	-119503	-3.83209	-3.69963	-3.84416	-3.58845	-3.57033	-3.66651	-3.51818	-119448	-3.4341	-3.3821	-3.42901	-3.16116
6	4.767273	-19.771	-119454	-119449	-119454	-3.54022	-119509	-3.84273	-3.6801	-3.85949	-3.549	-3.56201	-3.64007	-3.53476	-119453	-3.46647	-3.35307	-3.44039	-3.1677
7	6.358364	-19.769	-119451	-119448	-119451	-3.54565	-119505	-3.83282	-3.70737	-3.84307	-3.5748	-3.56039	-3.66168	-3.53099	-119449	-3.44691	-3.37712	-3.44354	-3.15819
8	7.946455	-19.769	-119447	-119453	-119447	-3.53604	-119502	-3.81344	-3.69573	-3.86117	-3.58773	-3.54592	-3.67833	-3.51401	-119446	-3.43782	-3.39331	-3.43001	-3.18365
9	9.536546	-19.769	-119452	-119450	-119452	-3.54885	-119507	-3.83183	-3.66203	-3.85396	-3.56089	-3.56461	-3.64127	-3.53007	-119451	-3.44459	-3.35887	-3.44201	-3.15404
10	11.13164	-19.768	-119451	-119449	-119451	-3.56092	-119506	-3.84113	-3.67728	-3.85341	-3.55819	-3.56516	-3.65158	-3.5386	-119450	-3.45312	-3.36952	-3.43362	-3.16945
11	12.72273	-19.767	-119450	-119453	-119450	-3.53969	-119504	-3.82314	-3.69461	-3.82241	-3.57607	-3.54216	-3.68061	-3.51469	-119449	-3.4413	-3.39589	-3.42794	-3.172
12	14.31382	-19.767	-119451	-119454	-119451	-3.51644	-119505	-3.79802	-3.6806	-3.83257	-3.56628	-3.55234	-3.65595	-3.51032	-119449	-3.43599	-3.38254	-3.41598	-3.14457
13	15.90091	-19.767	-119452	-119451	-119452	-3.54106	-119507	-3.83706	-3.67434	-3.85837	-3.55588	-3.55542	-3.64276	-3.51591	-119451	-3.44809	-3.3767	-3.42175	-3.15786
14	17.494	-19.766	-119448	-119452	-119448	-3.54496	-119503	-3.81354	-3.69567	-3.83602	-3.56007	-3.55171	-3.65671	-3.50556	-119447	-3.44053	-3.37888	-3.41465	-3.16947
15	19.08009	-19.766	-119449	-119453	-119449	-3.55116	-119503	-3.82486	-3.68344	-3.84749	-3.59034	-3.54388	-3.6684	-3.51608	-119447	-3.44176	-3.37578	-3.40736	-3.16769

Figure I-2 Excel File of Recorded Data

Once the entire range of predetermined bath temperature set points was completed, resulting data was used to determine a correction factor for each thermocouple. A scatter plot of RTD values vs. Thermocouple values was created and a second order polynomial fit applied for each thermocouple. The resulting fit became our equation to calculate corrected thermocouple

values evaluated at each thermocouple value. Figure I-3 is a screenshot of a PowerPoint slide demonstrating the methodology applied to generate a calibration curve and determine uncertainty.

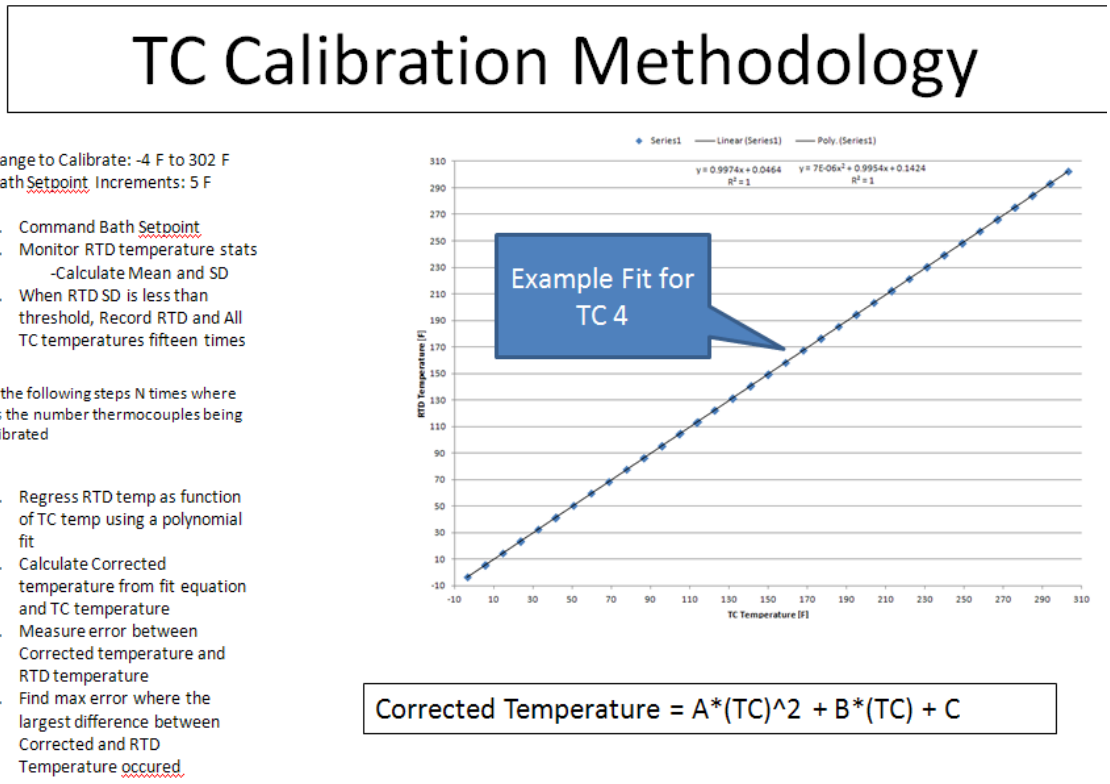

Figure I-3 EMA Pres 160 (2013-04-02) slide

RTD uncertainty reported by Air Force Standards Laboratory Certificate of Calibration sheet was ±0.033°C. The Certification Sheet accompanies the bath everywhere it goes.

The maximum standard deviation of the 15 RTD readings was the 0.005°C threshold. Maximum deviation of the corrected thermocouple value from the RTD value was calculated for each thermocouple in step 7 of Figure I-3 and the RTD uncertainty is reported in Figure I-4. From these values an overall uncertainty was established and used to describe the uncertainty of each thermocouple. The overall uncertainties of the thermocouples were estimated by adding the error of the RTD, bath threshold standard deviation, and maximum error of corrected thermocouple value from experimental RTD average. The largest error for the 24 thermocouples was 0.243°F (0.135 °C) as shown in Figure I-4.

	Coefficient 1	Coefficient 2	Coefficient 3	Maximum Error [F]
TC3	6.80E-06	0.99538	0.14236	0.22284
TC5	2.26E-06	0.99456	0.40851	0.21178
TC6	2.75E-06	0.99467	0.26293	0.205
TC7	2.61E-06	0.99447	0.42627	0.20563
TC8	2.33E-06	0.99468	0.15294	0.21064
TC9	2.40E-06	0.99491	0.14962	0.20696
TC10	4.55E-06	0.99504	0.25218	0.21803
TC11	1.07E-05	0.99564	0.14499	0.24312
TC13	-4.38E-07	0.99957	0.05527	0.21045
TC14	-5.19E-07	0.99976	-0.021158	0.21436
TC15	-6.98E-07	0.99972	0.035479	0.20788
TC16	-1.02E-06	0.99999	-0.23231	0.20713
TC17	-9.46E-07	0.99993	-0.17097	0.21634
TC18	-8.00E-07	0.99993	-0.14681	0.21621
TC19	-7.35E-07	0.99979	-0.13985	0.21525
TC20	-7.66E-07	0.99979	-0.083829	0.21791
TC21	-7.08E-07	0.99982	-0.038729	0.2196
TC22	-5.67E-07	0.99978	-0.095909	0.21776
TC23	-7.85E-07	0.99966	0.021822	0.21477
TC24	-8.66E-07	0.99983	-0.076882	0.21836
TC27	-3.23E-06	1.0034	-0.13909	0.21075
TC28	-3.22E-06	1.0034	-0.42883	0.22144
TC29	-3.59E-06	1.0037	-0.38574	0.21113
TC30	-2.69E-06	1.0029	-0.28064	0.21927
			Max	0.24312

Figure I-4 Tabulated Error for each Thermocouple

Overall uncertainty:

RTD error: ± 0.0297 °F (± 0.0165 °C)

Standard Deviation Threshold: ± 0.0045 °F (± 0.002 °C)

Max Corrected Thermocouple Deviation: ± 0.243 °F (± 0.135 °C)

Total Uncertainty:

± 0.0297 °F ± 0.0045 °F ± 0.243 °F = ± 0.277 °F (± 0.154 °C)

Range: -20 °C to 150 °C

Thermocouples 0, 1, 2 are in the motor and require a different methodology and thermocouples 4, 12, 25, 26 did not make it through the calibration. Therefore, data collected for theses thermocouples was void and not used to determine thermocouple uncertainty.

Motor Embedded Thermocouple Correction Process First Attempt:

The assumption for this methodology is that if the air around the motor is constant for long enough the motor should reach thermal equilibrium and all three motor TCs should read the same temperature.

With this in mind, the EMA was placed in the Environmental Chamber and sealed from the ambient. The temperature control was used to hold a steady temperature just above room temperature. The setpoint was 81.0 ^{0}F (27.2 ^{0}C). The cooling element was disabled in order to prevent overheating of the solenoid use to provide cooling. Unfortunately, during this process the chamber was unable to hold the setpoint and the chamber air gently rose to 94.0 ^{0}F (34.4 ^{0}C) where it settled over the course of several hours. Figure I-5 shows the time history of motor thermocouple data, a little over 17 hours of commanded constant temperature.

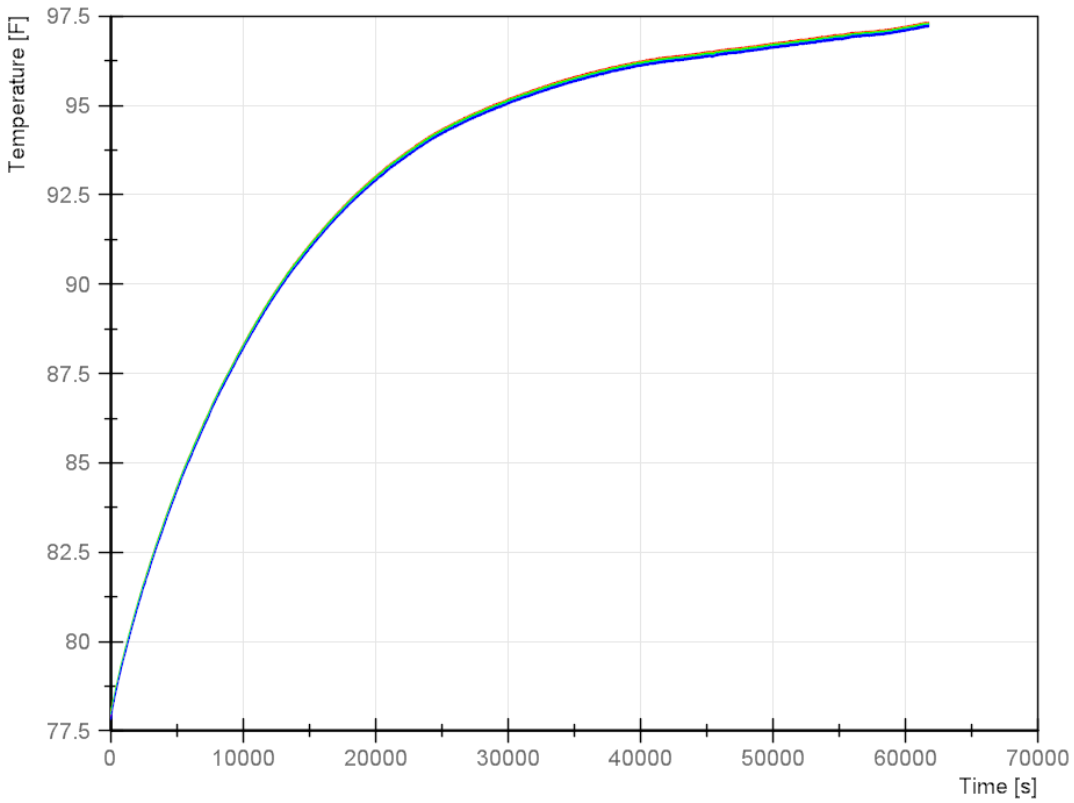

Figure I-5 Time history of Motor Temperature

Since we do not know which TC is the most correct without the use of a calibrated RTD or some other calibrated source we averaged the TC readings to create a reference. Next we calculated the average difference between each TC reading and this reference. The resulting difference is the bias or offset that will be used to correct the TC reading in our test. Figure I-6 shows the portion of time in which the chamber air and motor temperature was most steady, the reference created (purple/pink), and the resulting offsets for each motor thermocouple.

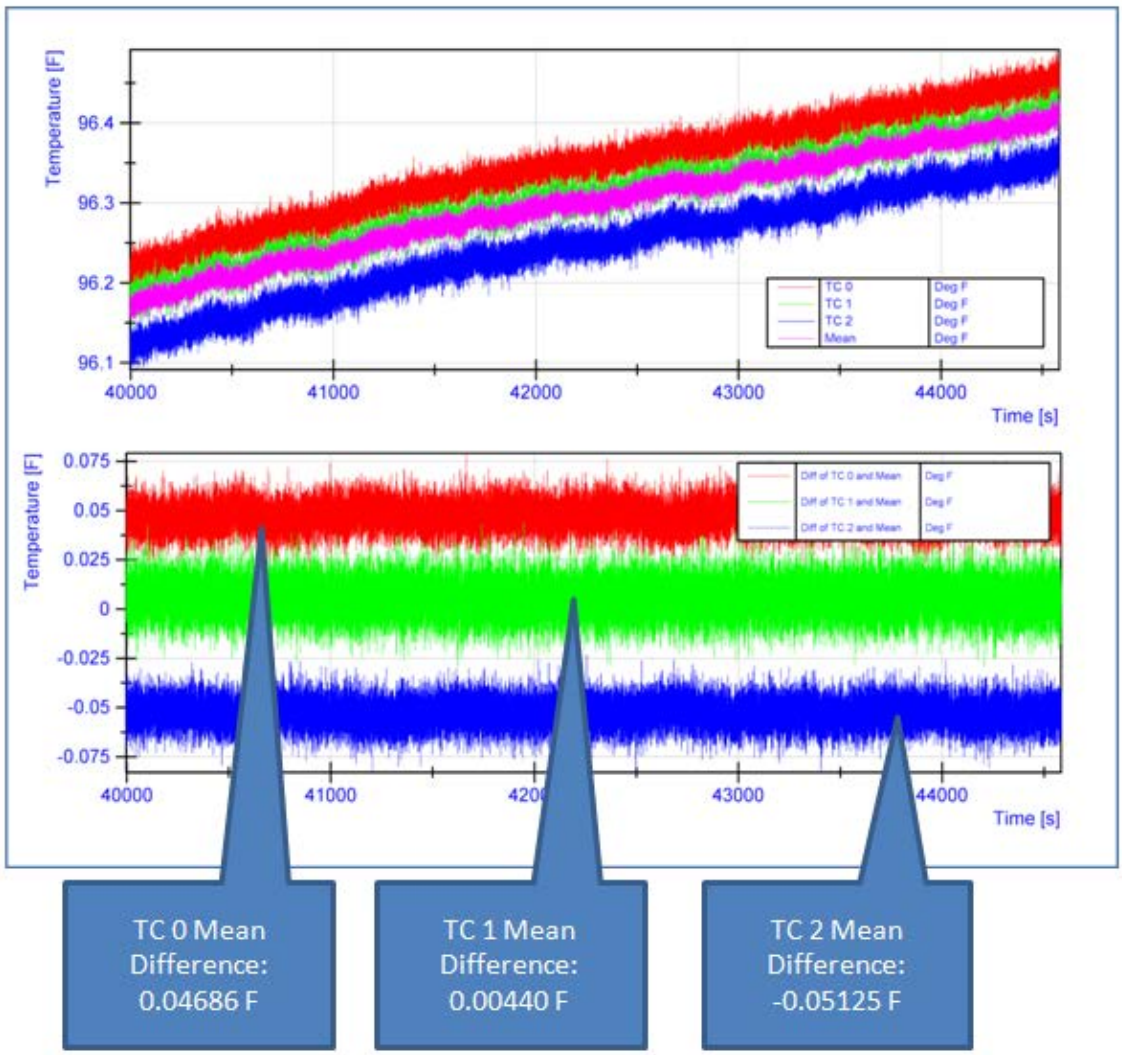

Figure I-6 Most Static Portion of Data Set

Under this procedure the bias error for each thermocouple was:

TC 0: 0.04686 F

TC 1: 0.00440 F

TC2 : -0.05125 F

Correction Process Second Attempt:

The first attempt was flawed in that the air temperature and thus motor temperature never reached true equilibrium. Therefore, temperature gradients may have still been present within the motor, voiding the assumption that all three thermocouples should produce the same temperature. And without knowing the exact location and thus thermal path from each motor thermocouple to the ambient their temperature would remain unknown.

A new approach was used to develop conditions which bring the motor to thermal equilibrium and thus an opportunity to calculate motor thermocouple error. The assumption that if the air around the motor is constant for long enough the motor should reach thermal

equilibrium and all three motor TCs should read the same temperature still holds. However, instead of actively controlling the chamber air, the motor was simply sealed inside the chamber without the chamber powered. This was done over the weekend and several hours of motor thermocouple and chamber air temperature were recorded. Figure I-7 shows the resulting data from this procedure. Chamber air temperature was recorded using one of the 24 thermocouples calibrated in the section above. Therefore the standard which motor thermocouple temperature was compared had an uncertainty of ± 0.277 °F (± 0.154 °C).

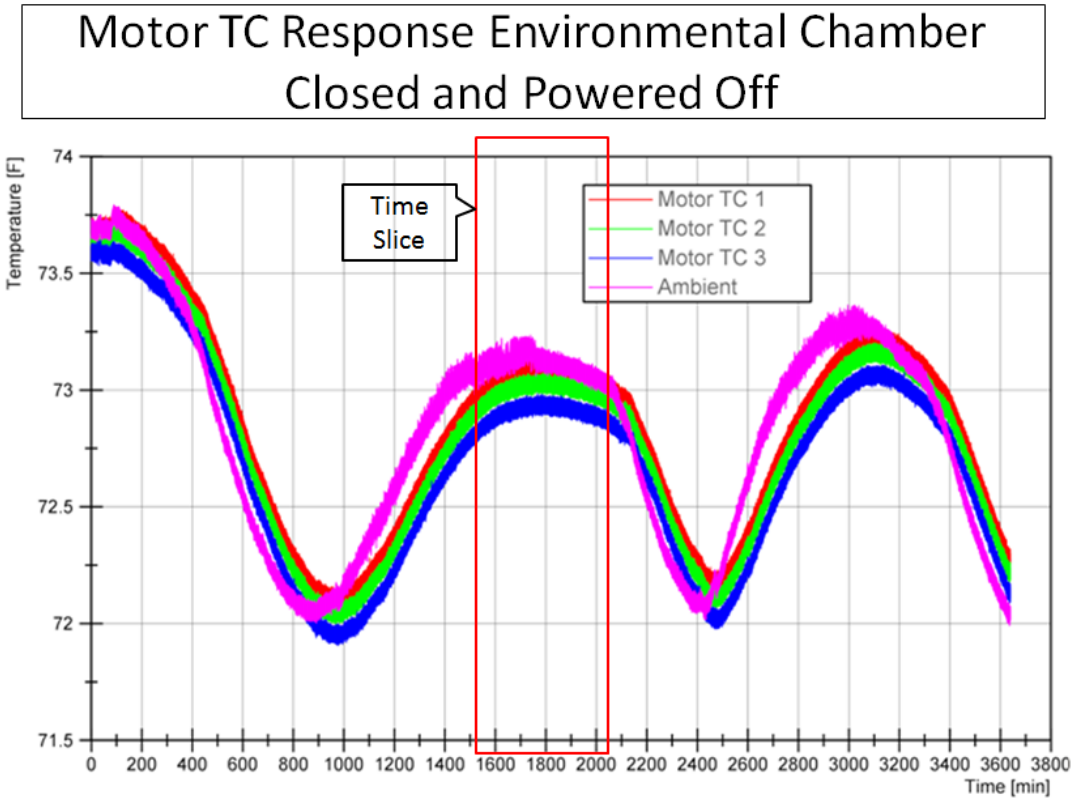

Figure I-7 Chamber Powered Off and Red Box Indicating Static Time Slice for Analysis

Unfortunately, this method resulted in a phase difference between the ambient air temperature and the motor temperature. Thus, comparing motor temperature to ambient temperature would require knowledge of the motor thermocouple lag behind ambient. Therefore, one last attempt was made in the next section to create thermal equilibrium between the motor interior and the air inside the chamber.

Correction Process Third Attempt:

The third and final attempt utilized both the heating and cooling capability of the environmental chamber to hold a constant temperature just above room temperature indefinitely. The result was motor thermocouples slowly approached the ambient value and ceased to change after an hour of maintaining chamber air temperature at approximately 74.5 °F (23.6 °C). Figure I-8 shows the recorded data from this test and how the motor thermocouples reach and maintain a steady state from 10,000 to 12,500 seconds.

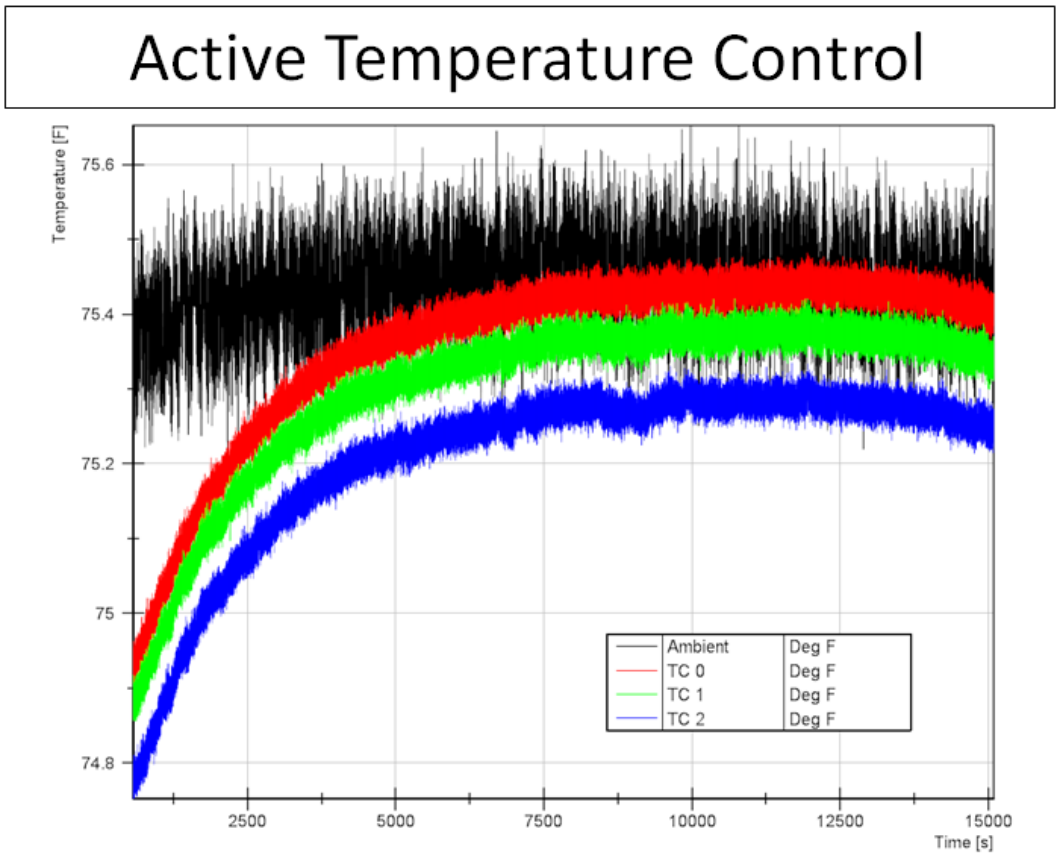

Figure I-8 Chamber used to actively control air temperature

A time slice of data from the steady state portion was used to determine motor thermocouple offset. The mean temperature of each motor thermocouple was compared to the mean of ambient for the time slice. The difference in motor thermocouple readings is considered the bias from the true value and will be used as an offset applied to future motor temperature measurements. The probe used to measure ambient temperature was calibrated in the oil bath calibration outlined above and therefore the correction equation generated form the oil bath calibration was applied. TC 0 was consistently greater than TC 1, and TC 1 greater than TC 2. TC 2 was closest to the ambient temperature and requires the least correction. TC 0 requires the most correction.

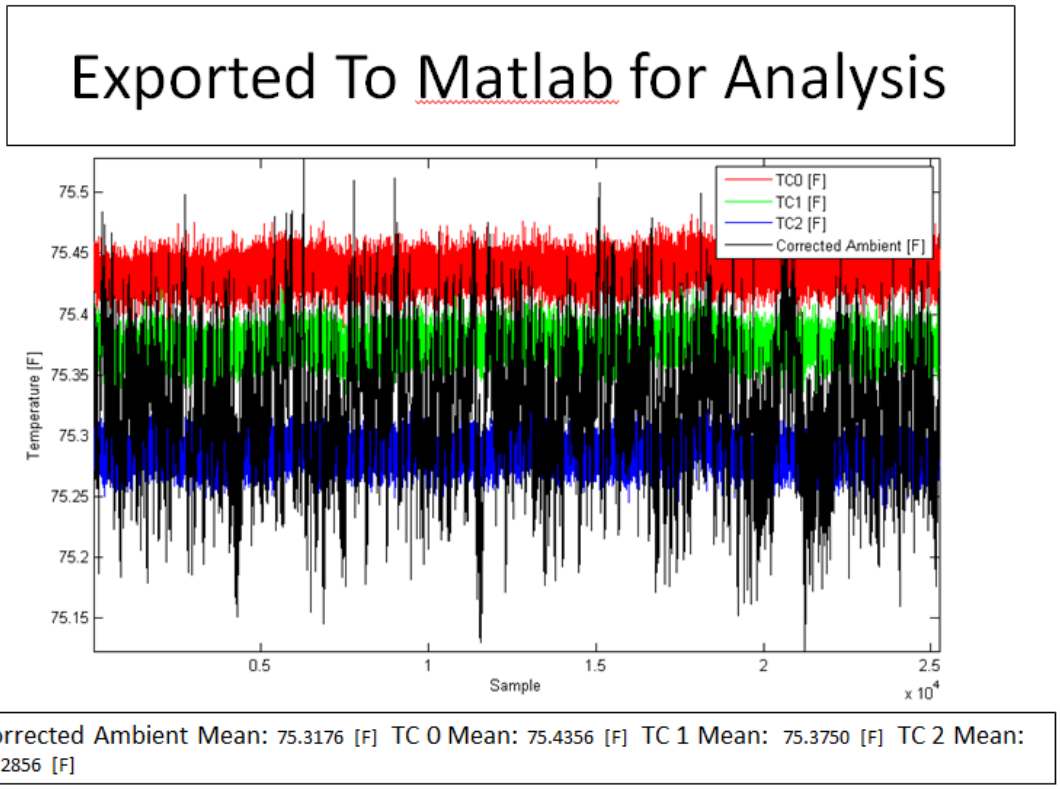

Figure I-9 Time Slice of Actively Controlled Temperature Test

Corrected Ambient indicates a correction equation generated from thermocouple calibration was applied to the ambient thermocouple probe. Next the average over this time slice was taken for each thermocouple and the difference from Ambient was calculated. This difference will be the offset applied to each motor TC when recording data. The uncertainty associated with each of these motor thermocouples is now the max uncertainty reported in the oil calibration above, ± 0.277 °F (± 0.154 °C).

During static time slice:

Average of TC0 = 75.4356 °F (24.1309 °C)
Average of TC1 = 75.3750 °F (24.0972 °C)
Average of TC2 = 75.2856 °F (24.0476 °C)
Average of Ambient Corrected = 75.3176 °F (24.0653 °C)
Difference between TC0 and Ambient Averages = 0.1180 °F (0.0656 °C)
Difference between TC1 Ambient Averages = 0.0574 °F (0.0319 °C)
Difference between TC2 Ambient Averages = -0.0320 °F (-0.0178 °C)

Thus,

TC0 correction: -0.1180 °F (-0.0656 °C)
TC1 correction: -0.0574 °F (-0.0319 °C)
TC2 correction: 0.0320 °F (0.0178 °C)

LEM 55P Current Transducer Calibration

A Hall Effect current transducer is used to measure DC Link current of a PMDC motor drive a part of an Electromechanical Actuation System. In order to quantify Hall Effect current transducer uncertainty a calibration process was undertaken which utilized a DC power supply, resistor load bank, and FLUKE multimeter. These items are highlighted in Figure I-10.

Method:

Configured a power supply capable of 60Vdc and 50A to drive various levels of known current through a resistor load bank while recording transducer output via DAQ card and simultaneously measuring current draw with a FLUKE multimeter. Current was manually incremented by 0.5 A from -10 to 10 A. In order to drive 10 A of current the resistor load bank was configured to provide approximately 6 Ω of resistance. Each resistor was rated for 200 W of power dissipation and the load bank configuration permitted several hundred Watts of heat dissipation. This was necessary because joule heating at maximum current would result in 600 W $[(10A)^2 * 6\Omega]$ of heat generation. Additionally the load bank was outfitted with a fan to increase convective heat transfer from the surface of resistors.

A LabVIEW control and measurement program was created to record transducer output and calculate average values. At each level of fixed current FLUKE Multimeter Output was recorded, 1000 samples of transducer output were recorded, and the average of those 1000 samples was calculated. This process was repeated 5 times at each fixed level of current. The FLUKE multimeter served as our standard and uncertainty associated with this device is reported below. Multimeter measurement uncertainty was accounted for in overall uncertainty calculation of the current transducer.

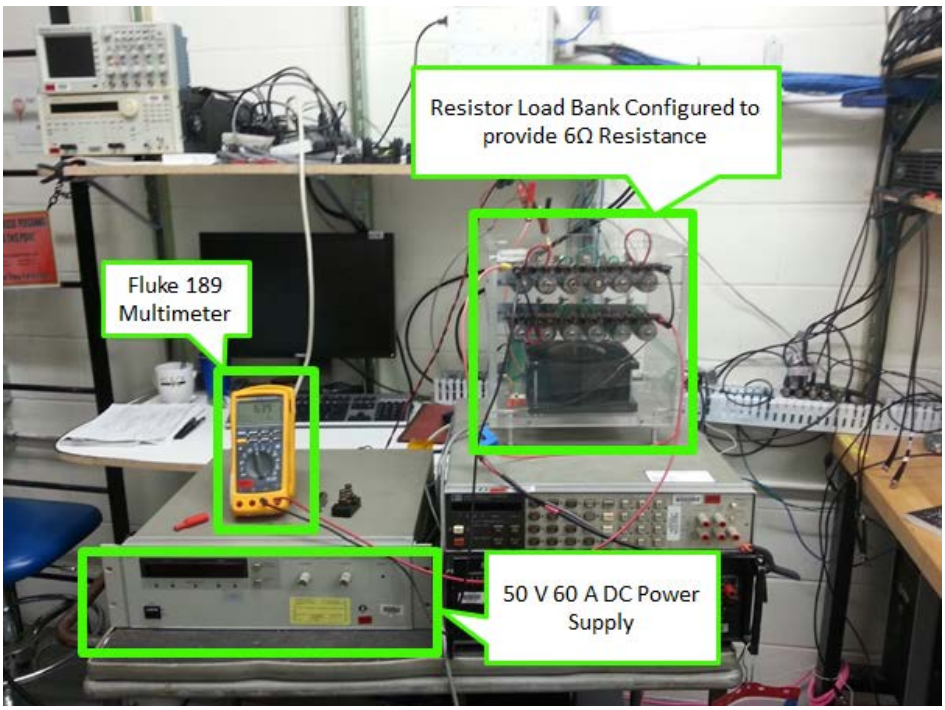

Figure I-10 Current Transducer Calibration Setup

Transducer output was extremely linear; therefore a linear fit was used to generate a calibration curve. The calibration curve relates transducer output in Volts to current draw in Amps. The upper plot in Figure I-11 shows a scatter of FLUKE multitmeter reading (standard) and Hall Effect transducer output. Additionally, this plot highlights the resulting fit equation and its metric for goodness of fit, R^2. This curve was used to evaluate sensed current and the error from the standard. Absolute measurement error for each level of is displayed in the lower plot in Figure I-11. The maximum absolute error from the standard was 0.013 A.

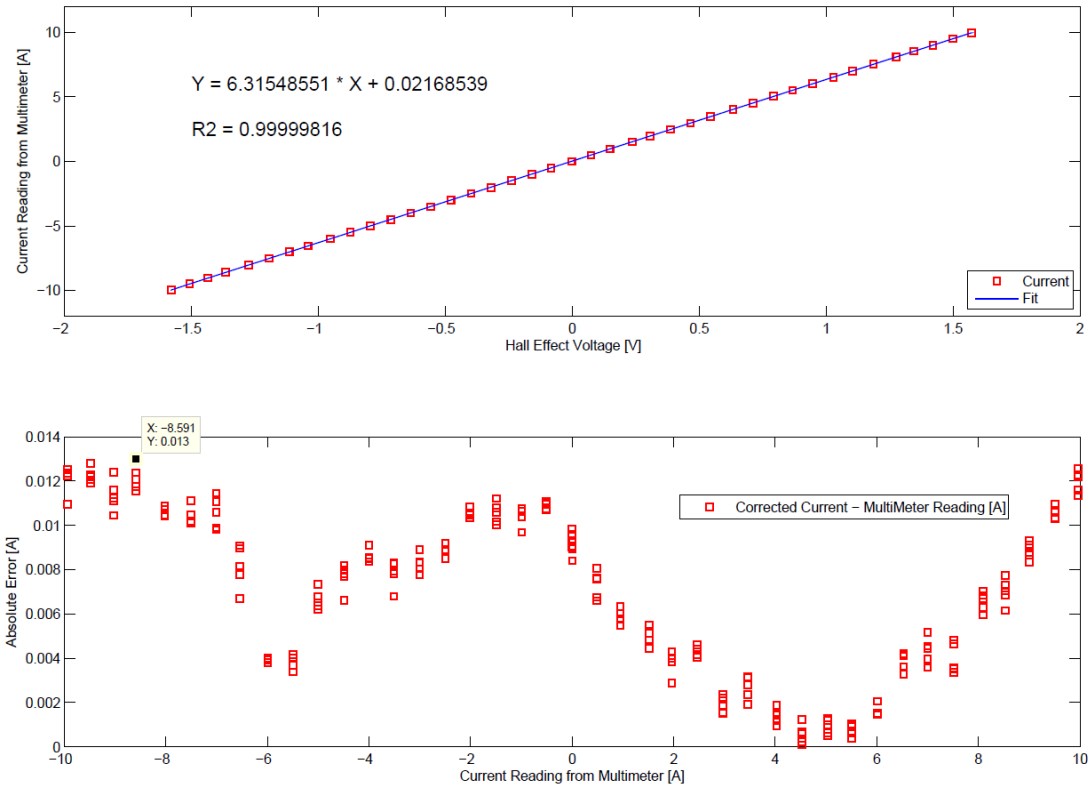

Figure I-11 Hall Effect Sensor Calibration Curve and Absolute Error

Figure I-12 is a screenshot of spreadsheet format used to determine sensor uncertainty. The sheet contains 4 columns of data: Transducer Output, Multimeter Reading, Measurement from Calibration Curve, and Absolute Error of Measurement from Calibration Curve and Multimeter Reading. There are 210 rows of data which corresponds to 5 readings at each interval of fixed current (-10, -9.5, -9…9, 9.5, 10). The maximum absolute error reported in the spreadsheet matched that of the lower plot in Figure I-12, 0.013 A.

Transducer Output [V]	MultiMeter Measurement [A] (standard)	Measured Amperage from Linear Fit Calibration Curve [A]	Absolute Measurement Error [A]
-0.001335	0.0043	0.013268808	0.008968808
-0.001422	0.0043	0.012719359	0.008419359
-0.001318	0.0043	0.013376171	0.009076171
-0.001286	0.0043	0.013578267	0.009278267
-0.001336	0.0043	0.013262492	0.008962492
0.073695	0.4795	0.487120773	0.007620772
0.073562	0.4795	0.486280811	0.006780811
0.073766	0.4795	0.487569173	0.008069173
0.073536	0.4795	0.486116608	0.006616608
0.07369	0.4795	0.487089195	0.007589195
0.148055	0.9504	0.956741353	0.006341353
0.147967	0.9504	0.956185589	0.005785588
0.14792	0.9504	0.95588876	0.00548876
0.148005	0.9504	0.956425578	0.006025577
0.147921	0.9504	0.955895076	0.005495076
0.237026	1.5131	1.518637703	0.005537703
0.236915	1.5131	1.517936683	0.004836683
0.236963	1.5131	1.518239827	0.005139827
0.236963	1.5131	1.518239827	0.005139827
0.236857	1.5131	1.517570384	0.004470384

Figure I-12 Screen shot of recorded data and error calculation

FLUKE multimeter accuracy when measuring DC Current was found in "FLUKE Model 187 & 189 True RMS Multimeter User's Manual" at assets.fluke.com/manuals/187_189_umeng0200.pdf. According to the specification section for 10 A range multimeter resolution is 0.001A and accuracy is ± 0.5% of reading.

FLUKE multimeter is within spec in accordance with mandatory annual calibration procedures executed by Precision Measurement Equipment Laboratory (PMEL); thus total uncertainty for the Hall Effect current sensor after calibration is the sum of the maximum reported error and the uncertainty of the FLUKE multimeter. Uncertainty of the FLUKE multimeter was calculated as ± 0.5% of -8.6 A, the value of current which corresponded to maximum transducer error.

Overall uncertainty:

FLUKE Multimeter: ± 0.043 A Max Transducer Error: ± 0.013 A

Max Sensor Uncertainty: ± 0.043 A ± 0.013 A = **± 0.056 A**

Range: ± 10.0 A

Tektronix P5200 Voltage Probe Calibration

A differential voltage probe is used to measure DC Link Voltage of a PMDC motor drive as part of an Electromechanical Actuation System. In order to quantify Voltage Probe uncertainty a calibration process was undertaken which utilized a High Voltage DC Source and High Precision Digital Voltmeter. These items are highlighted in Figure I-13.

Method:

Gathered a High DC Voltage Source and varied the output from -900Vdc to 900Vdc at increments of 50 Vdc while monitoring voltage probe output and comparing against Digital

Voltmeter Reading. Voltage was manually adjusted and Probe/Voltmeter output recorded by a LabVIEW control program. 1000 samples of probe output were recorded, and the average of those 1000 samples was calculated. This process was repeated 5 times at each fixed level of voltage. The HP 3456A Digital Voltmeter served as our standard and uncertainty associated with this device is reported below. Voltmeter measurement uncertainty was accounted for in overall uncertainty calculation of the voltage probe.

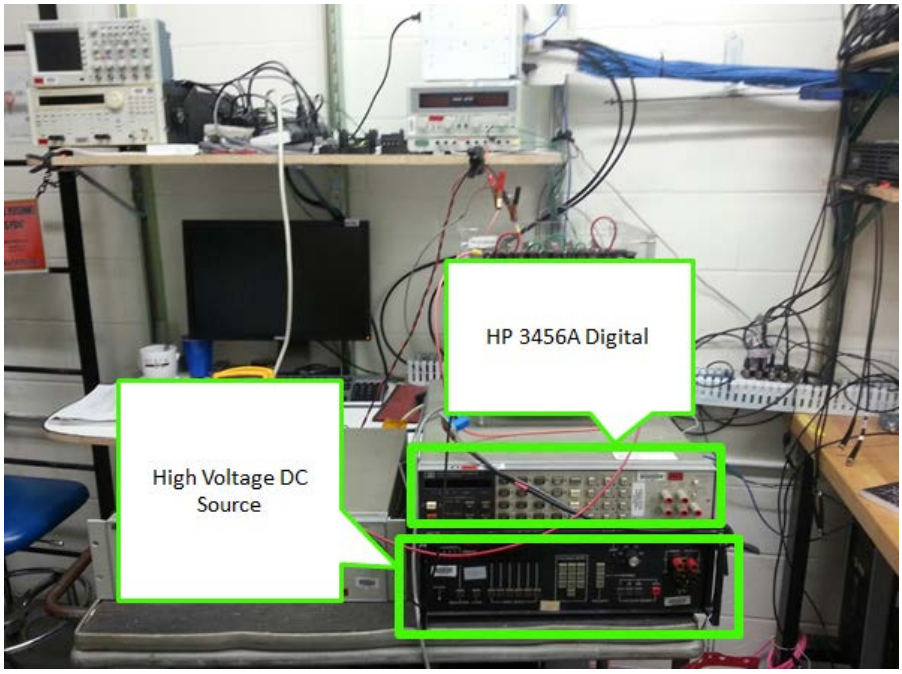

Figure I-13 Voltage Probe Calibration Setup

Transducer output was slightly nonlinear; therefore a 2nd order polynomial fit was used to generate a calibration curve. The calibration curve relates transducer attenuated output in Volts to Voltage of the Source. The upper plot in Figure I-14 shows a scatter of Voltmeter reading (standard) and P5200 Voltage Probe output. Additionally, this plot highlights the resulting fit equation and its metric for goodness of fit, R^2. This curve was used to evaluate sensed voltage and the error from standard. Absolute measurement error for each level of is displayed in the lower plot in Figure I-14. The maximum absolute error from the standard was 0.81 V.

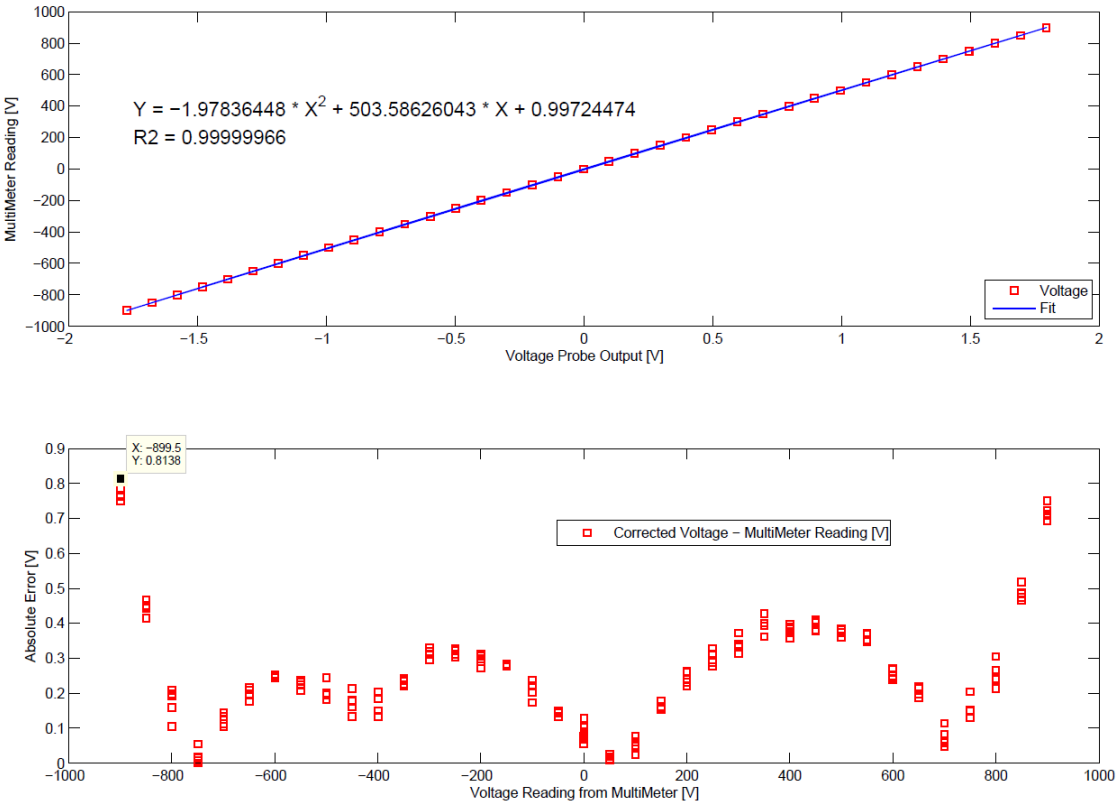

Figure I-14 Voltage Probe Calibration Curve and Absolute Error

Figure I-15 is a screenshot of spreadsheet format used to determine sensor uncertainty. The sheet contains 4 columns of data: Transducer Output, Voltmeter Reading, Measurement from Calibration Curve, and Absolute Error of Measurement from Calibration Curve and Voltmeter Reading. There are 190 rows of data which corresponds to 5 readings at each interval of fixed voltage (-900,-850,-800…800,850,900). The maximum absolute error reported in the spreadsheet matched that of the lower plot in Figure I-15, 0.81 V.

RMS Transducer Output [V]	Multimeter Voltage [V] (Standard)	Measured Voltage from Polynomial Fit Calibration Curve [V]	Absolute Measurement Error [V]
-0.002121	0.014	-0.07092329	0.08492329
-0.002096	0.014	-0.058333332	0.072333332
-0.002208	0.014	-0.114736365	0.128736365
-0.002155	0.014	-0.088045638	0.102045638
-0.00213	0.014	-0.075455676	0.089455676
-0.002145	-0.015	-0.083009653	0.068009653
-0.002147	-0.015	-0.08401685	0.06901685
-0.002161	-0.015	-0.091067229	0.076067229
-0.002122	-0.015	-0.071426889	0.056426889
-0.002164	-0.015	-0.092578025	0.077578025
-0.10146	-49.971	-50.11740731	0.14640731
-0.101465	-49.971	-50.11992727	0.148927267
-0.101434	-49.971	-50.10430353	0.133303533
-0.101456	-49.971	-50.11539134	0.144391344
-0.101436	-49.971	-50.10531152	0.134311516
0.097335	49.97	49.99538909	0.025389086
0.097248	49.97	49.95161025	0.018389752
0.097305	49.97	49.98029294	0.010292938
0.09731	49.97	49.98280896	0.012808963
0.097302	49.97	49.97878332	0.008783323
-0.200728	-99.945	-100.1671267	0.222126679
-0.200691	-99.945	-100.1484645	0.203464464
-0.200634	-99.945	-100.1197146	0.174714577
-0.200759	-99.945	-100.1827626	0.237762592
-0.200759	-99.945	-100.1827626	0.237762592
0.196781	99.94	100.0175347	0.077534678
0.196675	99.94	99.96423665	0.02423665
0.19675	99.94	100.0019475	0.061947523
0.196729	99.94	99.99138848	0.051388481
0.196725	99.94	99.98937723	0.049377234

Figure I-15 Screen shot of recorded data and error calculation

Accuracy of the HP 3456A Voltmeter when measuring DC Voltage was determined from "3456A Digital Voltmeter Operating and Service Manual" found at http://cp.literature.agilent.com/litweb/pdf/03456-90006.pdf. According to the specification section, for 1000 Vdc range and 4 Digit 0.01 PLC voltmeter accuracy is ± 0.06% of reading.

The voltmeter is within spec in accordance with mandatory annual calibration procedures executed by PMEL; thus total uncertainty for the voltage probe after calibration is the sum of the maximum reported error and the uncertainty of the HP voltmeter. Uncertainty of the voltmeter was calculated as ± 0.06% of -899.5 Vdc, the value which corresponded to maximum transducer error.

Overall uncertainty:

HP Voltmeter: ± 0.54 V Max Probe Error: ± 0.81 V

Max Sensor Uncertainty: ± 0.54 V ± 0.81 V = **± 1.35 V**

Range: ± 900 V

APPENDIX J

EXPERIMENT NOISE

High frequency switching power electronics apart of the EMA servo drive have plagued the experiment with electromagnetic interference (EMI) and noise issues throughout its existence. In an effort to quantify Drive's impact on measurement noise 30 seconds of data for each measurement was sampled for 3 different scenarios. Each measurement was captured at the same rate used during experiments—stroke and force (210 Hz), voltage and current (3012 Hz). First, the EMA system powered on, the drive enabled, and no load and stroke was commanded. In that state the DC link was energized and measured approximately 333 $V_{DC.}$ With no load or position command current draw should be zero and stroke/force should not change with time. The resulting variation in stroke, force, DC link voltage, and DC link current are shown in Figure J-1.

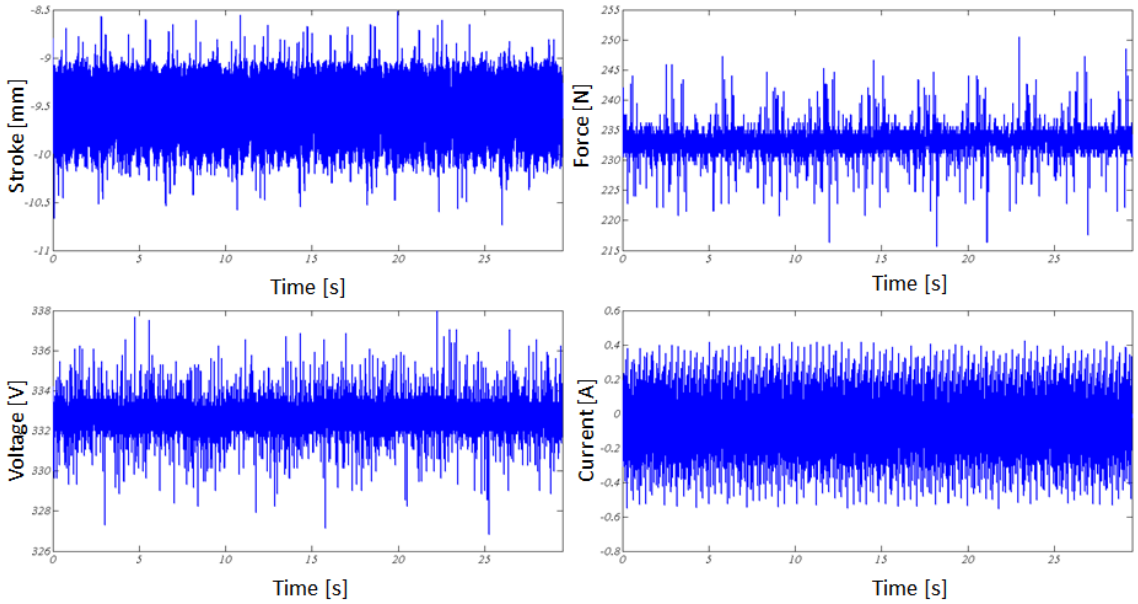

Figure J-1 EMA system powered on, drive enabled, and no load

Second, the EMA system was powered on, but the drive was not enabled. Under this scenario the DC link is still energized but the EMA is not able to execute position or load commands. Measurement results are shown in Figure J-2.

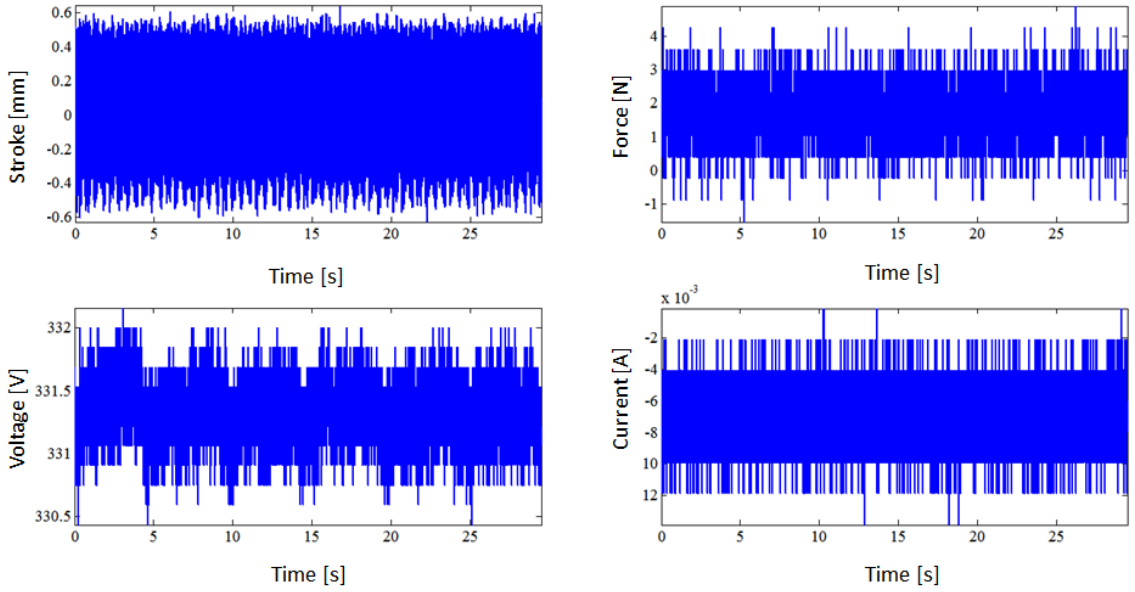

Figure J-2 EMA system powered on, drive disabled

Last, the EMA system was not powered on and 30 seconds of measurements was executed. Under this state, the DC link was not energized and therefore no stroke or load commands were possible either. Figure J-3 shows the measurement results.

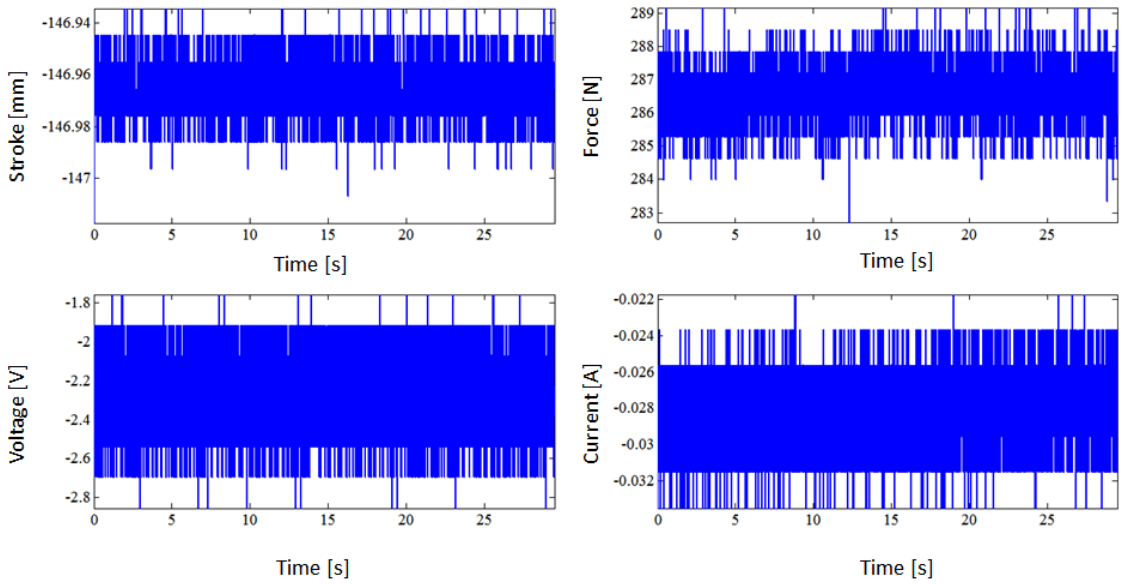

Figure J-3 EMA system powered off

The various levels of noise per measurement type are summarized in Table J-1.

Overall, each measurement experienced several times more variation when the EMA system was powered on and the servo drive enabled rather than powered on and disabled. Little change in magnitude for each measurement type occurred when the system was powered on and disabled as opposed to powered off. In general even with the EMA drive powered on and enabled the range of noise was less than 1% of the sensor's full scale range for stroke, force, and voltage.

Current transducers were more susceptible to noise and exhibited noise range upwards of 5% of the sensor's full scale range.

Table J-1

	Stroke [mm]		
System State	Noise Range	Sensor Range	% of Full Range
powered on, drive enabled, and no load	2.22	254	0.87%
powered on, drive disabled	1.27	254	0.50%
system powered off	0.08	254	0.03%

	Force [N]		
System State	Noise Range	Sensor Range	% of Full Range
powered on, drive enabled, and no load	34.8	20000	0.17%
powered on, drive disabled	6.45	20000	0.03%
system powered off	6.45	20000	0.03%

	Voltage [V]		
System State	Noise Range	Sensor Range	% of Full Range
powered on, drive enabled, and no load	11.16	2000	0.56%
powered on, drive disabled	1.73	2000	0.09%
system powered off	1.1	2000	0.06%

	Current [A]		
System State	Noise Range	Sensor Range	% of Full Range
powered on, drive enabled, and no load	0.979	20	4.90%
powered on, drive disabled	0.014	20	0.07%
system powered off	0.012	20	0.06%

Experiment Noise Mitigation

At even integer values of sampling frequency a consistent pulse shows up on all analog measurements when the EMA servo drive is enabled. After several hours of investigating and tracking potential reasons for these spikes it was determined offsetting the sampling frequency to an odd integer value alleviated the noise. It could not be determined if the noise was radiated or conducted from the servo drive. However, sampling at odd integer frequencies and employing analog low pass filters alleviated high frequency noise associated with power electronics switching within the servo drive.

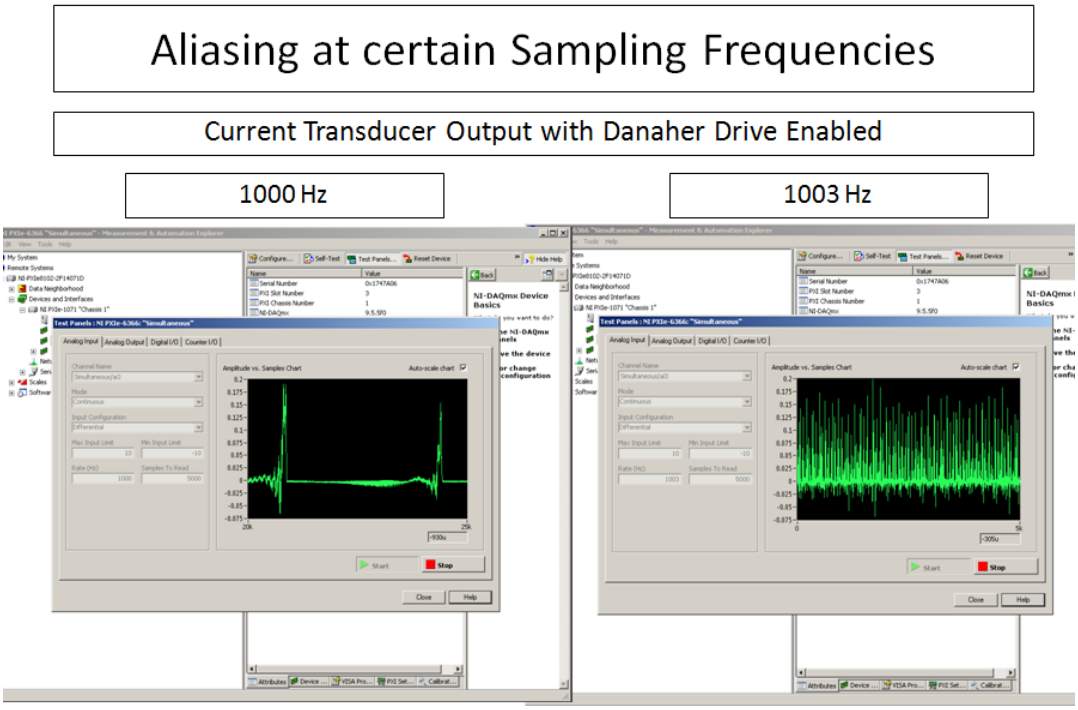

Figure J-4 NI-DAQmx Interface for two different sampling frequencies

***Aliasing of both mechanical and electrical measurements seems to be alleviated when sampling frequencies of odd integer values are used. For example, 2000Hz was used for DC Link Voltage and Current in Figure J-5 but in J-6 1550Hz was used. Mechanical parameters (force and stroke) were sampled at 200Hz in Figure J-5 but 210Hz in J-6.

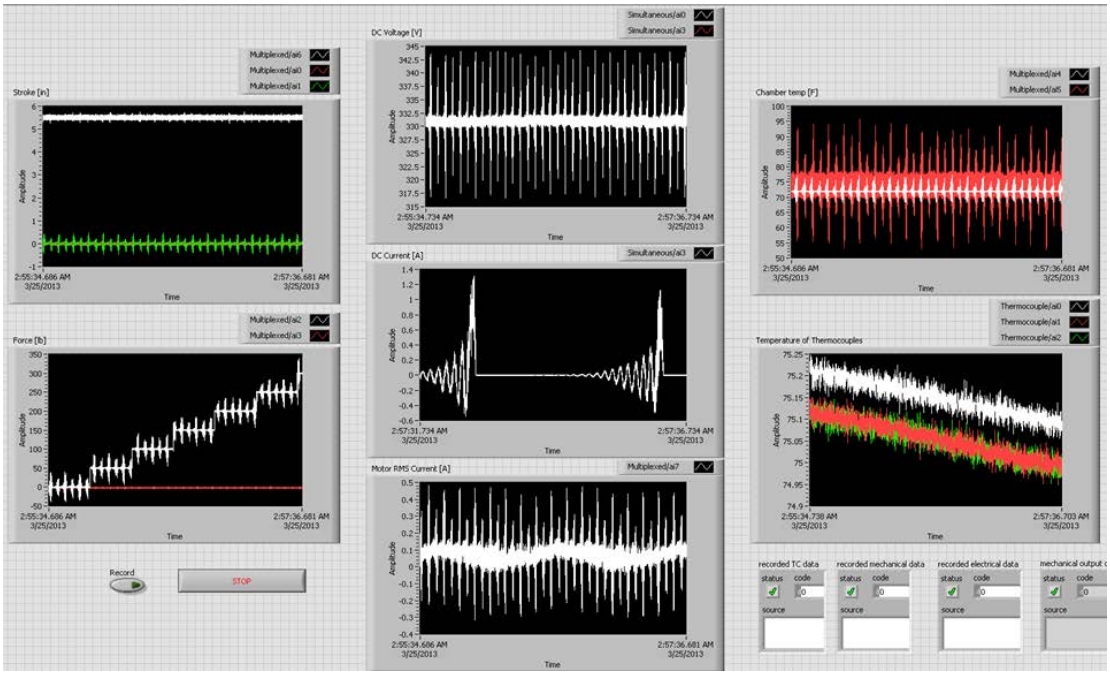

Figure J-5 LabVIEW VI used for Test Control and Data Acquisition—Even Sampling Frequency

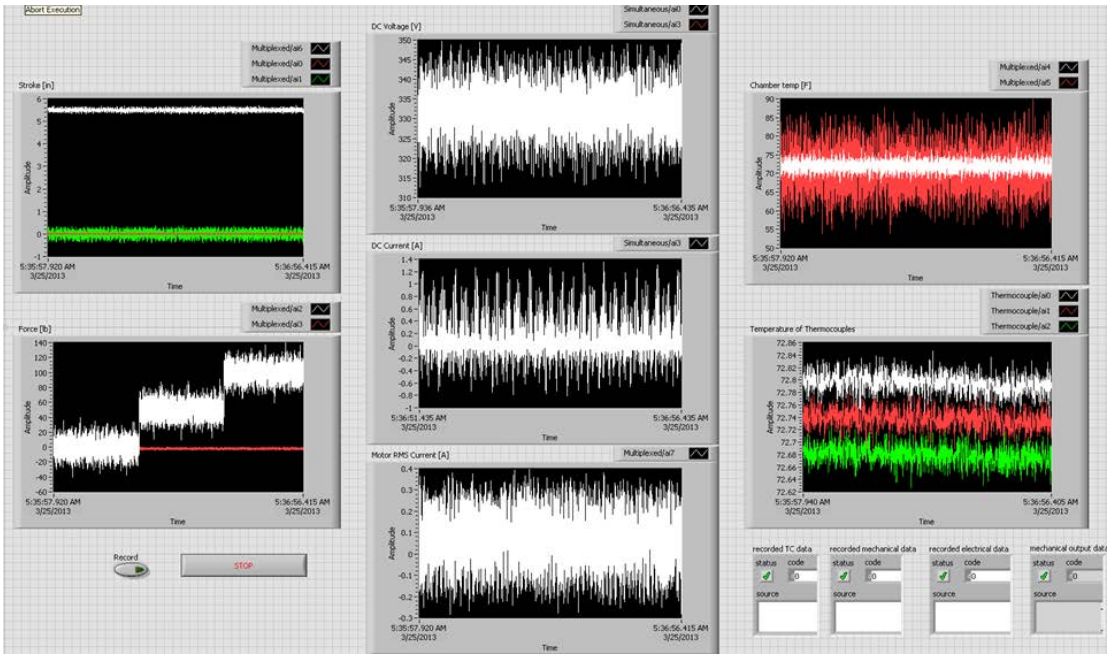

Figure J-6 LabVIEW VI used for Test Control and Data Acquisition—Odd Sampling Frequency

APPENDIX K
ADDITIONAL TEST RESULTS

Holding Tests Summary

All tests were executed with the actuator placed inside the environmental chamber but two types of holding test environments were completed, one without active temperature control and one with active temperature control. Tests completed without active temperature control did not utilize the chamber's heating or cooling capacity. Tests completed with active temperature control utilized the environmental chamber heating and cooling capacity to maintain the environmental temperature setpoint. The purpose of holding tests was to determine the impact of actively controlling chamber temperature on EMA power draw and heat loss. First, the ambient temperature was passively controlled by enclosing the environmental chamber around the EMA while it was loaded at 25% of stall force (1500 N). Without active control meant the environmental chamber was not powered and therefore no use of heating elements, nitrogen vapor, or fan to maintain the 22°C setpoint. By not actively controlling the chamber ambient, EMAS heat generation did in fact slightly increase chamber temperature. However, not actively controlling the chamber temperature did not significantly impact motor TC temperature rise. Average motor TC temperature rise for both no active control and active control was approximately 4°C. Energy results and thermal summary are presented in tables K-1 and K-2, respectively. Note, thermal energy was based on the energy analysis developed in section 4.7.3 and was calculated as the difference in electrical and mechanical energy.

Table K-1 Holding Tests COE Summary

Test		Post Test Analysis			
Profile	**Profile Description**	**Electrical Energy [J]**	**Mechanical Energy [J]**	**Thermal Energy [J]**	**Efficiency**
Hard Hold Tension	0 velocity against 25% of stall force *without active temperature control*	463,816 ± 2,783	4.7 ± .05	463,811 ± 2,783	0%
	0 velocity against 25% of stall force at environment temperature 22°C	478,477 ± 2,871	7 ± .07	478,470 ± 2,871	0%
	0 velocity against 25% of stall force at environment temperature 70°C	398,963 ± 2,394	2.6 ± .03	398,960 ± 2,394	0%
Hard Hold Compression	0 velocity against 25% of stall force at environment temperature 22°C	646,047 ± 3,876	1.7 ± .02	646,045 ± 3,876	0%

Table K-2 Holding Tests Thermal Summary

Test		Post Test Analysis			
Profile	Profile Description	Peak TC ROC [°C/s]	Max Motor Case-Ambient ΔT [°C]	Avg. Current [A]	Peak Current [A]
Hard Hold Tension	0 velocity against 25% of stall force *without active temperature control*	0.03	4.18	1.15	1.32
	0 velocity against 25% of stall force at environment temperature 22°C	0.03	2.95	1.19	1.35
	0 velocity against 25% of stall force at environment temperature 70°C	0.02	1.39	0.99	1.31
Hard Hold Compression	0 velocity against 25% of stall force at environment temperature 22°C	0.04	3.15	1.63	1.95

Holding in Tension without Active Temperature Control Mechanical Results

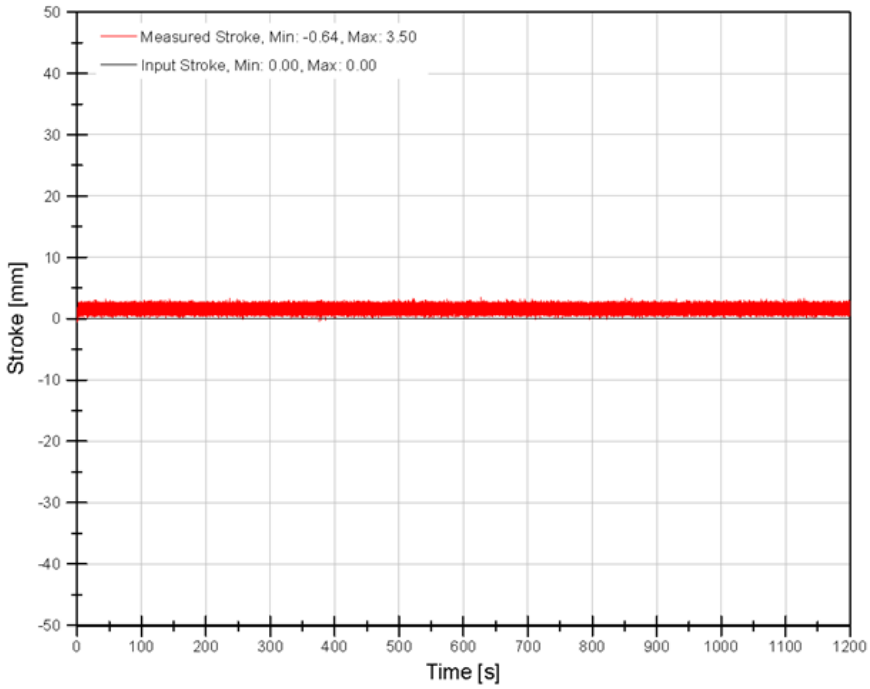

Figure K-1 Holding in Tension without Active Temperature Control—Input and Measured Stroke

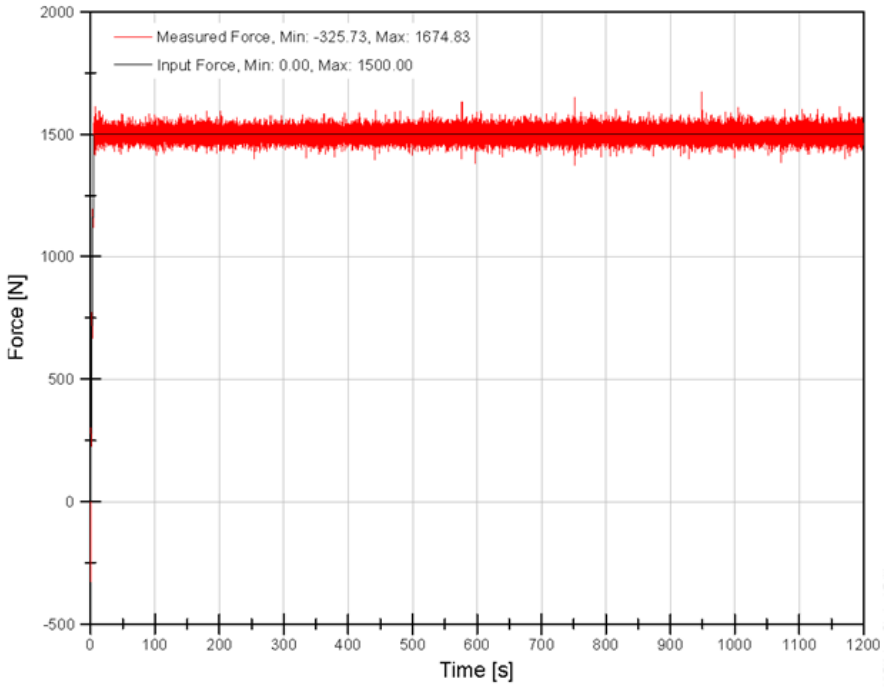

Figure K-2 Holding in Tension without Active Temperature Control—Input and Measured Force

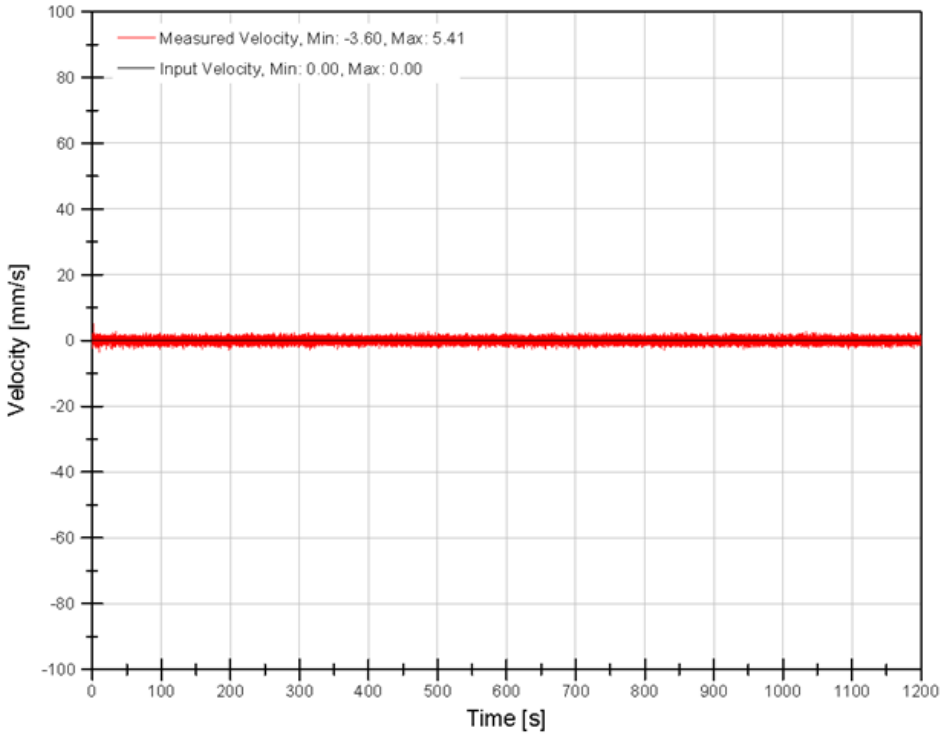

Figure K-3 Holding in Tension without Active Temperature Control—Calculated Velocity

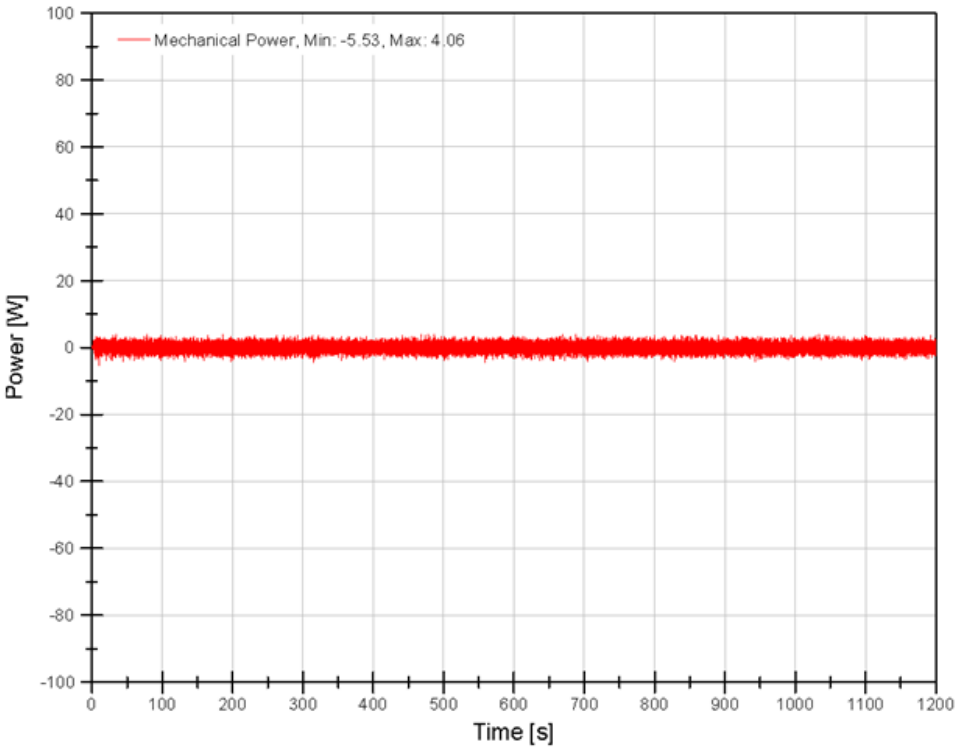

Figure K-4 Holding in Tension without Active Temperature Control—Calculated Mechanical Power

Holding in Tension without Active Temperature Control Electrical Results

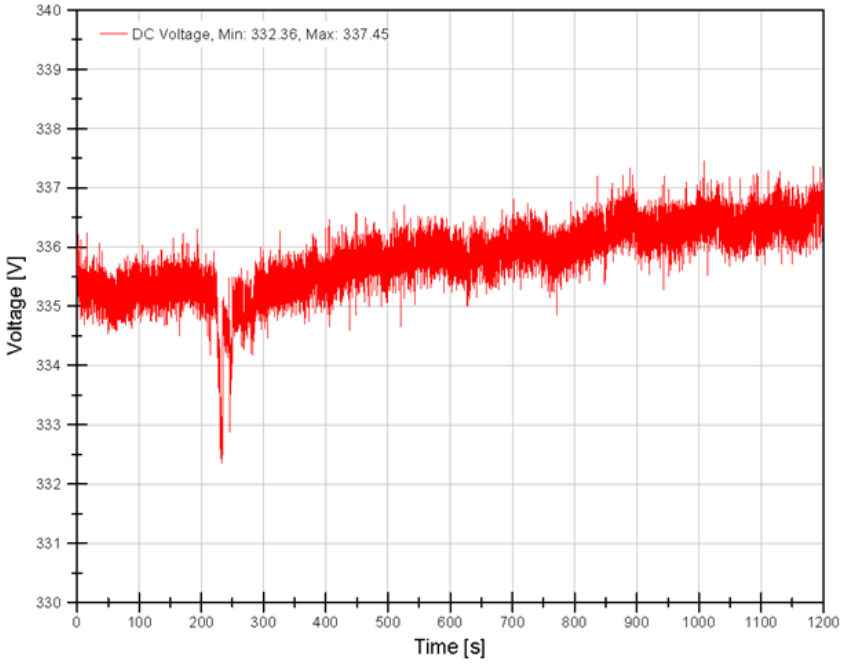

Figure K-5 Holding in Tension without Active Temperature Control—Measured DC Bus Voltage

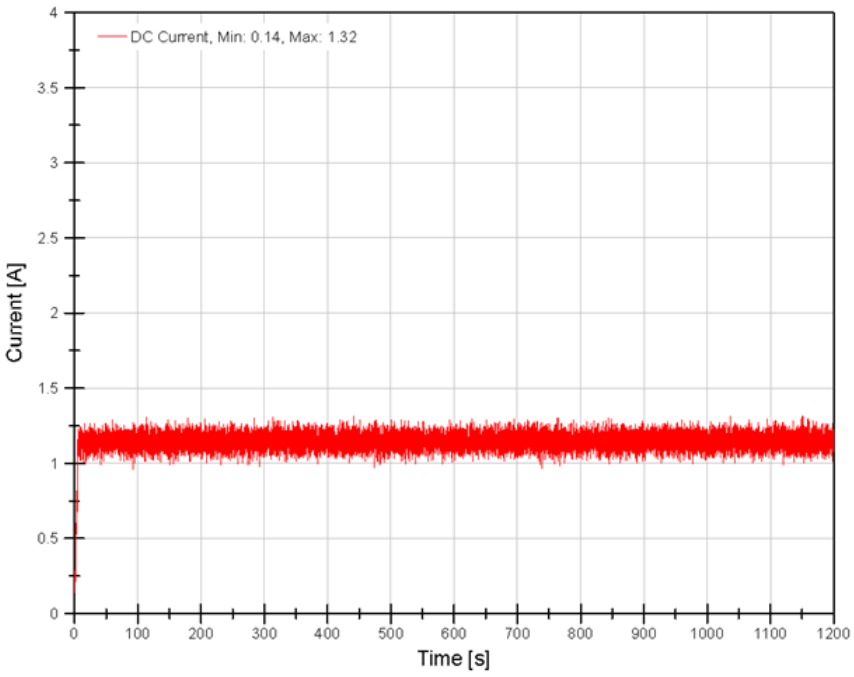

Figure K-6 Holding in Tension without Active Temperature Control—Measured DC Bus Current

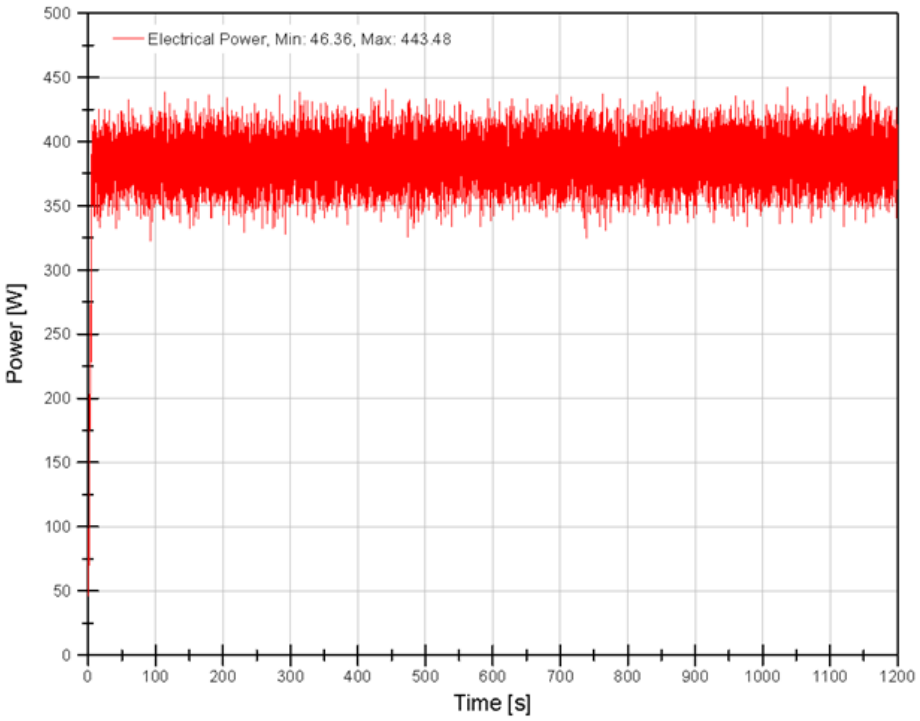

Figure K-7 Holding in Tension without Active Temperature Control—Calculated Electrical Power

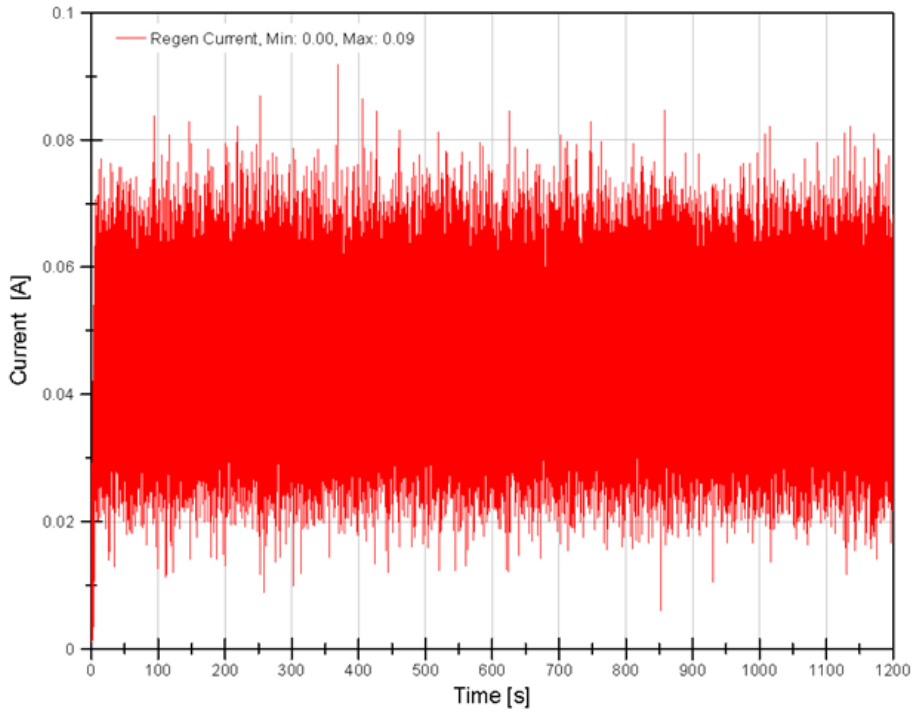

Figure K-8 Holding in Tension without Active Temperature Control—Measured Regen Circuit Current

Holding in Tension without Active Temperature Control Thermal Results

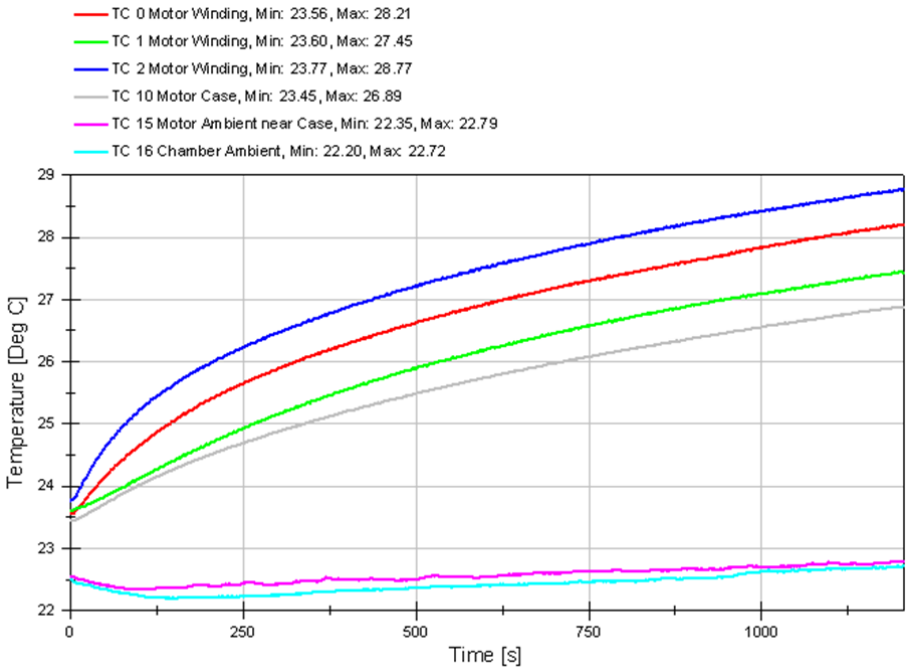

Figure K-9 Holding in Tension without Active Temperature Control—EMA Temperature

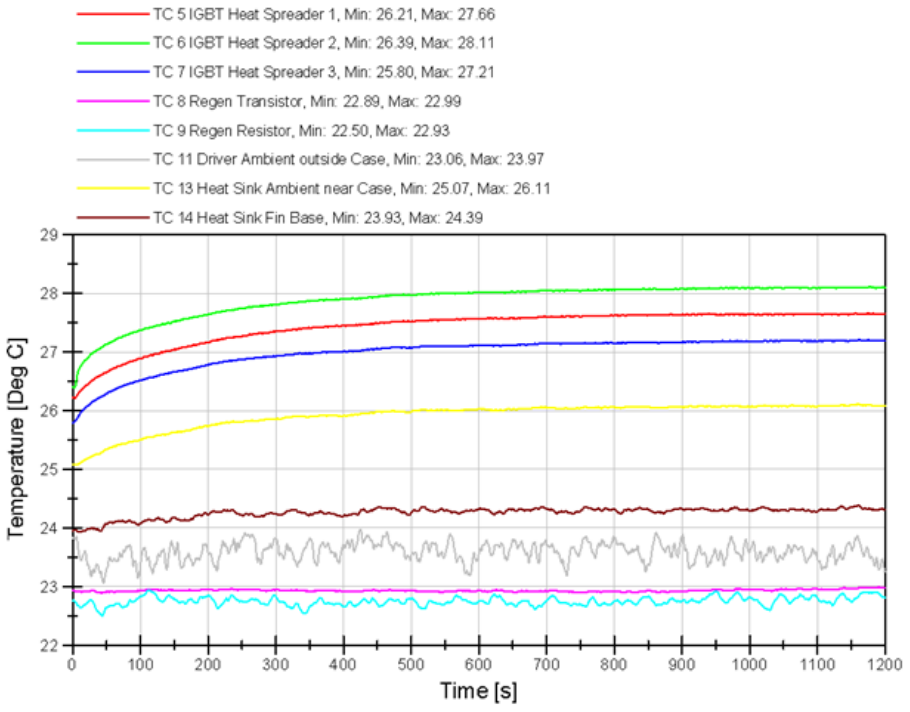

Figure K-10 Holding in Tension without Active Temperature Control—Motor Controller Temperature

Note: Motor Controller was outside the environmental chamber.

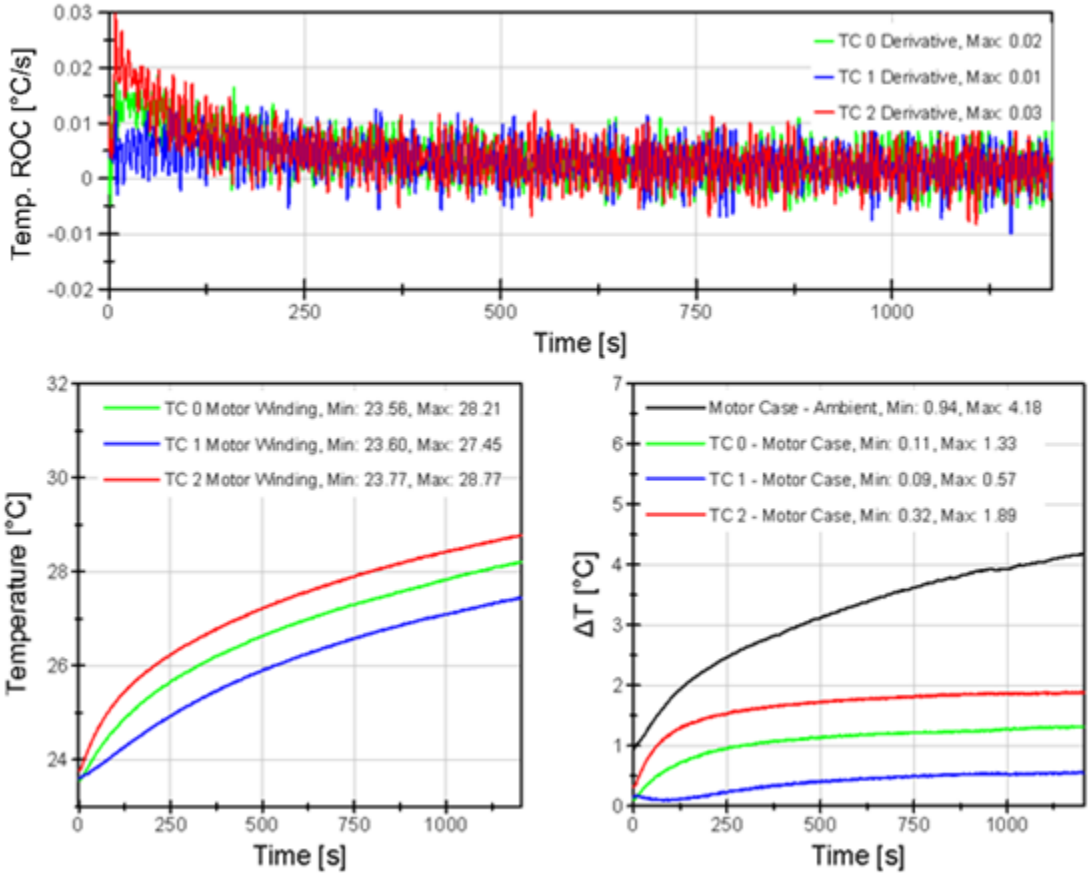

Figure K-11 Holding in Tension without Active Temperature Control—Thermal Results

Holding in Tension without Active Temperature Control Conservation of Energy

Note: Calculated electrical energy (green) was covered by calculated thermal energy (red) in Figure K-12 because both trends were very similar.

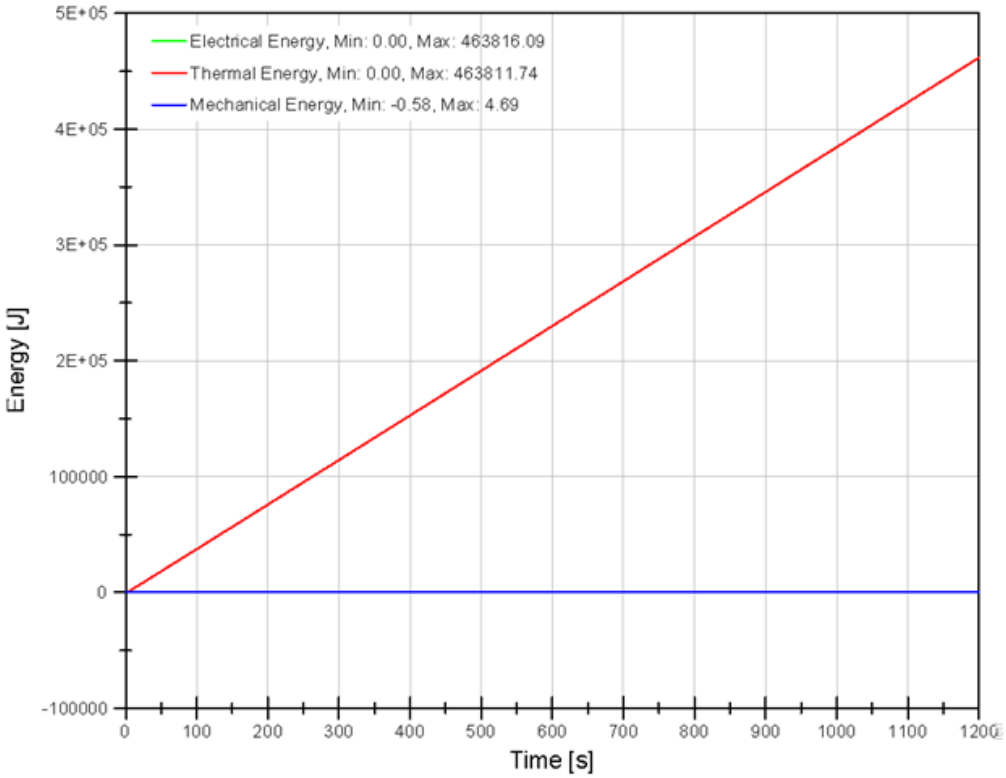

Figure K-12 Holding in Tension without Active Temperature Control—Calculated COE

Holding in Tension with Active Temperature Control Mechanical Results

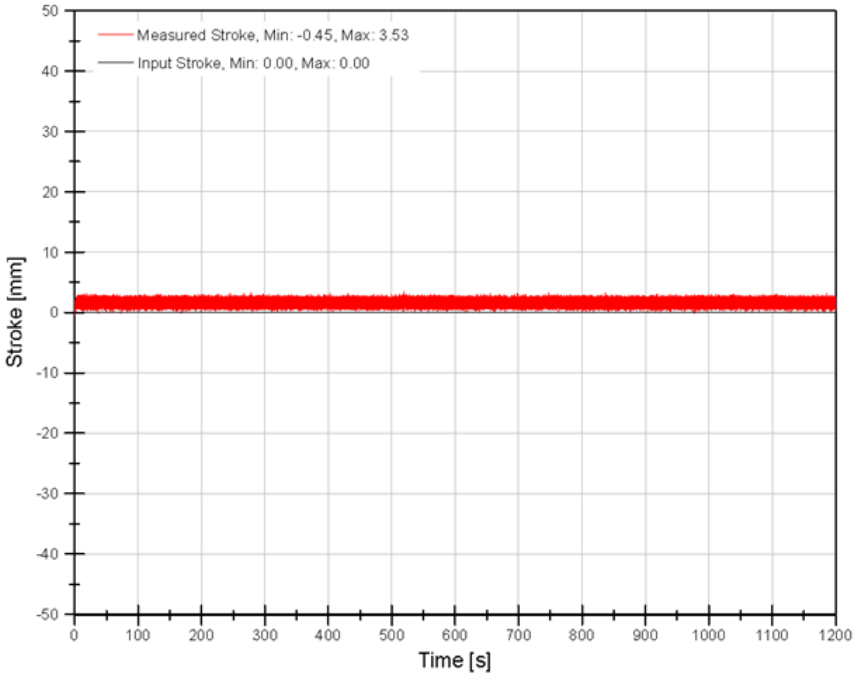

Figure K-13 Holding in Tension with Active Temperature Control—Input and Measured Stroke

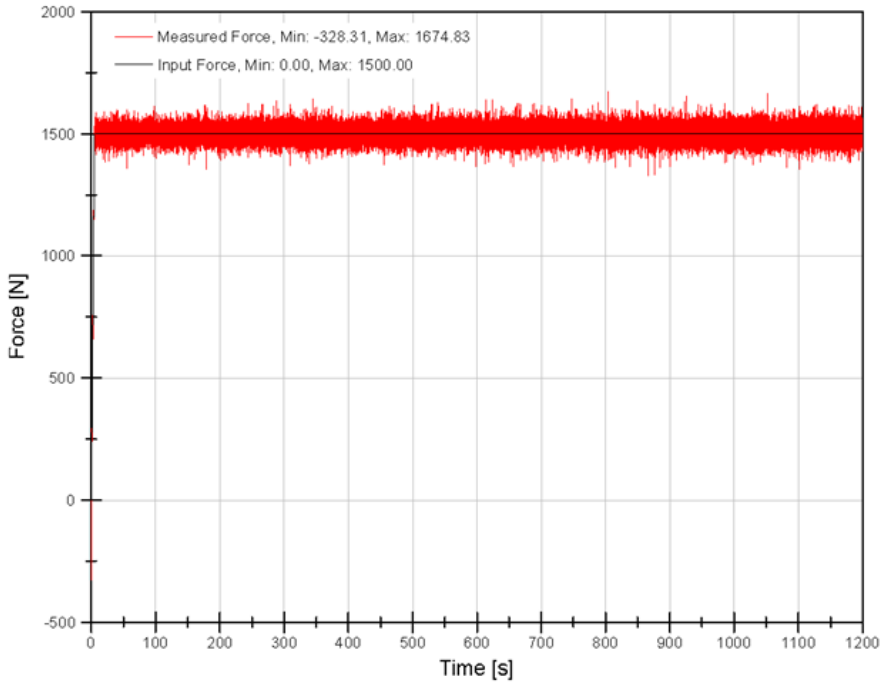

Figure K-14 Holding in Tension with Active Temperature Control—Input and Measured Force

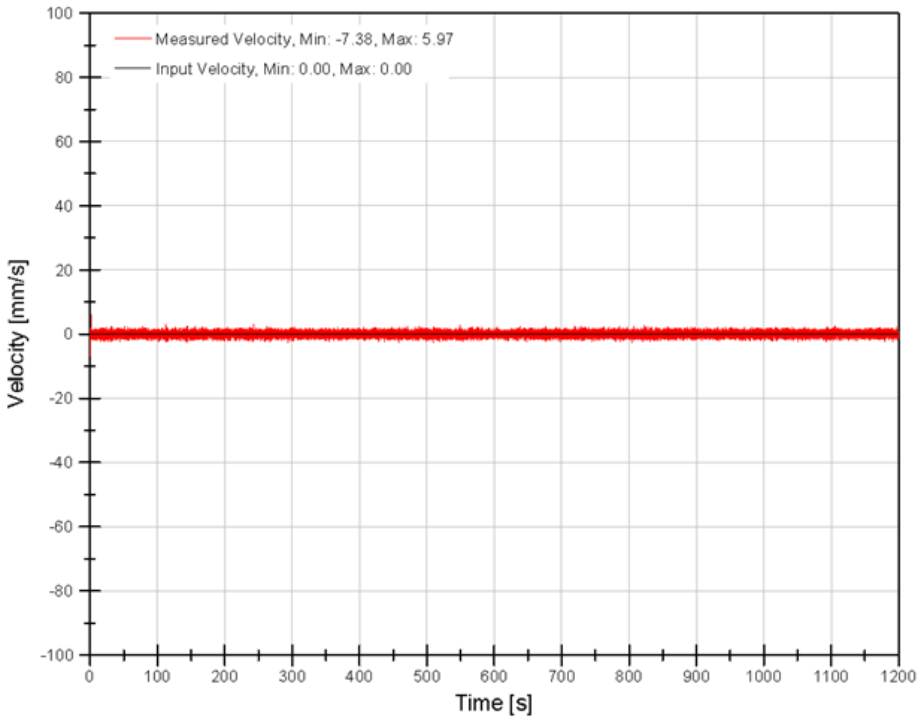

Figure K-15 Holding in Tension with Active Temperature Control—Calculated Velocity

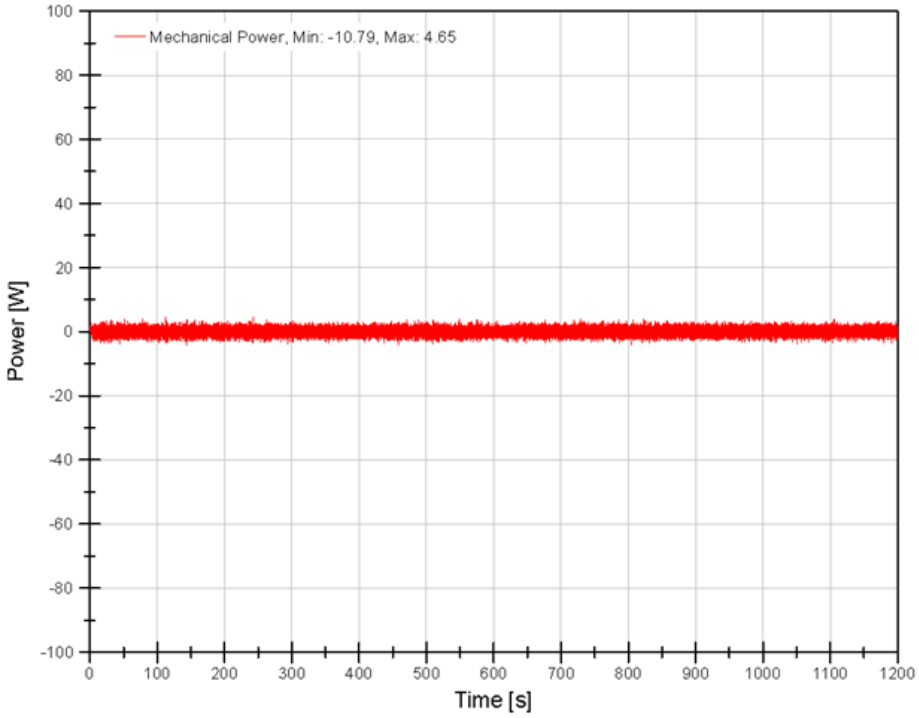

Figure K-16 Holding in Tension with Active Temperature Control—Calculated Mechanical Power

Holding in Tension with Active Temperature Control Electrical Results

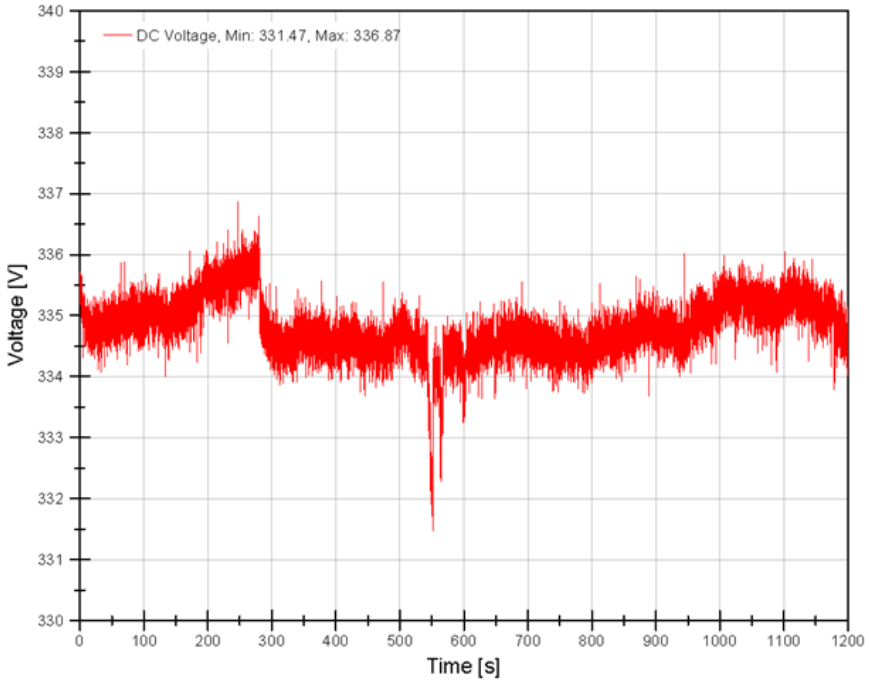

Figure K-17 Holding in Tension with Active Temperature Control—Measured DC Voltage

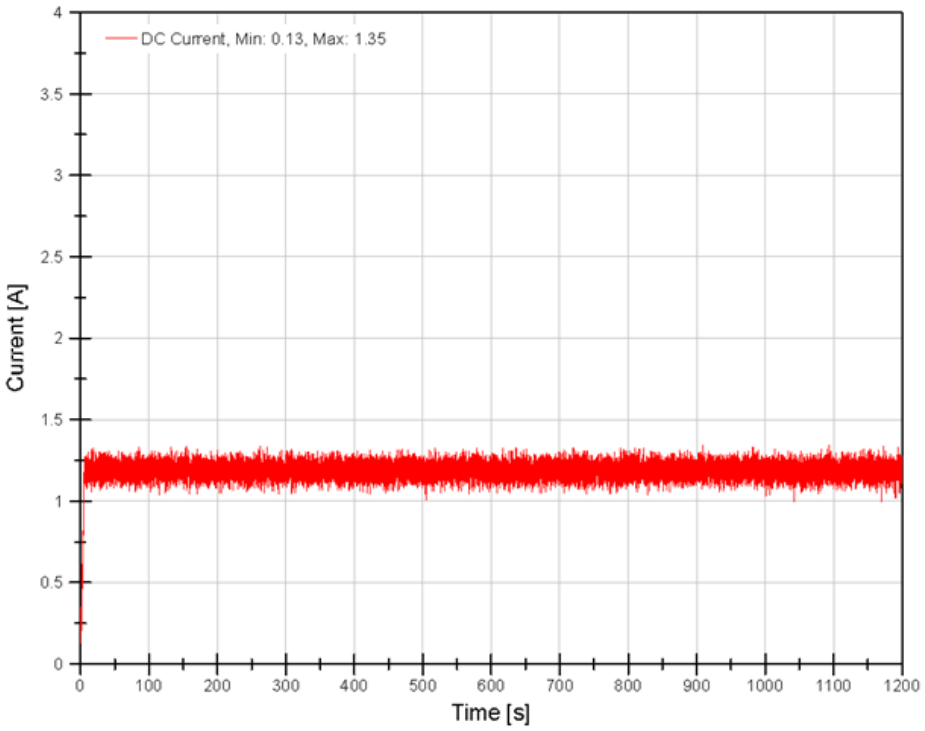

Figure K-18 Holding in Tension with Active Temperature Control—Measured DC Current

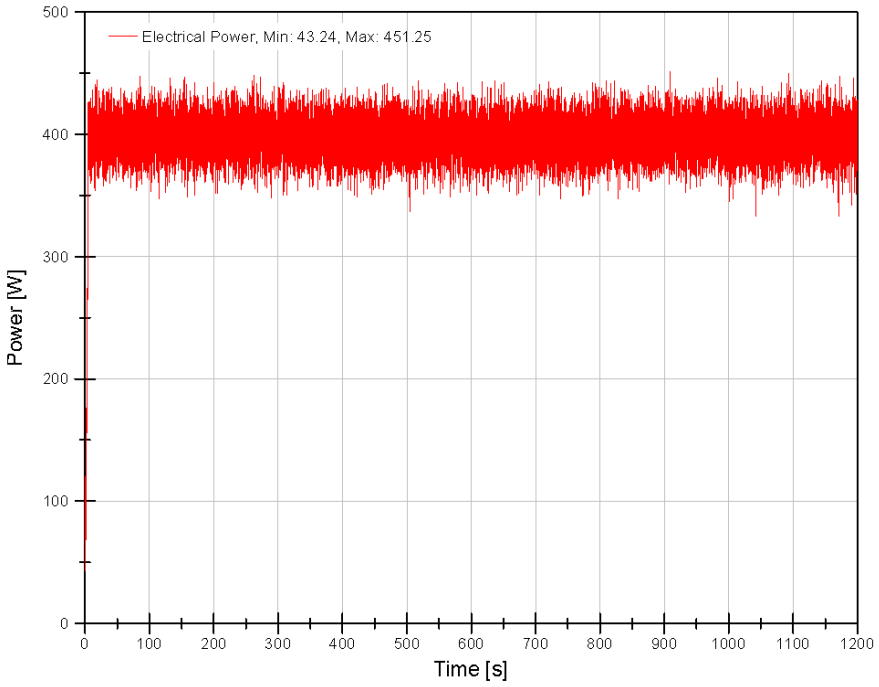

Figure K-19 Holding in Tension with Active Temperature Control—Calculated Electrical Power

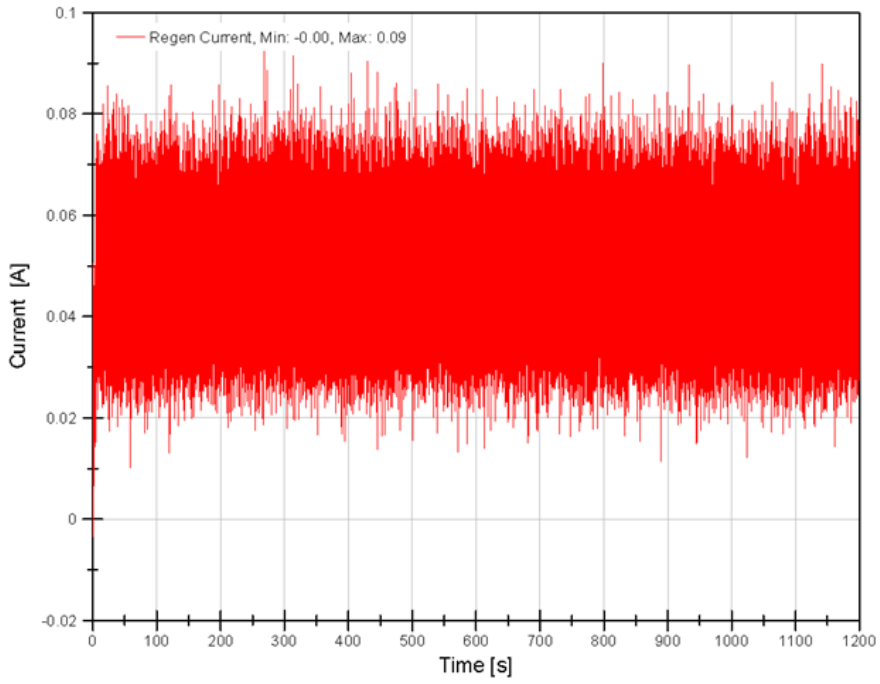

Figure K-20 Holding in Tension with Active Temperature Control—Measured Regen Circuit Current

Holding in Tension with Active Temperature Control Thermal Results

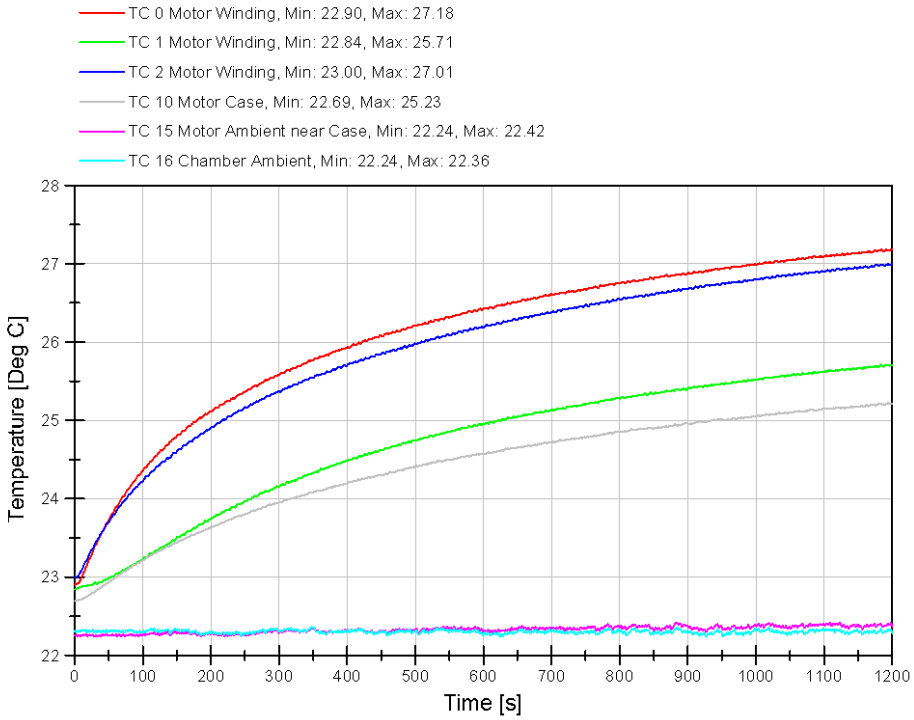

Figure K-21 Holding in Tension with Active Temperature Control—EMA Temperature

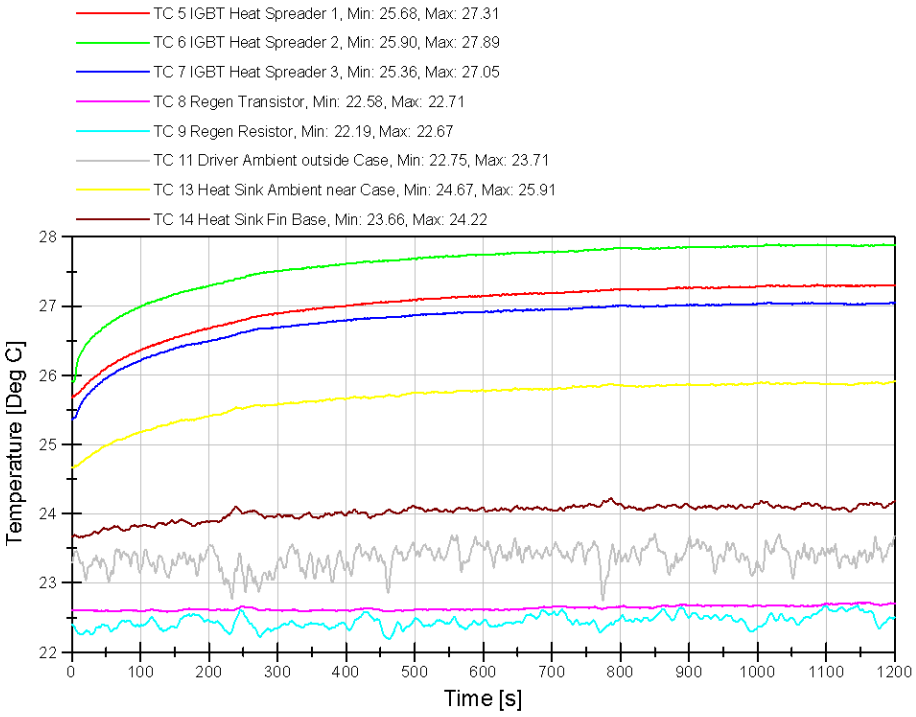

Figure K-22 Holding in Tension with Active Temperature Control—Motor Controller Temperature

Note: Motor Controller was outside the environmental chamber.

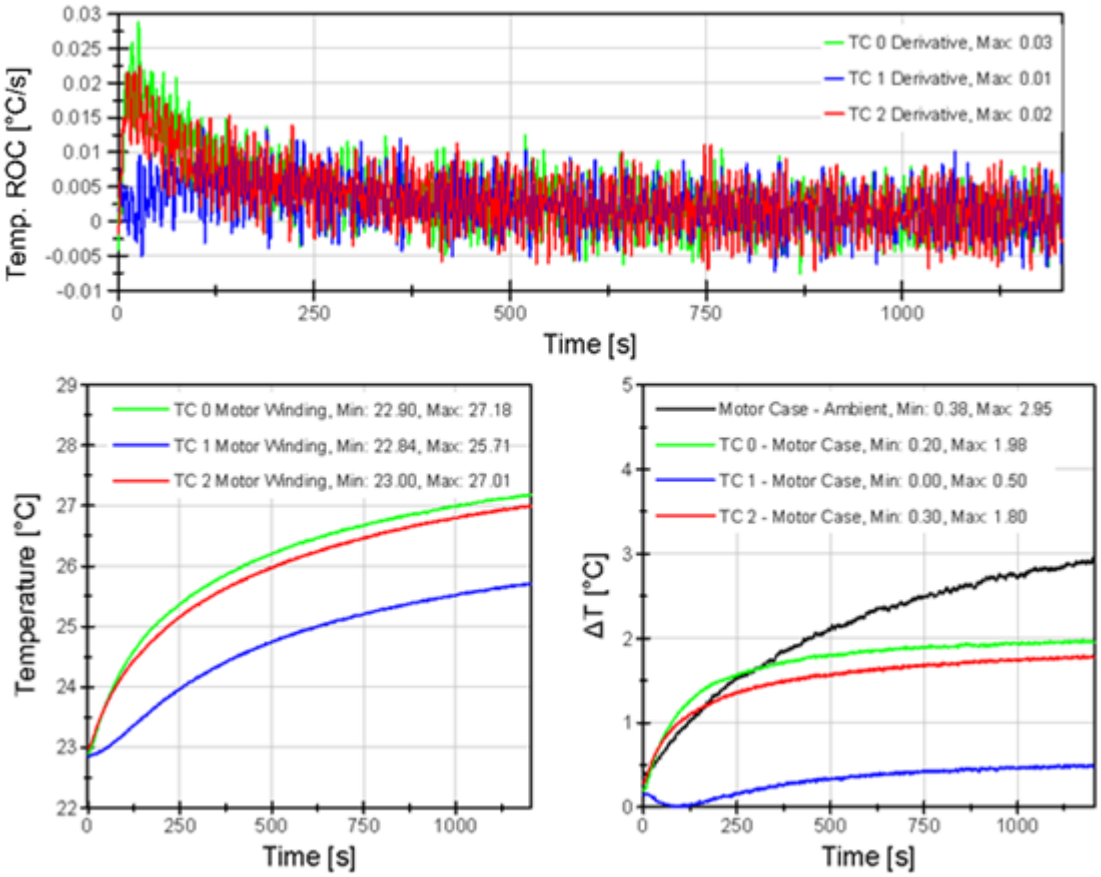

Figure K-23 Holding in Tension with Active Temperature Control—Thermal Results

Holding in Tension with Active Temperature Control Conservation of Energy

Note: Calculated electrical energy (green) was covered by calculated thermal energy (red) in Figure K-24 because both trends were very similar.

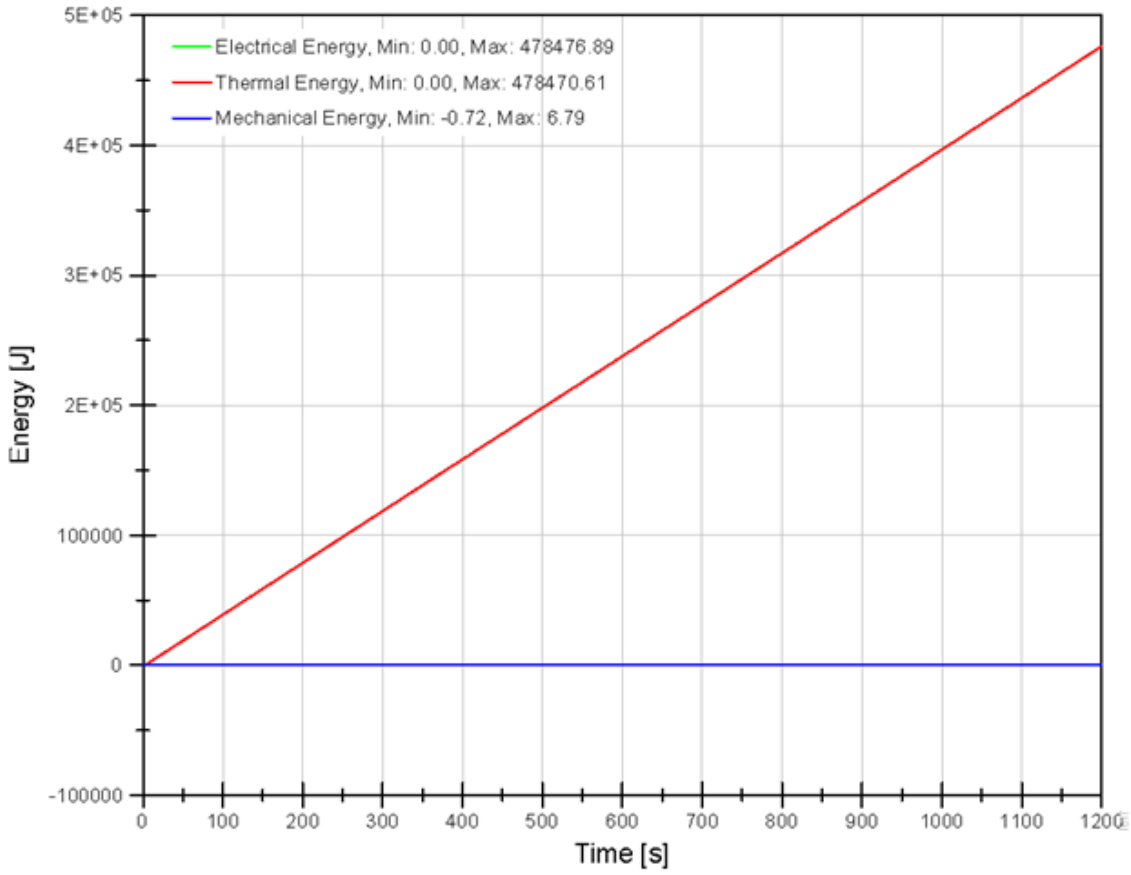

Figure K-24 Holding in Tension with Active Temperature Control—Calculated COE

Holding in Tension at 70°C Environment Temperature Mechanical Results

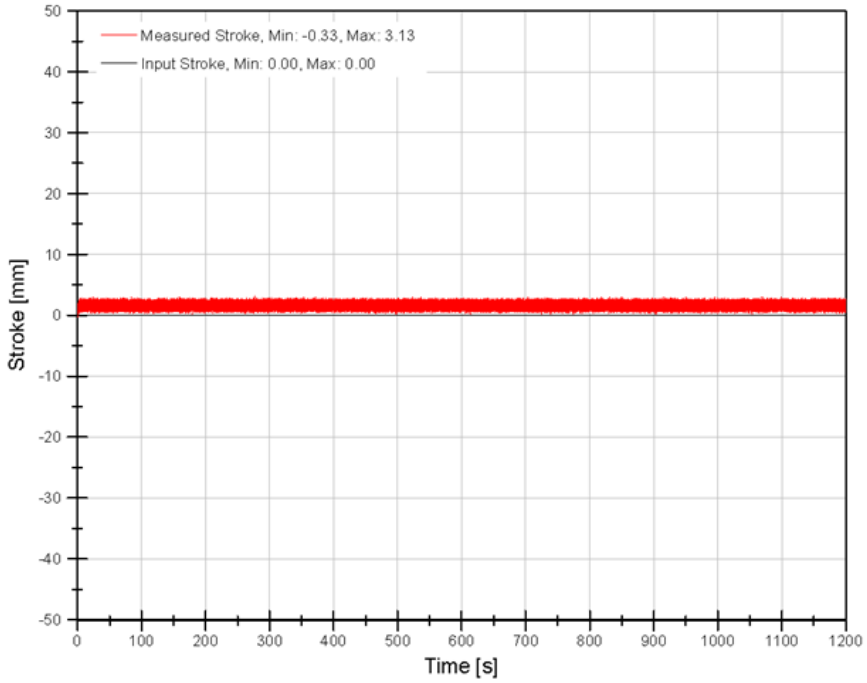

Figure K-25 Holding in Tension at 70°C Environment Temperature—Input and Measured Stroke

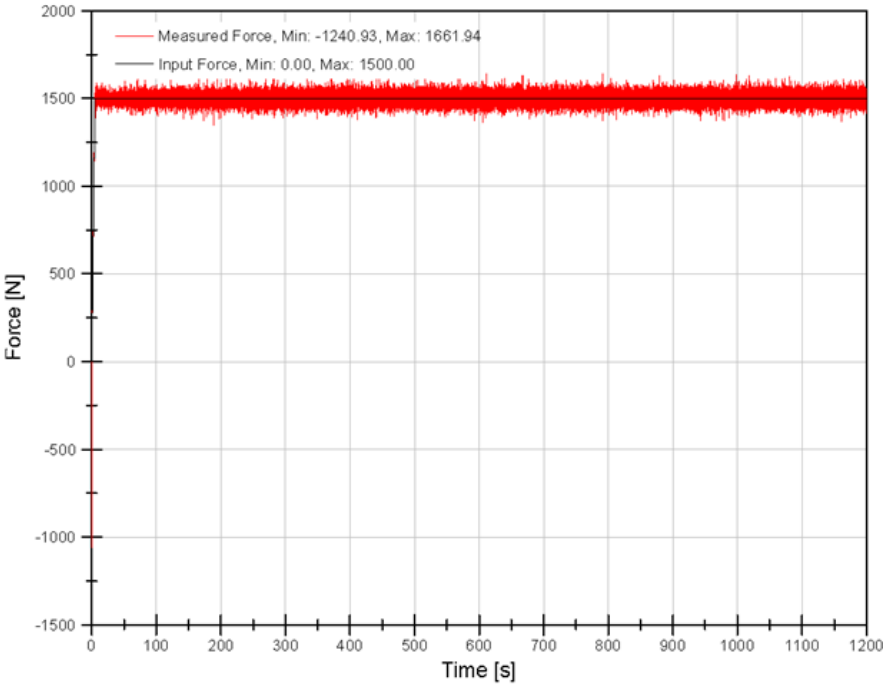

Figure K-26 Holding in Tension at 70°C Environment Temperature—Input and Measured Force

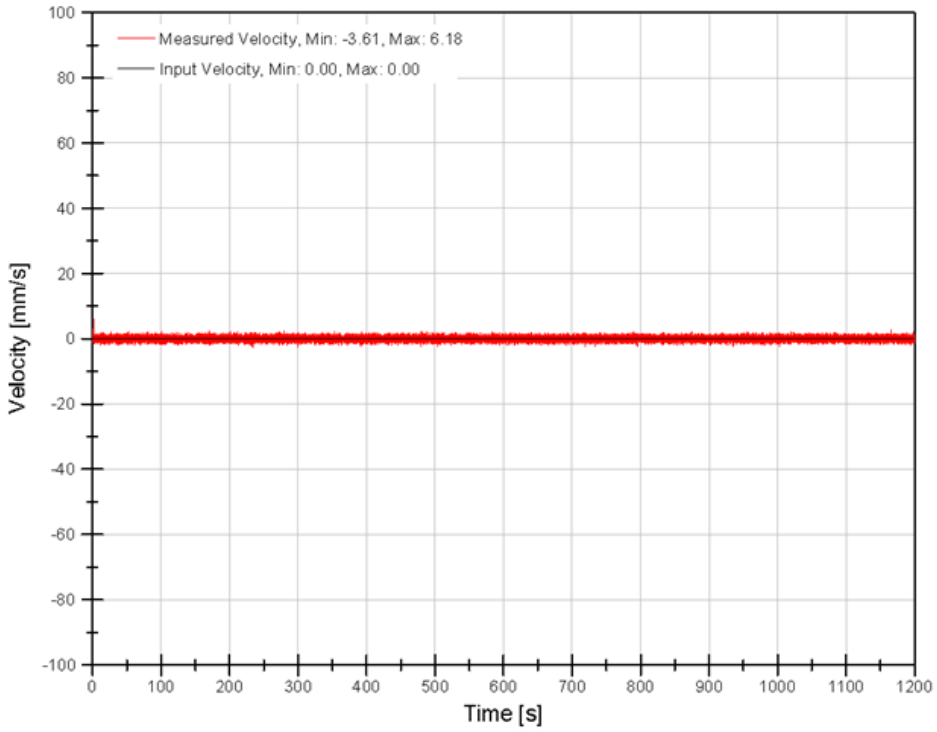

Figure K-27 Holding in Tension at 70°C Environment Temperature—Calculated Velocity

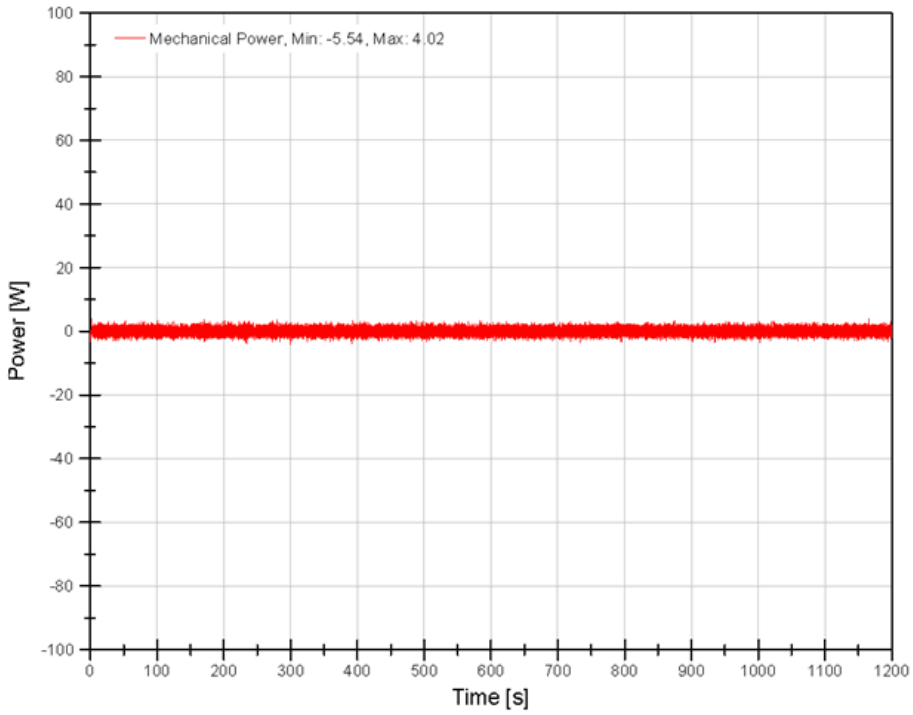

Figure K-28 Holding in Tension at 70°C Environment Temperature—Calculated Mechanical Power

Holding in Tension at 70°C Environment Temperature Electrical Results

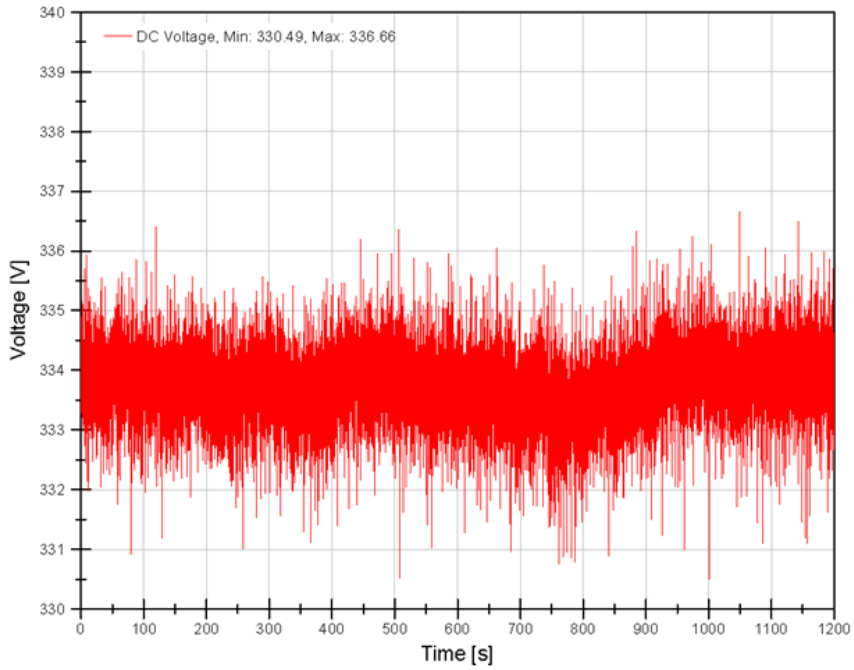

Figure K-29 Holding in Tension at 70°C Environment Temperature—Measured DC Bus Voltage

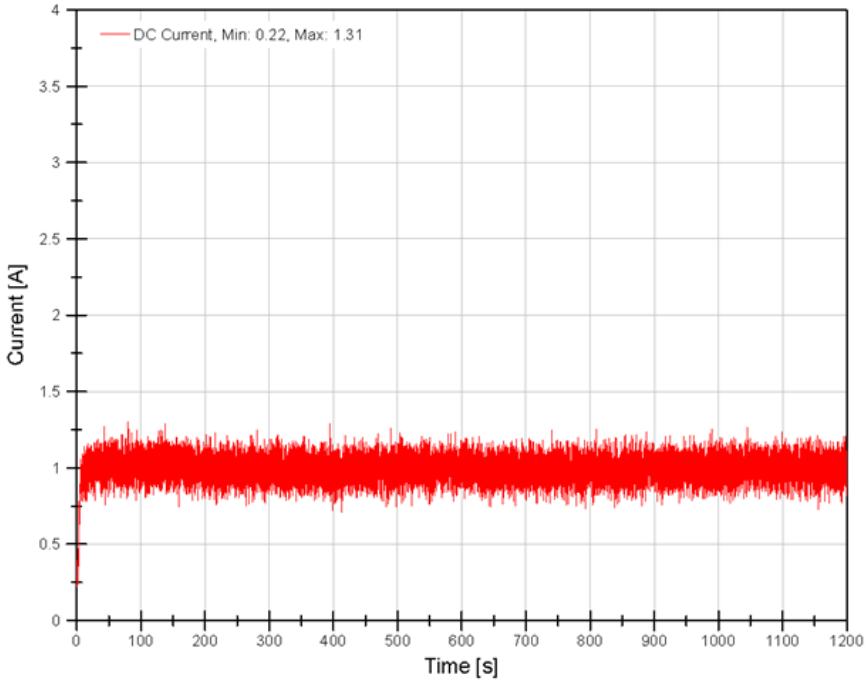

Figure K-30 Holding in Tension at 70°C Environment Temperature—Measured DC Bus Current

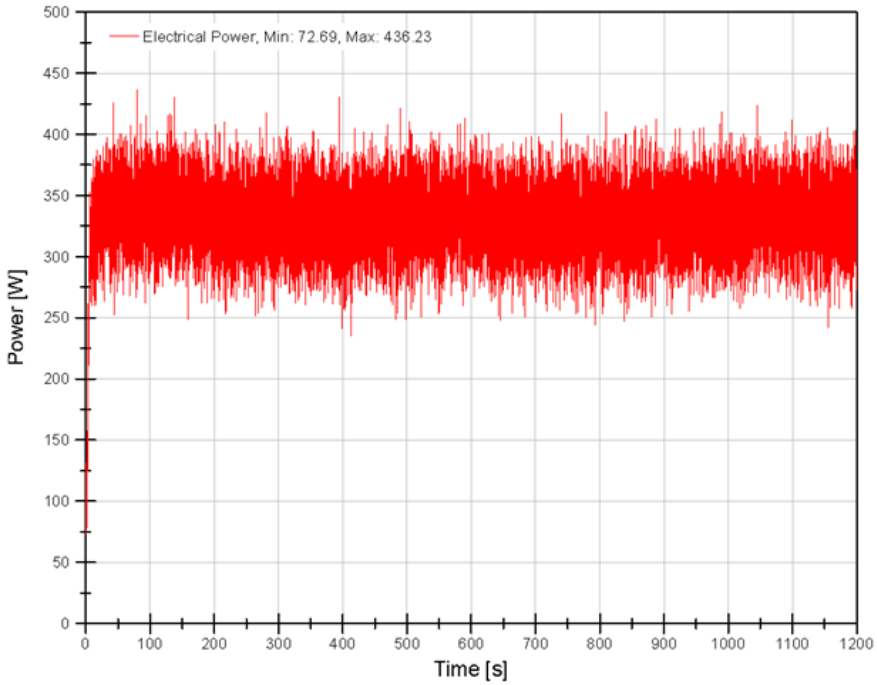

Figure K-31 Holding in Tension at 70°C Environment Temperature—Calculated Electrical Power

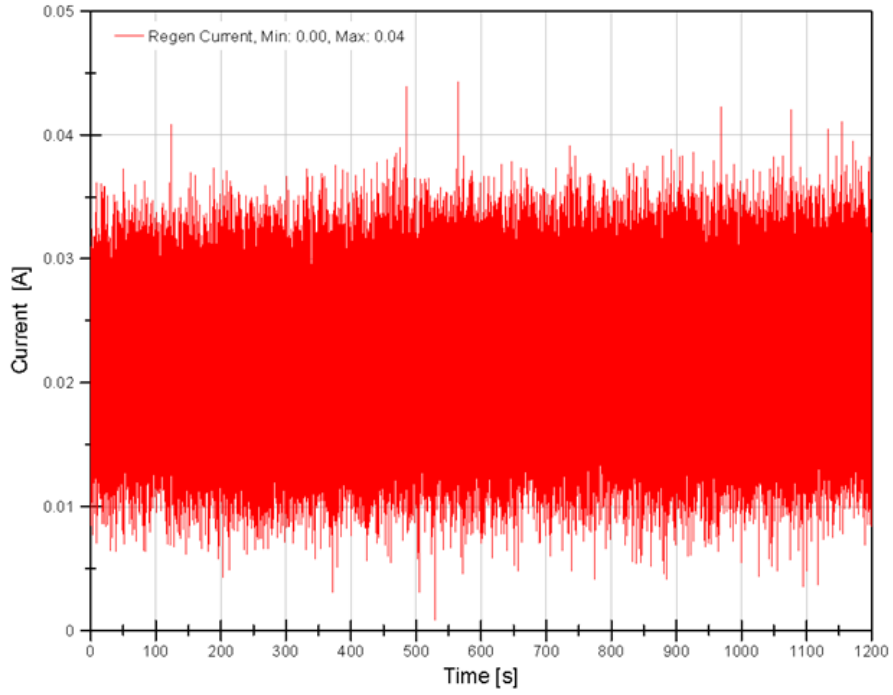

Figure K-32 Holding in Tension at 70°C Environment Temperature—Measured Regen Circuit Current

Holding in Tension at 70°C Environment Temperature Thermal Results

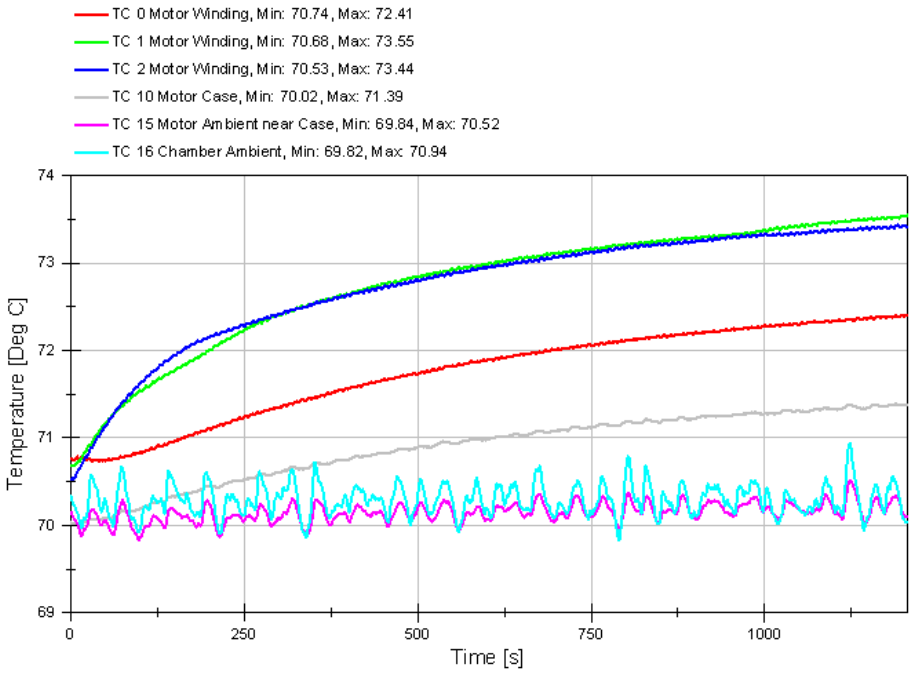

Figure K-33 Holding in Tension at 70°C Environment Temperature—EMA Temperature

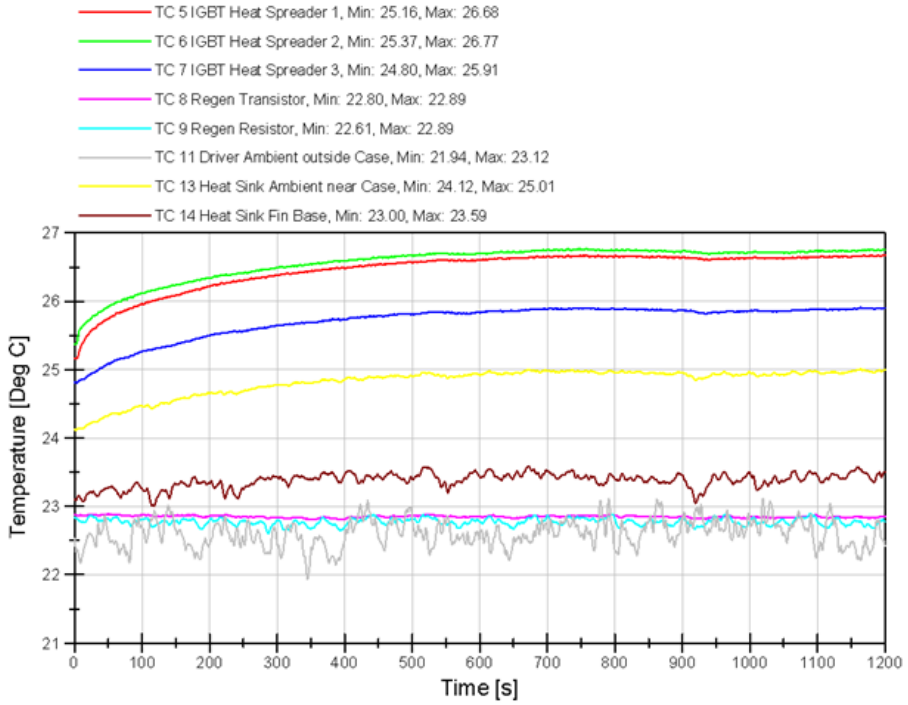

Figure K-34 Holding in Tension at 70°C Environment Temperature—Motor Controller Temperature

Note: Motor Controller was outside the environmental chamber.

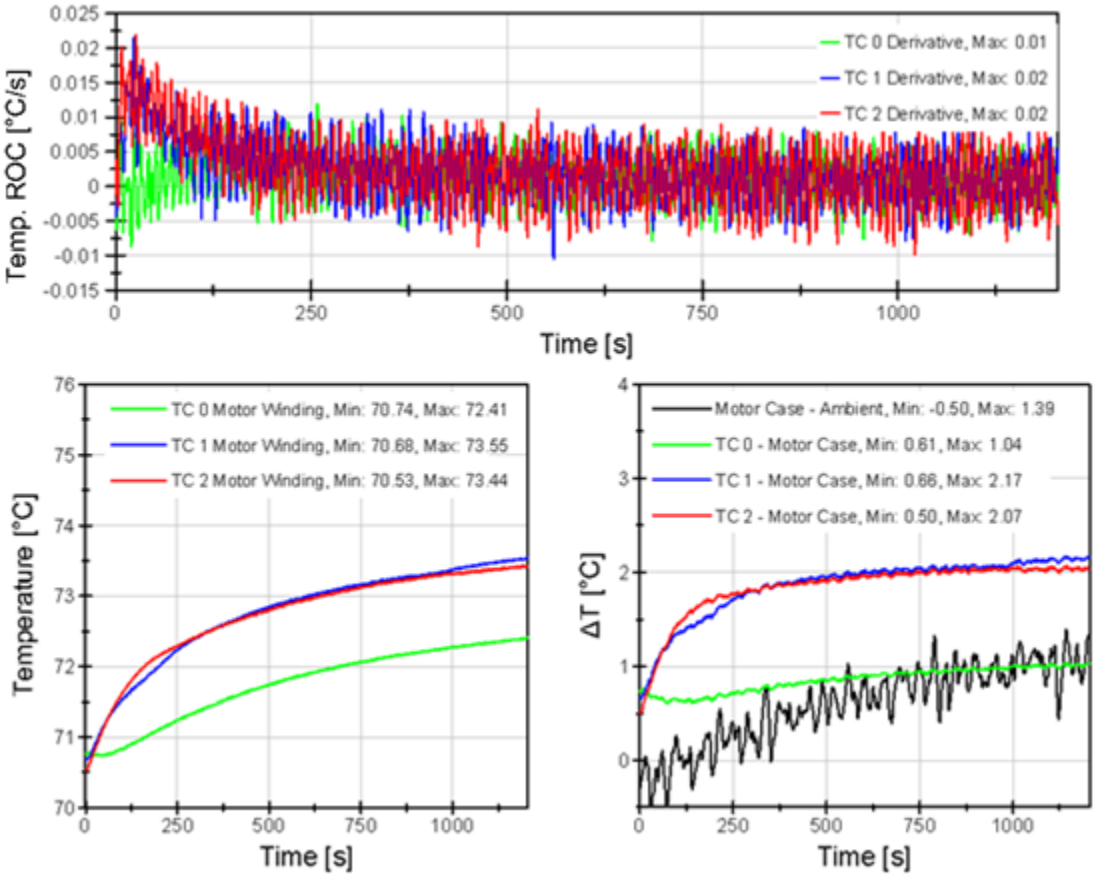

Figure K-35 Holding in Tension at 70°C Environment Temperature—Thermal Results

Holding in Tension at 70°C Environment Temperature Conservation of Energy

Note: Calculated electrical energy (green) was covered by calculated thermal energy (red) in Figure K-36 because both trends were very similar.

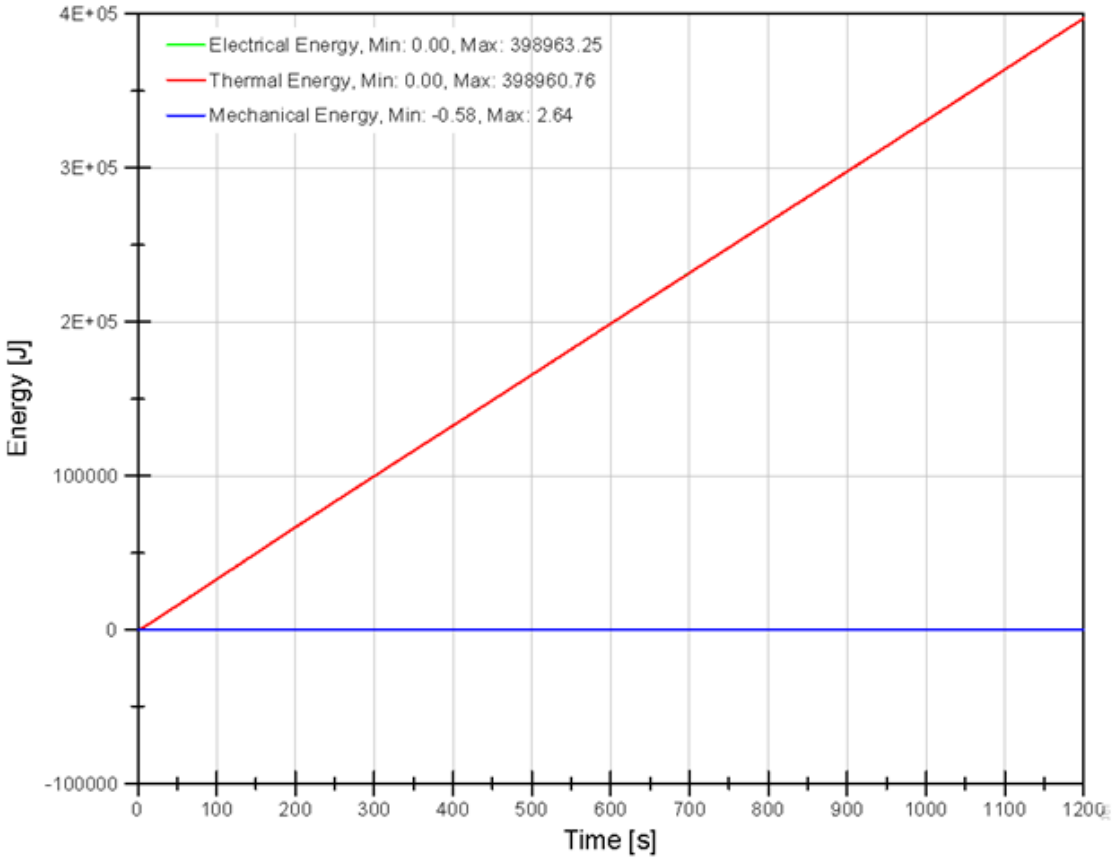

Figure K-36 Holding in Tension at 70°C Environment Temperature—Calculated COE

Holding in Compression at 22°C Environment Temperature Mechanical Results

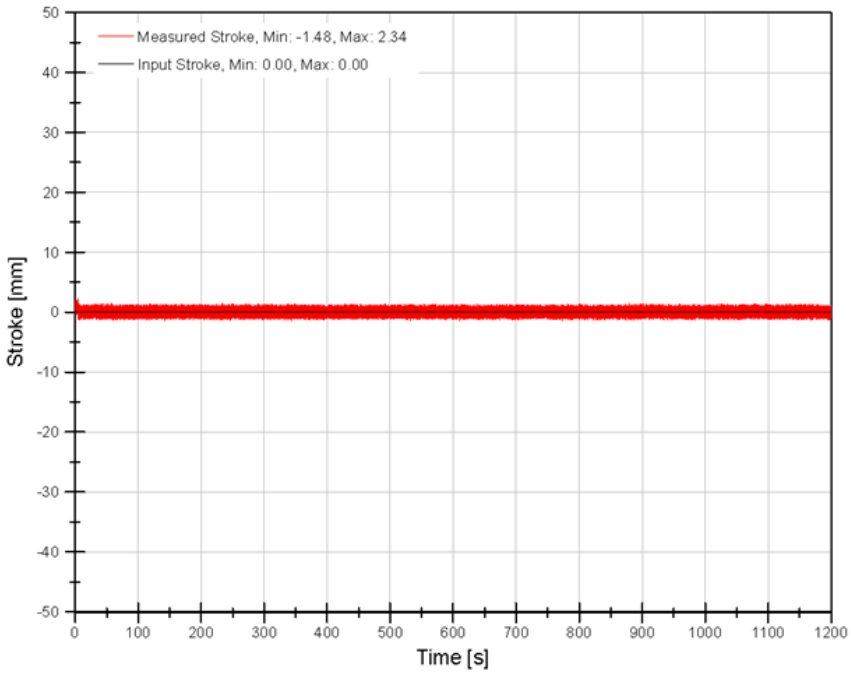

Figure K-37 Holding in Compression at 22°C Environment Temperature—Input and Measured Stroke

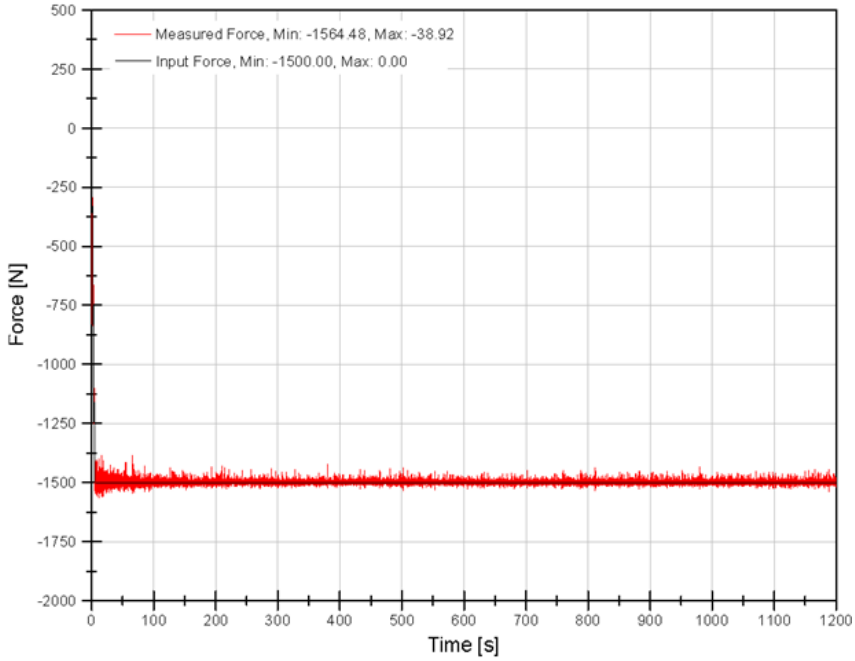

Figure K-38 Holding in Compression at 22°C Environment Temperature—Input and Measured Force

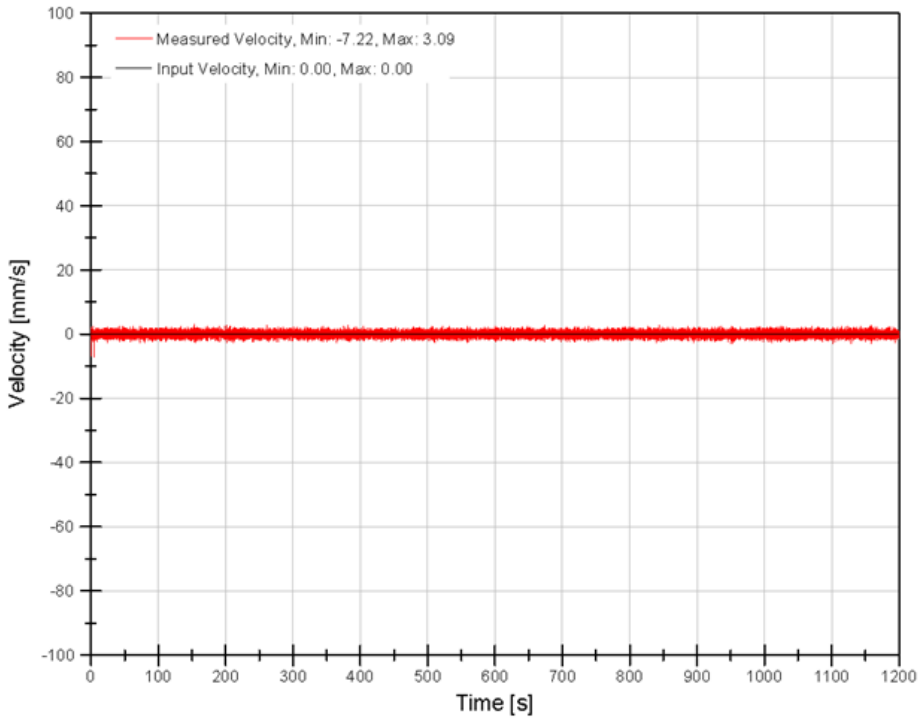

Figure K-39 Holding in Compression at 22°C Environment Temperature—Calculated Velocity

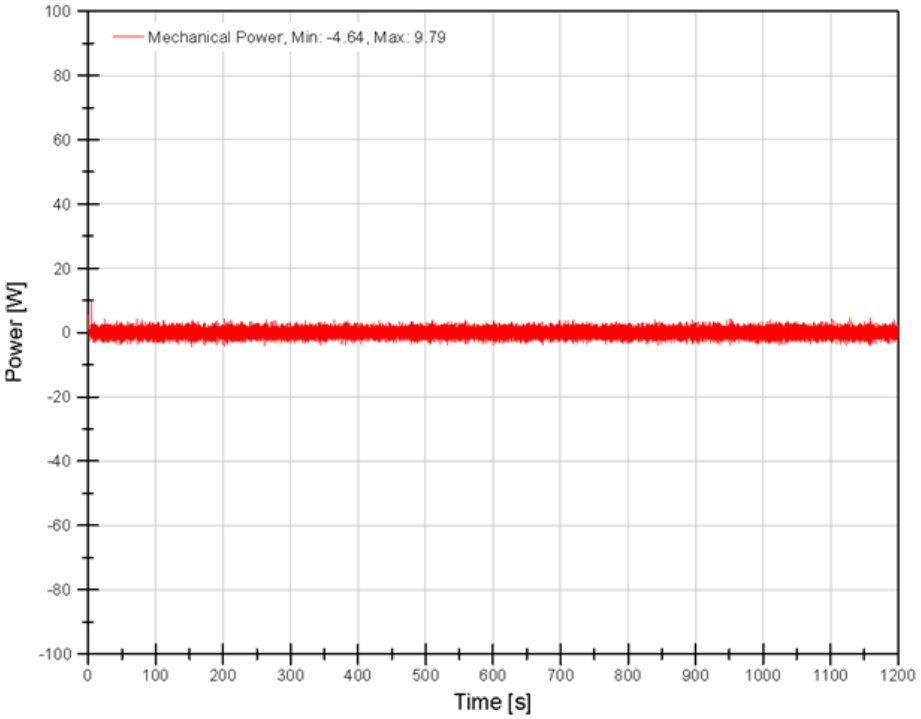

Figure K-40 Holding in Compression at 22°C Environment Temperature—Calculated Mechanical Power

Holding in Compression at 22°C Environment Temperature Electrical Results

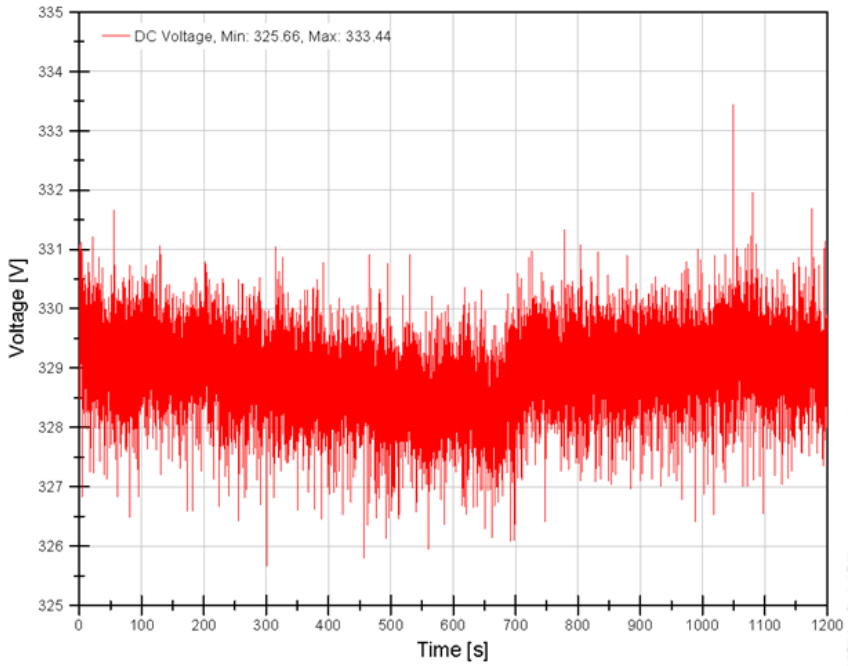

Figure K-41 Holding in Compression at 22°C Environment Temperature—Measured DC Bus Voltage

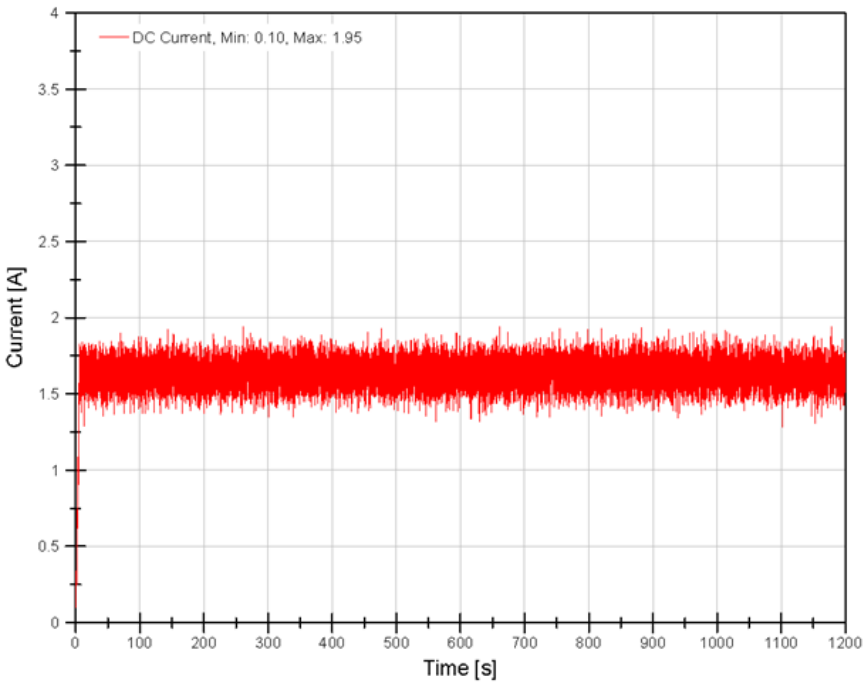

Figure K-42 Holding in Compression at 22°C Environment Temperature—Measured DC Bus Current

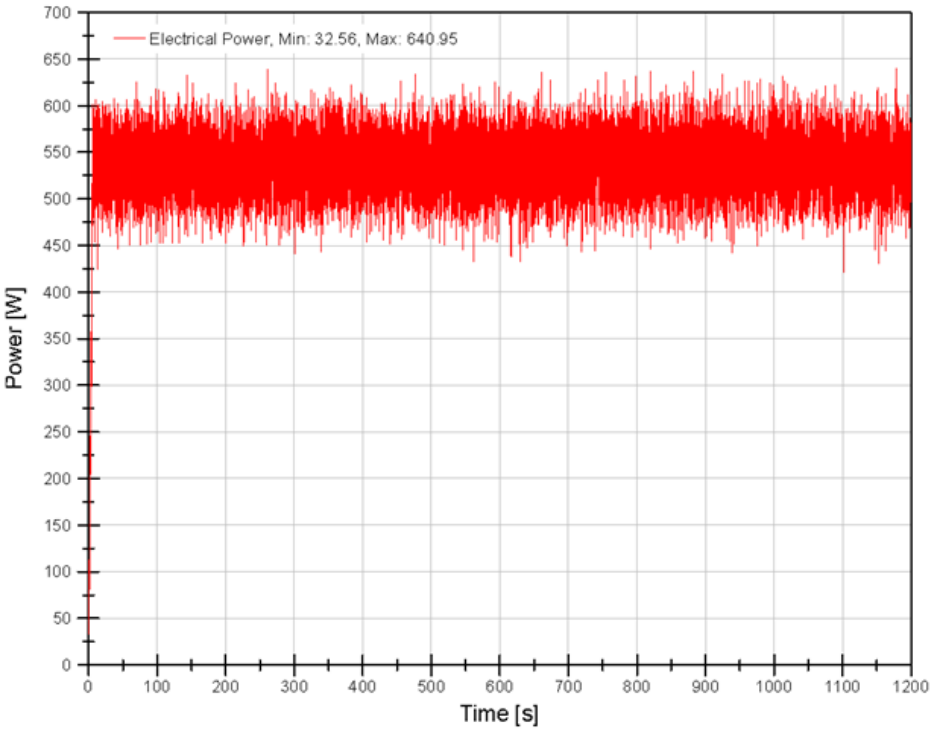

Figure K-43 Holding in Compression at 22°C Environment Temperature—Calculated Electrical Power

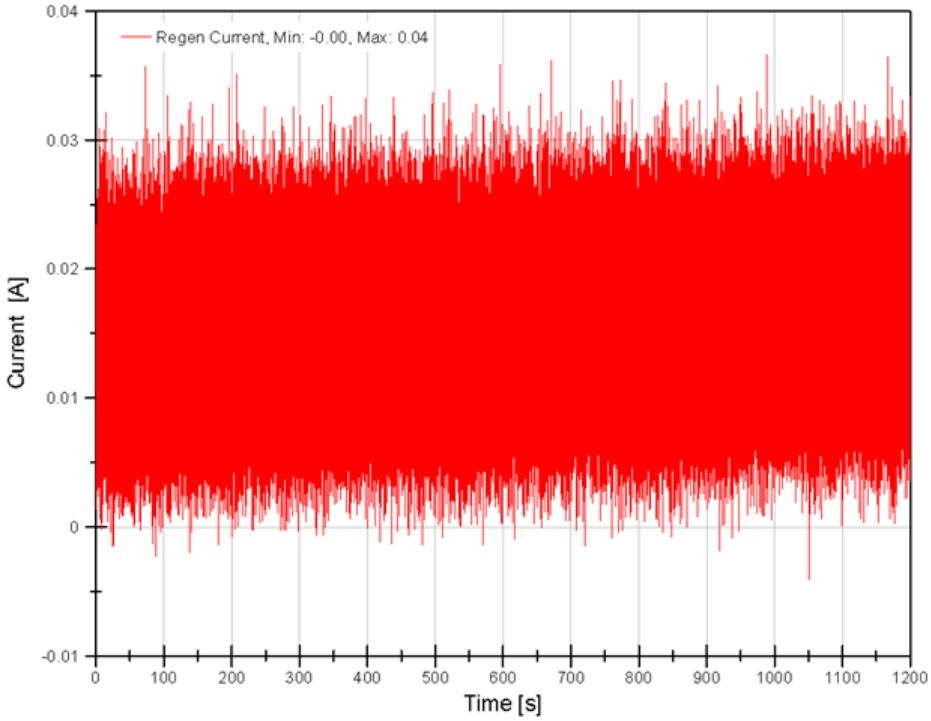

Figure K-44 Holding in Compression at 22°C Environment Temperature—Measured Regen Circuit Current

Holding in Compression at 22°C Environment Temperature Thermal Results

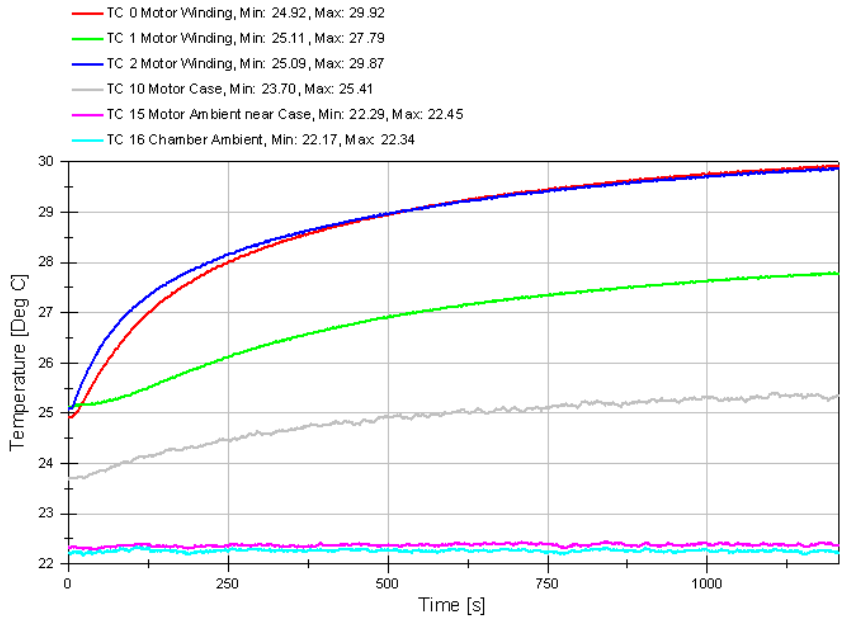

Figure K-45 Holding in Compression at 22°C Environment Temperature—EMA Temperature

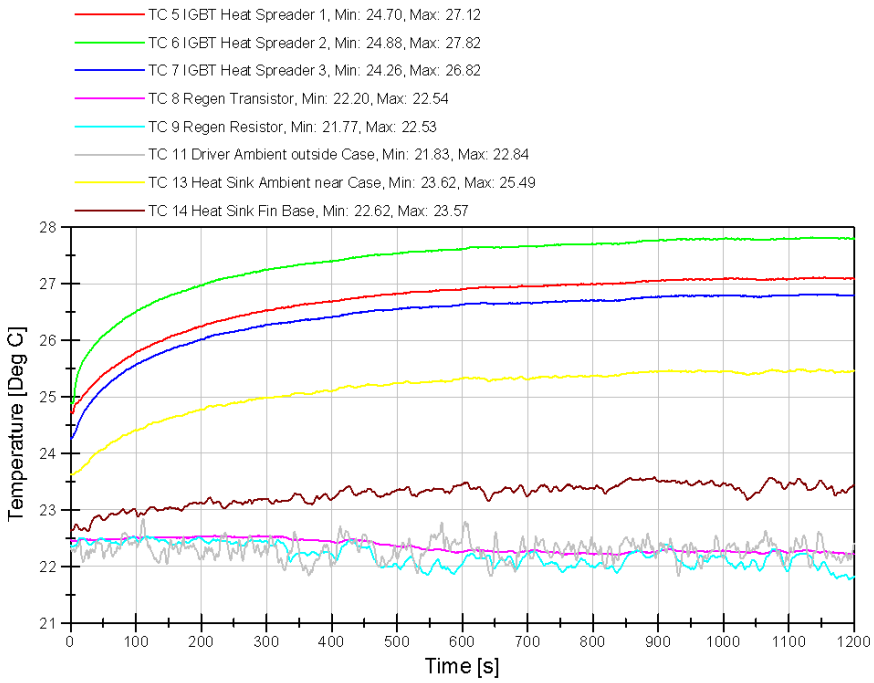

Figure K-46 Holding in Compression at 22°C Environment Temperature—Motor Controller Temperature

Note: Motor Controller was outside the environmental chamber.

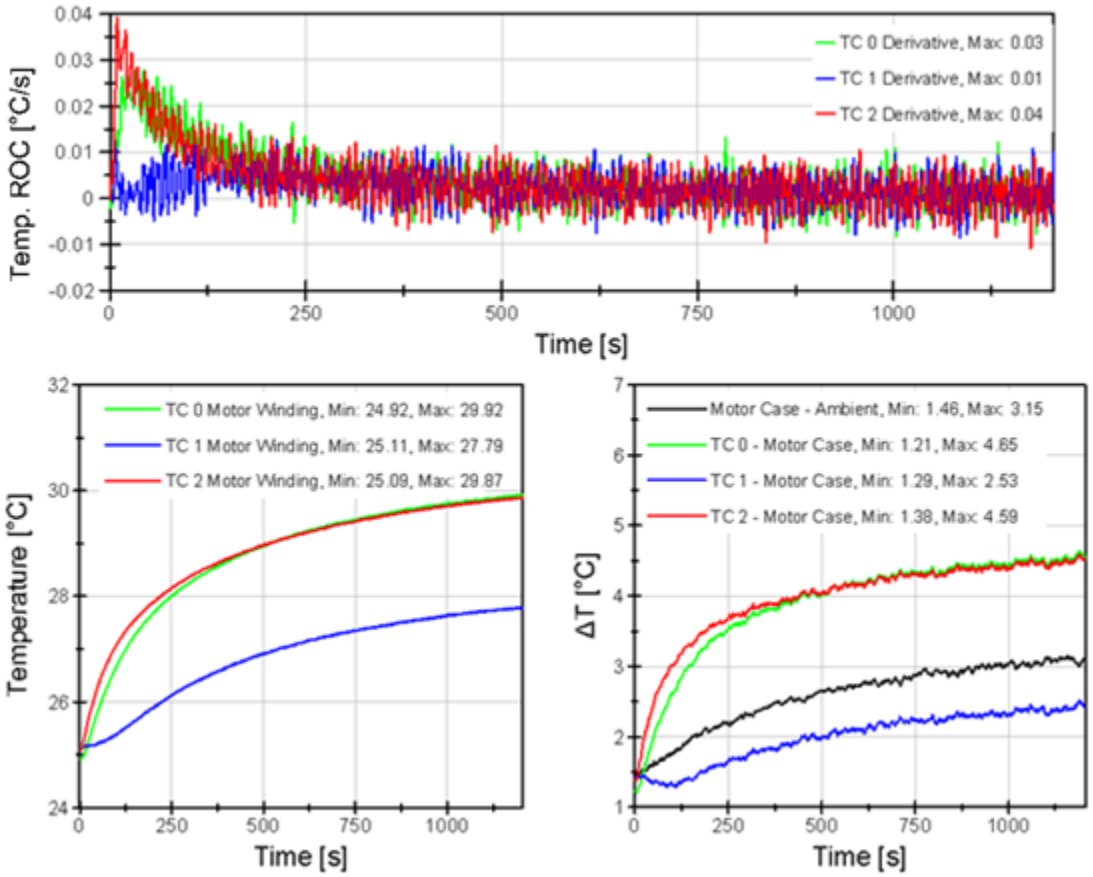

Figure K-47 Holding in Compression at 22°C Environment Temperature—Thermal Results

Holding in Compression at 22°C Environment Temperature Conservation of Energy

Note: Calculated electrical energy (green) was covered by calculated thermal energy (red) in Figure K-48 because both trends were very similar.

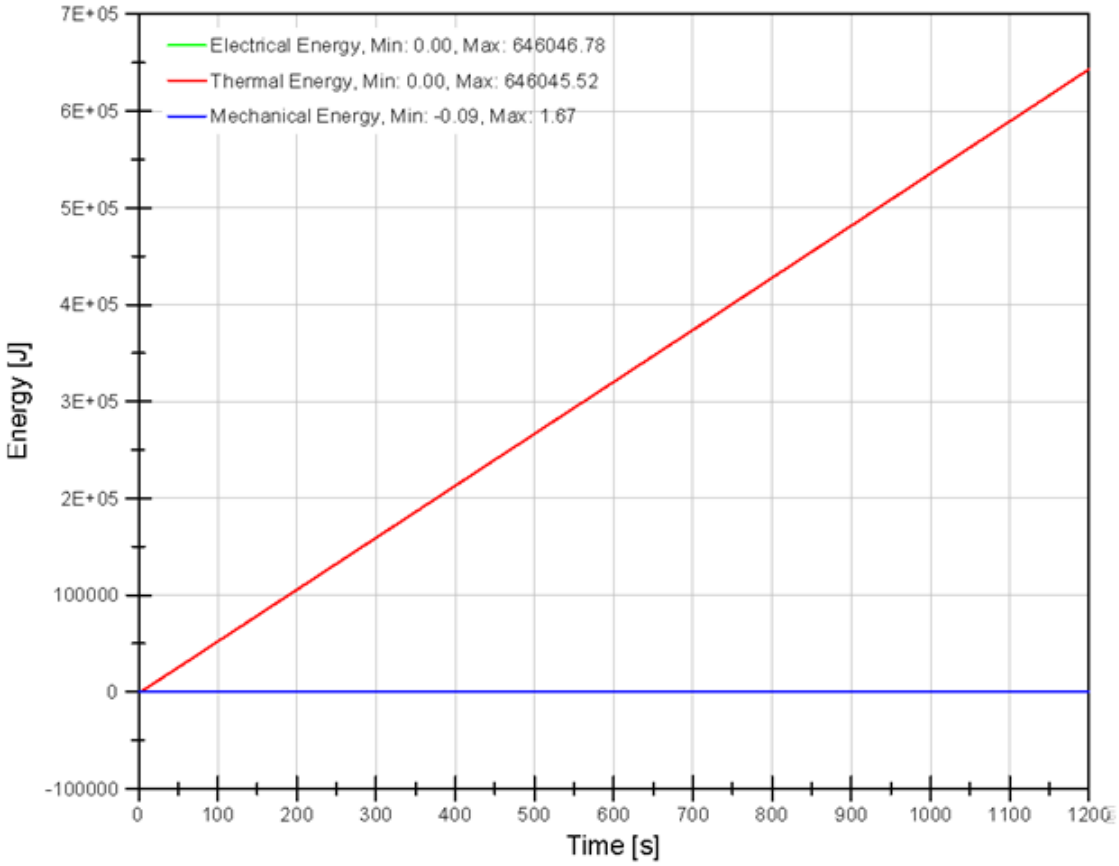

Figure K-48 Holding in Compression at 22°C Environment Temperature—Calculated COE

Short Mission Tests Summary

A short mission test was constructed to replicate a three minute highly dynamic mechanical profile and compare component temperature responses when executed in minimum bay temperature at altitude (~15°C) and maximum continuous bay temperature (70°). These tests were executed to gain insight on the electrical energy required to complete the same mechanical profile but at two vastly different ambient conditions. Note, thermal energy was based on the energy analysis developed in section 4.7.3 and was calculated as the difference in electrical and mechanical energy.

Table K-3 Short Mission Test COE Summary

Test		Post Test Analysis			
Profile	Profile Description	Electrical Energy [J]	Mechanical Energy [J]	Thermal Energy [J]	Efficiency
Short Mission	Mission segment representative stroke, force at environment temperature ~15°C	140,862 ± 845	3,423 ± 34	137,439 ± 825	2%
	Mission segment representative stroke and force at environment temperature 70°C	59,248 ± 356	7,374 ± 74	51,874 ± 311	12%

Table K-4 Short Mission Test Thermal Summary

Test		Post Test Analysis			
Profile	Profile Description	Peak TC ROC [°C/s]	Max Motor Case-Ambient ΔT [°C]	Avg. Current [A]	Peak Current [A]
Short Mission	Mission segment representative stroke, force at environment temperature ~15°C	0.22	15.11	1.86	8.23
	Mission segment representative stroke and force at environment temperature 70°C	0.06	1.04	0.77	5.13

Short Mission at ~15°C Simulated Bay Temperature Mechanical Results

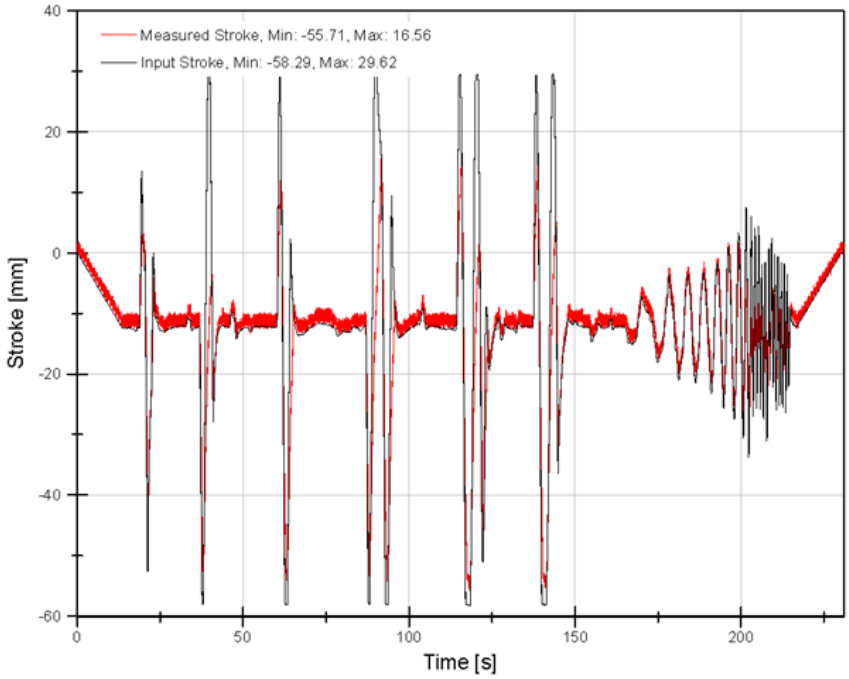

Figure K-49 Short Mission at ~15°C Simulated Bay Temperature—Input and Measured Stroke

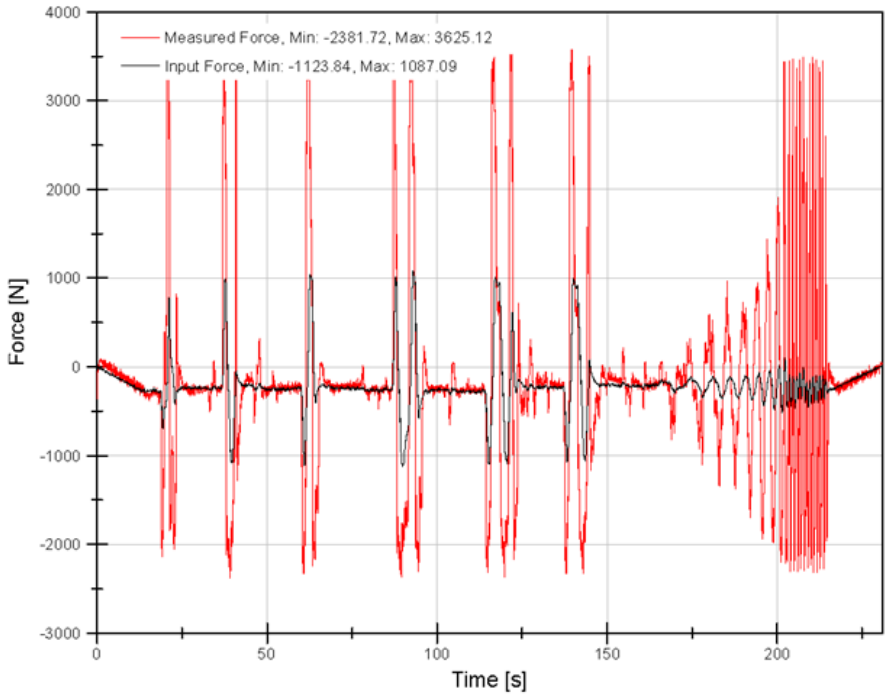

Figure K-50 Short Mission at ~15°C Simulated Bay Temperature—Input and Measured Force

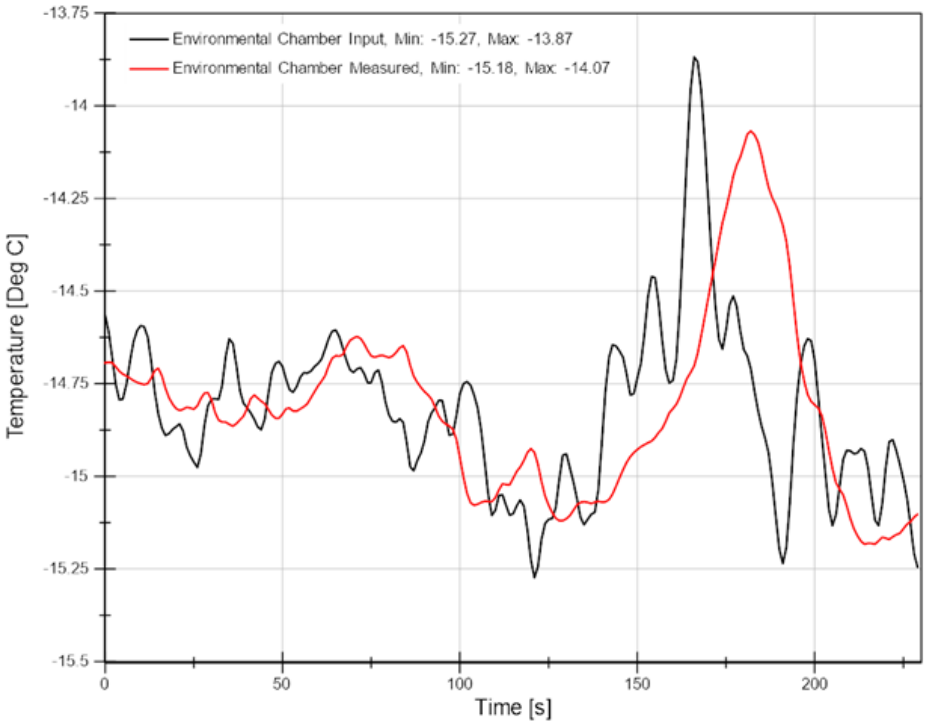

Figure K-51 Short Mission at ~15°C Simulated Bay Temperature—Input and Measured Environment Temperature

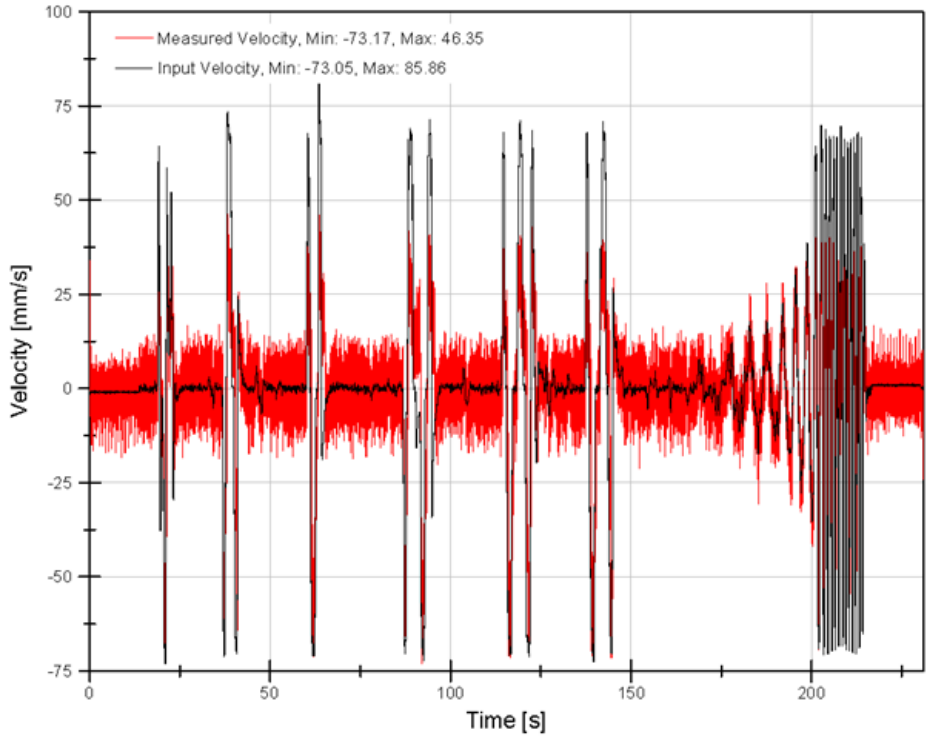

Figure K-52 Short Mission at ~15°C Simulated Bay Temperature—Calculated Velocity

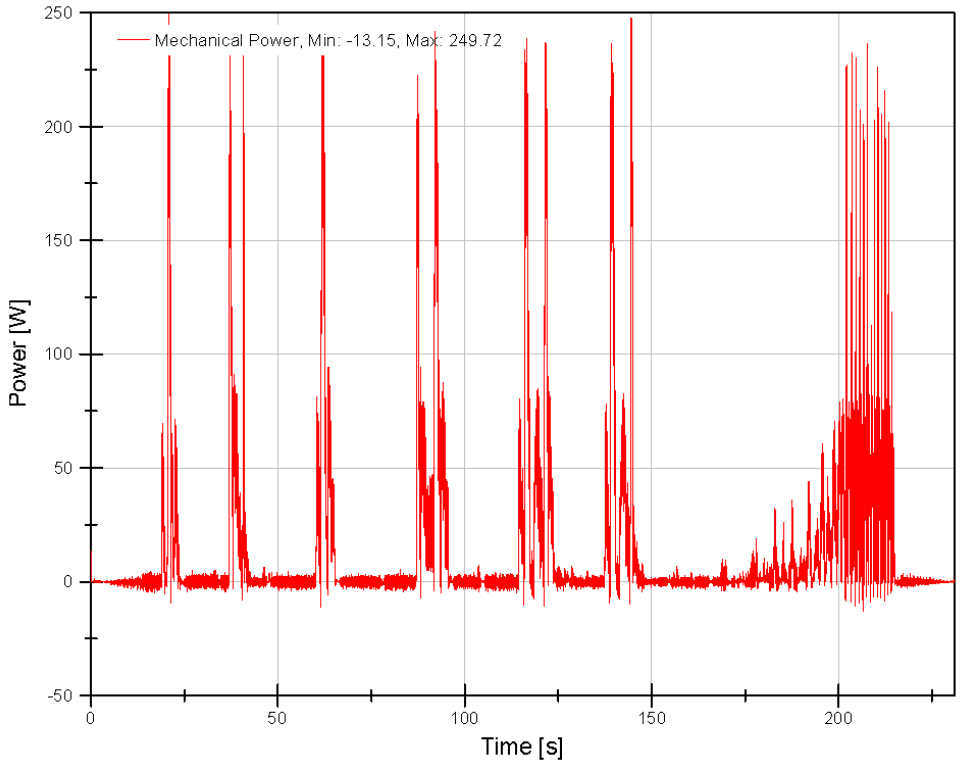

Figure K-53 Short Mission at ~15°C Simulated Bay Temperature—Calculated Mechanical Power

Short Mission at ~15°C Simulated Bay Temperature Electrical Results

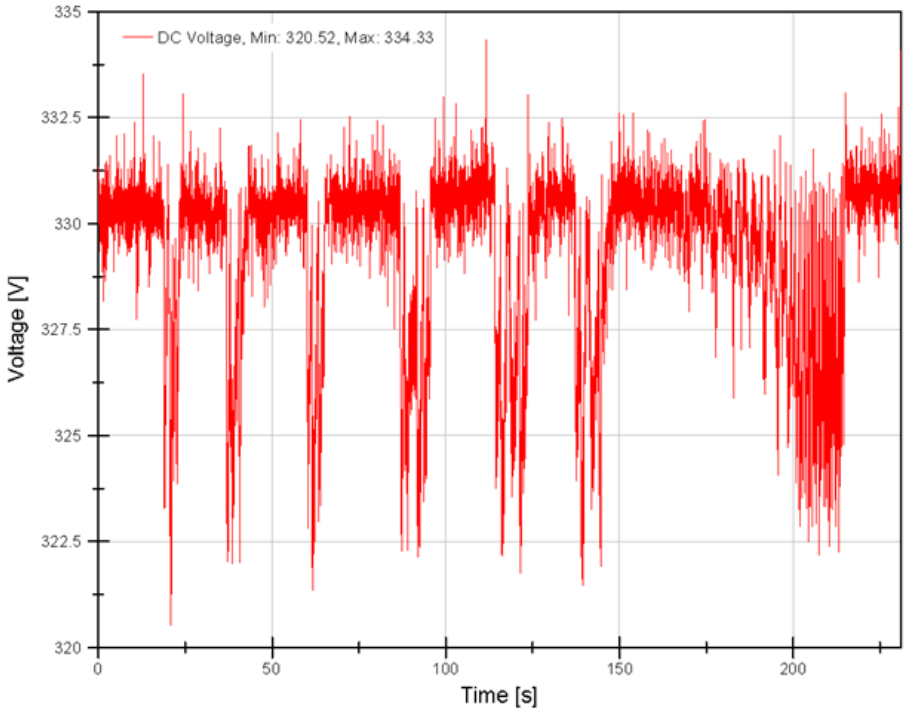

Figure K-54 Short Mission at ~15°C Simulated Bay Temperature—Measured DC Bus Voltage

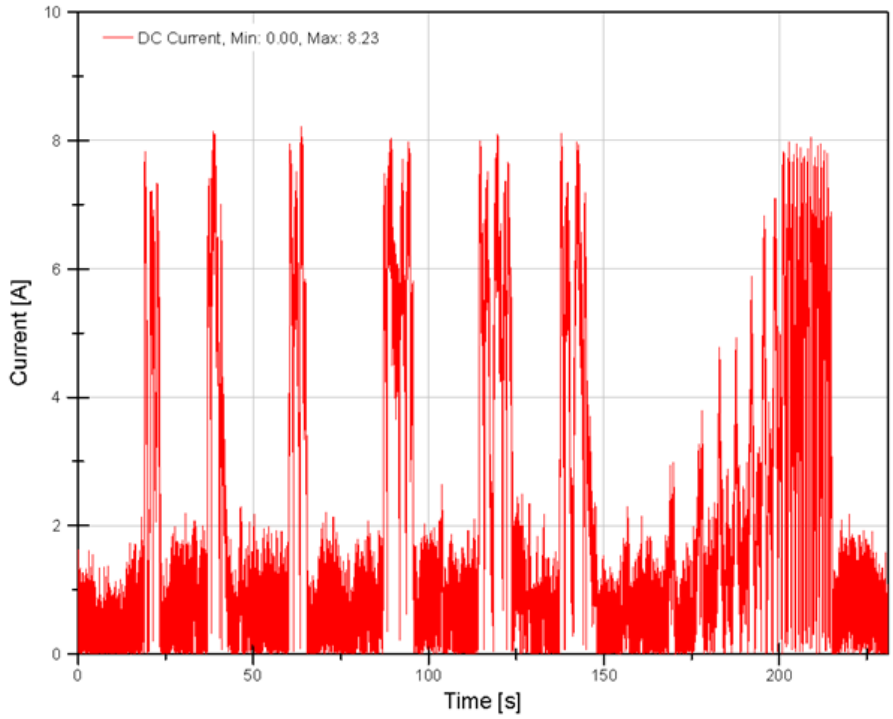

Figure K-55 Short Mission at ~15°C Simulated Bay Temperature—Measured DC Bus Current

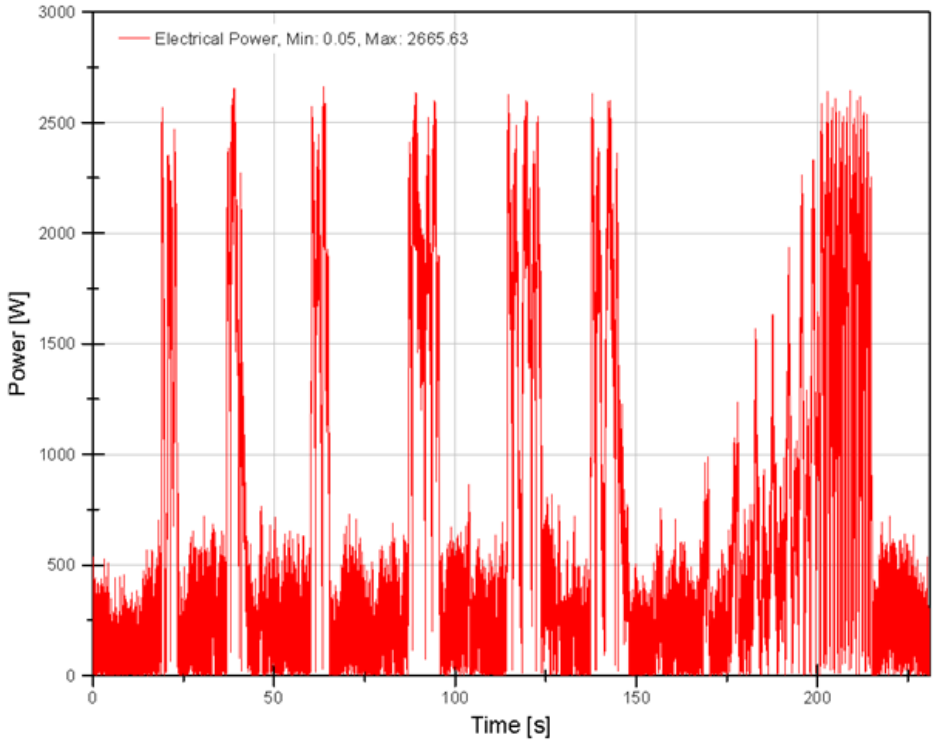

Figure K-56 Short Mission at ~15°C Simulated Bay Temperature—Calculated Electrical Power

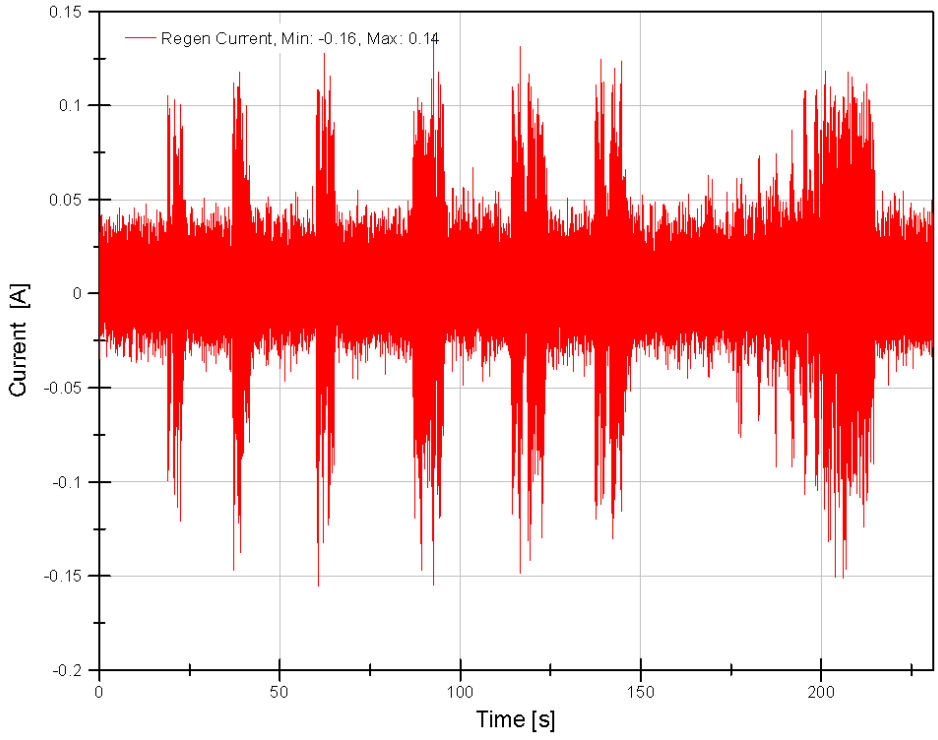

Figure K-57 Short Mission at ~15°C Simulated Bay Temperature—Measured Regen Circuit Current

Short Mission at ~15°C Simulated Bay Temperature Thermal Results

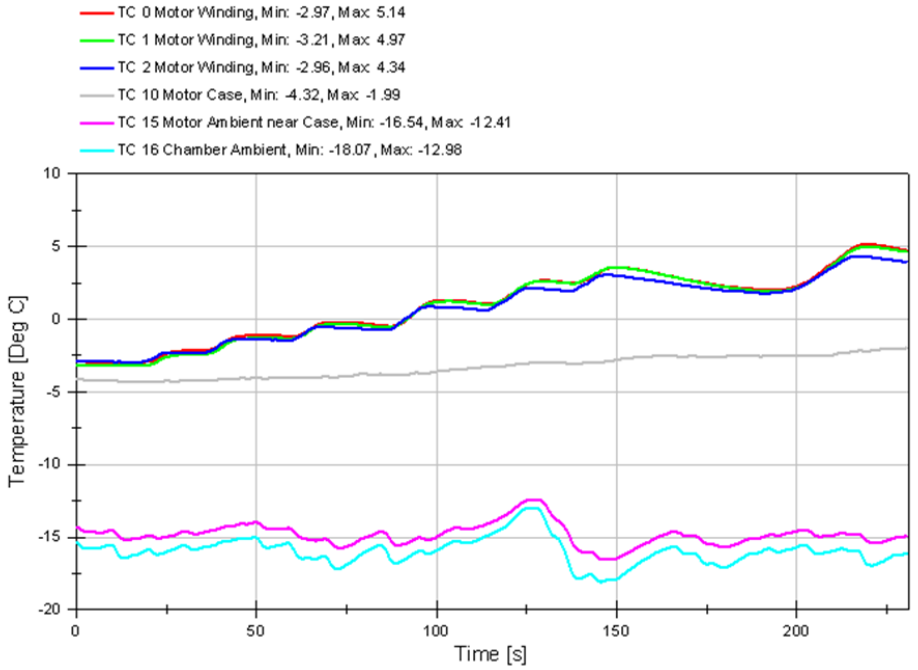

Figure K-58 Short Mission at ~15°C Simulated Bay Temperature—EMA Temperature

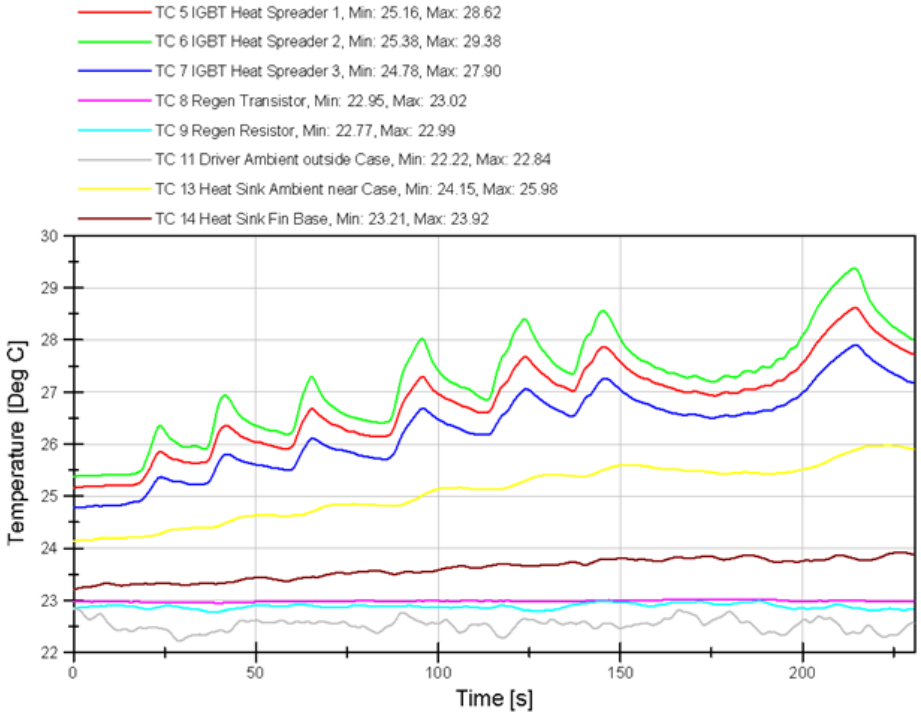

Figure K-59 Short Mission at ~15°C Simulated Bay Temperature—Motor Controller Temperature

Note: Motor Controller was outside the environmental chamber.

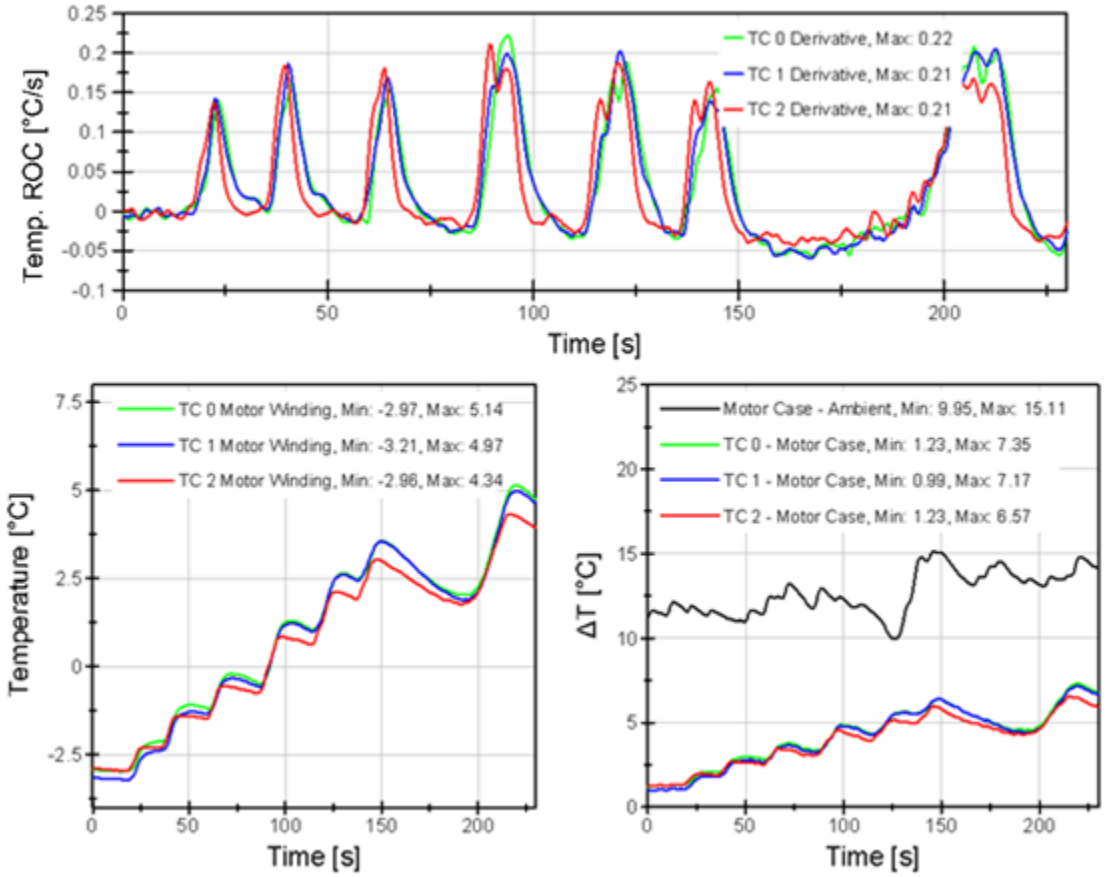

Figure K-60 Short Mission at ~15°C Simulated Bay Temperature—Thermal Results

Short Mission at ~15°C Simulated Bay Temperature Conservation of Energy

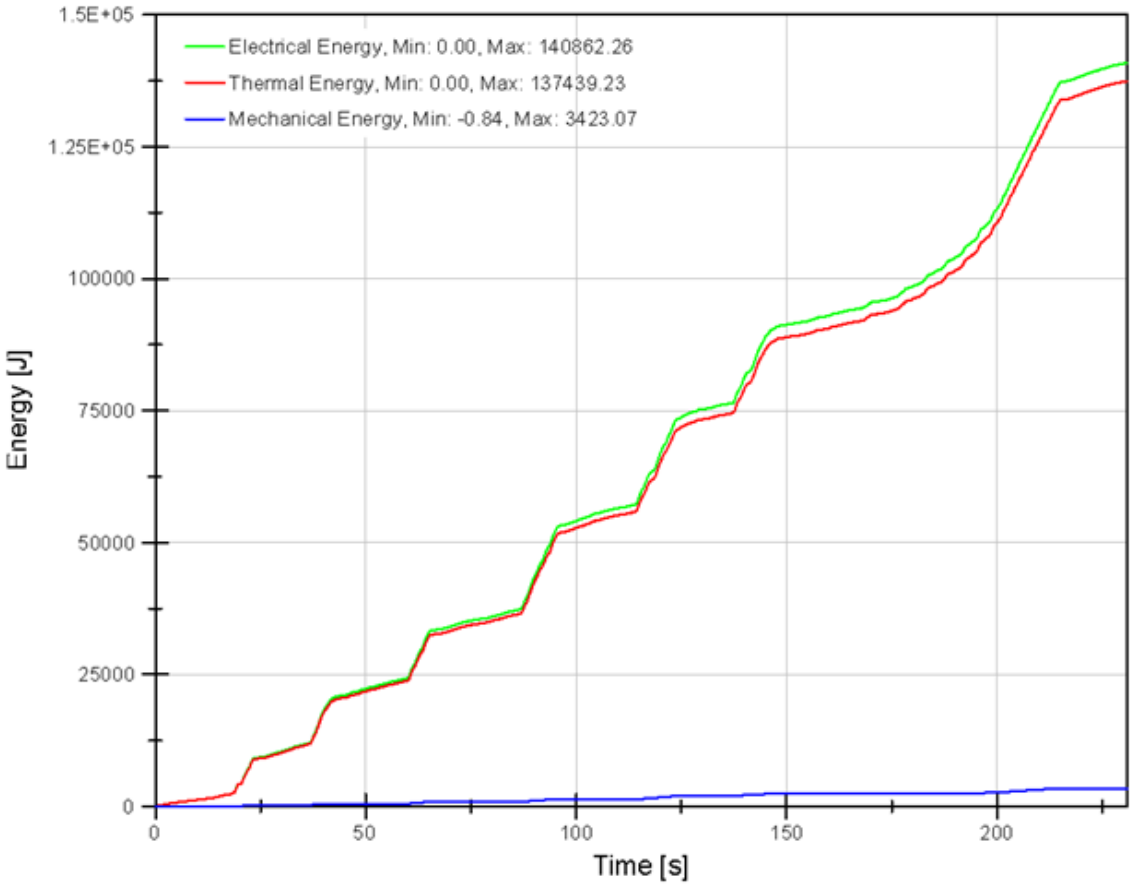

Figure K-61 Short Mission at ~15°C Simulated Bay Temperature—Calculated COE

Short Mission at 70°C Mechanical Results

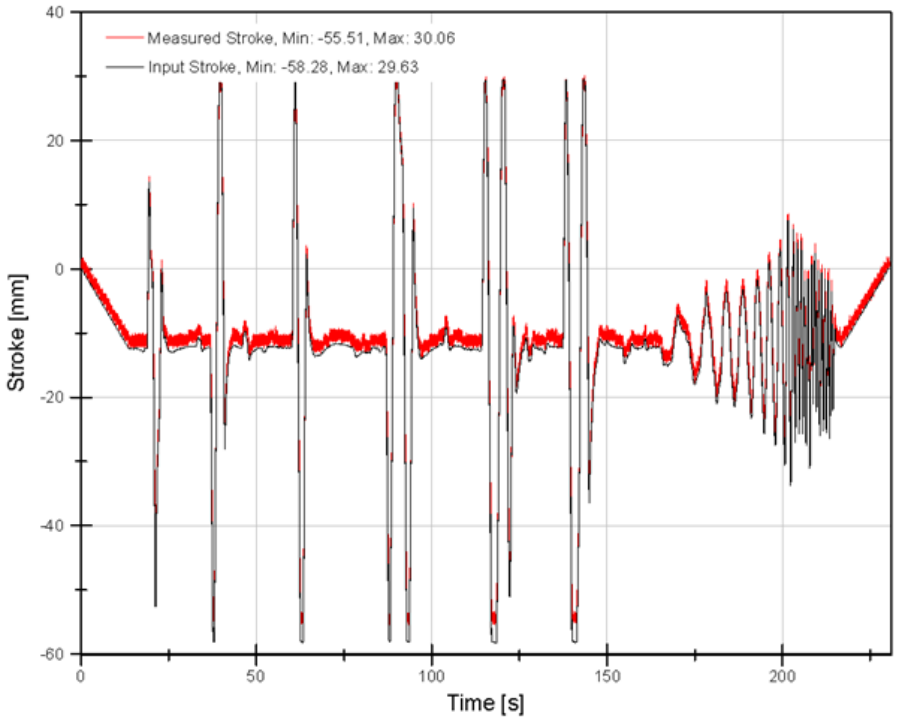

Figure K-62 Short Mission at 70°C Environment Temperature—Input and Measured Stroke

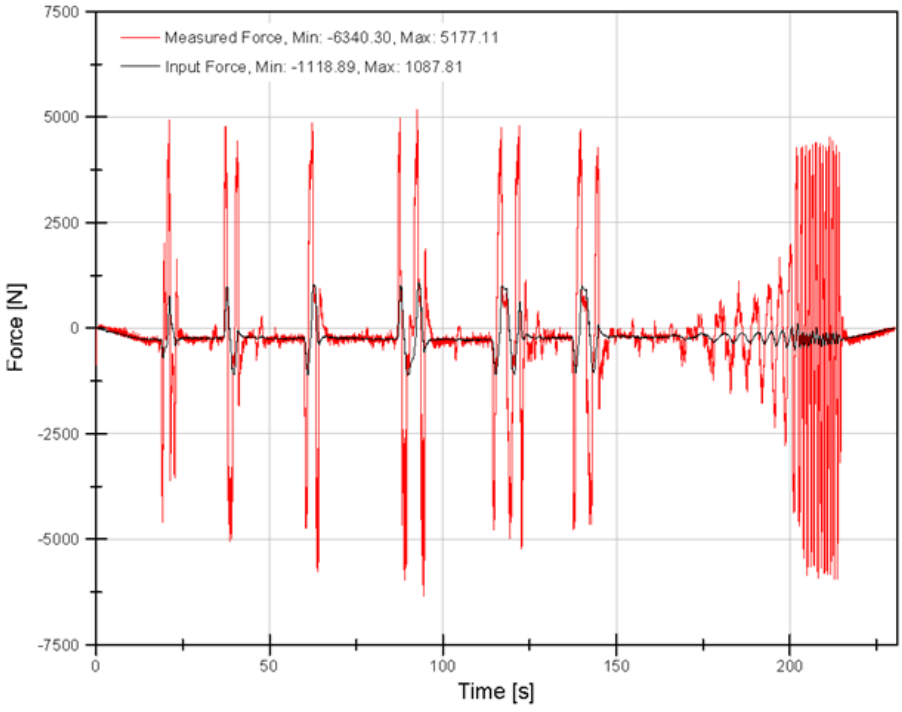

Figure K-63 Short Mission at 70°C Environment Temperature—Input and Measured Force

Figure K-64 Short Mission at 70°C Environment Temperature—Input and Measured Environment Temperature

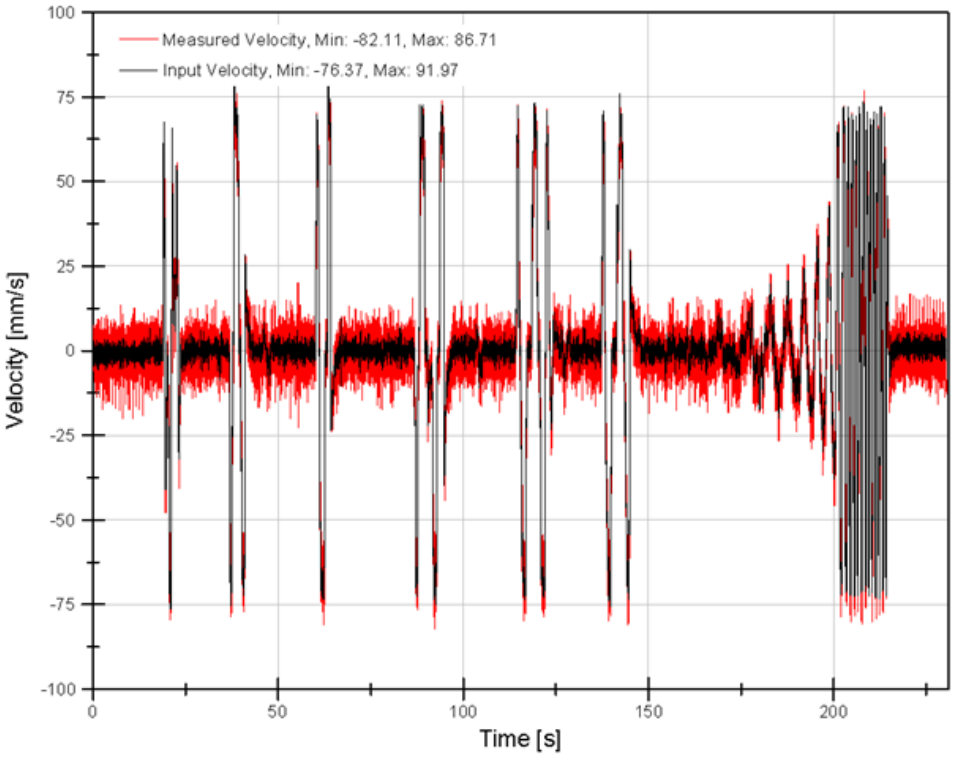

Figure K-65 Short Mission at 70°C Environment Temperature—Calculated Velocity

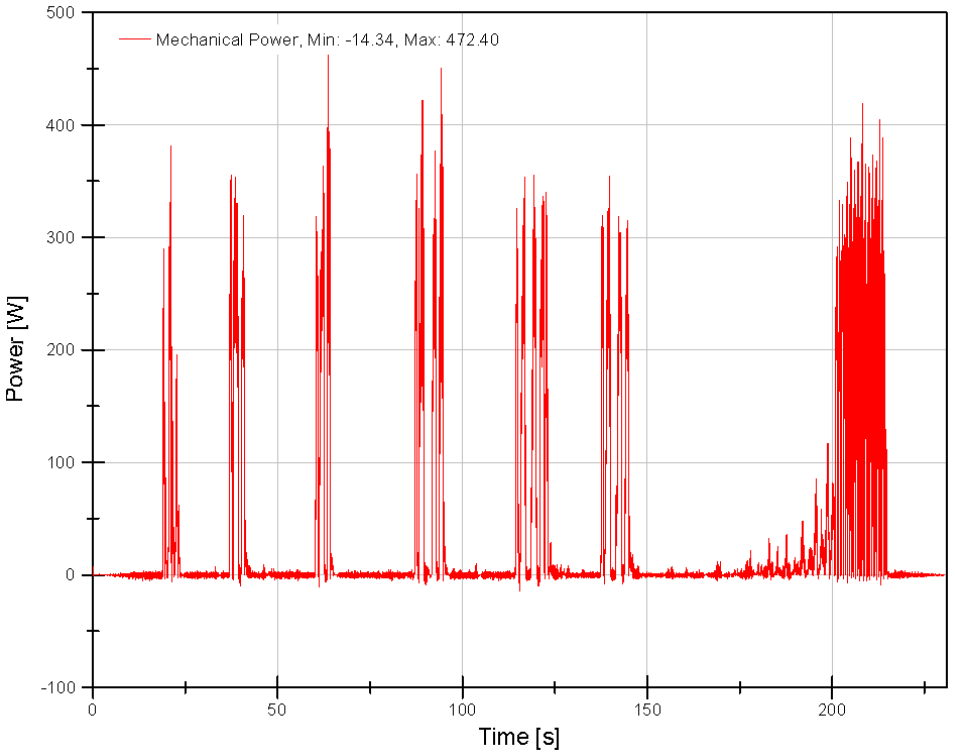

Figure K-66 Short Mission at 70°C Environment Temperature—Calculated Mechanical Power

Short Mission at 70°C Electrical Results

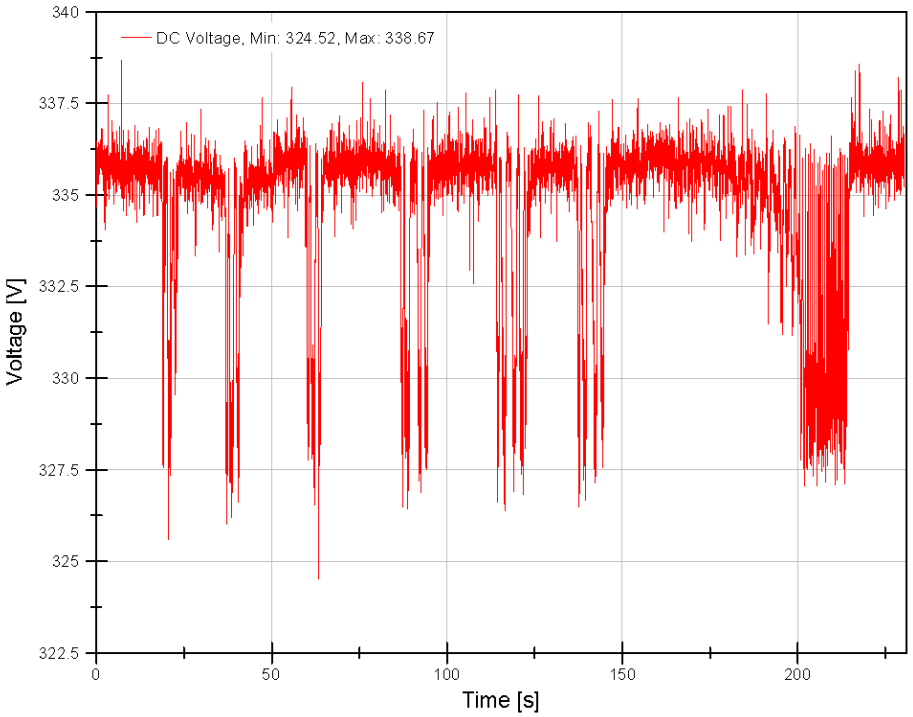

Figure K-67 Short Mission at 70°C Environment Temperature—Measured DC Bus Voltage

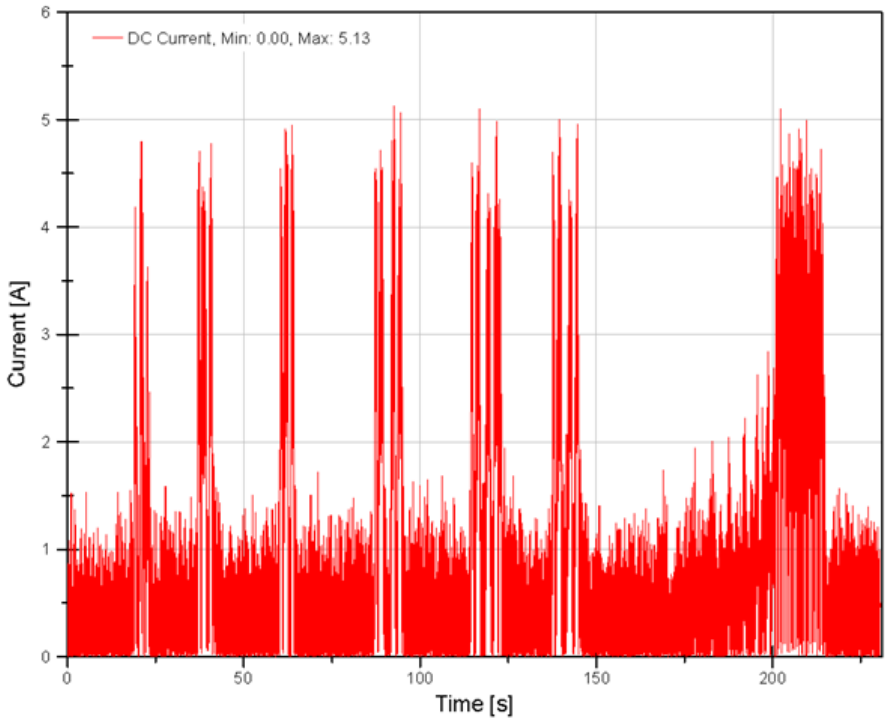

Figure K-68 Short Mission at 70°C Environment Temperature—Measured DC Bus Current

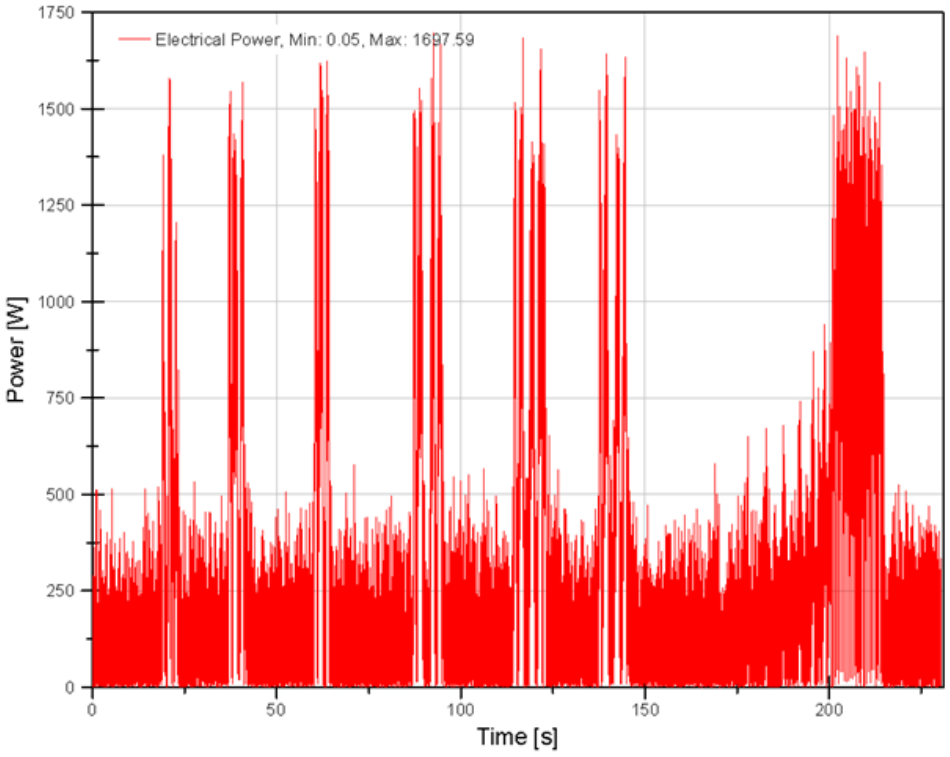

Figure K-69 Short Mission at 70°C Environment Temperature—Calculated Electrical Power

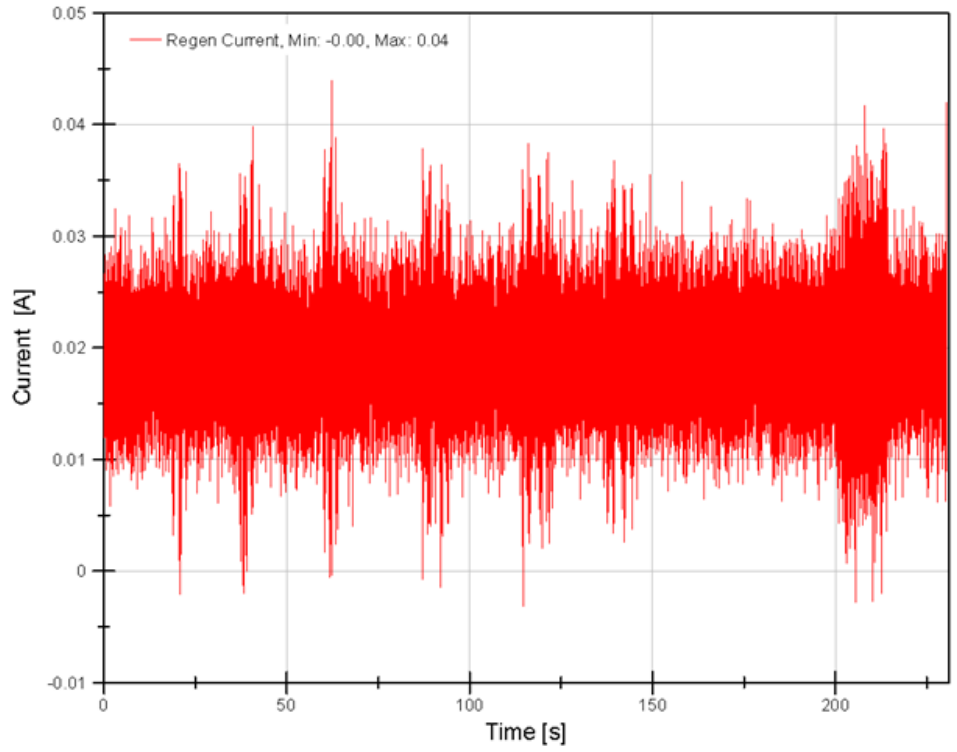

Figure K-70 Short Mission at 70°C Environment Temperature—Measured Regen Circuit Current

Short Mission at 70°C Thermal Results

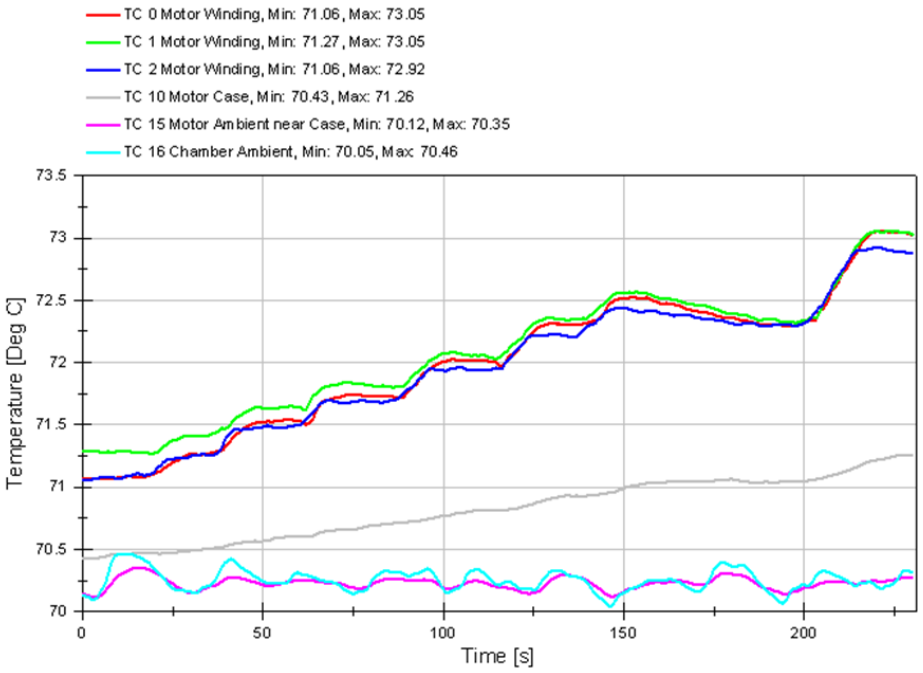

Figure K-71 Short Mission at 70°C Environment Temperature—EMA Temperature

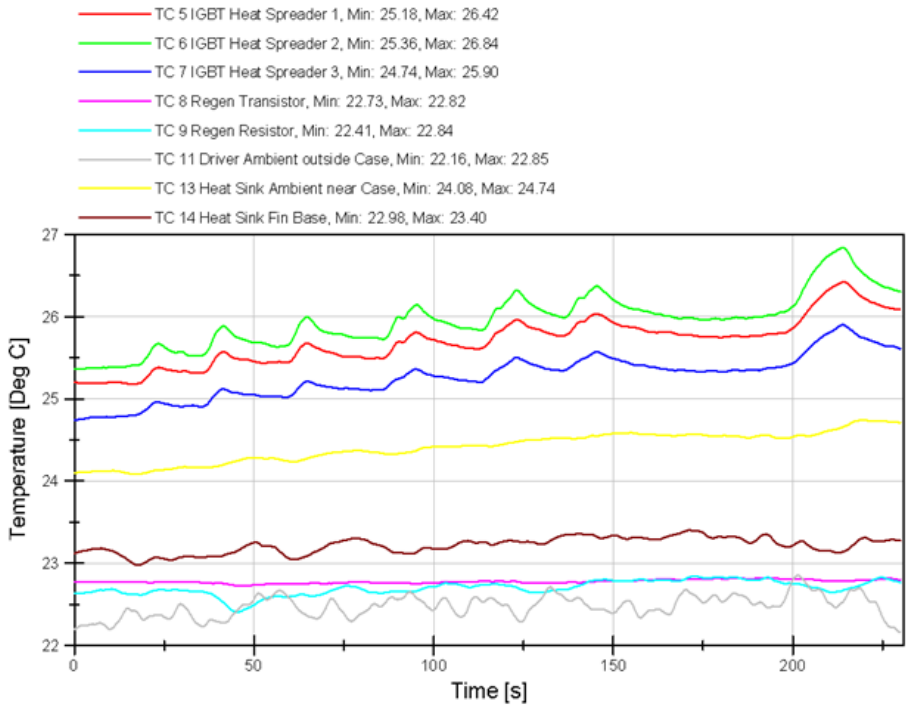

Figure K-72 Short Mission at 70°C Environment Temperature--Motor Controller Temperature

Note: Motor Controller was outside the environmental chamber.

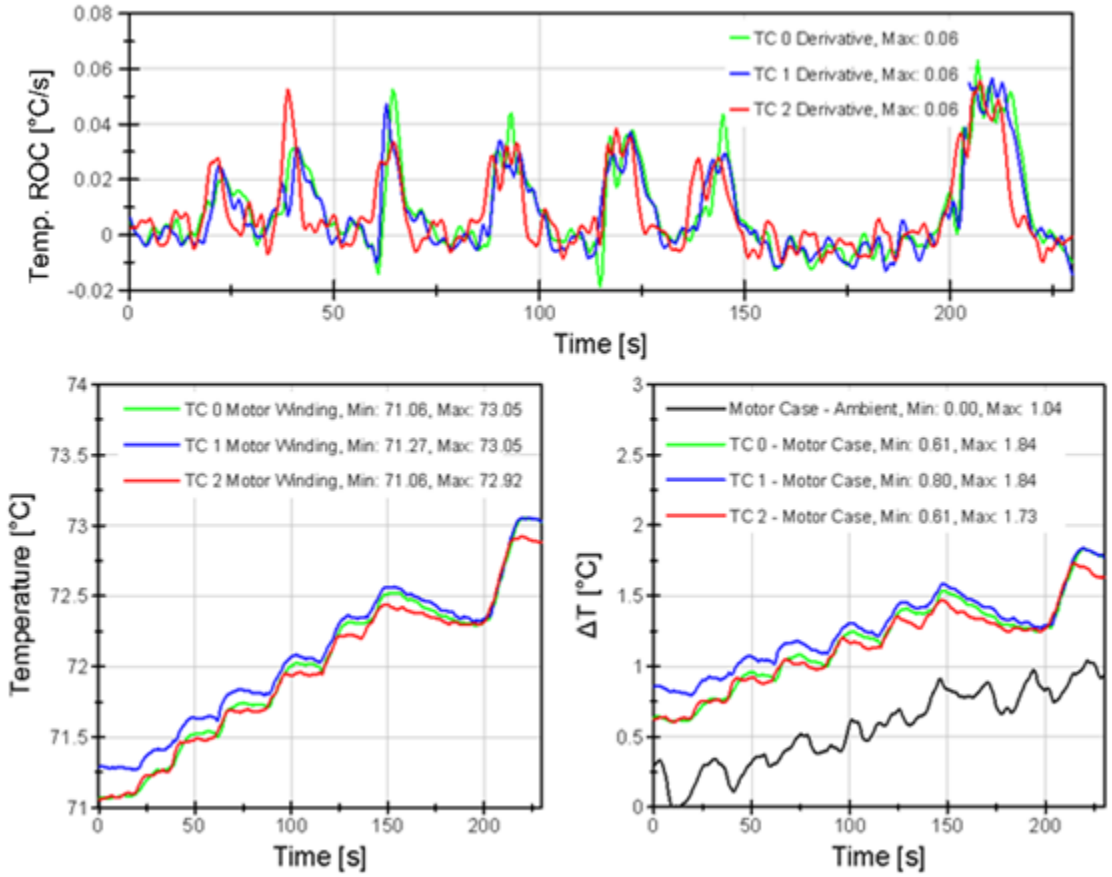

Figure K-73 Short Mission at 70°C Environment Temperature—Thermal Results

Short Mission at 70°C Conservation of Energy

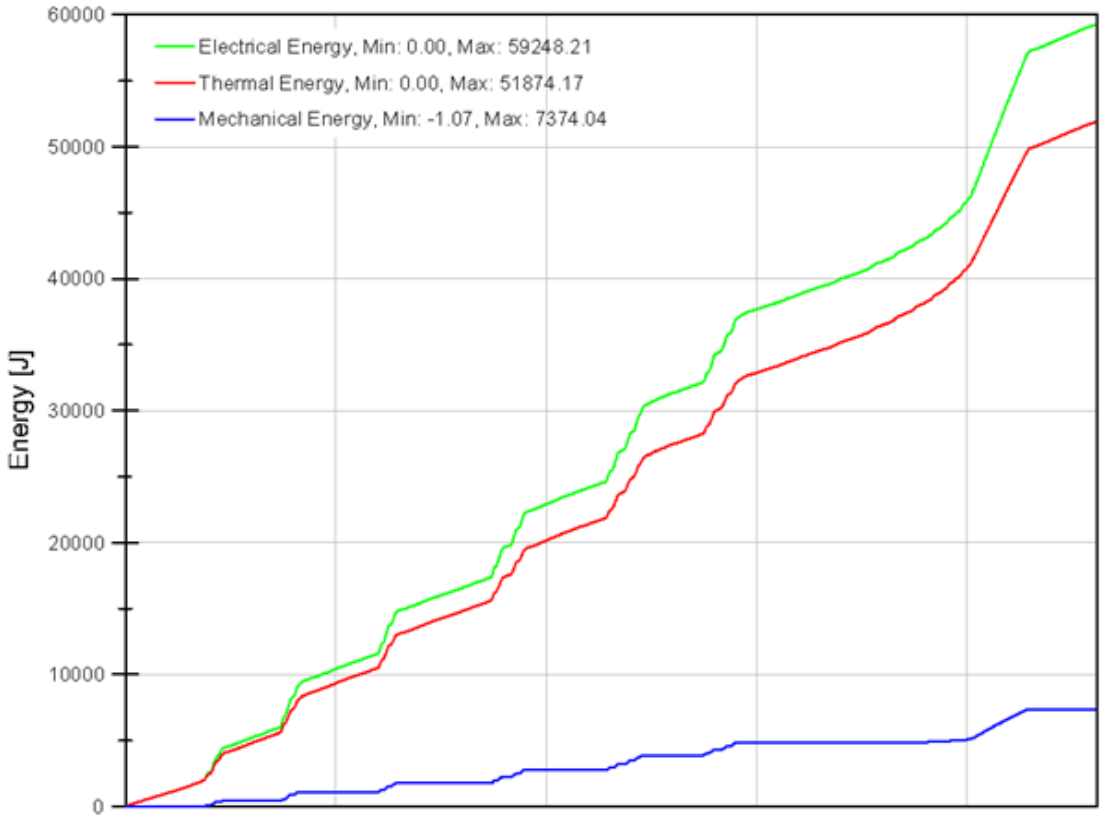

Figure K-74 Short Mission at 70°C Environment Temperature—Calculated COE

Extended Mission Test Summary

Extended mission profile was artificially created based on EMA performance data and simulated realistic mechanical duty cycle and ambient conditions. Extended mission was executed against an artificially created environment temperature profile based on 1% hot day conditions. Overall efficiency of the EMAS for the entire mission was 4% because EMAS was operating at low to near zero velocity for a large portion of the time. Note, thermal energy was based on the energy analysis developed in section 4.7.3 and was calculated as the difference in electrical and mechanical energy.

Table K-5 Extended Mission Test COE Summary

Test		Post Test Analysis			
Profile	Profile Description	Electrical Energy [J]	Mechanical Energy [J]	Thermal Energy [J]	Efficiency
Extended Mission	Full mission representative stroke, force at 1% Hot Day environment temperature	1,107,397 ± 6644	40,654 ± 407	1,066,743 ± 6401	4%

Table K-6 Extended Mission Test Thermal Summary

Test		Post Test Analysis			
Profile	Profile Description	Peak TC ROC [°C/s]	Max Motor Case-Ambient ΔT [°C]	Avg. Current [A]	Peak Current [A]
Extended Mission	Full mission representative stroke, force at 1% Hot Day environment temperature	0.09	22.00	0.46	6.43

Extended Mission Mechanical Results

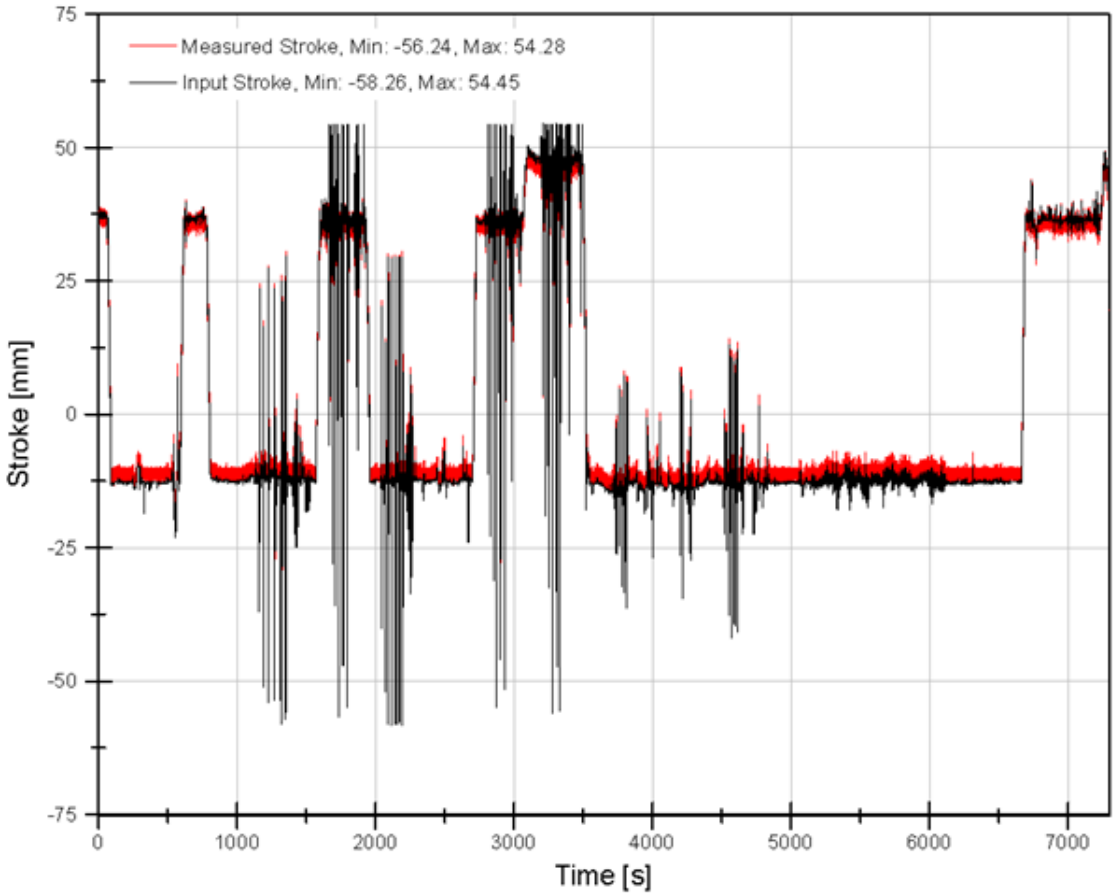

Figure K-75 Extended Mission—Input and Measured Stroke

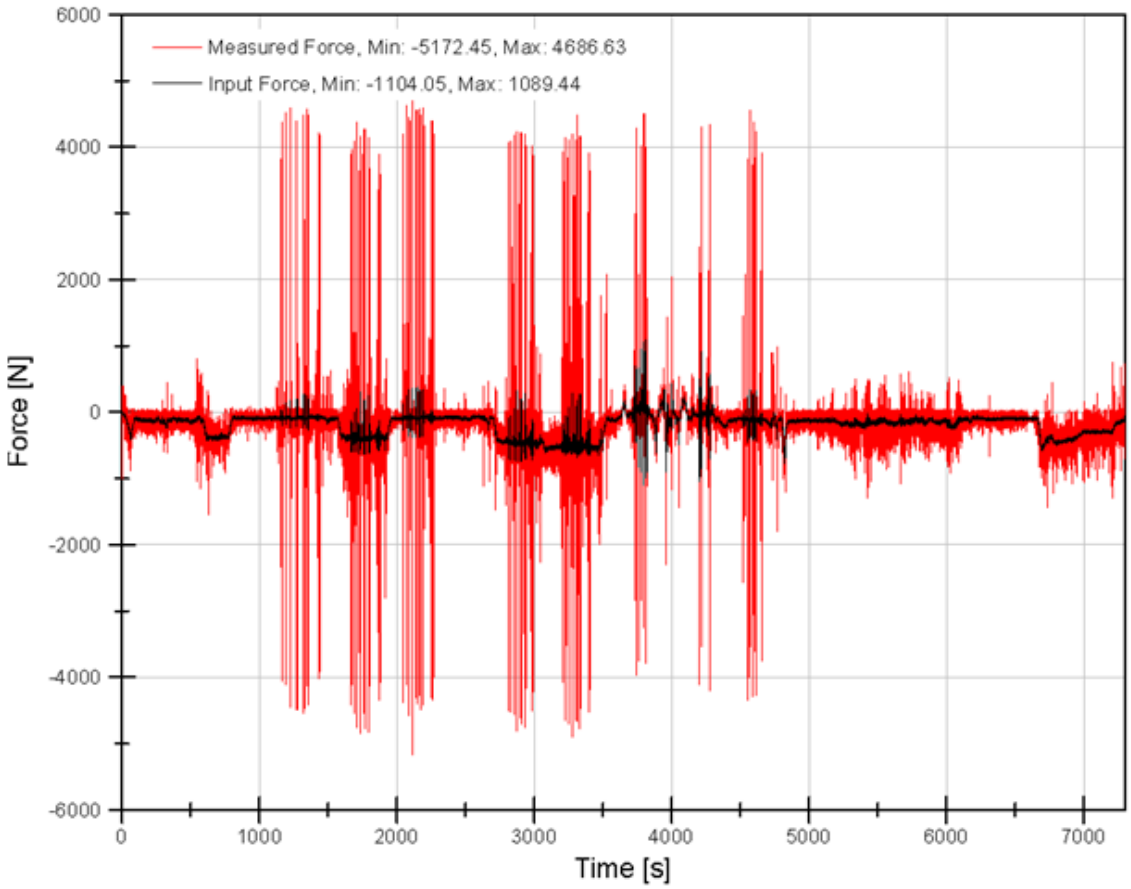

Figure K-76 Extended Mission—Input and Measured Force

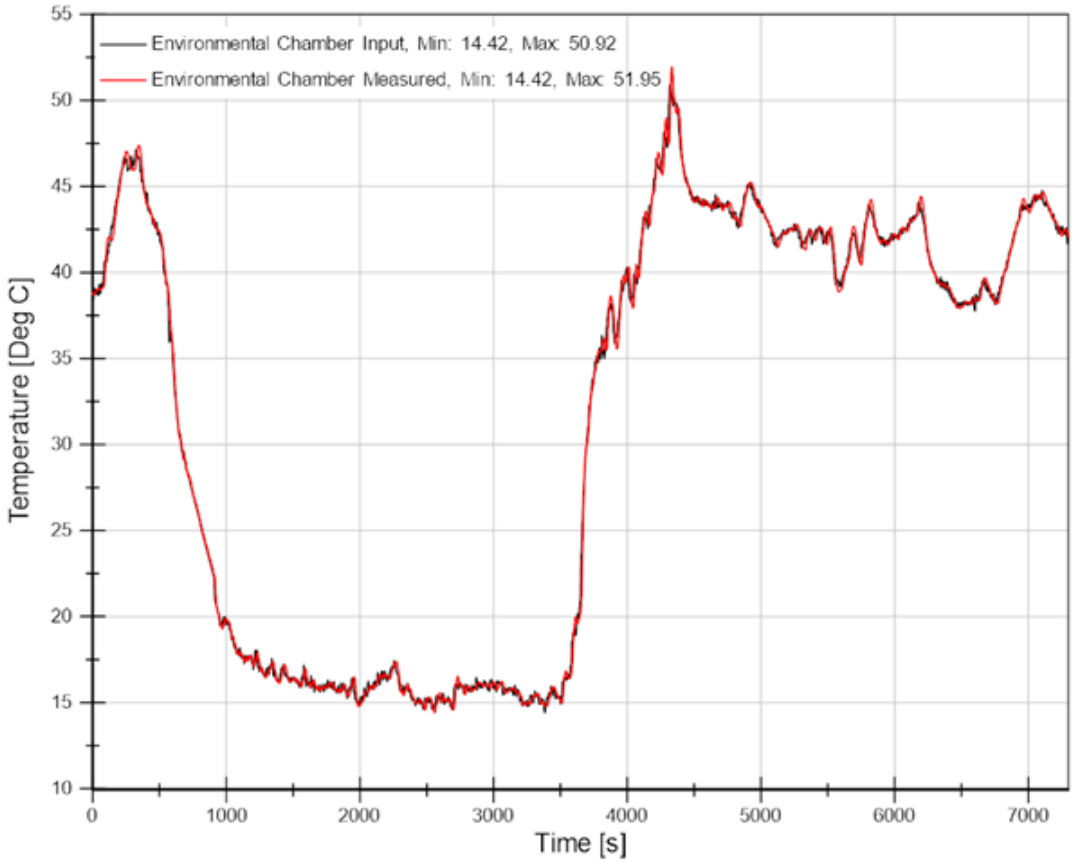

Figure K-77 Extended Mission—Input and Measured Environment Temperature

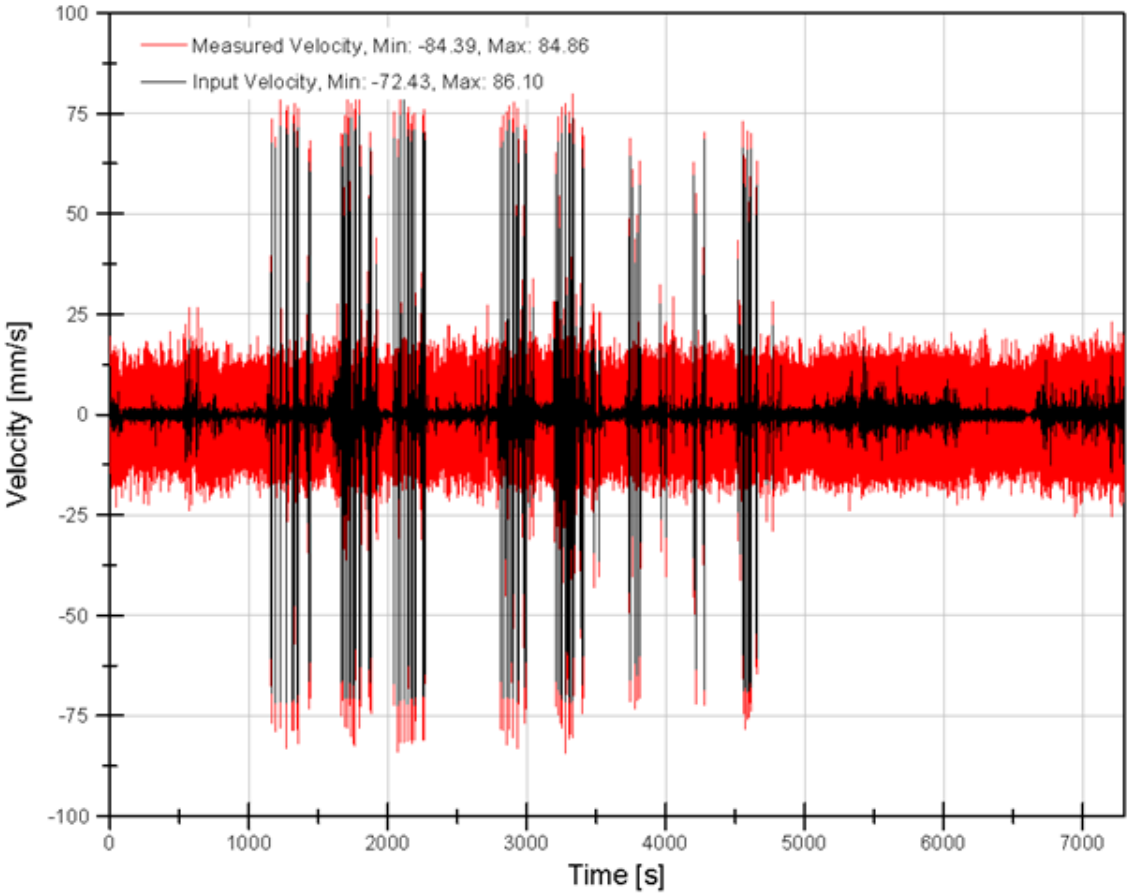

Figure K-78 Extended Mission—Calculated Velocity

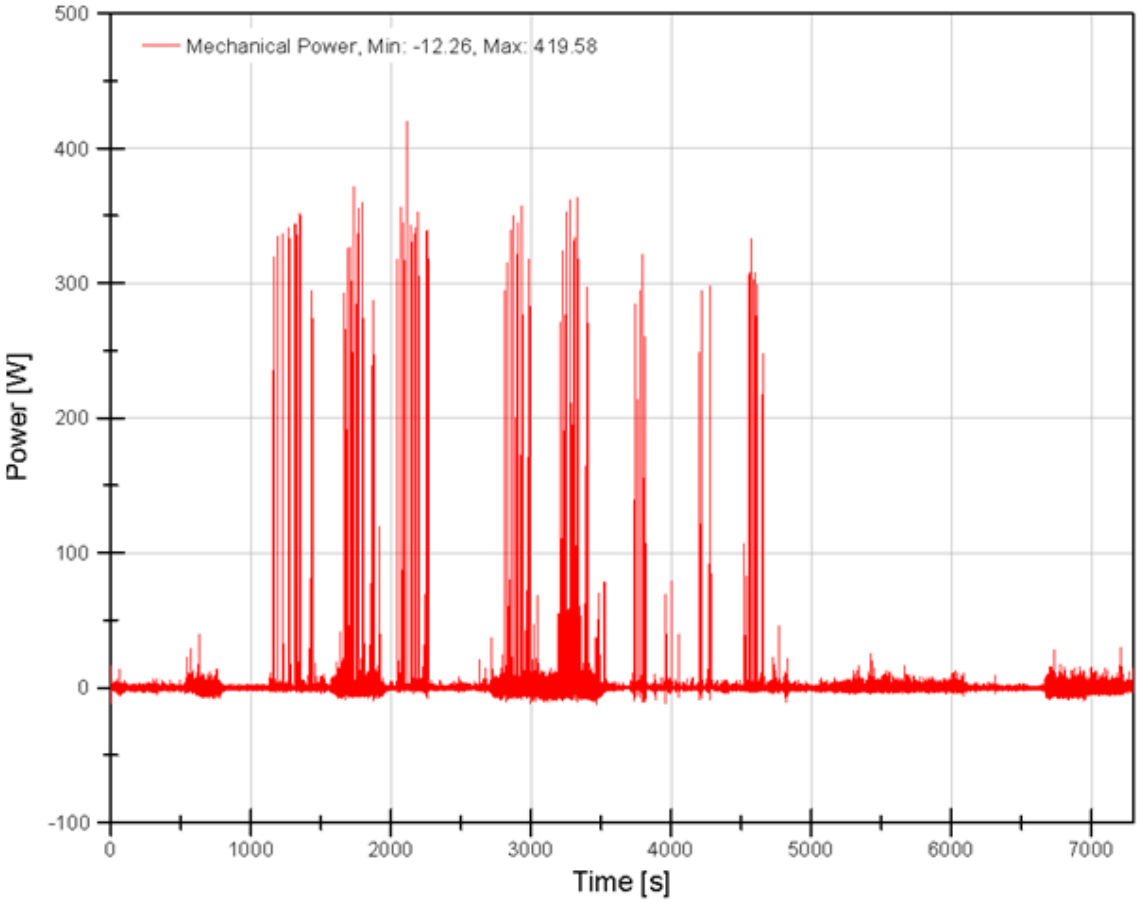

Figure K-79 Extended Mission—Calculated Mechanical Power

Extended Mission Electrical Results

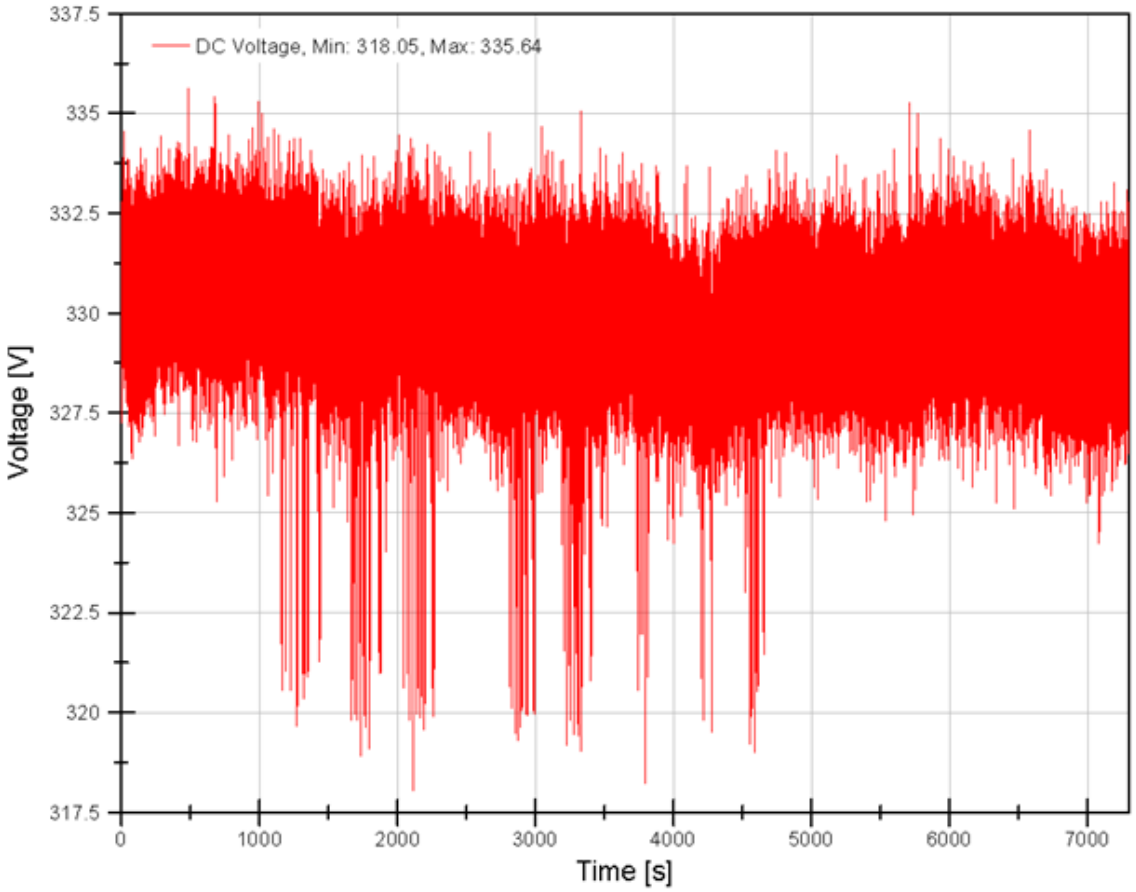

Figure K-80 Extended Mission—Measured DC Bus Voltage

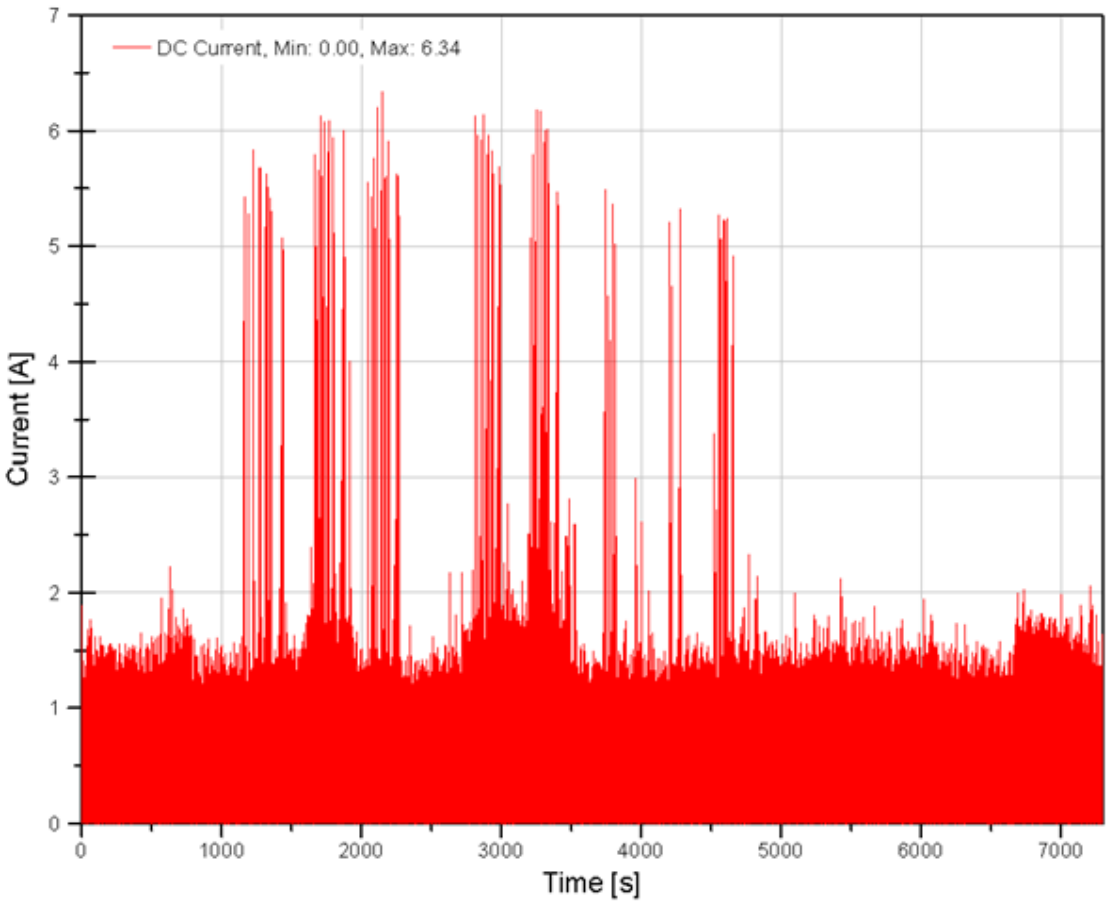

Figure K-81 Extended Mission—Measured DC Bus Current

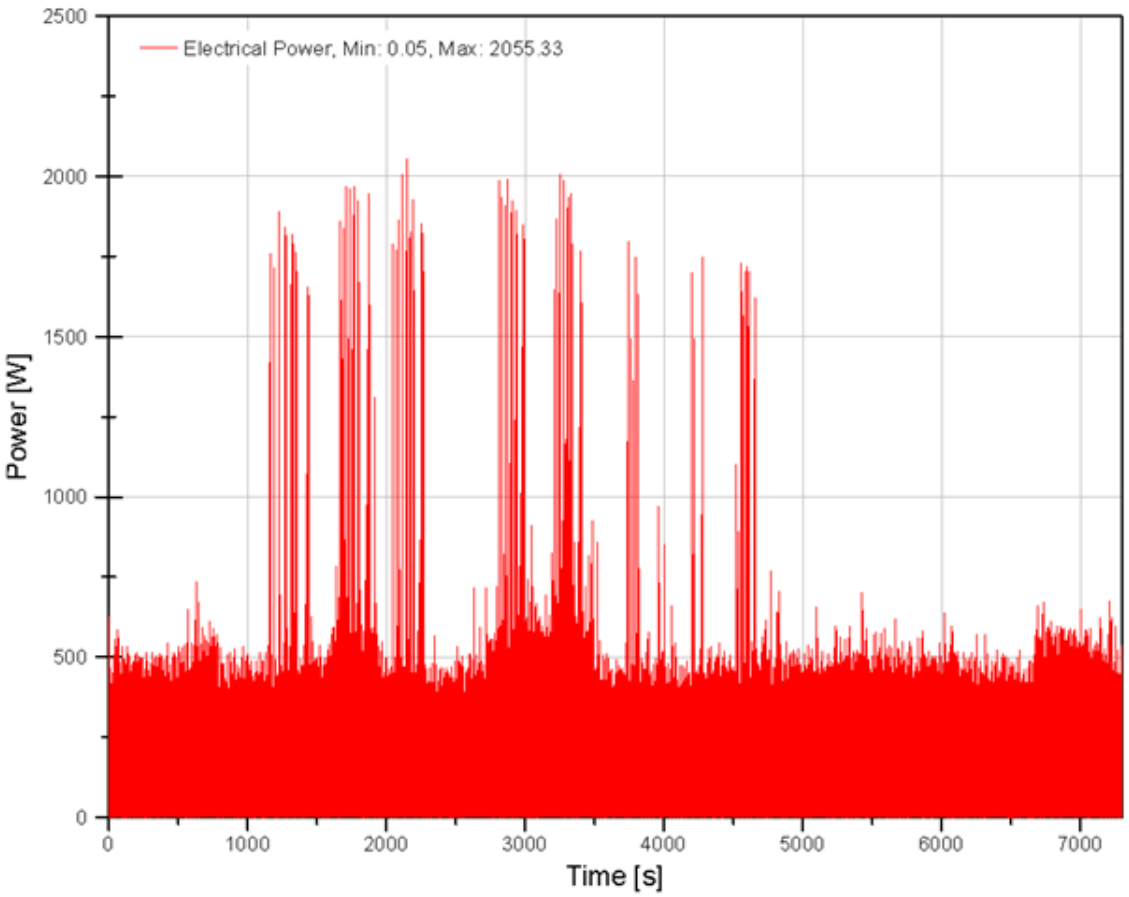

Figure K-82 Extended Mission—Calculated Electrical Power

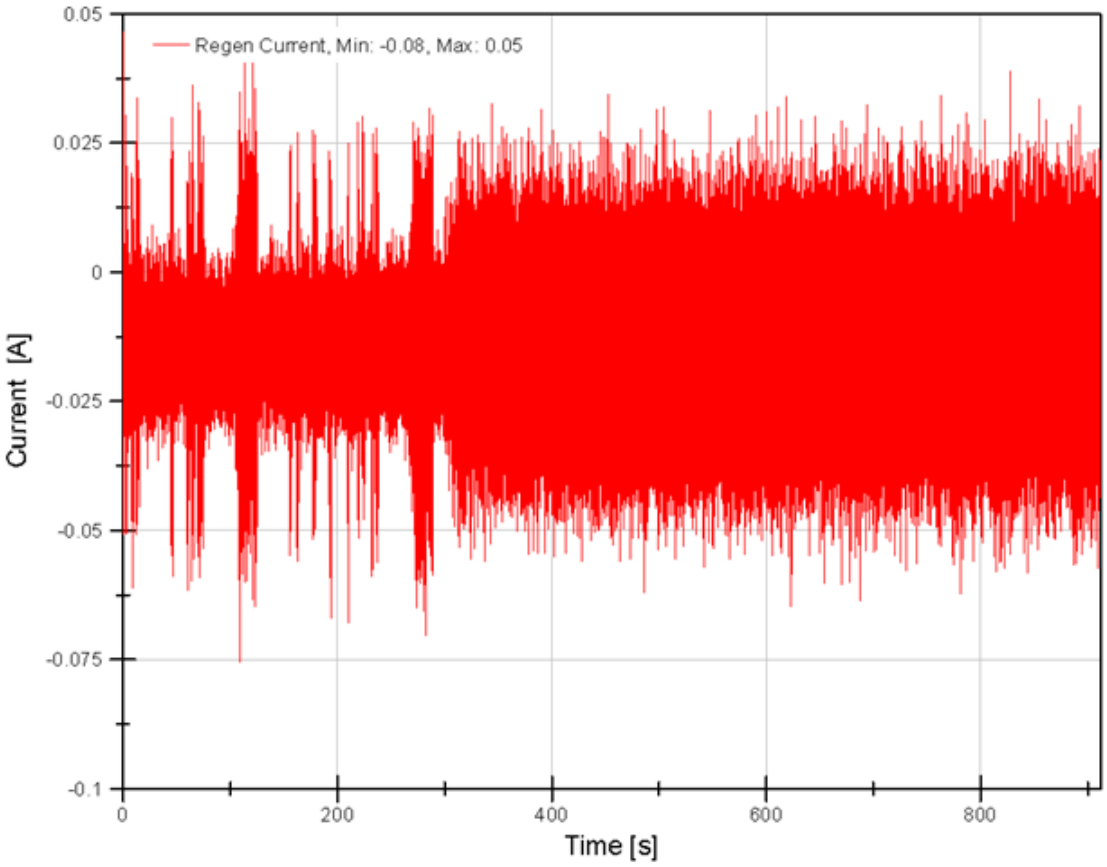

Figure K-83 Extended Mission—Measured Regen Circuit Current

Extended Mission Thermal Results

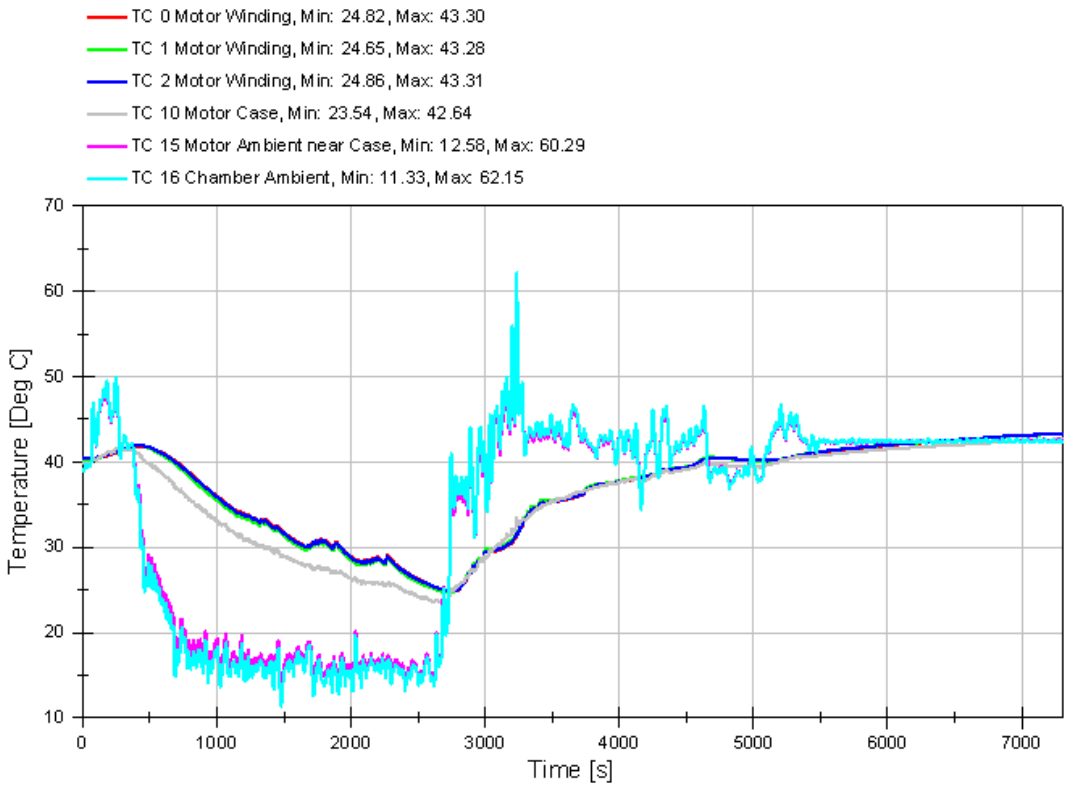

Figure K-84 Extended Mission—EMA Temperature

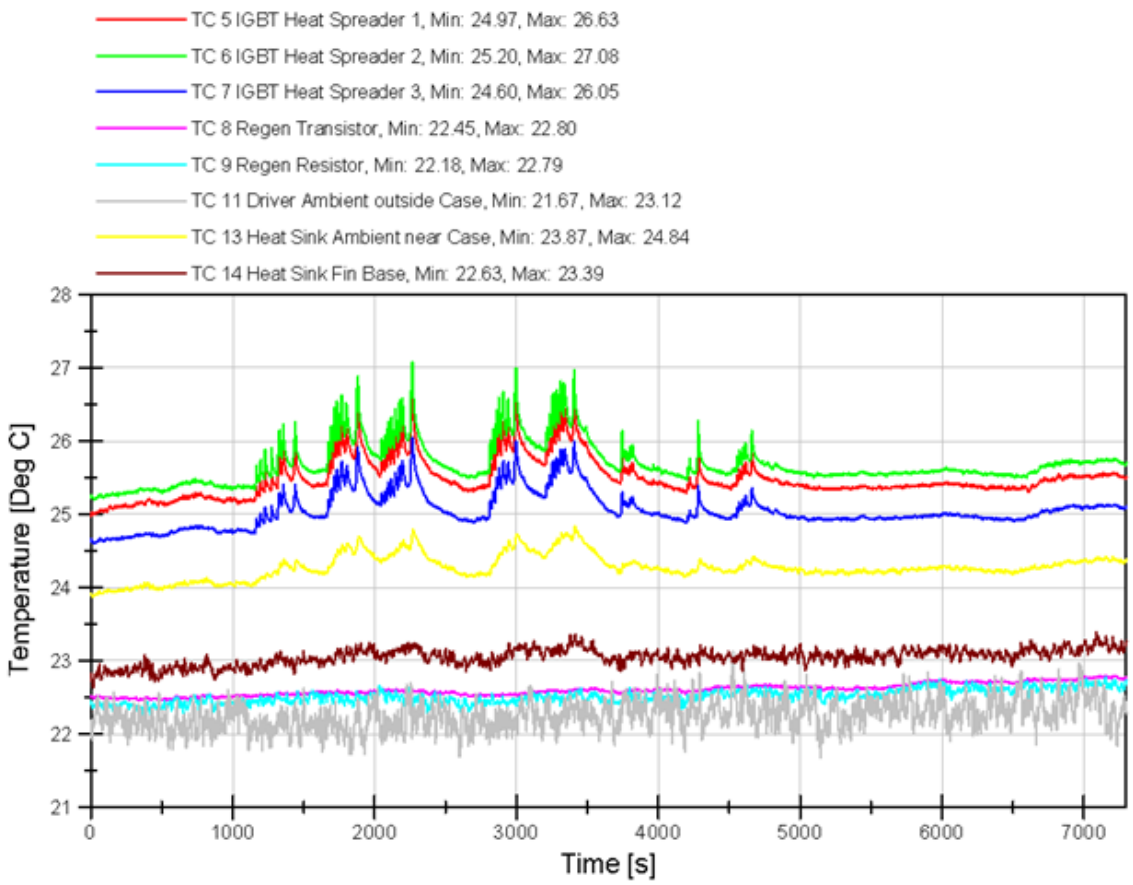

Figure K-85 Extended Mission—Motor Controller Temperature

Note: Motor Controller was outside the environmental chamber.

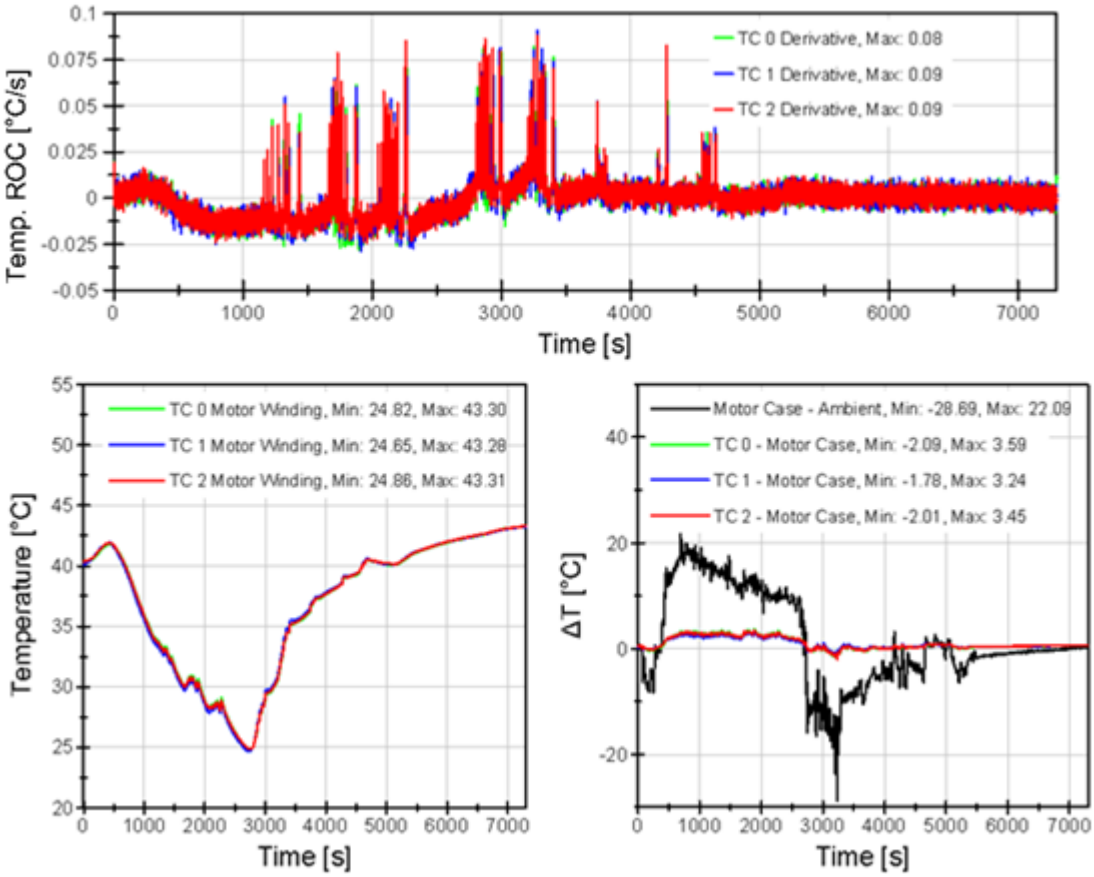

Figure K-86 Extended Mission—Thermal Results

Extended Mission Conservation of Energy

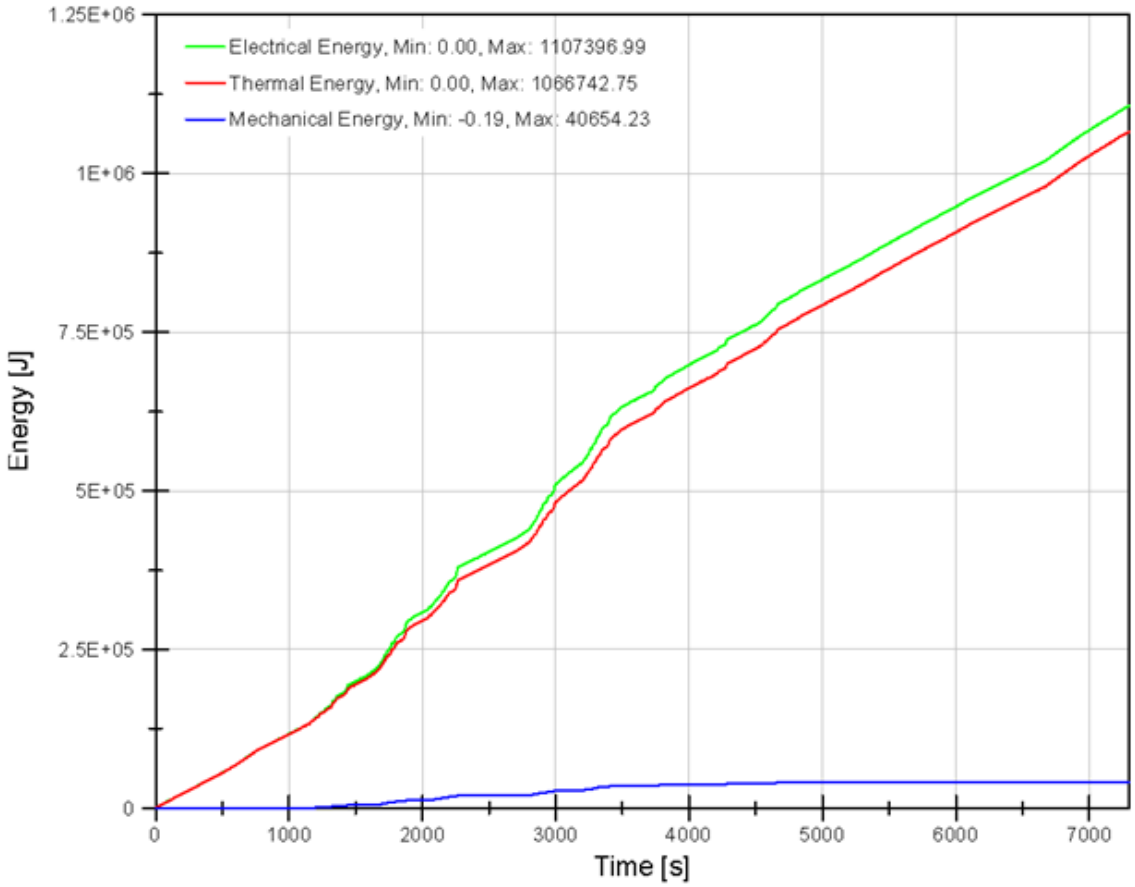

Figure K-87 Extended Mission—Calculated COE